A Symmetry of the Visual World in the Architecture of the Visual Cortex

Dissertation

zur Erlangung des Doktorgrades
der Mathematisch-Naturwissenschaftlichen Fakultäten
der Georg-August-Universität zu Göttingen

vorgelegt von

Michael Schnabel

aus Frankfurt am Main

Göttingen 2008

D7

For my parents, in gratitude
for their love and their trust.

In memory of my grandmother
Simone Marcellin.

Contents

1 Introduction

The brain is complex and dynamic. The spatial and temporal scales of interest to the neuroscientist range from the subcellular level of a few nanometers (membrane channels) to meters (neural circuits) and from the microsecond range (kinetics of ion channels) to several decades (long-term memory). Finding out how it functions is a formidable task, which first requires to arrive at an understanding of its architecture and of its principal building blocks. A prominent and well studied example of such a building block is the primary visual cortex (V1), the part of the brain where electrical signals conveyed by the retinal ganglion cells of both eyes enter the cerebral cortex [4]. Our picture of the type of information processing which occurs at this stage in the brain is owed to the pioneering work of Hubel and Wiesel in the 1960s, which studied the properties of visual cortical neurons by means of electrophysiological single cell recordings [5]. They found that neurons in the visual cortex can be activated by small, elongated stimuli. More precisely, a given neuron would only then respond when the position of the stimulus and its orientation angle matches its receptive field, i.e. its preferred position and preferred orientation. Furthermore they showed, that the preferred positions and orientations of neighbouring neurons tend to be similar and that they would gradually change when the electrode is progressively moved along the cortical surface. How this mapping of space and orientation to the cortical surface is organized over larger regions of the visual cortex, say on the scale of several mm^2, could at that time only be guessed since it had to be extrapolated from painstaking sessions of single cell recordings (Fig. 1.1(**a**)). With the advent of optical imaging techniques in the late 1980s it become possible to record the neural activity simultaneously over large regions of the visual cortex [6, 7, 2] which confirmed previous results obtained from electrode recordings. Whereas space in V1 is represented topographically in a faithful manner (see Chapter 2), preferred orientations of visual cortical neurons were found to form a complex two dimensional pattern, called the orientation preference map (Fig. 1.1(**b**)). At that time it became established, that the smooth progression of preferred orientation is disrupted at point singularities, called pinwheels, which are a characteristic feature of orientation maps [7, 8]. Nowadays, with two-photon calcium imaging it is even possible to record simultaneously the activity and orientation preference of hundreds of neurons with single cell resolution (Fig. 1.1(**c**)). How neurons in V1 become selective for a given orientation and which factors determine whether and when these selectivities become part of an orientation map, today still are open questions.

Experimental evidence suggests that the formation of orientation columns is a dynamical process guided by neural activity and sensitive to visual experience. In normal development, orientation
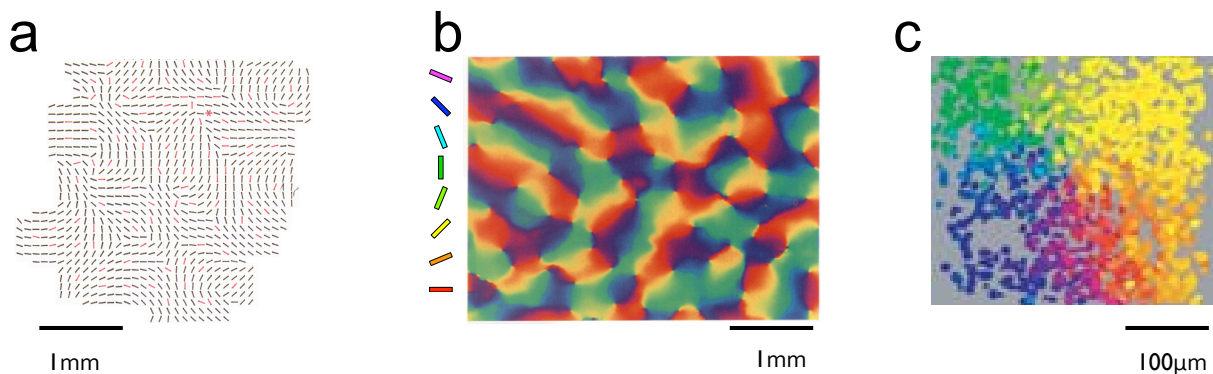
Figure 1.1: Organization of orientation preference in the visual cortex, revealed by different techniques. (**a**) Reconstruction of the orientation map for a roughly 2.5 x 2.5 mm area of the cortex of a cat. Experimentally determined orientation values are shown in red. Asterisk marks a non-oriented response. Scale bar, $1\,mm$. (*adapted from* [1]). (**b**) Distribution of preferred orientations (*left side:* colorcode) revealed by optical imaging of intrinsic signal in the primary visual cortex of a monkey. (*adapted from* [2]). (**c**) Two photon calcium imaging reveals the preferred orientations of cells forming a pinwheel. Scale bar, 100 μm. (*adapted from* [3])

columns first form at about the time of eye opening [9, 10, 11]. Comparison of this process to the development under conditions of modified visual experience demonstrates that adequate visual experience is essential for the complete maturation of orientation columns and that impaired visual experience, as with experimentally closed eye-lids can suppress or impair the formation of orientation columns [11]. Most intriguingly, when visual inputs are experimentally redirected to drive what would normally become primary auditory cortex, orientation selective neurons and a pattern of orientation columns even forms in this brain region that would normally not at all be involved in the processing of visual information [12]. In particular the latter observation strongly suggests that the capability to form a system of orientation columns is intrinsic to the learning dynamics of the cerebral cortex given appropriate inputs. Taken together, these lines of evidence mark the formation of orientation columns as a paradigmatic problem in the dynamics of cortical development and plasticity.

Due to the large number of degrees of freedom of any realistic scale microscopic model of visual cortical development, the description of the development of the pattern of orientation columns by equations for the synaptic connections between individual nerve cells is very complicated. On the order of 10^9 synaptic strengths would be required to realistically describe, for example, the pattern of orientation preference within $1\,mm^2$ of visual cortical tissue. This complexity and the presently very incomplete knowledge about the nature of realistic equations for the dynamics of visual cortical development demand that theoretical analyses concentrate on aspects that are relatively independent of the exact form of the equations and are representative for a large class of models. An appropriate framework for this is provided by models in which the emerging cortical architecture is described by order parameter fields and its development by a dynamics of such fields [13, 14, 15, 16, 17, 18, 19].

By now a couple of such models exist, e.g. [20, 15, 21, 22]. In all of these studies the preferred orientation θ of neurons at cortical location $\mathbf{x}$ is described by a director field $z(\mathbf{x})$ and its dynamics by

$$\partial_t z = F[z] \tag{1.1}$$

where F is some nonlinear functional of the field $z(\mathbf{x})$, which is chosen to be symmetric under certain operations acting on z. For example, since a director field is mapped to itself by orientation shifts of 180°, the dynamics F has to fulfill

$$S_\alpha F[z] = F[S_\alpha z] \tag{1.2}$$

for the special case $\alpha = \pi$, where S_α is the operator which acts on the director field $z(\mathbf{x})$ by shifting all orientations by an angle α while keeping their positions fixed. If, however, Eq.(1.1) applies for *any* value of α, then the dynamics (1.1) is said to be shift symmetric. All models in the reference given before have this type of symmetry. What does it imply? It implies that a given orientation map which is a solution of the dynamics (1.1) is "as good" as an orientation shifted version of it. In comparison, let us consider the invariance of the Schroedinger equation $i\partial_t \psi = H\psi$ under multiplications by a complex phase $\psi \to e^{i\alpha}\psi$. In quantum mechanics, both states are considered as equivalent, since the phase is not an observable. However, one should point out that for the system of orientation maps shift symmetry is not as natural as it is for the Schroedinger equation, and should be rather considered as an additional assumption. The reason for this is that neurons are selective for both, orientations *and* positions, which should therefore be handled within a *single* coordinate frame. As a consequence, operations which are acting on orientation and space in a coordinate way, so called "shift-twists" [23], are more appropriate. Therefore it is of interest to identify and characterize models of the form (1.1), which are symmetric under shift-twist, but not under orientation shifts, Eq. (1.2), and which might lead to a better description of orientation map development in the brain.

The work presented in this thesis is devoted entirely to this task. We will discover that this apparently simple observation leads to substantial but in a way subtle consequences for the type of patterns expected to form in the brain. The organization of this thesis is as follows. In Chapter 2 we present the basics on orientation map development and set the mathematical framework, in Chapter 3 we identify signatures of shift-twist symmetry in a model independent statistical framework and develop tools which allow to extract and to quantify these signatures from brain imaging data. In Chapter 4 we examine the general consequences of shift-twist symmetry on pattern selection and apply these results to a concrete model dynamics for which shift symmetry can be continuously broken. In Chapter 5 we apply the tools developed in the previous chapters to a large dataset of tree shrew orientation maps. In order explain the new effects found in the tree shrew dataset in Chapter 6 we examine a model in which pattern formation in the visual cortex is driven by the statistics of natural scene stimuli. A summary of each chapter and a discussion of the main results is given in Chapter 7.

2 Basics

2.1 Orientation Maps

In most areas of the cerebral cortex, information is processed in a 2-dimensional (2D) array of functional modules called cortical columns [24, 25]. Individual columns are groups of neurons extending vertically throughout the entire cortical thickness that share many functional properties. Orientation columns in the visual cortex are composed of neurons preferentially responding to visual contours of a particular stimulus orientation [5]. In a plane parallel to the cortical surface, neuronal selectivities vary systematically, so that columns of similar functional properties form highly organized 2D patterns, known as functional cortical maps. In the case of orientation columns this kind of pattern is called the orientation preference map (Fig. 2.1(**b**)).

Experimentally, the pattern of orientation preferences can be visualized using optical imaging of hemodynamic signals [26, 7]. In such an experiment, the activity patterns $E(\mathbf{x}|\phi_j)$ produced by stimulation with a grating of orientation ϕ_j are recorded. Here $\mathbf{x}$ represents the location of a column in the cortex. Using the activity patterns $E(\mathbf{x}|\phi_j)$, a field of complex numbers $z(\mathbf{x})$ can be constructed that completely describes the pattern of orientation columns,

$$z(x) = \sum_j e^{2i\phi_j} E(\mathbf{x}|\phi_j)$$

The pattern of orientation preferences $\theta(\mathbf{x})$ is then obtained from $z(\mathbf{x})$ as follows,

$$\theta(\mathbf{x}) = \frac{1}{2} \arg z(\mathbf{x}).$$

A typical example of such activity patterns $E(\mathbf{x}|\phi_j)$ and the patterns of orientation preferences derived from them is shown in Fig. 2.1.

2.2 Orientation Map Development

How orientation selectivity develops in visual cortical neurons and which factors control whether it organizes in orientation maps or not, still are open questions. Experimental studies on the ferret brain have shown that orientation maps, which are spatially modulated structures, emerge from an almost unselective, homogeneous state at around the time of eye opening [9, 28]. These modulations consolidate within a couple of days and reach adult levels after roughly two weeks. In this aspect they resemble other pattern forming systems occurring in different physical and biological contexts. For example, application of a thermal gradient to a thin fluid layer
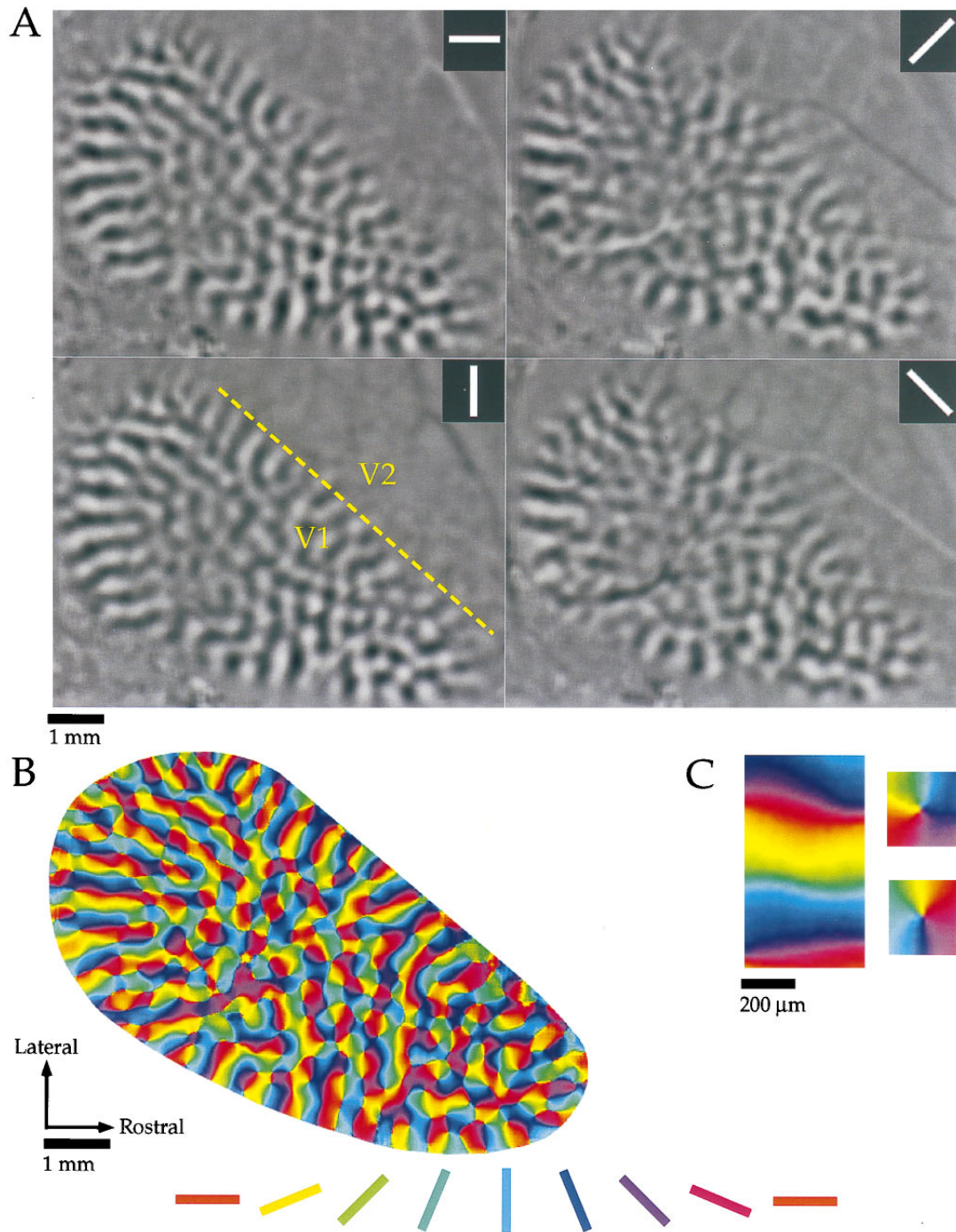
Figure 2.1: Patterns of orientation columns in the primary visual cortex of a tree shrew visualized using optical imaging of intrinsic signals (Figure adapted from [27]). Activity patterns resulting from stimulation with oriented gratings of four different orientations (0°, 45°, 90°, 135°) are shown in (**a**). White bars depict the orientation of the visual stimulus. Activated columns are labeled dark grey. The used stimuli activate only columns in the primary visual cortex (V1). The pattern of orientation preferences calculated from such activity patterns is shown in (**b**). The orientation preferences of the columns are color coded as indicated by the bars. (**c**) The pattern commonly exhibits both linear zones *(left)* and pinwheel arrangements *(right)*.

leads to the formation of convection rolls, which organize in regular patterns, such as stripes or hexagons [29, 30], a phenomenon called Rayleigh-Benard convection. Similar patterns are observed in the Faraday experiment, in which a shallow horizontal layer of fluid is periodically shaken up and down [31, 32]. In all of these cases the driving force, e.g. the size of the thermal gradient or the amplitude of the shaking, has to exceed a certain critical value, in oder to observe pattern formation. Below this value the homogeneous state is stable. Viewed from a dynamical systems perspective, the remodeling of the cortical network described above is a process of dynamical pattern formation. In this picture, spontaneous symmetry breaking in the developmental dynamics of the cortical network underlies the emergence of cortical selectivities such as orientation preference [33].

The particular scenario sketched above can be described in terms of a supercritical bifurcation where the homogeneous state looses its stability and spatial modulations of some typical wavelength Λ start to grow. A well studied model reproducing this type of behaviour is provided by the Swift-Hohenberg (SH) equation,

$$\partial_t u(\mathbf{x}) = \left(r - (k_c^2 + \Delta)^2 \right) u(\mathbf{x}) - u^3(\mathbf{x}) \tag{2.1}$$

where $u(\mathbf{x})$ denotes a real valued scalar field defined over $\mathbf{x} \in \mathbb{R}^2$ and $k_c = 2\pi/\Lambda$ is the typical wavenumber of the pattern. The homogeneous state $u(\mathbf{x}) = 0$ is a stationary solution of (2.1), however, its stability depends on the control parameter r. This can be seen by considering the linear part of (2.1) which has the Fourier representation

$$\partial_t \hat{u}(\mathbf{k}) = \lambda(|\mathbf{k}|)\hat{u}(\mathbf{k}) \tag{2.2}$$

where the growth rate $\lambda(k)$ of the Fourier modes $e^{i\mathbf{k}\mathbf{x}}$ with $|\mathbf{k}| = k$ is given by

$$\lambda(k) = r - (k_c^2 - k^2)^2. \tag{2.3}$$

As shown in Fig. 2.3 the profile of $\lambda(k)$ exhibits a maximum at $k = k_c$. For $r < 0$ all modes are damped since $\lambda(k) < 0$ for all wavenumbers k and the homogeneous state is stable. This is not longer the case for $r > 0$ when modes on the critical circle $|\mathbf{k}| = k_c$ acquire a positive growth rate and now start to grow, resulting in patterns with a typical wavelength Λ. After a transient phase of exponential growth the dynamics of the pattern is slowed down by the nonlinearity in (2.1) and eventually settles into an attractor which describes the final pattern. Usually, the field $u(\mathbf{x})$ represents the local value of some macroscopic order parameter of the system, such as the average velocity of the particles, and thus typically implies a local averaging over the microscopic degrees of freedom, such as individual particle velocities. As an effective model the Swift-Hohenberg equation does not depend on microscopic details and thus can be applied to a variety of different systems. In a pioneering study, published in 2005, Wolf devised a way to describe orientation map development by a generalized Swift-Hohenberg equation, which was extended in several important aspects in order to account for the patterns observed in the brain [34, 22]. The main aspects of this theory are presented next.

The goal is to characterize the class of models which are intended to describe the dynamics of the complex order parameter field $z(\mathbf{x})$, representing the orientation map, and which are able to predict irregular, aperiodic patterns as those found in the primary visual cortex. These models are assumed to have the following general form

a
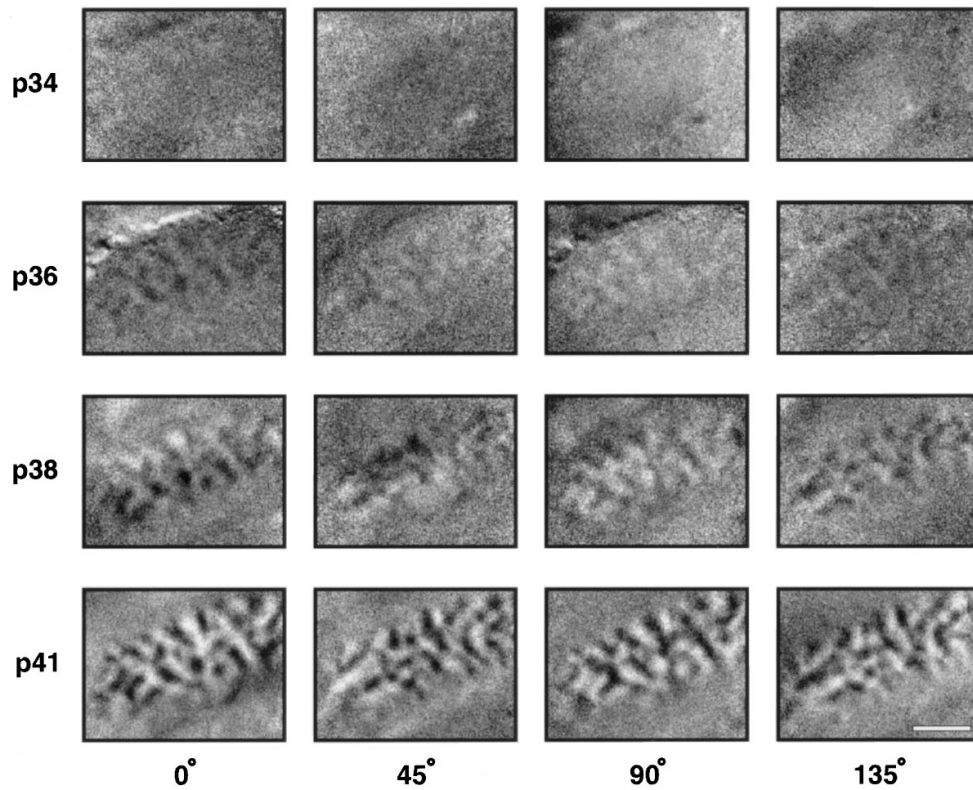
b
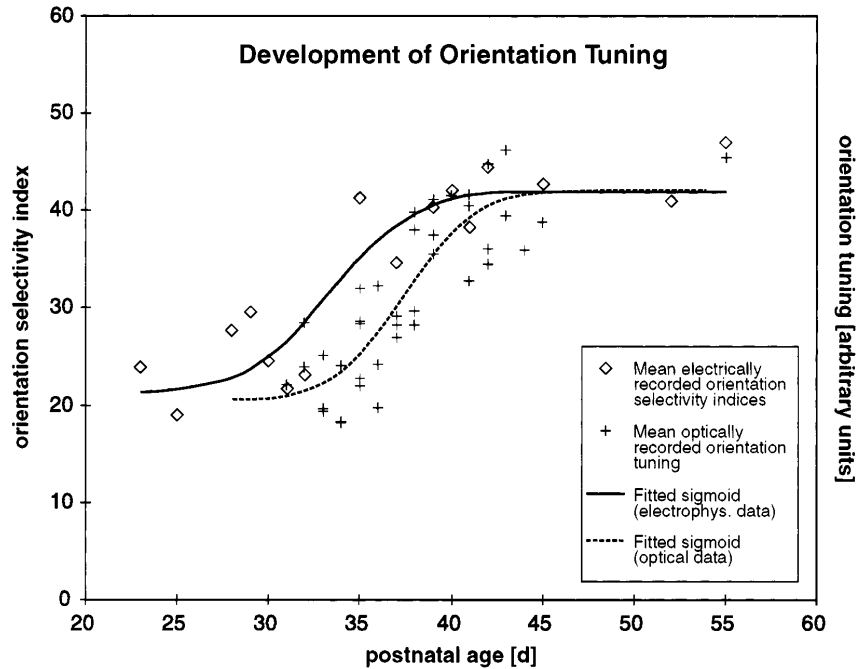
Figure 2.2: Orientation map development in the ferret. (**a**) Patterns of orientation columns in the primary visual cortex of a ferret at four different ages. Ages indicated in postnatal days on the *left* of the rows. Each column of single-condition maps shows orientation maps recorded in response to a particular orientation of a moving square-wave grating (0° = horizontal). Scale bar, *2mm.* (From [9]). (**b**) Age dependent orientation selectivity (pattern amplitude) in ferret visual cortex. (From [28]).
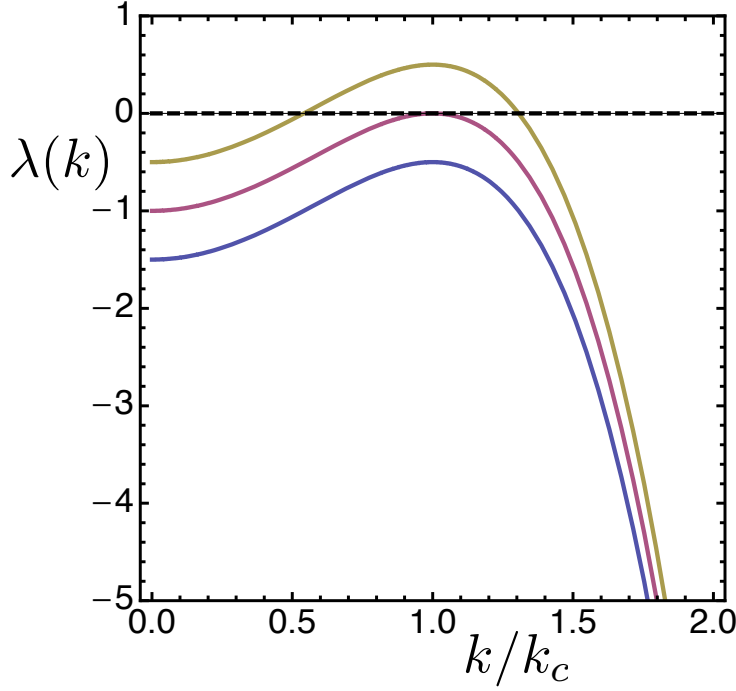
Figure 2.3: The spectrum of the linear Swift-Hohenberg operator $L = r - (k_c^2 + \Delta)^2$ for different values of r. For $r = -.5$, all modes are exponentially damped *(blue)*, for $r = 0$, modes with wavenumber $k = k_c$ become marginally unstable *(red)*, for $r = .5$, the entire interval of modes with $\lambda(k) > 0$ is susceptible to growth *(yellow)*.

$$\partial_t z(\mathbf{x}) = F[z] \tag{2.4}$$

where $F[z]$ is a nonlinear functional of $z(\mathbf{x})$ which remains to be specified. A first step in this direction can be made by considering the symmetries of the system which must be reflected in the functional form of Eq.(2.4). Considered anatomically, the cortical tissue appears rather homogeneous and isotropic [35]. It is thus very plausible to require that the dynamics of orientation map development is symmetric, i.e. transforms equivariantly, with respect to translations

$$F[T_{\mathbf{a}}z] = T_a F[z] \quad \text{with} \quad z(\mathbf{x}) \to T_{\mathbf{a}} \, z(\mathbf{x}) := z(\mathbf{x} + \mathbf{a}) \tag{2.5}$$

and the $O(2)$ group consisting of coordinate rotations

$$F[D_\phi z] = D_\phi F[z] \quad \text{with} \quad z(\mathbf{x}) \to D_\phi \, z(\mathbf{x}) := z(\Omega_\phi^{-1}\mathbf{x}) \tag{2.6}$$

and reflections

$$F[Pz] = PF[z] \quad \text{with} \quad z(\mathbf{x}) \to P \, z(\mathbf{x}) := z(\bar{\mathbf{x}}) \tag{2.7}$$

where $\bar{\mathbf{x}} = (x_1, -x_2)$. The functional form of $F[z]$ gets substantially further constrained if, in addition, equivariance of Eq.(2.10) under the $U(1)$ group generated by orientation shifts

$$z(\mathbf{x}) \to S_\theta \, z(\mathbf{x}) := e^{2i\theta} z(\mathbf{x}) \tag{2.8}$$

and the complex conjugation

$$z(\mathbf{x}) \to Cz(\mathbf{x}) := \bar{z}(\mathbf{x}). \tag{2.9}$$

is assumed, since for this case the operator $F[z]$, written as a power series in the field, can only depend of terms which involve odd powers of z. This kind of symmetry, simply called *shift symmetry* in the following, implies that the spatial arrangement of iso-orientation domains contains no information about the orientation preference of the columns. Finding out whether this is really the case or not is the primary purpose of this thesis. For the time being, in [34, 22], shift symmetry was simply added to the list of basic symmetry requirements for a candidate model of orientation map formation.

As a straightforward generalization of the Swift-Hohenberg equation from the real to the complex valued case it seems natural to study the following equation

$$\partial_t z(\mathbf{x}) = \left(r - (k_c^2 + \Delta)^2 \right) z(\mathbf{x}) - |z(\mathbf{x})|^2 z(\mathbf{x}) \qquad (2.10)$$

Unlike in the case of real values the dynamics (2.10) exhibits a nontrivial set of exact solutions, which consist of plane waves

$$z(\mathbf{x}) = \sqrt{r - (k_c^2 - |\mathbf{k}|^2)^2} \, e^{i\mathbf{k}\mathbf{x}}$$

with any wavevector $\mathbf{k}$ for which the growth rate $\lambda(|\mathbf{k}|)$ is positive. Unfortunately, this type of solutions has a severe drawback: Although each orientation is represented to the same amount in such a pattern, the patterns lack pinwheels, characteristic topological point defects around which each orientation is represented once (see Fig.2.4(**a**)). Pinwheels can be classified according to their topological charge

$$q_i = \frac{1}{2\pi} \oint_{\mathcal{C}_i} d\mathbf{s} \nabla \theta(\mathbf{x})$$

where $\mathcal{C}_i$ is a closed curve around a single pinwheel center at $\mathbf{x}_i$. Since θ is a cyclic variable within the interval $[0, \pi]$ and a continuous function of $\mathbf{x}$ except at the pinwheel centers, q_i can in principle only have the values

$$q_i = \pm \frac{n}{2}$$

where $n \in \mathbb{N}_+$ [36]. If its absolute value $|q_i|$ is $1/2$, each orientation is represented exactly once in the vicinity of a pinwheel center. In experiments only pinwheels with a topological charge of $\pm 1/2$ are observed, which are simple zeros of the field $z(\mathbf{x})$. This organization has been confirmed in a large number of species and is therefore believed to be a general feature of visual cortical orientation maps. Indeed, as shown in [37], the model (2.10) and many similar models with same symmetries and qualitative features are unable to explain the intricate patterns seen in real maps, since any pattern, even if it contained plenty of pinwheels at the beginning, is poised to evolve towards a solution with very low pinwheel density or no pinwheels at all.

2.3 The Wolf Model

In order to resolve this issue, Wolf proposed to extend the model (2.10) by introducing additional nonlocal 3rd order terms, where the coupling between two distal points of the field $z(\mathbf{x})$ and $z(\mathbf{y})$ is mediated by some interaction kernel $K(\mathbf{y} - \mathbf{x})$. For a Gaussian kernel the extended model is
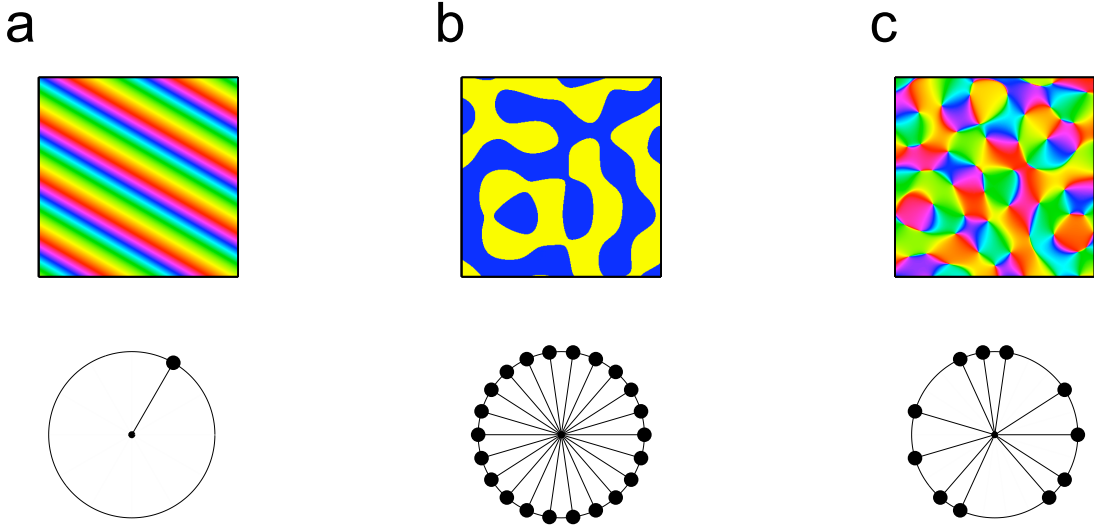
Figure 2.4: Examples of solutions predicted for different types of Swift-Hohenberg models. *Top row:* Pattern of the orientation map, *bottom row:* Fourier modes of the pattern on top. (**a**) Plane waves, no pinwheels. (**b**) Irregular, aperiodic pattern, which is blind to other than two orientations. (**c**) Essentially complex planform.

given by the following integro-differential equation

$$
\partial_t z(\mathbf{x}) = \underbrace{\left(r - (k_c^2 + \Delta)^2\right) z(\mathbf{x})}_{\text{linear, } \textbf{local}} + \underbrace{(1 - g)|z(\mathbf{x})|^2 z(\mathbf{x})}_{\text{nonlinear, } \textbf{local}} \tag{2.11}
$$
$$
- \frac{2 - g}{2\pi\sigma^2} \int d^2\mathbf{y} \underbrace{(|z(\mathbf{y})|^2 z(\mathbf{x}) + \frac{1}{2} z(\mathbf{y})^2 \bar{z}(\mathbf{x}))e^{-|\mathbf{y}-\mathbf{x}|^2/(2\sigma^2)}}_{\text{nonlinear, } \textbf{nonlocal}}
$$

which depends on two additional parameters. The parameter $\sigma \geq 0$ determines the range of the nonlocal interaction, and $g \in [0, 2]$ controls which type of nonlinearity stabilizes the dynamics. For $1 < g \leq 2$ both, the local and the nonlocal part, have a negative prefactor and thus exert a stabilizing effect, whereas for $0 \leq g \leq 1$ this applies just for the nonlocal part. With regard to other nonlinear model equations often encountered in physics, such as the nonlinear Schroedinger equation, where all terms are local, the concept of nonlocal terms first appears unusual and unfamiliar, however in the context of the brain it is actually very natural: In the visual cortex two neurons which are linked by a single axonal connection can lie several millimeters apart. Examples of connection profiles of V1 neurons in the tree shrew, obtained by local tracer injections, are shown in Fig. 2.5. They have the following properties:

- Connections occur over several millimeters, or correspondingly, over many hypercolumns, which typically are separated by the distance Λ. Thus, in the model (2.11) as a realistic choice for σ one would expect the range $\sigma/\Lambda \gg 1$.

- They are patchy. In other words, groups of neurons with a similar orientation preference, as for example $90°$ preferring neurons in Fig. 2.5(**a**), are more likely to be connected than groups of neurons whose orientation preferences do not match. Very similar results are
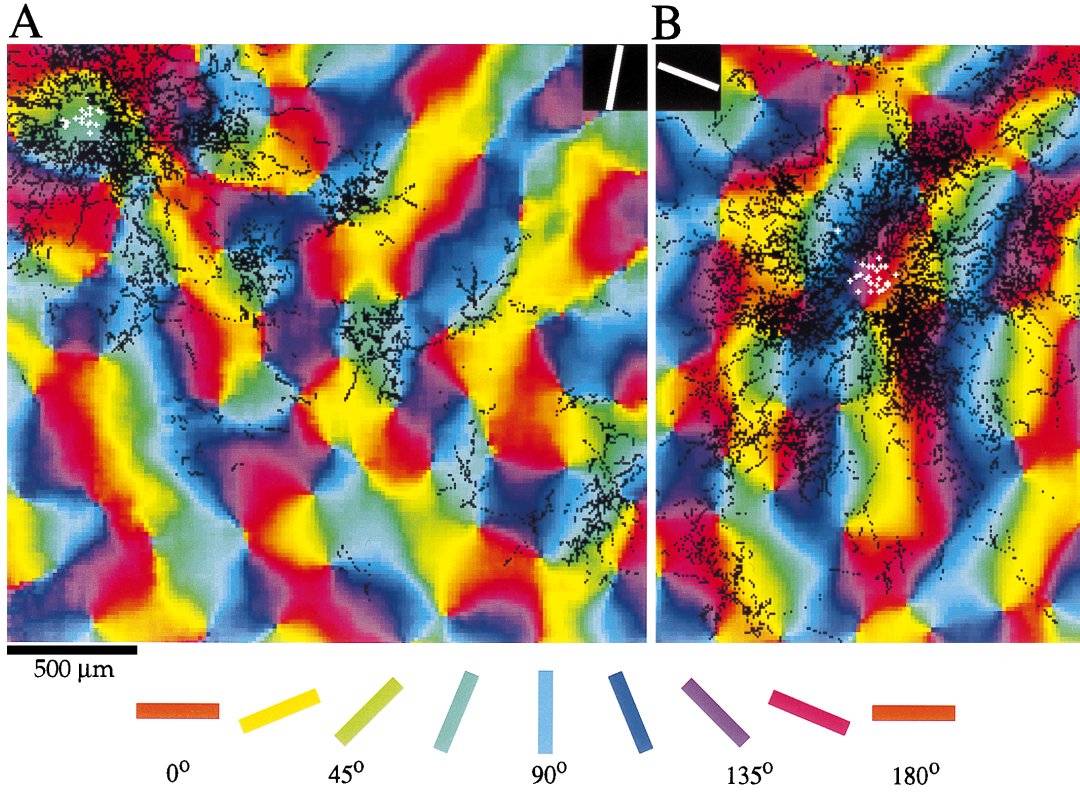
Figure 2.5: Lateral synaptic connections of orientation columns in the primary visual cortex of a tree shrew. Preferred orientations are color coded as indicated by the bars. Black dots represent individual output synapses of the neurons whose cell body positions are marked by white crosses. (From [27]).

found in other mammals with orientation maps, such as in the cat [38, 39, 40], ferret[41, 42] or in the monkey [43, 44].

The nonlocal terms in Eq.(2.11) consist of two different types, $|z(\mathbf{y})|^2 z(\mathbf{x})$ and $z(\mathbf{y})^2 \bar{z}(\mathbf{x})$, both of which transform equivariantly with respect to orientation shifts. As shown in [37] both are necessary in order to obtain realistic orientation maps. For example, just including the first type of nonlocal nonlinearity leads to patterns as in Fig. 2.4(**b**), which develop orientation preferences only for two angles which are orthogonal to each other, i.e. θ and $\theta + \pi/2$, and thus are "blind" to other orientations. For $\theta = 0$ those patterns correspond to fields $z(\mathbf{x})$ which are real valued. In contrast, when both terms are included, the dynamics has quasiperiodic attractors which resemble realistic patterns. This type of solutions can be written as a superposition of a finite number of modes, also called *planform*s,

$$z(\mathbf{x}) = \sum_{j=0}^{N-1} A_j e^{i\mathbf{k}_j \mathbf{x}} \qquad (2.12)$$

with $N = 2n$ wavevectors $\mathbf{k}_j$ which are equidistantly distributed on the critical circle, i.e. $|\mathbf{k}_j| = k_c(\cos\frac{\pi}{n}j, \sin\frac{\pi}{n}j)$. The stationary amplitudes of the solutions as well as their stability can be calculated analytically from the system of *amplitude equations* which for (2.11) has the

general form

$$\dot{A}_j = rA_j + \sum_k g_{jk}|A_k|^2 A_j + \sum_k f_{jk} A_k A_{k-}\bar{A}_{j-} \tag{2.13}$$

where A_{j-} denotes the amplitude of the mode with wavevector $-\mathbf{k}_j$. Amplitude equations are universal, since the general form of Eq.(2.13) is dictated by the symmetries and the type of the bifurcation, not by the details of the model, which enter only in the coupling matrices g_{jk} and f_{jk}. Hence, knowing the appropriate symmetries of a system and the type of the bifurcation one could also, in principle, directly write down the corresponding set of amplitude equations and use them as a starting point for finding solutions. In Chapter 4 we will present in detail how the particular expressions for the coupling matrices g_{jk} and f_{jk} are obtained from the nonlinearities in (2.10) by a multiscale expansion of the dynamics. The family of solutions can be classified according to their number n of active modes and is depicted in Fig. 2.6. The model has the important feature that for a given wavevector $\mathbf{k}_j$ either the mode A_j (to the wavevector $\mathbf{k}_j$) or the mode A_{j-} (to the wavevector $-\mathbf{k}_j$) is zero. Hence, a particular solution can be written as a particular planform with $N = 2n$ modes,

$$z(\mathbf{x}) = \sum_{j=0}^{n-1} A_j e^{il_j \mathbf{k}_j \mathbf{x}}, \tag{2.14}$$

where the binary variables $l_j \in \{-1, +1\}$ determine which of the n modes $-\mathbf{k}_j$ or $\mathbf{k}_j$ are active. These solutions are called *essentially complex planforms* since $z(\mathbf{x})$ is, by construction, complex valued. For a given n there are 2^n possibilities, however, many of which can be transformed into each other by rotations or reflections thus defining equivalence classes. The actual number of distinct classes is smaller but nevertheless grows exponentially with n. The nonlinearity of the Wolf model when written as a three argument operator

$$N_3[z] = N_3[z, z, \bar{z}]$$

with

$$\begin{aligned} N_3[u, v, w](\mathbf{x}) &= (1-g)u(\mathbf{x})v(\mathbf{x})w(\mathbf{x}) \\ &\quad -\frac{2-g}{4\pi\sigma^2}\int d^2\mathbf{y}\, e^{-|\mathbf{y}-\mathbf{x}|^2/(2\sigma^2)}\left[u(\mathbf{x})v(\mathbf{y})w(\mathbf{y}) + v(\mathbf{x})w(\mathbf{y})u(\mathbf{y}) + w(\mathbf{x})u(\mathbf{y})v(\mathbf{y})\right] \end{aligned}$$

is symmetric under cyclic permutations $N_3[u, v, w] \to N_3[v, w, u]$. As shown in [22] with this permutation symmetry all of these isomers have the same energy and stability properties. Hence, the model (2.10) exhibits a vast number of multistable solutions, which parallels the situation in the visual cortex, where a multitude of qualitatively similar but not identical patterns is found. As is visible from the phase diagram, where the stability regions of essentially complex planforms for different n is plotted as a function of the parameters σ and g, realistic patterns are obtained for $g < 1$ and long-range connections with range $\sigma \gg \Lambda$, which also corresponds to the situation in the brain. We close this section with the remark that the dynamics (2.11) can be written as a gradient descent

$$\partial_t z(\mathbf{x}) = -\frac{\delta}{\delta\bar{z}(\mathbf{x})}E[z]$$

of the Lyapunov (or energy) functional

$$\begin{aligned} E[z] &= -\int d^2\mathbf{x}\left(\bar{z}(\mathbf{x})\left(r - (k_c^2 + \Delta)^2\right)z(\mathbf{x}) + (1-g)|z(\mathbf{x})|^4\right) \\ &\quad +\frac{2-g}{4\pi\sigma^2}\int d^2\mathbf{x}\int d^2\mathbf{y}\left(|z(\mathbf{y})|^2|z(\mathbf{x})|^2 + \frac{1}{2}z(\mathbf{y})^2\bar{z}^2(\mathbf{x})\right)e^{-|\mathbf{y}-\mathbf{x}|^2/(2\sigma^2)} \end{aligned} \tag{2.15}$$
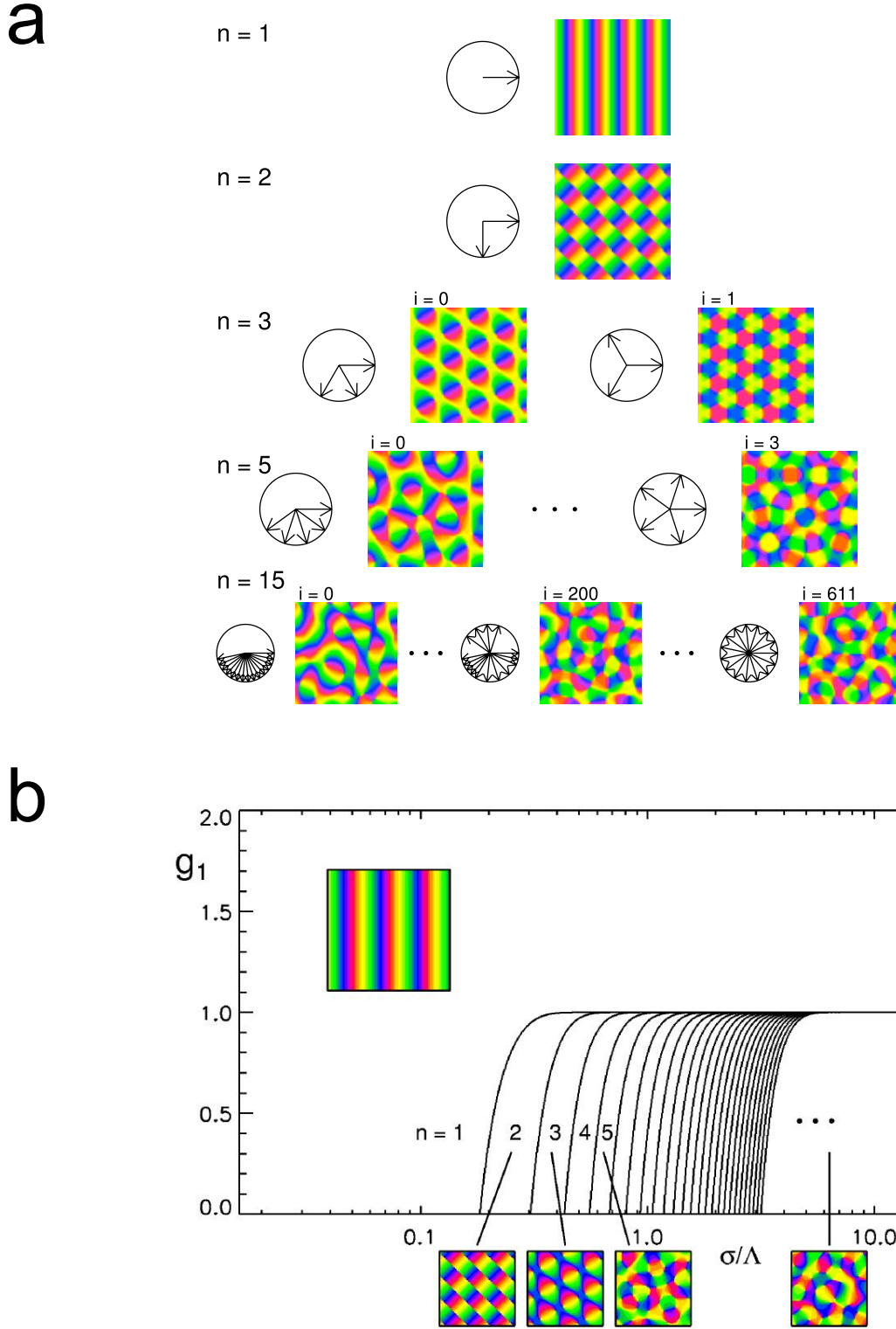
Figure 2.6: Solutions and phase diagram of the generalized Swift-Hohenberg model, Eq.(2.11). (**a**) Examples of essentially complex planforms (n-ECPs) for different numbers of active modes n. The diagrams to the left of each pattern display the position of the wavevectors of active modes on the critical circle. For $n = 3$, 5 and 15 there are 2, 4 and 612 different equivalence classes of ECPs, respectively. (**b**) Phase diagram of the model Eq.(2.11). The graph shows the region in the $(g, \sigma/\Lambda)$-plane in which n-ECPs have minimal energy ($n = 1 - 25$), $n > 25$ dots).

Equivariance of Eq.(2.11) under the operations (2.5)-(2.9), yields to *invariance* of the right hand side of Eq.(2.15) and thus to symmetry of the energy functional under these operations.

2.4 Shift Symmetry Revisited

Is shift symmetry a good assumption? The remaining parts of this thesis are devoted to providing a satisfactory answer to this question. Indeed, a number of well-known equations in physics, such as the complex Ginzburg-Landau or the Schroedinger equation, just to mention a few, are equivariant under global phase shifts, $z(\mathbf{x}) \to e^{i\phi} z(\mathbf{x})$. In particular, this is also the case for the model (2.11), which apparently is a promising candidate for modeling orientation map development. Nevertheless, there are reasons to believe that shift symmetry cannot be taken for granted and why, as a consequence, this assumption has to be carefully reconsidered in the context of models for orientation map development. These are discussed next.

A fundamental concern is raised by the fact that a map of visual space, the visuotopic map, is superimposed onto the same part of the primary visual cortex where the orientation map is found, see Fig. 2.7. In visual cortical neurons orientation selectivity always occurs together with selectivity for stimulus location, such that for animals with orientation maps both systems of maps coexist. Therefore it is in principle required to represent the preferred angles and preferred locations within a single coordinate system. But this view has direct consequences for the symmetries of our model. For instance it is not obvious that rotations of the preferred locations (D_ϕ) can be considered independently from shifts in the preferred orientation (S_θ). Instead, it seems much more appropriate to require symmetry under transformations where *both* kinds of rotations are applied together, so called "shift-twists"[23]. The same is true for the discrete operations, like reflections in space (P) and in angle of preferred orientation (C). In conclusion we argue that the list of symmetries given above, Eqns.(2.6)-(2.9), should be replaced by the following set, which consists of shift-twist rotations

$$
\begin{aligned}
z(\mathbf{x}) \to R_\phi z(\mathbf{x}) \quad &:= \quad S_\phi \circ D_\phi \, z(\mathbf{x}) \\
&= \quad e^{2i\phi} z(\Omega_\phi^{-1} \mathbf{x})
\end{aligned}
\tag{2.16}
$$

and shift-twist reflections

$$
\begin{aligned}
z(\mathbf{x}) \to CP \, z(\mathbf{x}) \quad &:= \quad C \circ P \, z(\mathbf{x}) \\
&= \quad \bar{z}(\bar{\mathbf{x}}),
\end{aligned}
\tag{2.17}
$$

and forms a representation of the $O(2)$ group of orthogonal transformation in two dimensions. Together with the translations, Eq.(2.5), thereby we obtain a representation of the Euclidean group $E(2)$, which can be written as a semidirect product of $2d$-translations and rotations, i.e. $E(2) = \mathbb{R}^2 \rtimes O(2)$. Only if, in addition, symmetry under $U(1)$ orientation shifts is assumed we are back to the symmetry group of the model (2.11), which is given by $\mathbb{R}^2 \times O(2) \times U(1)$ and is isomorphic to $E(2) \times U(1)$. Clearly, such an additional $U(1)$ shift symmetry implies that the spatial arrangement of iso-orientation domains contains no information about the orientation preference of the columns. This might or might not be true in the brain - in Chapter 5 we will provide an answer to this question. In conclusion, whereas symmetry under $E(2)$ shift-twist seems a plausible assumption as it occurs in a natural way, symmetry under $U(1)$ phase shifts is not obvious and awaits further justification.
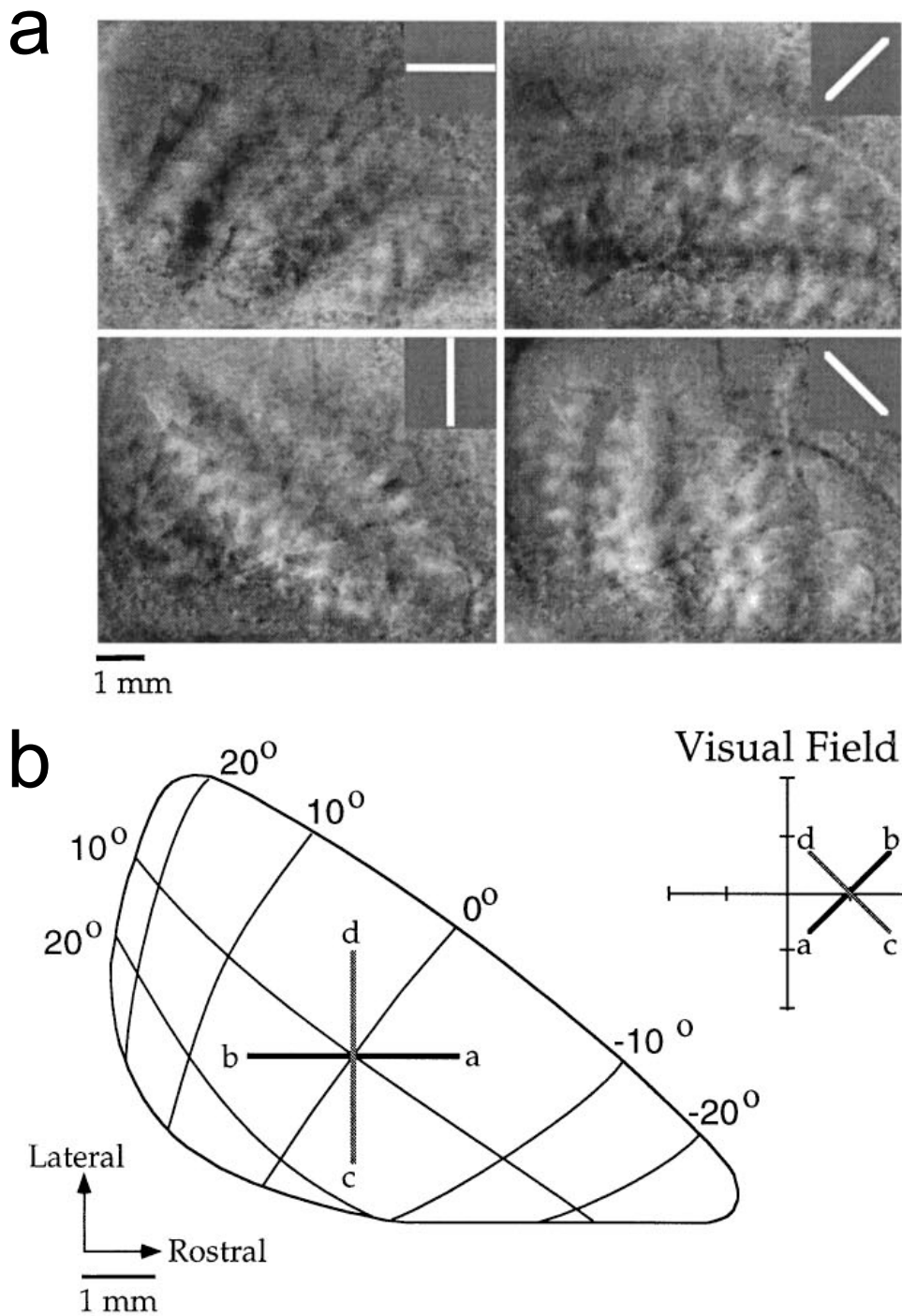
Figure 2.7: Visuotopic organization of the tree shrew visual cortex. (**a**) Activity patterns elicited by widely spaced stripes of four different orientations. (**b**) Azimuth-elevation coordinate system of the visual field projected on the visual cortex, defining the visuotopic map. (From [27]).
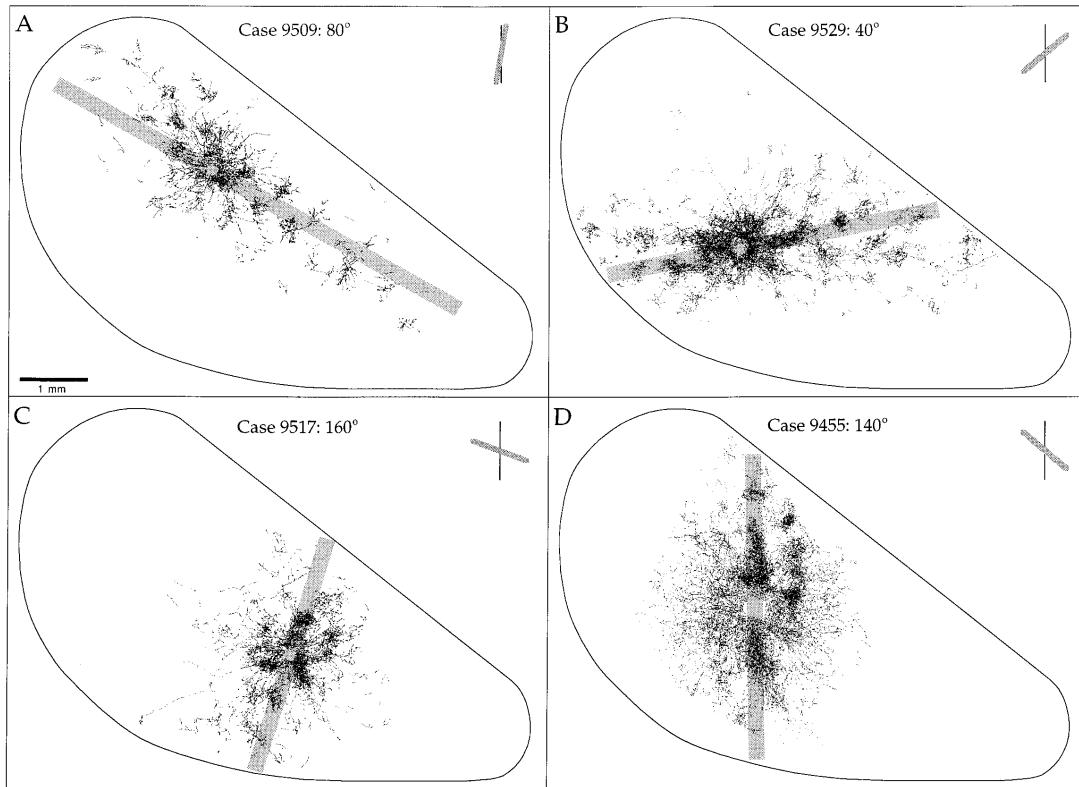
Figure 2.8: Patterns of lateral connections of four orientation columns with different preferred orientations. Gray bars represent the axis of the preferred orientation projected onto cortical coordinates. (From [27]).

Another clear indication of shift-twist symmetry is provided by the anatomy of the long-range connections in the visual cortex. In addition to the properties already mentioned before, connections in the tree shrew exhibit another characteristic feature, termed axial specificity [27]:

- Long-range connections preferentially link neurons with co-oriented, coaxially aligned receptive fields.

This has been demonstrated in experiments by Bosking et al. [27], shown in Fig. 2.8. Similar has been found in [45, 44]. It has been suggested that axial specificity of long-range connections contributes to mechanisms of visual perception such as grouping of collinear line segments [46, 27]. Shift-twist operations respect this particular connectivity rule, since they preserve collinear arrangements of neurons. However, in general this is not the case for orientation shifts. In conclusion, anatomical data provides clear indications that shift-twist symmetry has an important role for understanding the design principles of the visual cortex (see also [23, 47]). At this point several questions arise:

First, when considering modelling of orientation map development: How critically do the results of the model (2.11) depend on the shift symmetry assumption? Would a similar model based on shift-twist symmetry predict a similar type of solutions? These issues will form the topic of Chapter 4.

Second, independent of any specific model, motivated by general symmetry considerations alone: Can we tell, in principle, the difference between two sets of orientation maps, the first one being

the outcome of a $E(2)$ shift-twist symmetric, the second one being the outcome of an $E(2) \times U(1)$ shift symmetric dynamics? Are there any differences in the predicted orientation map layout? These questions will be discussed in Chapter 3.

Third, last but not least: Even if shift-twist symmetry seems *a priori* more appropriate to underly orientation map development, it may turn out that shift symmetry is not at all a bad assumption. Can we quantify the actual degree of shift symmetry breaking for a given optical imaging dataset? Having identified possible signatures of shift and of shift-twist symmetry in Chapter 3 we have the necessary tools to address this question in Chapter 5.

2.5 Towards a Shift-Twist Symmetric Swift-Hohenberg Model

At the end of this chapter we sketch how to generalize the model (2.11) in a way which respects shift-twist symmetry and also accounts for the possibility that shift symmetry may be broken. The model (2.11) is symmetric under shift-twists and also under orientation shifts, since the energy functional Eq.(2.15) stays invariant under these transformations. Shift symmetry can be broken by adding new terms to the energy functional, which, however have to fulfill general rules, in order to guarantee invariance under shift-twists. For example, such a contribution which is quadratic in the fields is provided by

$$\delta E[z] = \int d^2\mathbf{x} \int d^2\mathbf{y}\, z(\mathbf{x}) K(|\mathbf{y} - \mathbf{x}|) e^{-4i\arg(\mathbf{y}-\mathbf{x})} z(\mathbf{y}) + \text{c.c.}, \qquad (2.18)$$

where c.c. denotes the complex conjugation of the expression. The complex phase $e^{-4i\arg(\mathbf{y}-\mathbf{x})}$ is necessary in order to balance the phase which arises from shift-twist rotations $z(\mathbf{x}) \to e^{2i\phi} z(\Omega_\phi^{-1}\mathbf{x})$, i.e.

$$
\begin{aligned}
\delta E[R_\phi z] &= \int d^2\mathbf{x} \int d^2\mathbf{y}\, e^{4i\phi} z(\Omega_{-\phi}\mathbf{x}) K(|\mathbf{y} - \mathbf{x}|) e^{-4i\arg(\mathbf{y}-\mathbf{x})} z(\Omega_{-\phi}\mathbf{y}) + \text{c.c.} \\
&= \int d^2\mathbf{x} \int d^2\mathbf{y}\, e^{4i\phi} z(\mathbf{x}) K(|\Omega_\phi(\mathbf{y} - \mathbf{x})|) e^{-4i\arg(\Omega_\phi(\mathbf{y}-\mathbf{x}))} z(\mathbf{y}) + \text{c.c.} \\
&= \int d^2\mathbf{x} \int d^2\mathbf{y}\, e^{4i\phi} z(\mathbf{x}) K(|\mathbf{y} - \mathbf{x}|) e^{-4i\arg(\mathbf{y}-\mathbf{x})} e^{-4i\phi} z(\mathbf{y}) + \text{c.c.} \\
&= \delta E[z]
\end{aligned}
$$

In addition, invariance under shift-twist reflections $z(\mathbf{x}) \to \bar{z}(\bar{\mathbf{x}})$ requires a real valued convolution kernel $K(r) \in \mathbb{R}$, since only then

$$
\begin{aligned}
\delta E[CP z] &= \int d^2\mathbf{x} \int d^2\mathbf{y}\, \bar{z}(\bar{\mathbf{x}}) K(|\bar{\mathbf{y}} - \bar{\mathbf{x}}|) e^{-4i\arg(\mathbf{y}-\mathbf{x})} \bar{z}(\bar{\mathbf{y}}) + \text{c.c.} \\
&= \int d^2\mathbf{x} \int d^2\mathbf{y}\, \bar{z}(\mathbf{x}) K(|\mathbf{y} - \mathbf{x}|) e^{+4i\arg(\mathbf{y}-\mathbf{x})} \bar{z}(\mathbf{y}) + \text{c.c.} \\
&= \int d^2\mathbf{x} \int d^2\mathbf{y}\, z(\mathbf{x}) \bar{K}(|\mathbf{y} - \mathbf{x}|) e^{-4i\arg(\mathbf{y}-\mathbf{x})} z(\mathbf{y}) + \text{c.c.} \\
&= \delta E[z]
\end{aligned}
$$

Just adding the simplest term, which is provided by (2.18), to the the energy functional of the Wolf model, Eq. (2.15) yields the dynamics

$$\partial_t z(\mathbf{x}) = \left(r - (k_c^2 + \Delta)^2\right) z(\mathbf{x}) + \int d^2\mathbf{y}\, K(|\mathbf{x} - \mathbf{y}|) e^{4i\arg(\mathbf{y}-\mathbf{x})} \bar{z}(\mathbf{y}) + N_3[z, z, \bar{z}], \qquad (2.19)$$

where the expression $N_3[z, z, \bar{z}]$ refers to the original third order nonlinearity of (2.11). Clearly, for non-vanishing $K(r)$ this dynamics is not equivariant under phase shifts $z(\mathbf{x}) \rightarrow e^{2i\theta} z(\mathbf{x})$. We will take this minimal extension of the model (2.11) as the basis of our discussion in Chapter 3 and Chapter 4.

3 Shift-Twist Symmetry in Ensembles of Orientation Maps

3.1 Overview

In this chapter we develop a theory of statistical ensembles of orientation preference maps (OPMs). In trying to understand pattern formation in the visual cortex studying ensembles of OPMs is important for at least three reasons: Firstly, because of the strong interindividual variability of the layout of cortical columns theoretical predictions can never be compared to individual observations but have to be compared to ensembles of patterns obtained from different brains and their statistics. It is thus essential to achieve the clearest possible view of the theoretically expected structure of such statistics and to have well characterized model ensembles that can be used to optimize and validate quantitative analysis techniques. Secondly, as we will see in Chapter 4 even deterministic models of pattern formation in the visual cortex can exhibit excessively many degenerate ground states. Starting from random initial conditions such models do not predict the formation of one particular pattern, but predict that patterns converge over time to instances of an ensemble of patterns. Thus characterizing ensembles of maps is also necessary in order to characterize the predictions of deterministic models. Finally, even if a unique ground state exists, finite time transients towards this ground state can be characterized with great generality using ensemble notions.

The chapter consists of three parts. In the first part we introduce Gaussian random fields and study how shift symmetry breaking is affecting their statistics. Gaussian random fields are defined by their 2-point correlation functions and exhibit a close resemblance to orientation maps when the correlation functions are chosen to match those from the data. Furthermore, they are likely to provide a good approximation for the emerging orientation map shortly after spontaneous symmetry breaking [13]. First we derive the general forms of the 2-point correlation functions for the $E(2) \times U(1)$ symmetric case. Then we show that shift symmetry breaking, $E(2) \times U(1) \to E(2)$, induces correlations among pairs of antiparallel Fourier modes, which for higher symmetry were uncorrelated. The strength of this additional correlations can be quantified by a correlation coefficient, which varies in the range $[-1, 1]$ and thus provides a suitable order parameter, which we call q, to define the *degree* of shift symmetry breaking. For $q = 0$ shift symmetry is restored, for $q = 1$ and $q = -1$ it is maximally broken. Examples of artificial orientation maps, generated for different values of q, show that shift symmetry breaking induces a coupling of the orientation map to the visuotopic map. The coupling occurs in one of two ways, depending on the sign of q: For $q > 0$ domains with a preference to horizontal and vertical orientations tend to align with the horizontal and vertical directions of the visuotopic map. Similarly, domains with a preference to left- and right-oblique orientations tend to organize

along diagonal directions of the visuotopic map. Exactly the opposite is observed for $q < 0$.

In the second part we study whether shift symmetry breaking affects the pinwheel density. The pinwheel density is of particular interest to understand the mechanisms underlying map formation since a scenario, in which orientation preferences arise through activity-dependent refinement of initially unselective patterns of synaptic connections, implies a strict lower bound on the pinwheel density at the initial stage of map formation [13]. Since this lower bound is set by the pinwheel density of a Gaussian random field having the 'right' symmetries of the microscopic dynamics it is important to know whether the lower bound to the pinwheel density of Wolf and Geisel [13], derived under the assumption of shift symmetry, is modified or not. We calculate the pinwheel density for $q \neq 0$ and find that its expectation value remains unaffected. As a consequence, the predictions of [13] are also valid when the shift symmetry assumption is relaxed.

In the third part we develop a general theory for the joint statistics of pairs of oriented objects, given that Euclidean symmetry $E(2)$ holds. Primarily, we aim at describing the joint probability distribution of orientation preferences at two separated locations for orientation maps. Nevertheless, our theory can be applied more generally to any planar assembly of oriented objects, e.g. to oriented line segments in natural scenes, to nematic liquid crystals or to colonies of rod-shaped bacteria. We calculate the pair cooccurence distribution of orientations in Gaussian random fields for arbitrary correlation functions and arbitrary q. The theoretical predictions are compared to numerical simulations for a specific set of model correlation functions.

3.2 Ensembles of Orientation Preference Maps

The layout of an orientation map $z(\mathbf{x}, t)$ at time t whose development is modeled by a dynamics as in Eq.(2.19) will depend on the initial condition $z(\mathbf{x}, 0)$ at $t = 0$. As suggested by experimental findings (cf. Chapter 2, [48, 9, 28]) the unselective initial state may be modeled by low amplitude random fluctuations of the orientation preferences around the homogeneous state $z(\mathbf{x}) = 0$. Since *a priori* there is no reason to prefer one initial condition to another a natural approach is to consider the ensemble $\mathcal{Z}_t = \{z(\mathbf{x}, t)\}$ of all possible orientation maps evolving from this set of random initial conditions. Statistical properties of this ensemble are, in principle, determined by a functional $\mathcal{P}_t[z]$, which assigns a statistical weight to each orientation map $z(\mathbf{x})$ at time t. The dynamics of the ensemble $\mathcal{Z}_t$ is then reflected in the time dependence of the functional $\mathcal{P}_t$.

3.3 Correlation Functions

At each particular point in time the statistical functional $\mathcal{P}_t[z]$ defines an ensemble of random fields and thus contains all the information about the ensemble. An equivalent characterization of this ensemble is provided by the complete set of n-point correlation functions (supposed they exist) defined by

$$C_m^n(\mathbf{x}_1, \mathbf{x}_2, \ldots, \mathbf{x}_m, \mathbf{x}_{m+1}, \ldots \mathbf{x}_n; t) := \langle z(\mathbf{x}_1) z(\mathbf{x}_2) \ldots z(\mathbf{x}_m) \bar{z}(\mathbf{x}_{m+1}) \ldots \bar{z}(\mathbf{x}_n) \rangle_{z \in \mathcal{Z}_t},$$

where $n \in \mathbb{N}$, $m \leq n$ and with the angular brackets representing the ensemble average (cf. for example [49]). The form of these correlation functions is constrained by the symmetries of the ensemble, which are transformations of the field $z(\mathbf{x})$ which leave the functional $\mathcal{P}_t[z]$ and thus

all correlation functions invariant. For Gaussian random fields, which we discuss in section 3.8, the n-point functions can be expressed in terms of 1-point and 2-point correlation functions, by a Wick decomposition [49] such that the knowledge of $\langle z(\mathbf{x})\rangle$, $\langle \bar{z}(\mathbf{x})\rangle$, $\langle z(\mathbf{x})\bar{z}(\mathbf{y})\rangle$, $\langle z(\mathbf{x})z(\mathbf{y})\rangle$ already provides a complete description of the ensemble. In the next section we give a motivation why the Gaussian case is important.

3.4 Initial Maps have Gaussian Statistics

In this section we show that at the early stage, when the dynamics is dominated by the linear terms, the ensemble of emerging orientation maps is expected to be Gaussian. We consider a general class of models whose dynamics has the following form

$$\partial_t z(\mathbf{x}) = F[z](\mathbf{x}) + \xi(\mathbf{x}, t) \tag{3.1}$$

where $F[z]$ denotes a nonlinear operator as discussed in Chapter 2 and $\xi(\mathbf{x}, t)$ is a random noise term, which could, for example, represent fluctuating input. In the vicinity of the homogeneous state $z(\mathbf{x}) = 0$ the dynamics can be approximated by the first order terms

$$\partial_t z(\mathbf{x}) \approx (L_1 z)(\mathbf{x}) + (L_2 \bar{z})(\mathbf{x}) + \xi(\mathbf{x}, t) \tag{3.2}$$

where the linear operators L_1 and L_2 are defined by the functional derivatives $L_1 = (\delta F[z]/\delta z)_{z=0}$ and $L_2 = (\delta F[z]/\delta \bar{z})_{z=0}$. Due to translation invariance these operators are diagonal in the Fourier representation and have a spectrum $\lambda_1(\mathbf{k})$ and $\lambda_2(\mathbf{k})$, respectively. With

$$z(\mathbf{x}) = \frac{1}{2\pi} \int d^2\mathbf{k}\, a(\mathbf{k}) e^{i\mathbf{k}\mathbf{x}}$$

the dynamics of the Fourier modes $a(\mathbf{k})$ states

$$\begin{aligned}
\partial_t a(\mathbf{k}) &= \lambda_1(\mathbf{k}) a(\mathbf{k}) + \lambda_2(\mathbf{k}) \bar{a}(-\mathbf{k}) + \eta(\mathbf{k}, t) \\
\partial_t \bar{a}(-\mathbf{k}) &= \lambda_1(\mathbf{k}) \bar{a}(-\mathbf{k}) + \bar{\lambda}_2(\mathbf{k}) a(\mathbf{k}) + \bar{\eta}(-\mathbf{k}, t)
\end{aligned} \tag{3.3}$$

where $\eta(\mathbf{k})$ denotes the Fourier transform of the noise. As shown in Chapter 2, $E(2)$ symmetry of the dynamics (3.1) implies

$$\lambda_1(\mathbf{k}) = \lambda(k)$$

and

$$\lambda_2(\mathbf{k}) = |\lambda_2(|\mathbf{k}|)| e^{4i \arg \mathbf{k}},$$

which we can also write

$$\lambda_2(\mathbf{k}) = \epsilon(k)\lambda(k) e^{4i \arg \mathbf{k}},$$

where $\lambda(k)$ and $\epsilon(k)$ are real valued functions and $k := |\mathbf{k}|$, such that

$$\begin{aligned}
\partial_t a(\mathbf{k}) &= \lambda(k)[a(\mathbf{k}) + \epsilon(k) e^{4i \arg \mathbf{k}} \bar{a}(-\mathbf{k})] + \eta(\mathbf{k}, t) \\
\partial_t \bar{a}(-\mathbf{k}) &= \lambda(k)[\bar{a}(-\mathbf{k}) + \epsilon(k) e^{-4i \arg \mathbf{k}} a(\mathbf{k})] + \bar{\eta}(-\mathbf{k}, t)
\end{aligned} \tag{3.4}$$

The case $\epsilon = 0$ corresponds to the shift symmetric case. For $\epsilon \neq 0$, i.e. for broken shift symmetry, the antiparallel modes $a(\mathbf{k})$ and $a(-\mathbf{k})$ are coupled. A basis which diagonalizes the dynamics is provided by the change of variables

$$b_\pm(\mathbf{k}) = \frac{1}{2}\left(e^{-2i\arg\mathbf{k}}a(\mathbf{k}) \pm e^{2i\arg\mathbf{k}}\bar{a}(-\mathbf{k})\right) \tag{3.5}$$

$$\zeta_\pm(\mathbf{k},t) = \frac{1}{2}\left(e^{-2i\arg\mathbf{k}}\eta(\mathbf{k},t) \pm e^{2i\arg\mathbf{k}}\bar{\eta}(-\mathbf{k},t)\right)$$

In that new basis the dynamics states

$$\partial_t b_\pm(\mathbf{k}) = \lambda(k)[1 \pm \epsilon(k)]b_+(\mathbf{k}) + \zeta_\pm(\mathbf{k},t) \tag{3.6}$$

The solution of this differential equation is given by

$$b_\pm(\mathbf{k},t) = \hat{G}_\pm(\mathbf{k},t)b_\pm(\mathbf{k},0) + \int_0^t dt' \hat{G}_\pm(\mathbf{k},t-t')\zeta_\pm(\mathbf{k},t'). \tag{3.7}$$

where

$$\hat{G}_\pm(\mathbf{k},t) = e^{\lambda(k)[1\pm\epsilon(k)]t}$$

are the propagators of the homogeneous equations. The statistics of $b_\pm(\mathbf{k},t)$ at some finite time t will depend on the statistics of the random initial state $b_\pm(\mathbf{k},0)$ as well as on the statistics of the noise $\zeta_\pm(\mathbf{k},t)$. For simplicity we assume that $\zeta_\pm(\mathbf{k},t)$ is described by some random process for which the integral in Eq.(3.7) can be approximated by a sum

$$b_\pm(\mathbf{k},t) \approx \hat{G}_\pm(\mathbf{k},t)b_\pm(\mathbf{k},0) + \sum_i \Delta t\, \hat{G}_\pm(\mathbf{k},t-t'_i)\zeta_\pm(\mathbf{k},t'_i). \tag{3.8}$$

We can invoke the central limit theorem if the following two conditions are fulfilled:

1. The distribution of $b_\pm(\mathbf{k},0)$ and $\zeta(\mathbf{k},t)$ fulfills the Lindeberg criterion

$$\lim_{\beta \to 0} \int_{|w|>\beta} dw\, |w|^2 P_w(w) = 0, \tag{3.9}$$

   where w stands for $b_\pm(k,0)$ or $\zeta_\pm(k,t)$ and $P_w(w)$ denotes the individual probability density of those quantities.

2. The correlation time of the noise, τ_ζ, is much smaller than the characteristic time scales of $\hat{G}_\pm$,

$$\tau_\pm = 1/\max(\lambda(k)[1 \pm \epsilon(k)])$$

   such that the sum in Eq.(3.8) consists of a large number of independent contributions.

The first condition is met if $b_\pm(k,0)$ and $\zeta_\pm(k,t)$ are bounded or have finite variance, which is plausible since neural response always occurs within some physiological range. The second assumption is also consistent with the biological findings, since orientation maps are observed to develop on a time scale of several hours or days and that fluctuations induced by afferent activity patterns exhibit correlation times of up to a few hundreds of milliseconds [34].

In conclusion, for a general class of models the statistics of $b_\pm(\mathbf{k},t)$ approaches a Gaussian distribution at the initial stage of the dynamics. In particular, since linear transformations of Gaussian random variables are again Gaussian, this also applies to $a(\mathbf{k},t)$ and to $z(\mathbf{x},t)$. For times $t \sim \tau_\pm$ the ensemble $\mathcal{Z}_t = \{z(\mathbf{x},t)\}$ thus constitutes a Gaussian random field ensemble.

3.5 Gaussian Random Fields

A Gaussian random field $Z(\mathbf{x})$ is defined by the following property: For any positive integer $n \in \mathbb{N}$ and arbitrary positions $\mathbf{x}_1, \mathbf{x}_2, \ldots, \mathbf{x}_n$ the joint probability density of the n random variables $Z(\mathbf{x}_1), Z(\mathbf{x}_2), \ldots, Z(\mathbf{x}_n)$ is given by a multivariate Gaussian distribution [50]. This means that its first and second order moments, i.e. $\langle Z(\mathbf{x})\rangle$, $\langle Z(\mathbf{x})\bar{Z}(\mathbf{y})\rangle$ and $\langle Z(\mathbf{x})Z(\mathbf{y})\rangle$ already specify the ensemble. One can show that any linear transformation of a Gaussian random field is again Gaussian [50]. Gaussian random fields inherit the virtues of the Gaussian distribution and in this chapter we will encounter many situations where statistical averages can be performed analytically. Although one should distinguish the random field $Z(\mathbf{x})$, which is a random variable, from its individual realizations $z(\mathbf{x})$, which are functions, we will simply denote both by the same symbol $z(\mathbf{x})$.

First we give the general definition of a Gaussian random field assuming symmetry under $E(2) \times U(1)$ (shift symmetry). Then we show how this definition has to be modified when shift symmetry is broken down to its $E(2)$ subgroup (shift-twist symmetry).

Shift Symmetry $\big(E(2) \times U(1)\big)$

Here we calculate the general form of the first and second order moments of $z(\mathbf{x})$, which are required to be invariant under the $E(2) \times U(1)$ group of transformations discussed in Chapter 2.

Invariance under translations and shift-twists requires

$$\langle z(\mathbf{x})\rangle = \langle z(\mathbf{0})\rangle = e^{2i\phi}\langle z(\Omega_{-\phi}\mathbf{0})\rangle = e^{2i\phi}\langle z(\mathbf{0})\rangle \;\; \forall \phi \in [0, 2\pi]$$

and thus the vanishing of $\langle z(\mathbf{x})\rangle$ and $\langle \bar{z}(\mathbf{x})\rangle$ for arbitrary positions $\mathbf{x}$. Due to translation invariance, the 2-point correlation functions $\langle z(\mathbf{x})\bar{z}(\mathbf{y})\rangle$ and $\langle z(\mathbf{x})z(\mathbf{y})\rangle$ only depend on the difference vector $\mathbf{r} = \mathbf{y} - \mathbf{x}$ and we define

$$\begin{aligned}
C_1(\mathbf{r}) &:= \langle z(\mathbf{x})\bar{z}(\mathbf{x}+\mathbf{r})\rangle \\
C_2(\mathbf{r}) &:= \langle z(\mathbf{x})z(\mathbf{x}+\mathbf{r})\rangle.
\end{aligned}$$

$C_1(\mathbf{r})$ is real valued due to translation and inversion symmetry, since

$$C_1(\mathbf{r}) = \langle z(\mathbf{x})\bar{z}(\mathbf{x}+\mathbf{r})\rangle = \langle z(-\mathbf{x}-\mathbf{r})\bar{z}(-\mathbf{x})\rangle = \langle z(\mathbf{x}+\mathbf{r})\bar{z}(\mathbf{x})\rangle = \bar{C}_1(\mathbf{r}). \tag{3.10}$$

In addition, invariance under shift-twist rotations implies

$$C_1(\mathbf{r}) = \langle z(\mathbf{0})\bar{z}(\mathbf{r})\rangle = \langle z(\Omega_{-\phi}\mathbf{0})\bar{z}(\Omega_{-\phi}\mathbf{r})\rangle = \langle z(\mathbf{0})\bar{z}(\Omega_{-\phi}\mathbf{r})\rangle = C_1(\Omega_{-\phi}\mathbf{r})$$

which means that $C_1(\mathbf{r})$ is rotation symmetric and only depends on $|\mathbf{r}|$.

Shift symmetry requires

$$C_2(\mathbf{r}) = \langle z(\mathbf{x})z(\mathbf{x}+\mathbf{r})\rangle = e^{4i\phi}\langle z(\mathbf{x})z(\mathbf{x}+\mathbf{r})\rangle = e^{4i\phi}C_2(\mathbf{r}) \;\; \forall \phi \in [0, \pi]$$

and thus the vanishing of $C_2(\mathbf{r})$.

Shift-Twist Symmetry ($E(2)$)

What is the general form of the correlation function for broken shift symmetry? As we show next, in this case $C_2(\mathbf{r})$ does not have to vanish. It is complex valued and can be written in the general form

$$C_2(\mathbf{r}) = (r_1 + i\,r_2)^4 f(|\mathbf{r}|) \tag{3.11}$$

with some radially symmetric, real valued function $f(|\mathbf{r}|)$.

In the following we will need to take higher order derivatives of the random field and also of the correlation functions at $\mathbf{r} = 0$. In optical imaging one usually applies low pass filtering of the single condition maps in order to remove the high frequency components due to the shot noise of the camera signal. The resulting pattern of orientation preferences is smooth and has continuous higher order derivatives. Hence this should also be the case for the random fields considered here. It can be shown that a random field is continuously differentiable (in the mean square sense) up to the n-th order if all m-th order derivatives ($m \leq 2n$) of the 2-point correlation functions exist and are continuous, and vice-versa [50]. In the following we simply assume that all derivatives exist and are continuous.

We now give a proof of the statement above, Eq.(3.11). A series expansion of $C_1(\mathbf{r})$ and $C_2(\mathbf{r})$ around the origin $\mathbf{r} = 0$ reads

$$
\begin{aligned}
C_1(\mathbf{r}) &= \sum_{m,n=0}^{\infty} a_{mn}\, \mathbf{r}^m \bar{\mathbf{r}}^n \\
C_2(\mathbf{r}) &= \sum_{m,n=0}^{\infty} b_{mn}\, \mathbf{r}^m \bar{\mathbf{r}}^n
\end{aligned}
$$

with $m, n \in \mathbb{N}$ and $a_{mn}, b_{mn} \in \mathbb{C}$. Here we identified the vector $\mathbf{r} = (r_1, r_2)$ with the complex number $\mathbf{r} = r_1 + i\,r_2$ and performed an expansion in $\mathbf{r}$ and $\bar{\mathbf{r}}$, which is equivalent to the usual expansion in r_1 and r_2, but has the advantage that spatial rotations $\mathbf{r} \to \Omega_\phi \mathbf{r}$ are simply represented by a multiplication with a complex phase, $\mathbf{r} \to e^{i\phi}\mathbf{r}$.

Under shift-twist rotations, $z(\mathbf{x}) \to e^{2i\phi}z(\Omega_{-\phi}\mathbf{x})$, the correlation functions transform as follows:

$$
\begin{aligned}
C_1(\mathbf{r}) &= \langle z(0)\bar{z}(\mathbf{r})\rangle \to \langle z(0)\bar{z}(\Omega_{-\phi}\mathbf{r})\rangle = C_1(\Omega_{-\phi}\mathbf{r}) \\
C_2(\mathbf{r}) &= \langle z(0)z(\mathbf{r})\rangle \to e^{4i\phi}\langle z(0)z(\Omega_{-\phi}\mathbf{r})\rangle = e^{4i\phi}C_2(\Omega_{-\phi}\mathbf{r}).
\end{aligned}
$$

$E(2)$ invariance thus requires

$$
\begin{aligned}
C_1(\mathbf{r}) &\overset{!}{=} C_1(e^{-\phi}\mathbf{r}) \\
C_2(\mathbf{r}) &\overset{!}{=} e^{4i\phi}C_2(e^{-\phi}\mathbf{r}).
\end{aligned}
$$

As the left sides of these equations do not depend on the angle ϕ we can average over all angles and obtain

$$
\begin{aligned}
C_1(\mathbf{r}) &= \sum a_{mn}\, \mathbf{r}^m \bar{\mathbf{r}}^n \frac{1}{2\pi}\int_0^{2\pi} d\phi\, e^{i\phi(n-m)} = \sum a_n\,(\mathbf{r}\bar{\mathbf{r}})^n \\
C_2(\mathbf{r}) &= \sum b_{mn}\, \mathbf{r}^m \bar{\mathbf{r}}^n \frac{1}{2\pi}\int_0^{2\pi} d\phi\, e^{i\phi(4+n-m)} = (r_1 + ir_2)^4 \sum b_n\,(\mathbf{r}\bar{\mathbf{r}})^n
\end{aligned}
$$

from which one can read off that $C_1(\mathbf{r})$ is radially symmetric as it only depends on $\mathbf{r}\bar{\mathbf{r}} = |\mathbf{r}|^2$. As shown in Eq.3.10, $C_1(\mathbf{r})$ is real, and therefore $a_n \in \mathbb{R}$. Furthermore, symmetry under reflections , $z(\mathbf{x}) \to \bar{z}(\bar{\mathbf{x}})$, requires $C_2(\mathbf{r}) = \bar{C}_2(\bar{\mathbf{r}})$, such that $b_n \in \mathbb{R}$. All together we obtain

$$C_2(\mathbf{r}) = (r_1 + i\,r_2)^4 f(|\mathbf{r}|) = \left(r_1^4 - 6r_1^2 r_2^2 + r_2^4 + i\,4r_1 r_2(r_1^2 - r_2^2)\right) f(|\mathbf{r}|) \qquad (3.12)$$

with a real, radially symmetric function $f(|\mathbf{r}|) = \sum_{n=0}^{\infty} b_n\,(\mathbf{r}\bar{\mathbf{r}})^n$.

3.6 Correlation Functions in Fourier Representation

An equivalent definition of the Gaussian random field ensemble can be given in the Fourier representation. The second order correlations of the Fourier modes $a(\mathbf{k}) = 1/2\pi \int d^2\mathbf{k}\, z(\mathbf{x}) e^{-i\mathbf{k}\mathbf{x}}$ are given by

$$
\begin{aligned}
\langle a(\mathbf{k})\bar{a}(\mathbf{k}')\rangle &= \frac{1}{(2\pi)^2} \int d^2\mathbf{x} \int d^2\mathbf{x}'\, e^{-i\mathbf{k}\mathbf{x}} e^{-i\mathbf{k}'\mathbf{x}'} \langle z(\mathbf{x})\bar{z}(\mathbf{x}')\rangle \\
&= \frac{1}{(2\pi)^2} \int d^2\mathbf{x} \int d^2\mathbf{x}'\, e^{-i\mathbf{k}\mathbf{x}} e^{-i\mathbf{k}'\mathbf{x}'} \langle z(0)\bar{z}(\mathbf{x}' - \mathbf{x})\rangle \\
&= \frac{1}{(2\pi)^2} \int d^2\mathbf{x}\, e^{-i(\mathbf{k}'-\mathbf{k})\mathbf{x}} \int d^2\mathbf{x}'\, e^{i\mathbf{k}'\mathbf{x}'} \langle z(0)\bar{z}(\mathbf{x}')\rangle \\
&= \delta(\mathbf{k} - \mathbf{k}')\, P_1(\mathbf{k})
\end{aligned}
$$

$$
\begin{aligned}
\langle a(\mathbf{k}) a(\mathbf{k}')\rangle &= \frac{1}{(2\pi)^2} \int d^2\mathbf{x} \int d^2\mathbf{x}'\, e^{-i\mathbf{k}\mathbf{x}} e^{-i\mathbf{k}'\mathbf{x}'} \langle z(\mathbf{x}) z(\mathbf{x}')\rangle \\
&= \frac{1}{(2\pi)^2} \int d^2\mathbf{x} \int d^2\mathbf{x}'\, e^{-i\mathbf{k}\mathbf{x}} e^{-i\mathbf{k}'\mathbf{x}'} \langle z(0) z(\mathbf{x}' - \mathbf{x})\rangle \\
&= \frac{1}{(2\pi)^2} \int d^2\mathbf{x}\, e^{-i(\mathbf{k}+\mathbf{k}')\mathbf{x}} \int d^2\mathbf{x}'\, e^{-i\mathbf{k}'\mathbf{x}'} \langle z(0) z(\mathbf{x}')\rangle \\
&= \delta(\mathbf{k} + \mathbf{k}')\, P_2(\mathbf{k})
\end{aligned}
$$

where $P_1(\mathbf{k})$ and $P_2(\mathbf{k})$ denote the Fourier transforms of $C_1(\mathbf{r})$ and $C_2(\mathbf{r})$. From these expressions we see that, due to translation symmetry, almost all correlations vanish, except of $\langle a(\mathbf{k})\bar{a}(\mathbf{k})\rangle$ and $\langle a(\mathbf{k})a(-\mathbf{k})\rangle$.

Invariance under shift-twist rotations $a(\mathbf{k}) \to e^{2i\phi} a(\Omega_{-\phi}\mathbf{k})$ and reflections $a(\mathbf{k}) \to \bar{a}(\pm\bar{\mathbf{k}})$ implies rotation invariant, real and positive valued $P_1(\mathbf{k})$, whereas $P_2(\mathbf{k})$ has to be of the general form

$$P_2(\mathbf{k}) = e^{4i\arg\mathbf{k}} g(|\mathbf{k}|) \qquad (3.13)$$

with $\arg\mathbf{k} := \arg(k_1 + i\,k_2)$ denoting the direction angle of the $\mathbf{k}$-vector and $g(|\mathbf{k}|) \in \mathbb{R}$.

If, in addition, symmetry under orientation shifts $a(\mathbf{k}) \to e^{2i\phi} a(\mathbf{k})$ is also assumed, $P_2(\mathbf{k})$ has to vanish. We conclude that in general, when shift symmetry is broken, the anti-parallel modes $a(\mathbf{k})$ and $a(-\mathbf{k})$ are correlated in a particular way described by $P_2(\mathbf{k})$ in Eq.(3.13).

3.7 The Degree of Shift-Symmetry Breaking

From the results of the previous section follows that the covariance matrix of $(a(\mathbf{k}), \bar{a}(\mathbf{k}), a(-\mathbf{k}), \bar{a}(-\mathbf{k}))$, i.e.

$$
\mathcal{C}(\mathbf{k}) = \begin{pmatrix}
\langle a(\mathbf{k})\bar{a}(\mathbf{k})\rangle & \langle a(\mathbf{k})a(\mathbf{k})\rangle & \langle a(\mathbf{k})\bar{a}(-\mathbf{k})\rangle & \langle a(\mathbf{k})a(-\mathbf{k})\rangle \\
\langle \bar{a}(\mathbf{k})\bar{a}(\mathbf{k})\rangle & \langle \bar{a}(\mathbf{k})a(\mathbf{k})\rangle & \langle \bar{a}(\mathbf{k})\bar{a}(-\mathbf{k})\rangle & \langle \bar{a}(\mathbf{k})a(-\mathbf{k})\rangle \\
\langle a(-\mathbf{k})\bar{a}(\mathbf{k})\rangle & \langle a(-\mathbf{k})a(\mathbf{k})\rangle & \langle a(-\mathbf{k})\bar{a}(-\mathbf{k})\rangle & \langle a(-\mathbf{k})a(-\mathbf{k})\rangle \\
\langle \bar{a}(-\mathbf{k})\bar{a}(\mathbf{k})\rangle & \langle \bar{a}(-\mathbf{k})a(\mathbf{k})\rangle & \langle \bar{a}(-\mathbf{k})\bar{a}(-\mathbf{k})\rangle & \langle \bar{a}(-\mathbf{k})a(-\mathbf{k})\rangle
\end{pmatrix}
$$

reads

$$
\mathcal{C}(\mathbf{k}) = \delta(\mathbf{0}) \cdot \begin{pmatrix}
P_1(\mathbf{k}) & 0 & 0 & P_2(\mathbf{k}) \\
0 & P_1(\mathbf{k}) & \bar{P}_2(\mathbf{k}) & 0 \\
0 & P_2(\mathbf{k}) & P_1(\mathbf{k}) & 0 \\
\bar{P}_2(\mathbf{k}) & 0 & 0 & P_1(\mathbf{k})
\end{pmatrix}
$$

It has the eigenvalues

$$
\lambda_\pm(\mathbf{k}) = P_1(\mathbf{k}) \pm |P_2(\mathbf{k})|,
$$

each of which is twice degenerate. Since a covariance matrix is positive definite, $P_1(\mathbf{k})$ and $P_2(\mathbf{k})$ must satisfy the inequality

$$
|P_2(\mathbf{k})| \leq P_1(\mathbf{k}). \tag{3.14}
$$

Together with Eq.(3.13) it means that $P_2(\mathbf{k})$ can be written as

$$
P_2(\mathbf{k}) = Q(k)\, e^{4i\arg\mathbf{k}}\, P_1(k), \quad -1 \leq Q(k) \leq 1 \tag{3.15}
$$

We can quantify the *degree* of shift symmetry breaking by means of the index q

$$
\begin{aligned}
q &:= \langle Q(k)\rangle \\
&:= \left(\int dk\, P_1(k)\, Q(k)\right) \Big/ \int dk\, P_1(k) \tag{3.16}
\end{aligned}
$$

which assumes its values in the range $q \in [-1, 1]$. For the shift symmetric case, $P_2(\mathbf{k}) = 0$, the index q vanishes and $a(\mathbf{k})$ and $a(-\mathbf{k})$ are uncorrelated. For $|P_2(\mathbf{k})| = P_1(\mathbf{k})$, where either $q = 1$ or $q = -1$ shift symmetry is maximally broken and $a(\mathbf{k})$ and $a(-\mathbf{k})$ are maximally correlated.

All together, the probability functional of the $E(2)$ shift-twist symmetric Gaussian random field ensemble has the form

$$
\mathcal{P}_a[a] = \mathcal{N}_a \cdot e^{-F_a[a]}
$$

with

$$
F_a[a] = \int d^2\mathbf{k}\, \frac{2a(\mathbf{k})\bar{a}(\mathbf{k}) - [e^{4i\arg\mathbf{k}}Q(k)a(\mathbf{k})a(-\mathbf{k}) + c.c]}{2\, P_1(k)[1 - Q^2(k)]},
$$

or, in terms of the basis $b_\pm(\mathbf{k})$ introduced in Section 3.4 in which the covariance matrix is diagonal,

$$
\mathcal{P}_b[b_+, b_-] = \mathcal{N}_b \cdot e^{-F_b[b_+, b_-]} \tag{3.17}
$$

with

$$
F_b[b_+, b_-] = 2\int d^2\mathbf{k}\, \frac{b_+(\mathbf{k})\bar{b}_+(\mathbf{k})}{P_1(k)[1 + q(k)]} + \frac{b_-(\mathbf{k})\bar{b}_-(\mathbf{k})}{P_1(k)[1 - q(k)]},
$$

where $\mathcal{N}_a$ and $\mathcal{N}_b$ denote appropriate normalization constants.

3.8 Model Correlation Functions

Now that we have specified the general functional form of the 2-point functions we will next define a family of model correlation functions intended to fit the experimental data. Optical imaging data reveals that the power spectrum $P_1(\mathbf{k})$ of orientation preference maps occupies an annulus in the two dimensional $\mathbf{k}$-plane with a typical wave number k_0, which reflects the fact that orientation preference maps are arranged in repetitive hypercolumns of typical spacing $\Lambda = 2\pi/k_0$ (c.f. [51] and references therein). The powerspectrum has a finite width, which can vary from animal to animal and within different species (e.g. see Fig. 5.5(**e**) of Chapter 5).

As correlation functions of the model ensemble we introduce

$$
\begin{aligned}
P_1(\mathbf{k}) &= A|\mathbf{k}|^{\beta}e^{-B|\mathbf{k}|^2} \\
P_2(\mathbf{k}) &= q\,e^{4i\arg\mathbf{k}}\,P_1(\mathbf{k})
\end{aligned}
\tag{3.18}
$$

where the constants A and B are given by

$$
\begin{aligned}
A &= \frac{2}{\Gamma[\frac{1+\beta}{2}]}\left(\frac{\Gamma[\frac{2+\beta}{2}]}{\Gamma[\frac{1+\beta}{2}]}\right)^{1+\beta} \\
B &= \left(\frac{\Gamma[\frac{2+\beta}{2}]}{\Gamma[\frac{1+\beta}{2}]}\right)^2
\end{aligned}
$$

This family of correlation functions depends on just two parameters, β and q, controlling the powerspectral width and the degree of shift symmetry breaking, respectively. It has following properties:

1. The radial part $p(k)$ of $P_1(\mathbf{k})$ is normalized to 1,

$$
\int_0^\infty dk\,p(k) = 1
\tag{3.19}
$$

2. The typical wavenumber k_0 defined as

$$
k_0 := \int_0^\infty dk\,k\,p(k)
\tag{3.20}
$$

   is normalized to 1. For the typical wavelength $\Lambda = 2\pi/k_0$ this implies $\Lambda = 2\pi$.

3. The degree of shift symmetry breaking is assumed to be constant over the entire range of wavenumbers and spatial scales,
$$
Q(k) = q.
$$

For $\beta = 1$ the annulus of the powerspectrum is broad, for $\beta \to \infty$ it becomes arbitrarily narrow. We only consider values $\beta \geq 1$. Examples of $P_1(\mathbf{k})$ and $P_2(\mathbf{k})$ for different values of β are displayed in Fig. 3.1 and 3.2.
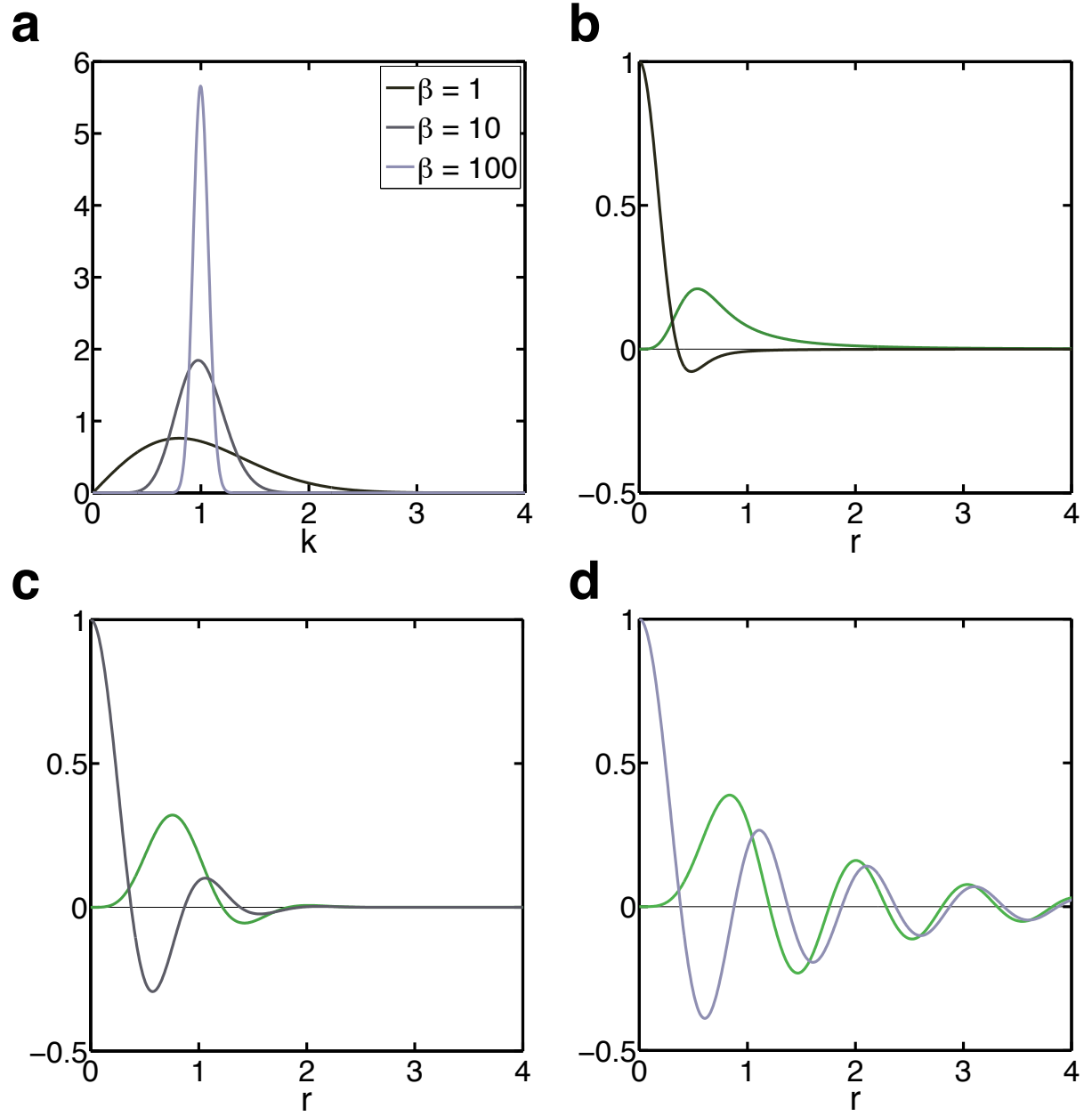
Figure 3.1: Powerspectral densities and spatial correlation functions of the model ensembles as defined in Eq.(3.18) and (3.21), respectively. (**a**) Powerspectral densities for $\beta = 1, 10, 100$. (**b-d**) $C_1(r, 0)$ (*gray traces*) and Re $C_2(r, 0)$ (*green traces*) for $\beta = 1, 10, 100$, respectively.
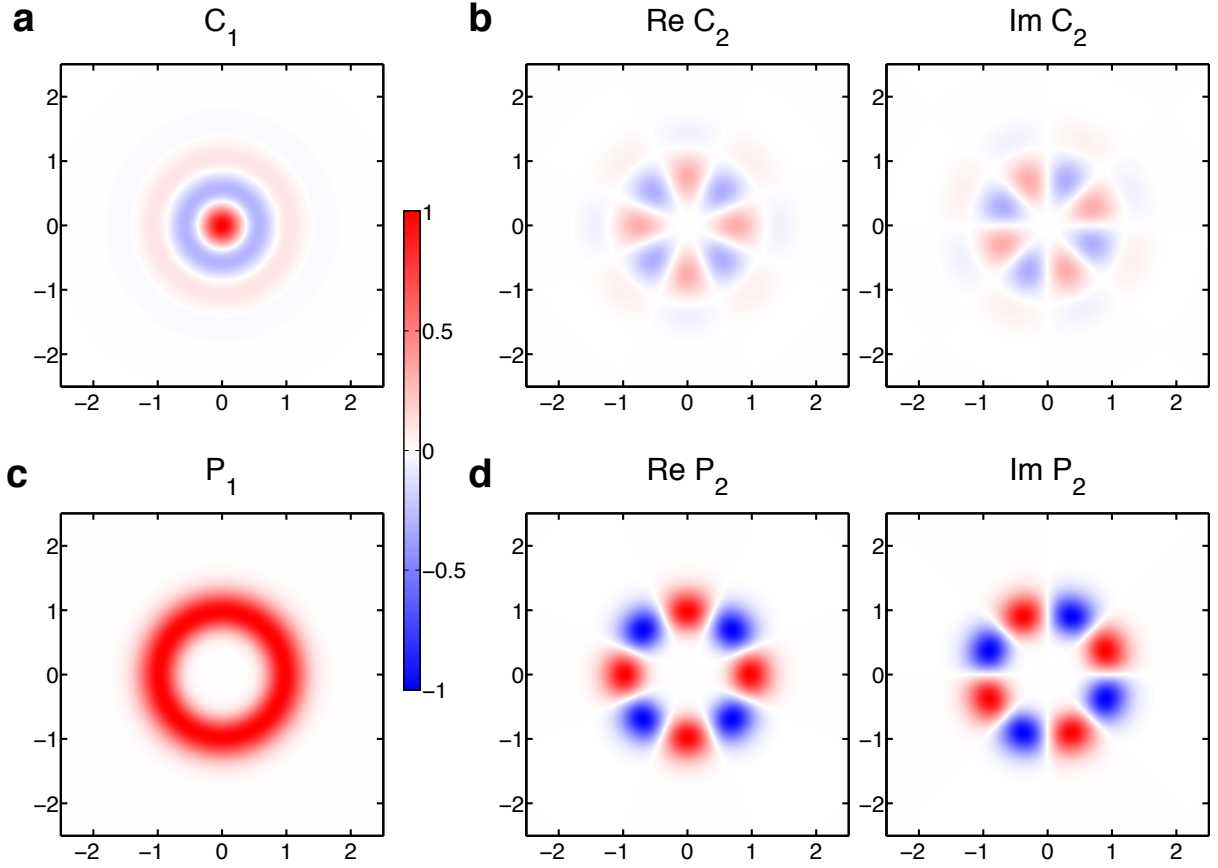
Figure 3.2: Spatial organization of 2d model correlation functions for $q = 1$. (**a**, **b**) $C_1(\mathbf{r})$ and $C_2(\mathbf{r})$. (**c**, **d**) Fourier representation: $P_1(\mathbf{k})$ and $P_2(\mathbf{k})$. Whereas $P_1(\mathbf{k})$ and $C_1(\mathbf{r})$ are real, $P_2(\mathbf{k})$ and $C_2(\mathbf{r})$ are complex valued and have a characteristic cloverleaf shape ($\beta = 10$, $q = 1$). Colorbar applies to all plots. P_1 and P_2 have been rescaled by the same factor such that the maximal value of P_1 is 1. The case $q = -1$ (*not shown*) looks similar, with the only difference that the positive and negative phases in (**b**) and (**d**) are exchanged. This follows from Eq.(3.18).

The correlation functions in spatial representation are given by

$$
\begin{aligned}
C_1(\mathbf{r}) &= {}_1F_1\left(\frac{2+\beta}{2}; 1; -\frac{|\mathbf{r}|^2}{4B}\right) \\
C_2(\mathbf{r}) &= (r_1 + i\, r_2)^4 {}_1F_1\left(\frac{6+\beta}{2}; 5; -\frac{|\mathbf{r}|^2}{4B}\right) A\, B^{-(6+\beta)/2}/768
\end{aligned}
\tag{3.21}
$$

where ${}_1F_1$ denotes the confluent hypergeometric function of the first kind (cf. Appendix 3.16 for the calculation details). Note that these expressions match the general form discussed in Section 3.5.

3.9 Generating Individual Realizations

Next we show how to generate realizations of Gaussian random fields for a given set of correlation functions $P_1(\mathbf{k})$ and $P_2(\mathbf{k})$ numerically. Fourier space is discretized such that the $\mathbf{k}$-vectors are located on a lattice. We use the decomposition of $z(\mathbf{x})$ in terms of the basis functions $b_+(\mathbf{k})$ and $b_-(\mathbf{k})$, Eq.(3.5),

$$
z(\mathbf{x}) = \frac{1}{2\pi}\sum_{\mathbf{k}} e^{2i\arg\mathbf{k}}\left((b_+(\mathbf{k}) + b_-(\mathbf{k}))\, e^{i\mathbf{k}\mathbf{x}} + \left(\bar{b}_+(\mathbf{k}) - \bar{b}_-(\mathbf{k})\right) e^{-i\mathbf{k}\mathbf{x}}\right)
$$

and treat $b_+(\mathbf{k}) \in \mathbb{C}$ and $b_-(\mathbf{k}) \in \mathbb{C}$ as Gaussian random fields defined by the probability density Eq.((3.17)). Thus, $b_+(\mathbf{k})$ and $b_-(\mathbf{k})$ are independently drawn from Gaussian distributions with respective variances

$$
\sigma_\pm^2(\mathbf{k}) = \langle b_\pm(\mathbf{k})\bar{b}_\pm(\mathbf{k})\rangle = P_1(k)[1 \pm q(k)].
$$

3.10 Spatial Locking of Orientation Domains

Figures 3.3 and 3.4 show the consequences of shift symmetry breaking on the spatial organization of orientation preference maps. They display realizations of Gaussian random fields for different degrees of shift symmetry breaking. When shift symmetry is *not* broken ($q = 0$) the layout of orientation domains preferring cardinal (0° and 90°) orientations and oblique (45° and 135°) orientations, which are described by the real and imaginary parts of $z(\mathbf{x})$, respectively, are statistically independent and exhibit a patchy, irregular and statistically isotropic organization. When shift symmetry is gradually broken ($q = \pm0.5, \pm1$) iso-orientation domains acquire a band-like appearance and the orientation of the bands becomes spatially locked to specific cortical axes. The sign of q matters, since

- for $q > 0$ cardinal domains are preferentially extending along the horizontal and vertical axes, whereas oblique domains are preferentially extending along the two oblique axes.

- for $q < 0$ cardinal domains are preferentially extending along the oblique axes, whereas oblique domains are preferentially extending along the horizontal and vertical axes.

This spatial locking of iso-orientation domains to specific directions of the visuotopic map becomes more pronounced with increasing degree of symmetry breaking.
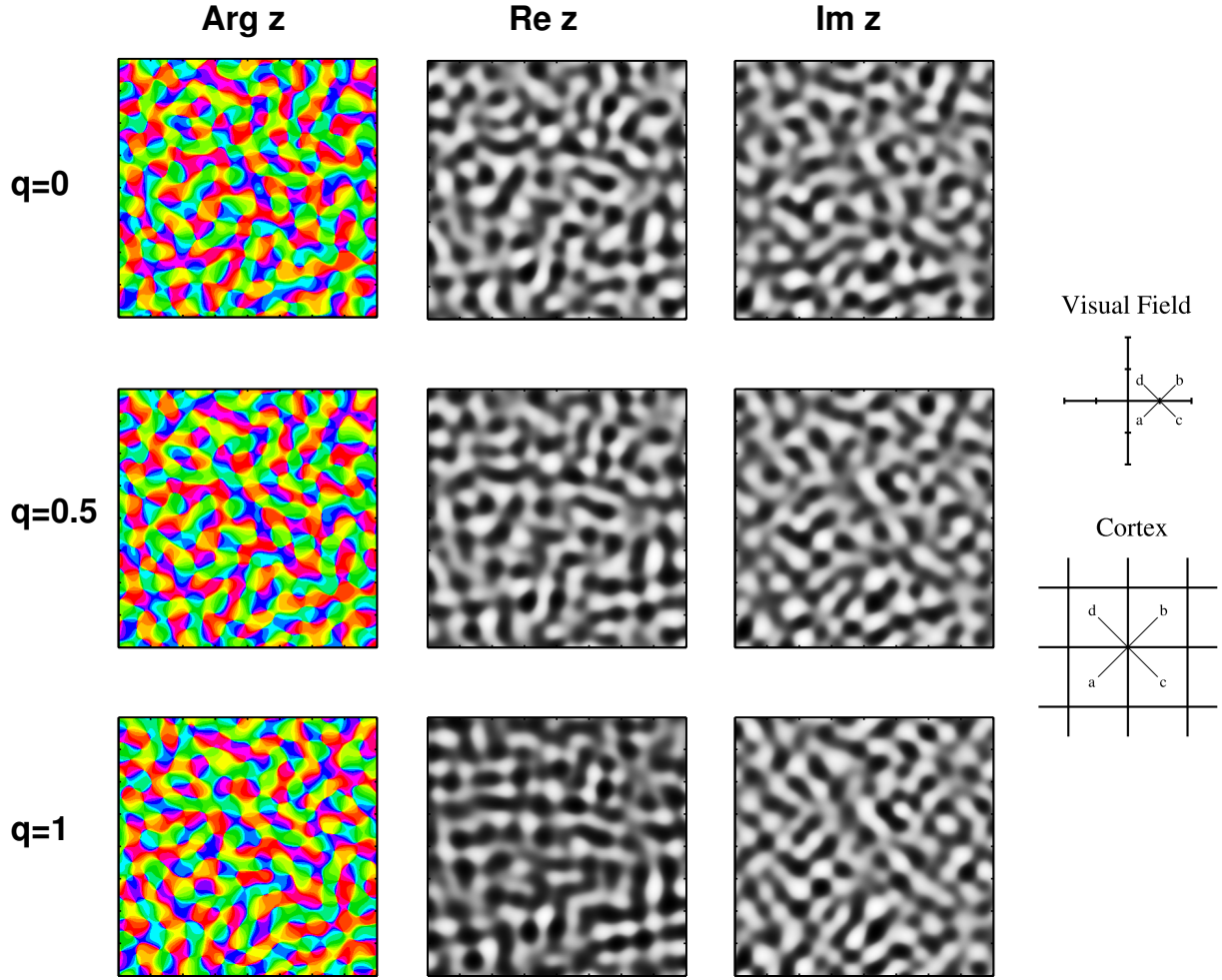
Figure 3.3: Examples of Gaussian random fields for ***positive*** degree of shift symmetry breaking. Shown on the *left* is arg $z(\mathbf{x})$, Re $z(\mathbf{x})$ and Im $z(\mathbf{x})$ of a random map for different values of shift symmetry breaking q. *Upper row:* $q = 0$ (shift symmetric case), *middle row*: $q = 0.5$, *bottom row*: $q = 1$ (shift symmetry is maximally broken). For all cases $\beta = 10$. *Right:* Scheme of the underlying visuotopic map. For simplicity, in the model visuotopic and cortical coordinates are identified.
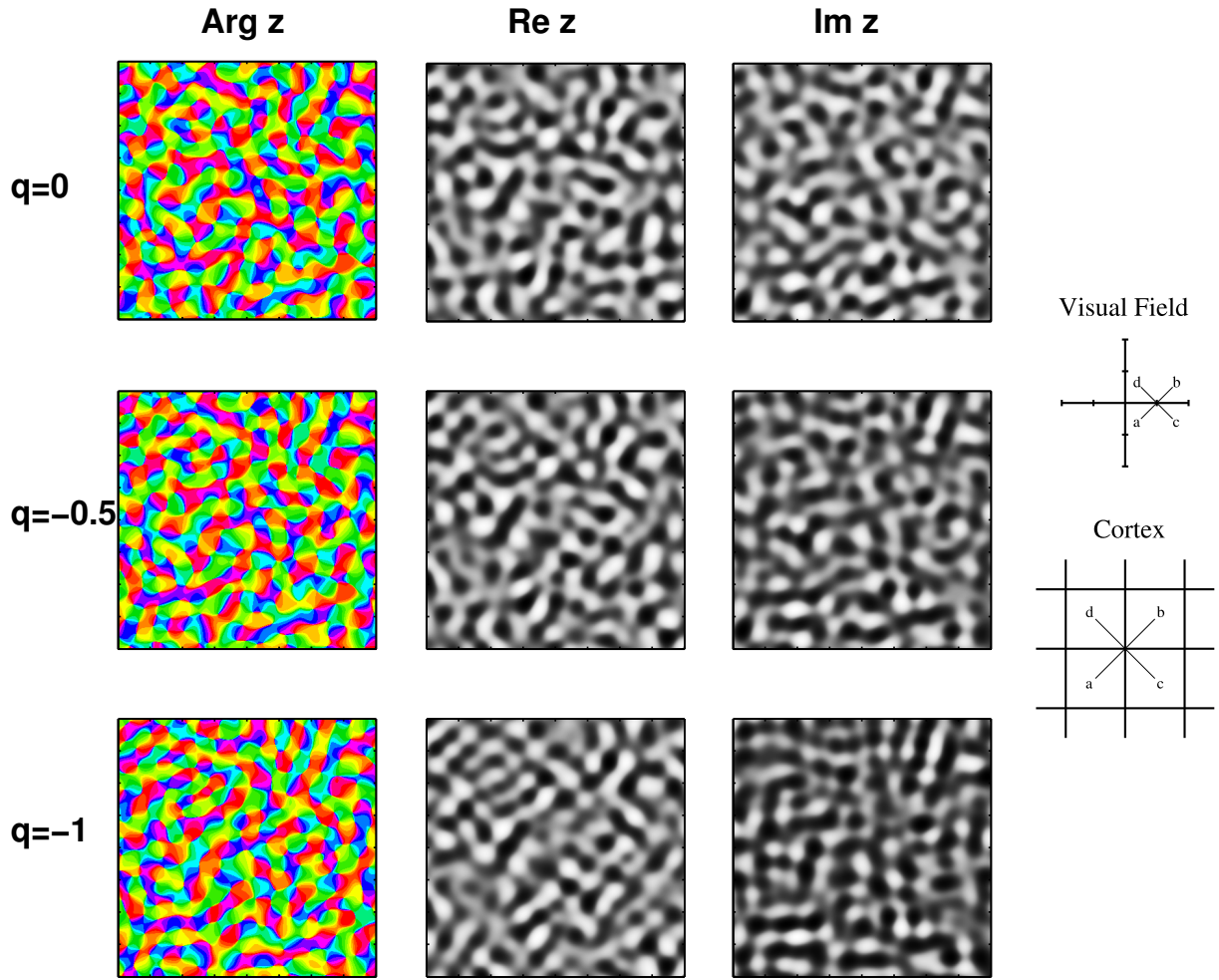
Figure 3.4: Examples of Gaussian random fields for ***negative*** degree of shift symmetry breaking. Same realization as in Fig. 3.3, however drawn for $q = 0$ (shift symmetric case, *upper row*), $q = -0.5$ (*middle row*), $q = -1$ (shift symmetry is maximally broken, *bottom row*).

3.11 Pinwheel Densities

A few years ago, Geisel and Wolf demonstrated that the number of pinwheels generated early in development exhibits a universal minimal value that depends only on general symmetry properties of the cortical network. This result suggested that in species exhibiting a lower number of pinwheels in the adult, pinwheels must move and annihilate in pairs during the refinement of cortical circuitry [13]. Verification of this intriguing prediction would therefore provide striking evidence for the activity-dependent generation of the basic visual cortical processing architecture. In this section we revisit the problem of early pinwheel densities for Gaussian random fields with arbitrary degree of shift symmetry breaking in order to analyze in how far symmetry breaking influences pinwheel generation and affects the previously calculated lower bound.

Pinwheel centers are the zeros of the complex field

$$z(\mathbf{x}) = R(\mathbf{x}) + i \, I(\mathbf{x}),$$

which means that at pinwheels the real and imaginary parts both vanish,

$$R(\mathbf{x}_{pw}) = 0, \quad I(\mathbf{x}_{pw}) = 0.$$

The number $N(A)$ of pinwheels in a given area A is therefore given by

$$N(A) = \int_A d^2\mathbf{x} \, \delta\left(R(\mathbf{x})\right) \, \delta\left(I(\mathbf{x})\right) |\mathcal{J}(\mathbf{x})| \tag{3.22}$$

with the Jacobian

$$\mathcal{J}(\mathbf{x}) := \frac{\partial R(\mathbf{x})}{\partial x_1}\frac{\partial I(\mathbf{x})}{\partial x_2} - \frac{\partial I(\mathbf{x})}{\partial x_1}\frac{\partial R(\mathbf{x})}{\partial x_2}$$

The Jacobian ensures that in the integral of Eq.(3.22) every pinwheel increments $N(A)$ by one. The expectation value of the number of pinwheels in the ensemble of Gaussian random fields is then given by the ensemble average

$$\langle N(A)\rangle = \left\langle \int_A d^2\mathbf{x} \, \delta\left(R(\mathbf{x})\right) \, \delta\left(I(\mathbf{x})\right) |\mathcal{J}(\mathbf{x})| \right\rangle \tag{3.23}$$

from which follows that the average pinwheel density $\rho(\mathbf{r})$ equals

$$\rho(\mathbf{x}) = \langle \delta\left(R(\mathbf{x})\right) \, \delta\left(I(\mathbf{x})\right) |\mathcal{J}(\mathbf{x})| \rangle . \tag{3.24}$$

Since we assume translation invariance of the ensemble this value must be the same for all $\mathbf{x}$ and we drop the explicit dependence on $\mathbf{x}$ in the following, writing

$$\rho = \langle \delta\left(R\right) \, \delta\left(I\right) |\mathcal{J}| \rangle . \tag{3.25}$$

In order to evaluate this expression it is sufficient to know the joint probability density of z and ∇z. Since any linear functional of a Gaussian random variable is also Gaussian, it follows that derivatives ∇z are normally distributed. For this reason $p(R, I, \nabla R, \nabla I)$ is a multivariate Gaussian of the form

$$p(\zeta) = \frac{1}{(2\pi)^3\sqrt{\det W}} \exp\left(-\frac{1}{2}\mathbf{v}^T W^{-1}\mathbf{v}\right) \tag{3.26}$$

with $\mathbf{v} = (R, I, \partial_x R, \partial_y R, \partial_x I, \partial_y I)^T$ and symmetric covariance matrix W,

$$
W = \begin{pmatrix}
\langle R^2 \rangle & \langle R I \rangle & \langle R(\partial_x R) \rangle & \langle R(\partial_y R) \rangle & \langle R(\partial_x I) \rangle & \langle R(\partial_y I) \rangle \\
\cdot & \langle I^2 \rangle & \langle I(\partial_x R) \rangle & \langle I(\partial_y R) \rangle & \langle I(\partial_x I) \rangle & \langle I(\partial_y I) \rangle \\
\cdot & \cdot & \langle (\partial_x R)^2 \rangle & \langle (\partial_x R)(\partial_y R) \rangle & \langle (\partial_x R)(\partial_x I) \rangle & \langle (\partial_x R)(\partial_y I) \rangle \\
\cdot & \cdot & \cdot & \langle (\partial_y R)^2 \rangle & \langle (\partial_y R)(\partial_x I) \rangle & \langle (\partial_y R)(\partial_y I) \rangle \\
\cdot & \cdot & \cdot & \cdot & \langle (\partial_x I)^2 \rangle & \langle (\partial_x I)(\partial_y I) \rangle \\
\cdot & \cdot & \cdot & \cdot & \cdot & \langle (\partial_y I)^2 \rangle
\end{pmatrix} \quad (3.27)
$$

where the matrix elements are expressible in terms of $C_1(\mathbf{r})$ and $C_2(\mathbf{r})$ as follows:

$$
\begin{aligned}
\langle R^2 \rangle &= 1/2 \, [C_1(\mathbf{r}) + \mathrm{Re}\, C_2(\mathbf{r})]_{\mathbf{r}=0} \\
\langle I^2 \rangle &= 1/2 \, [C_1(\mathbf{r}) - \mathrm{Re}\, C_2(\mathbf{r})]_{\mathbf{r}=0} \\
\langle R I \rangle &= 1/2 \, [\mathrm{Im}\, C_2(\mathbf{r})]_{\mathbf{r}=0}
\end{aligned}
$$

The remaining matrix elements involving derivatives can be obtained from the previous expressions by differentiation, e.g.

$$
\begin{aligned}
\langle R(\partial_j R) \rangle &= 1/2 \, \partial_j \, [C_1(\mathbf{r}) + \mathrm{Re}\, C_2(\mathbf{r})]_{\mathbf{r}=0} \\
\langle (\partial_i R)(\partial_j R) \rangle &= -1/2 \, \partial_i \partial_j \, [C_1(\mathbf{r}) + \mathrm{Re}\, C_2(\mathbf{r})]_{\mathbf{r}=0}
\end{aligned}
$$

Note the occurrence of a minus sign in terms with two derivatives. It is important to realize that due to the prefactor $(r_1 + i\, r_2)^4$ occurring in the general formula for $C_2(\mathbf{r})$, Eq.(3.11), all terms containing $C_2(\mathbf{r})$, $\partial_i C_2(\mathbf{r})$, $\partial_i \partial_j C_2(\mathbf{r})$ vanish when evaluated at $\mathbf{r} = 0$. For that reason the pinwheel density exclusively depends on the rotation and, by definition, shift invariant correlation function $C_1(\mathbf{r})$ and thus is independent of $C_2(\mathbf{r})$. In particular, this means that the pinwheel density is independent of the degree of shift symmetry breaking q. The covariance matrix W thus states

$$
W = \frac{1}{2} \begin{pmatrix}
C_1(\mathbf{0}) & 0 & (\partial_x C_1)(\mathbf{0}) & (\partial_y C_1)(\mathbf{0}) & 0 & 0 \\
\cdot & C_1(\mathbf{0}) & 0 & 0 & (\partial_x C_1)(\mathbf{0}) & (\partial_y C_1)(\mathbf{0}) \\
\cdot & \cdot & -(\partial_{xx} C_1)(\mathbf{0}) & -(\partial_{xy} C_1)(\mathbf{0}) & 0 & 0 \\
\cdot & \cdot & \cdot & -(\partial_{yy} C_1)(\mathbf{0}) & 0 & 0 \\
\cdot & \cdot & \cdot & \cdot & -(\partial_{xx} C_1)(\mathbf{0}) & -(\partial_{xy} C_1)(\mathbf{0}) \\
\cdot & \cdot & \cdot & \cdot & \cdot & -(\partial_{yy} C_1)(\mathbf{0})
\end{pmatrix} \quad (3.28)
$$

Due to rotation symmetry also the terms $(\partial_i C_1)(\mathbf{0})$ and the mixed derivatives $(\partial_i \partial_j C_1)(\mathbf{0})$ $(i \neq j)$ vanish, such that

$$
W = \mathrm{diag}(c_z, c_z, c_g, c_g, c_g, c_g)
$$

where we used the abbreviation

$$
c_z = \frac{1}{2} \, C_1(\mathbf{0}), \qquad c_g = -\frac{1}{4} \, (\Delta C_1)(\mathbf{0})
$$

and the fact that $(\partial_{xx} C_1)(\mathbf{r}) = (\partial_{yy} C_1)(\mathbf{r})$ due to rotation invariance of $C_1(\mathbf{r})$. The joint probability distribution $p(\zeta)$ thus reads

$$
p(\zeta) = \frac{1}{(2\pi)^3 c_z c_g^2} \, \exp\left(-\frac{z\bar{z}}{2c_z} \right) \exp\left(-\frac{\nabla z \nabla \bar{z}}{2c_g} \right).
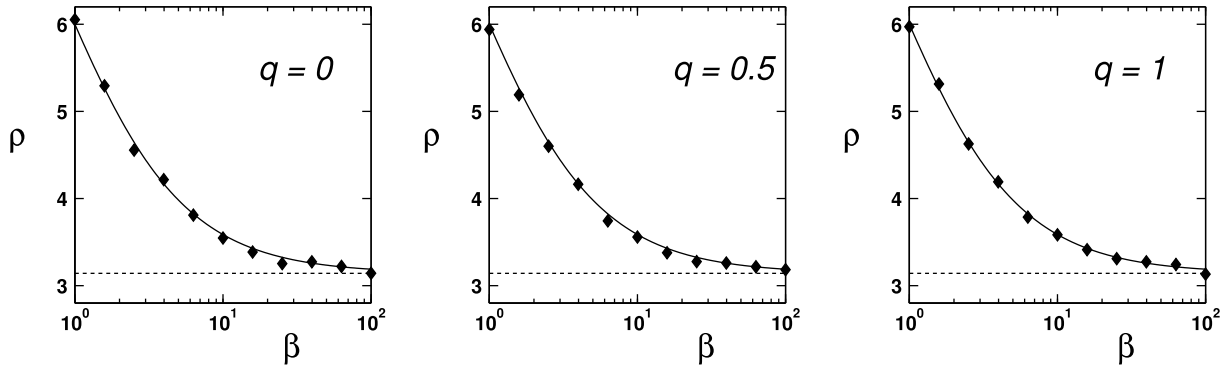$$

Figure 3.5: Dimensionless pinwheel densities $\hat{\rho} = \rho\Lambda^2$ as a function of powerspectral width β for various degree of shift symmetry breaking $|q| = 0$, 0.5, 1. *Full Line:* Analytical prediction, *Data points:* Numerical simulations, from an average over $N = 50$ Gaussian random fields.

We can now perform the ensemble average, given by the integral

$$\rho = \int d\zeta \, p(\zeta) \, \delta(R) \, \delta(I) \, |\mathcal{J}|$$

to obtain the pinwheel density ρ. The result of this calculation (see Appendix 3.17) yields

$$\rho = -\frac{\Delta C_1(\mathbf{0})}{4\pi \, C_1(\mathbf{0})} \tag{3.29}$$

3.12 Model Pinwheel Densities

Next we evaluate the analytical expression Eq.(3.29) for ensembles of Gaussian random fields defined by the correlation functions Eq.(3.21). The calculation of the dimensionless, rescaled pinwheel density $\hat{\rho} = \rho\,\Lambda^2$ yields

$$\hat{\rho} = \pi \, \frac{(2+\beta)\Gamma[\frac{1+\beta}{2}]^2}{2\Gamma[\frac{2+\beta}{2}]^2}.$$

This expression depends on the parameter β, controlling the powerspectral width, but is independent of q, the degree of shift symmetry breaking. A numerical check of this formula was obtained from 50 realizations of random fields for several values of $\beta \in [1, \ldots 100]$ and for three different values of $q \in [0, 0.5, 1]$, confirming the prediction that pinwheel densities are independent of q. The results are shown in Fig. 3.5. For $\beta = 1$ (broad powerspectrum) $\hat{\rho} = 6$ and for $\beta \to \infty$ (powerspectrum on circle) $\hat{\rho} \to \pi$. Thus, the pinwheel density gets smaller for decreasing powerspectral width (increasing β) and asymptotically approaches π from above.

3.13 Lower Bound on Pinwheel Densities

Next we prove analytically that pinwheel densities of Gaussian random fields have an expectation value larger than π. Following the line of arguments given in [34] we switch into Fourier representation. First, we express $C_1(\mathbf{0})$ and $(\Delta C_1)(\mathbf{0})$ as functionals of $P_1(\mathbf{k})$,

$$C_1(\mathbf{0}) = \frac{1}{2\pi} \int d^2\mathbf{k}\, P_1(\mathbf{k}) \quad (\Delta C_1)(\mathbf{0}) = -\frac{1}{2\pi} \int d^2\mathbf{k}\, |\mathbf{k}|^2 P_1(\mathbf{k})$$

The pinwheel density is then given by

$$\rho = \frac{1}{4\pi} \frac{\int d^2\mathbf{k}|\mathbf{k}|^2 P_1(\mathbf{k})}{\int d^2\mathbf{k}\, P_1(\mathbf{k})}. \tag{3.30}$$

The exact form of the correlation function $C_1(\mathbf{r})$ or $P_1(\mathbf{k})$ at the beginning of orientation map development is not known. In particular, it is to be expected that these functions vary from species to species and from individual to individual. The following argument shows that Eq.(3.30) implies a quantitative estimate of the pinwheel density. With the definition of k_0 (c.f. Eq.(3.20))

$$k_0 = \int\limits_0^\infty dk\, k\, p(k)$$

where $p(k)$ denotes the radial part of $P_1(\mathbf{k})$, normalized to 1 (c.f. Eq.(3.19))

$$\int\limits_0^\infty dk\, p(k) = 1$$

expression Eq.(3.30) equals

$$\rho = \frac{\pi}{\Lambda^2} \frac{\int_0^\infty dk\, k^3 p(k)}{(\int_0^\infty dk\, k\, p(k))^3}.$$

Using Jensen's inequality,

$$\int\limits_0^\infty dk\, k^3 p(k) \geq (\int_0^\infty dk\, k\, p(k))^3$$

it follows that ρ can be written

$$\rho = \frac{\pi}{\Lambda^2}(1 + \alpha)$$

where $\alpha \geq 0$ is given by the functional

$$\alpha = 3/k_0^2 \int\limits_0^\infty dk\, (k - k_0)^2 p(k) + 1/k_0^3 \int\limits_0^\infty dk (k - k_0)^3\, p(k)$$

from which follows that $\alpha = 0$ when $p(k) = \delta(k - k_0)$. Thus, Gaussian random patterns of orientation preferences have a minimum lower bound on their pinwheel density,

$$\rho_{\min} = \frac{\pi}{\Lambda^2}.$$

Due to the ergodicity of Gaussian random fields [50] this lower limit also applies to the pinwheel density of individual realizations.
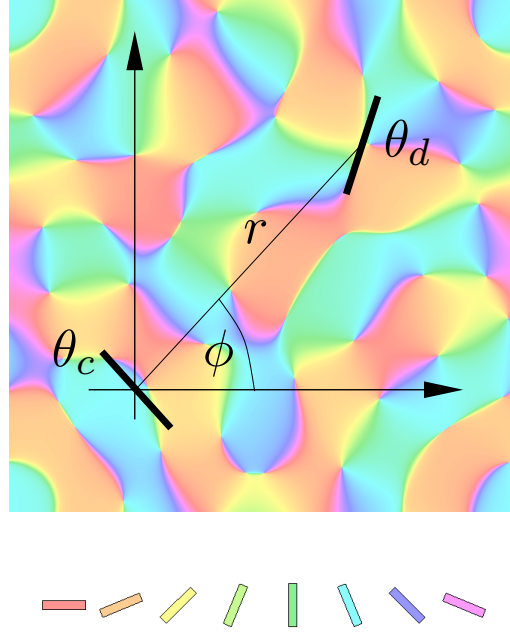
Figure 3.6: Scheme which illustrates the definition of the co-occurrence statistics $P_{\mathbf{r}}(\theta_c, \theta_d)$, the probability that two groups of neurons separated by a vector $\mathbf{r} = r(\cos\phi, \sin\phi)$ have orientation preferences θ_c and θ_d, respectively.

3.14 Edge Statistics and Shift-Twist Symmetry

In the remaining part of this chapter we discuss yet another statistics, the pair occurrence statistics $P_{\mathbf{r}}(\theta_c, \theta_d)$, defined as the probability that two groups of neurons separated by a vector $\mathbf{r} = r(\cos\phi, \sin\phi)$ have orientation preferences θ_c and θ_d, respectively (see Fig. 3.6). Beyond its applicability to the analysis of orientation maps this statistics can also be computed for any datasets which consist of planar arrangements of oriented entities, such as line segments in natural scenes (c.f. [52] and Section 6.4) or nematic liquid crystals [53]. Often in such systems Euclidean symmetry is a good approximation. Here we derive the general form of $P_{\mathbf{r}}(\theta_c, \theta_d)$ assuming that Euclidean $E(2)$ symmetry holds. Furthermore, we discuss how this statistics can be applied to orientation maps in order to reveal signatures of shift symmetry breaking in the data. We find that shift symmetry breaking leads to characteristic modulations of the probability histogram which, in general, can be written as a sum of two components: (a) cloverleaf modulations with a 4-fold symmetry and (b) bipolar modulations with a 2-fold symmetry. Since these modulations do not occur in the shift symmetric case their appearance can be used as signatures of shift symmetry breaking.

Pair cooccurence statistics

Suppose we were given an ensemble of orientation maps and would like to test the hypothesis that shift symmetry is broken in this dataset, say, to some - presumably small - degree which we want to specify. How should we proceed? One possibility would be to calculate the second order correlation functions, $C_1(\mathbf{r})$ and $C_2(\mathbf{r})$, and to test for any cloverleaf signature in $C_2(\mathbf{r})$
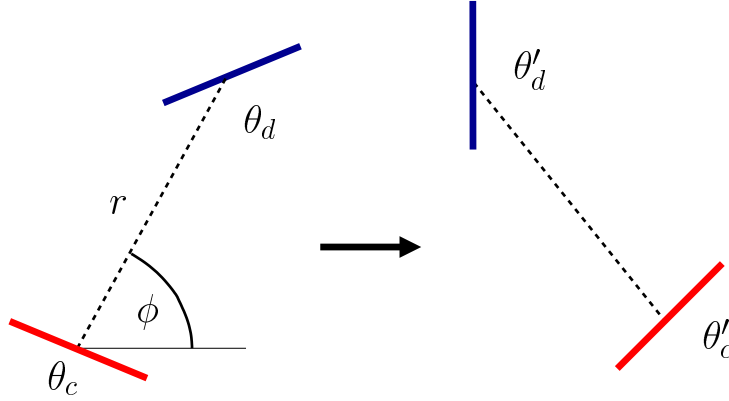
Figure 3.7: When rotated by an angle α, a pair of orientations θ_c and θ_d separated by a distance r and angle ϕ is mapped to $(r, \phi', \theta_c', \theta_d') = (r, \phi + \alpha, \theta_c + \alpha, \theta_d + \alpha)$.

by determining its q value, as described in Section 3.7. As an alternative, here we propose to measure the pair cooccurrence statistics of orientation preferences, which we define as the joint probability distribution of finding a pair of oriented elements, say, located at $\mathbf{x}_c$ and $\mathbf{x}_d$, with orientations θ_c and θ_d, respectively (see Fig. 3.6). For orientation maps θ_c and θ_d denote the preferred orientations at two locations in the map, whereas for natural scenes they may represent the orientations of local line segments in an image (see Fig. 6.2 in Chapter 6). Since we assume translation symmetry of the ensemble this statistics only depends on the difference vector $\mathbf{r} = \mathbf{x}_d - \mathbf{x}_c$, which we will also denote by (r, ϕ), its representation in polar coordinates. Accordingly, in the following we write $P_{\mathbf{r}}(\theta_c, \theta_d)$ or $P_{r,\phi}(\theta_c, \theta_d)$ for the joint probability density. For orientation maps θ_c and θ_d are random variables and r and ϕ are parameters. For natural scenes r and ϕ may also be conceived as random variables since for a given image there is not necessarily a contour at every position.

Symmetries

Next we derive the general functional form of $P_{r,\phi}(\theta_c, \theta_d)$ assuming Euclidean $E(2)$ symmetry. Up to which point this assumption holds remains to be quantified, especially for ensembles of natural images. For orientation maps it provides a valuable framework, as we will see in Chapter 5. The functional form $P_{r,\phi}(\theta_c, \theta_d)$ has to fulfill following requirements:

1. $P(r, \phi, \theta_c, \theta_d)$ is π-periodic in θ_c and θ_d since orientations are defined modulo π :

$$P_{r,\phi}(\theta_c, \theta_d) = P_{r,\phi}(\theta_c + \mathbb{Z}\pi, \theta_d + \mathbb{Z}\pi) \tag{3.31}$$

2. Symmetry under (shift-twist) rotations requires that

$$P_{r,\phi}(\theta_c, \theta_d) = P_{r,\phi+\alpha}(\theta_c + \alpha, \theta_d + \alpha) \tag{3.32}$$

   for any angle α, see Fig.3.7. Inversion symmetry is included as the particular case $\alpha = \pi$.

3. Reflection symmetry (e.g. with respect to reflections at the x-axis) implies

$$P_{r,\phi}(\theta_c, \theta_d) = P_{r,-\phi}(-\theta_c, -\theta_d) \tag{3.33}$$

4. When symmetry under inversions holds we also have

$$P_{r,\phi}(\theta_c, \theta_d) = P_{r,\phi}(\theta_d, \theta_c) \tag{3.34}$$

A decomposition of $P_{r,\phi}(\theta_c, \theta_d)$ into its Fourier components with respect to the angular variables ϕ, θ_c and θ_d reads

$$P_{r,\phi}(\theta_c, \theta_d) = \sum_{\mu,\nu,\kappa \in \mathbb{Z}} \tilde{a}_{\mu\nu\kappa}(r) e^{i(2\mu\theta_c + 2\nu\theta_d + \kappa\phi)}$$

with Fourier coefficients $\tilde{a}_{\mu\nu\kappa}(r)$. This ansatz already respects requirement (1). If P is going to fulfill conditions (2-4) then only a subset of coefficients don't vanish:

For example, invariance under rotations requires

$$
\begin{aligned}
P_{r,\phi}(\theta_c, \theta_d) &= \frac{1}{2\pi} \int_0^{2\pi} d\alpha \, P_{r,\phi+\alpha}(\theta_c + \alpha, \theta_d + \alpha) \\
&= \frac{1}{2\pi} \sum_{\mu,\nu,\kappa \in \mathbb{Z}} \tilde{a}_{\mu\nu\kappa}(r) e^{i(2\mu\theta_c + 2\nu\theta_d + \kappa\phi)} \int_0^{2\pi} d\alpha \, e^{i(2\mu + 2\nu + \kappa)\alpha} \\
&= \sum_{\mu,\nu,\kappa} \tilde{a}_{\mu\nu\kappa}(r) e^{i(2\mu\theta_c + 2\nu\theta_d + \kappa\phi)} \delta(2\mu + 2\nu + \kappa)
\end{aligned}
$$

such that $\tilde{a}_{\mu\nu\kappa}(r) = a_{\mu\nu}(r)\,\delta(2\mu + 2\nu + \kappa)$. Thus, any rotation invariant $P_{r,\phi}(\theta_c, \theta_d)$ can be written as

$$\sum_{\mu,\nu \in \mathbb{Z}} a_{\mu\nu}(r) e^{i(2\mu\theta_c + 2\nu\theta_d - 2(\mu+\nu)\phi)}$$

with some appropriate set of coefficient functions $a_{\mu\nu}(r)$.

Similarly, reflection symmetry requires

$$a_{\mu\nu} = a_{\nu\mu}$$

and

$$a_{\mu\nu} = a_{-\mu,-\nu},$$

respectively. Furthermore, since $P_{r,\phi}(\theta_c, \theta_d) \in \mathbb{R}$ we have

$$a_{\mu\nu} = \bar{a}_{-\mu,-\nu} = \bar{a}_{\mu\nu},$$

such that

$$a_{\mu\nu} \in \mathbb{R}.$$

Therefore, the general form of P satisfying conditions (1-4) reads

$$
\begin{aligned}
P_{r,\phi}(\theta_c, \theta_d) &= \frac{1}{4} \sum_{\mu,\nu \in \mathbb{Z}} (a_{\mu\nu}(r) + a_{\nu\mu}(r) + a_{-\mu,-\nu}(r) + a_{-\nu,-\mu}(r)) e^{i(2\mu\theta_c + 2\nu\theta_d - 2(\mu+\nu)\phi)} \\
&= \sum_{\mu,\nu \in \mathbb{Z}} a_{\mu\nu}(r) \cos\left((\mu+\nu)(\theta_c + \theta_d - 2\phi)\right) \cos\left((\mu-\nu)(\theta_d - \theta_c)\right)
\end{aligned}
$$

By means of the symmetries of $a_{\mu\nu}$ this expression further simplifies to

$$P_{r,\phi}(\theta_c, \theta_d) = \sum_{m,n\in\mathbb{N}} p_{mn}(r)\cos\left(m(\theta_c + \theta_d - 2\phi)\right)\cos(n(\theta_d - \theta_c)) \tag{3.35}$$

with indices $m, n \in \mathbb{N}$ and

$$p_{mn} = \begin{cases} a_{\frac{1}{2}(m+n),\frac{1}{2}(m-n)} + a_{\frac{1}{2}(m-n),\frac{1}{2}(m+n)} + \\ +a_{-\frac{1}{2}(m+n),-\frac{1}{2}(m-n)} + a_{-\frac{1}{2}(m-n),-\frac{1}{2}(m+n)} & \text{if } m+n \text{ is even} \\ 0 & \text{if } m+n \text{ is odd.} \end{cases}$$

The matrix p_{mn} thus has the structure

$$\begin{matrix} p_{00} & 0 & p_{02} & 0 & p_{04} & \dots \\ 0 & p_{11} & 0 & p_{13} & 0 & \dots \\ p_{20} & 0 & p_{22} & 0 & p_{24} & \dots \\ 0 & p_{31} & 0 & p_{33} & 0 & \dots \\ p_{40} & 0 & p_{42} & 0 & p_{44} & \dots \\ \vdots & \vdots & \vdots & \vdots & \vdots & \end{matrix}$$

The terms of Eq.(3.35) depend on θ_c and θ_d through the product of $\cos\left(m(\theta_c + \theta_d - 2\phi)\right)$ and $\cos(n(\theta_d - \theta_c))$. Both terms are invariant under (shift-twist) rotations and the second term is also invariant under orientation shifts, since it only depends on the angle difference

$$\Delta = \theta_d - \theta_c \tag{3.36}$$

Denoting the average angle as

$$\Sigma = \frac{1}{2}(\theta_d + \theta_c) \tag{3.37}$$

we can express $P_{r,\phi}(\theta_c, \theta_d)$ in the set of new coordinates Σ and Δ,

$$P'_{r,\phi}(\Sigma, \Delta) := P_{r,\phi}(\theta_c(\Sigma, \Delta), \theta_d(\Sigma, \Delta)) \cdot J$$

where J denotes the Jacobian of the coordinate transform

$$J = \|\partial(\theta_c, \theta_d)/\partial(\Sigma, \Delta)\| = 1.$$

By rotation symmetry

$$P'_{r,\phi}(\Sigma, \Delta) = P'_{r,0}(\Sigma - \phi, \Delta).$$

Thus, in the following it is sufficient to consider

$$P'_r(\Sigma, \Delta) := P'_{r,0}(\Sigma, \Delta) = \sum_{m,n\in\mathbb{N}} p_{mn}(r)\cos\left(2m\Sigma\right)\cos(n\Delta). \tag{3.38}$$

The back transform is simply given by

$$P_{r,\phi}(\theta_c, \theta_d) = P'_r\left(\Sigma(\theta_c, \theta_d) - \phi, \Delta(\theta_c, \theta_d)\right). \tag{3.39}$$

We can, without loss of generality, restrict the range to $\Delta \in [-\pi/2, \pi/2)$ and $\Sigma \in [0, \pi)$. Figure 3.8 explains this mapping in more detail.

a
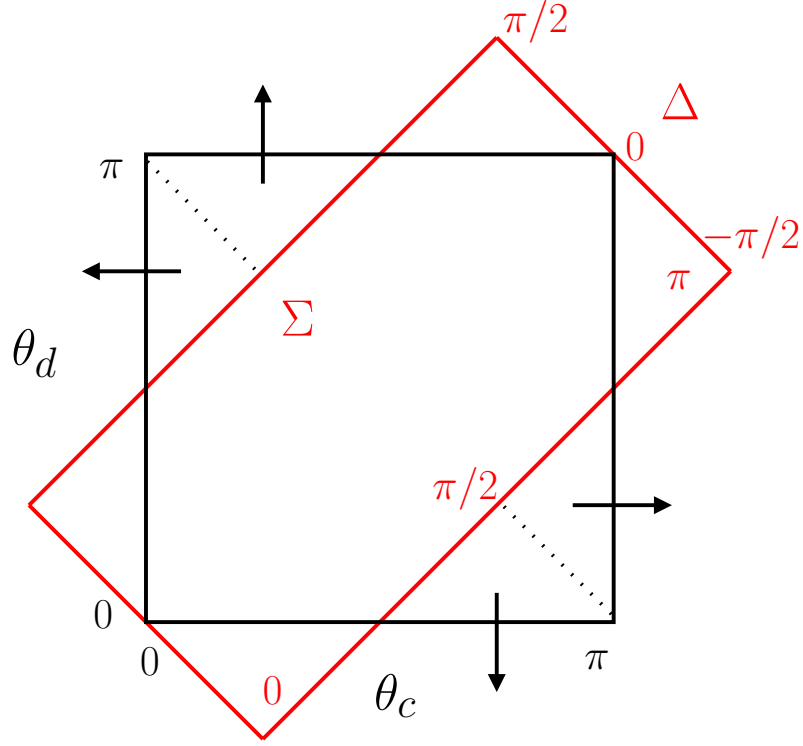
b
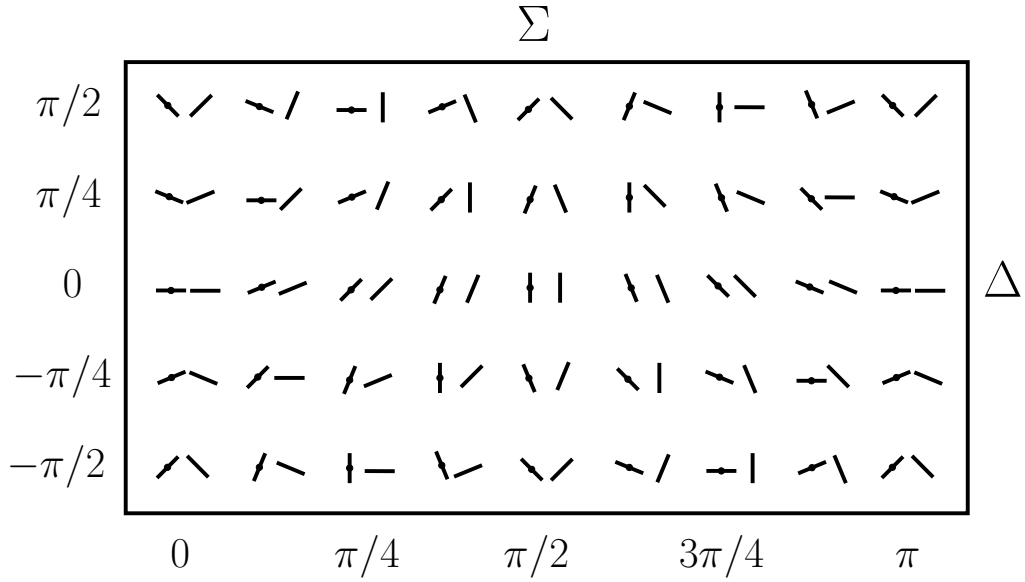
Figure 3.8: Illustration of the coordinate transform from (θ_c, θ_d) to (Σ, Δ), Eq.(3.36) and (3.37) . (**a**) The plot is periodic in θ_c and θ_d, arrows denote wrap around in the indicated directions which are necessary in order to achieve $\Sigma \in [0, \pi]$ and $\Delta \in [-\pi/2, \pi/2]$. (**b**) Configurations of θ_c and θ_d for each combination of Σ and Δ. Collinear arrangements correspond to $\Sigma = 0 \mod 2\pi$ and $\Delta = 0$, parallel arrangements to $\Sigma = \pi/2 \mod 2\pi$ and $\Delta = 0$.

Let us discuss how to measure $P_r(\Sigma, \Delta)$, in practice, for a given orientation map $z(\mathbf{x})$. First we calculate the angle map $\theta(\mathbf{x}) = \frac{1}{2} \arg z(\mathbf{x})$. Then we consider every pair $\mathbf{x}_c$ and $\mathbf{x}_d$ in the map and determine $\theta_c = \theta(\mathbf{x}_c)$ and $\theta_d = \theta(\mathbf{x}_d)$. We calculate its relative distance $r = |\mathbf{x}_d - \mathbf{x}_c|$ and angle ϕ. Every pair $(r, \phi, \theta_c, \theta_d)$ is then brought into a 'standard form' $(r', \phi', \theta'_c, \theta'_d) = (r, 0, \theta_c - \phi, \theta_d - \phi)$ by applying a rotation $-\phi$. For this pair we determine the difference angle $\Delta = \theta'_d - \theta'_c = \theta_d - \theta_c$ and the average angle $\Sigma = (\theta'_c + \theta'_d)/2 = (\theta_c + \theta_d - \phi)/2$ and increase the corresponding bin in the histogram $P'_r(\Sigma, \Delta)$ by one. The resulting $P'_r(\Sigma, \Delta)$ is expected to approach the form (3.38) for a sufficiently large dataset.

Now, given such a histogram $P'_r(\Sigma, \Delta)$ how can we decide whether shift symmetry is broken or not? Using Bayes' theorem, $P'_r(\Sigma, \Delta)$ can always be written as the product of two components,

$$P'_r(\Sigma, \Delta) = P'_r(\Sigma|\Delta) P'_r(\Delta)$$

The marginal probability distribution of Δ,

$$P'_r(\Delta) = \int d\Sigma P'_r(\Sigma, \Delta)$$

and the conditional probability distribution of Σ for a given Δ,

$$P'_r(\Sigma|\Delta) = P'_r(\Sigma, \Delta)/P'_r(\Delta).$$

By construction $P'_r(\Delta)$ is shift symmetric. In general, this does not apply for $P'_r(\Sigma|\Delta)$. For a shift invariant ensemble $P'_r(\Sigma|\Delta)$ would be flat, i.e.

$$P'_r(\Sigma|\Delta) = 1/\pi.$$

Thus, a departure of $P'_r(\Sigma|\Delta)$ from that constant value is a signature of shift symmetry breaking. In conclusion, for our purpose it is more convenient to consider the conditional probability density $P'_r(\Sigma|\Delta)$ than the entire distribution $P'_r(\Sigma, \Delta)$. It also has the advantage that we do not have to cope with the singular behaviour of $P'_r(\Sigma, \Delta)$ for $r \to 0$, which comes from the fact that for continuous arrangements of edges, i.e. for orientation maps,

$$\lim_{r \to 0}(\theta_d - \theta_c) = 0$$

such that

$$\lim_{r \to 0} P'_r(\Delta) = \delta(\Delta)$$

Therefore, in the limit $r \to 0$ we expect $P'_r(\Sigma, \Delta)$ to become singular,

$$\lim_{r \to 0} P'_r(\Sigma, \Delta) = P'_r(\Sigma|\Delta) \delta(\Delta).$$

As shown above $P'_r(\Sigma|\Delta)$ can be decomposed as follows

$$P'_r(\Sigma|\Delta) = \sum_{m,n \in \mathbb{N}} c_{mn}(r) \cos(2m\Sigma) \cos(n\Delta) \tag{3.40}$$

with $c_{00} = 1/\pi$ and $c_{mn} = 0$ for odd numbers $m + n$. For even numbers $m + n$ there are two possibilities, (1) m and n are even, (2) m and n are odd. As we will see in Chapter (5) this distinction is useful since it allows to decompose $P'_r(\Sigma|\Delta)$ into a direct sum

$$P'_r(\Sigma|\Delta) = \frac{1}{\pi} \oplus P'^{(2)}_r(\Sigma|\Delta) \oplus P'^{(4)}_r(\Sigma|\Delta) \tag{3.41}$$

where $P'^{(4)}_r$ refers to subset (1) and is called the *cloverleaf component*, whereas $P'^{(2)}_r$ refers to subset (2) and is called the *collinear component* in the following.

3.15 Predictions for Gaussian Random Fields

In this section we calculate the probability distribution $P_{r,\phi}(\theta_d, \theta_c)$ for Gaussian random fields with arbitrary correlation functions and arbitrary degree of shift symmetry breaking. We then derive a closed form expression for $P'_{r,\phi}(\Sigma, \Delta)$ as well as a useful approximation for $P'_r(\Sigma|\Delta)$.

We begin by calculating the probability density

$$P_{r,\phi}(\theta_c, \theta_d) = \langle \delta \left(\arg z(\mathbf{0}) - 2\theta_c \right) \delta \left(\arg z(\mathbf{r}) - 2\theta_d \right) \rangle$$

where the average is taken with respect to the joint probability density of $\mathbf{v} = (R(\mathbf{0}), I(\mathbf{0}), R(\mathbf{r}), I(\mathbf{r}))$,

$$\mathcal{P}(\mathbf{v}) = \frac{1}{(2\pi)^2 \sqrt{\det M}} \exp \left(-\frac{1}{2} \mathbf{v} \, \mathcal{C}^{-1} \, \mathbf{v} \right)$$

With $\mathbf{r} = r \left(\cos\phi, \sin\phi \right)$ the covariance matrix $\mathcal{C}$ reads

$$\frac{1}{2} \begin{pmatrix} C_1(0) & 0 & C_1(r) + |C_2(r)| \cos 4\phi & |C_2(r)| \sin 4\phi \\ 0 & C_1(0) & |C_2(r)| \sin 4\phi & C_1(r) - |C_2(r)| \cos 4\phi \\ C_1(r) + |C_2(r)| \cos 4\phi & |C_2(r)| \sin 4\phi & C_1(0) & 0 \\ |C_2(r)| \sin 4\phi & C_1(r) - |C_2(r)| \cos 4\phi & 0 & C_1(0) \end{pmatrix}.$$

Its eigenvalues are

$$\lambda_{1...4} = \frac{1}{2} \left(C_1(0) \pm C_1(r) \pm |C_2(r)| \right),$$

thus $\mathcal{C}$ is positive definite if $C_1(0) > |C_1(r)| + |C_2(r)|$. Furthermore,

$$\begin{aligned} \det \mathcal{C} &= \prod_i \lambda_i = \frac{1}{16} \left[(C_1(0) + C_1(r))^2 - |C_2(r)|^2 \right] \left[(C_1(0) - C_1(r))^2 - |C_2(r)|^2 \right] \\ &= \frac{C_1^4(0)}{16} \left[(1 + c_1(r))^2 - |c_2(r)|^2 \right] \left[(1 - c_1(r))^2 - |c_2(r)|^2 \right] \end{aligned}$$

where we set

$$\begin{aligned} c_1(r) &= C_1(r)/C_1(0) \\ c_2(r) &= C_2(r)/C_1(0) \end{aligned}$$

Positive definiteness of $\mathcal{C}$ requires

$$|c_1(r)| + |c_2(r)| < 1$$

and is assumed for the following. We substitute

$$\mathbf{v} = (s \cos 2\theta_c, s \sin 2\theta_c, t \cos 2\theta_d, t \sin 2\theta_d)$$

such that

$$\begin{aligned} P_{r,\phi}(\theta_c, \theta_d) &= \frac{4}{(2\pi)^2 \sqrt{\det \mathcal{C}}} \int_0^\infty ds \int_0^\infty dt \, s \, t \, \exp -\frac{1}{2} \sum_{ij} (\mathcal{C}^{-1})_{ij} v_i v_j \\ &= \frac{4m^{3/2}}{\pi^2} \int_0^\infty ds \int_0^\infty dt \, s \, t \, \exp \left(-a \, s^2 - b \, t^2 - 2c \, s \, t \right) \end{aligned}$$

with

$$m = \left[(1 + c_1(r))^2 - |c_2(r)|^2\right] \left[(1 - c_1(r))^2 - |c_2(r)|^2\right]$$

and

$$
\begin{aligned}
a &= 1 - c_1^2(r) + 2c_1(r)|c_2(r)|\cos(4(\theta_c - \phi)) - |c_2(r)|^2 \\
b &= 1 - c_1^2(r) + 2c_1(r)|c_2(r)|\cos(4(\theta_d - \phi)) - |c_2(r)|^2 \\
c &= -c_1(r)\left(1 - c_1^2(r) + |c_2(r)|^2\right)\cos(2\theta_c - 2\theta_d) \\
&\quad + |c_2(r)|\left(1 + c_1^2(r) - |c_2(r)|^2\right)\cos(2\theta_c + 2\theta_d - 4\phi)
\end{aligned}
$$

We integrate over s and t as follows

$$
\begin{aligned}
P_{r,\phi}(\theta_c, \theta_d) &= -\frac{2m^{3/2}}{\pi^2}\frac{d}{dc}\left[\int_0^\infty ds \int_0^\infty dt \exp\left(-a\,s^2 - b\,t^2 - 2c\,s\,t\right)\right] \\
&= -\frac{2m^{3/2}}{\pi^2}\frac{d}{dc}\left[\frac{\pi - 2\arctan\left(c/\sqrt{a\,b - c^2}\right)}{4\sqrt{ab - c^2}}\right] \\
&= \frac{m^{3/2}}{\pi^2}\left[\frac{1}{(a\,b - c^2)} + c\,\frac{(2\arctan(c/\sqrt{a\,b - c^2}) - \pi)}{2(a\,b - c^2)^{3/2}}\right] \quad (3.42)
\end{aligned}
$$

Since $\mathcal{C}$ is positive definite $a, b > 0$ and $c^2 \leq a\,b$. Assuming $\lim_{r\to\infty} c_1(r) = 0$ and $\lim_{r\to\infty} c_2(r) = 0$ one finds

$$\lim_{r\to\infty} P_{r,\phi}(\theta_c, \theta_d) = \frac{1}{\pi^2}$$

which means that θ_c and θ_d become statistically independent for large separations r. From the expression (3.42) $P'_{r,\phi}(\Sigma, \Delta)$ is obtained simply by the substitution $\theta_c = \Sigma - \Delta/2$, $\theta_d = \Sigma + \Delta/2$. For the marginal probability distribution of Δ we find

$$
\begin{aligned}
P'_{r,\phi}(\Delta) &= \int_0^\pi d\Sigma\, P'_{r,\phi}(\Sigma, \Delta) \\
&= \int_0^\pi d\Sigma\, P'_r(\Sigma - \phi, \Delta) \\
&= \frac{1}{2}\int_0^{2\pi} d\phi\, P'_r(\Sigma - \phi, \Delta) \quad (3.43)
\end{aligned}
$$

from which we see that integration over Σ can be replaced by integration over the angle ϕ. Since we could not solve this integral analytically we tried to approximate this distribution by simply setting $c_2(r) \equiv 0$ in the Eq.(3.42), which also yields a shift symmetric distribution since shift symmetry breaking is mediated by the c_2 terms. The result states

$$
\begin{aligned}
P'^{c_2=0}_r(\Delta) &= \frac{1 - c_1^2(r)}{2\pi\left(1 - c_1^2(r)\cos^2(2\Delta)\right)} \\
&\quad \times \left[1 + c_1(r)\cos(2\Delta)\left(\frac{\pi + 2\arctan\left(\frac{c_1(r)\cos(2\Delta)}{\sqrt{1 - c_1^2(r)\cos^2(2\Delta)}}\right)}{2\sqrt{1 - c_1^2(r)\cos^2(2\Delta)}}\right)\right]. \quad (3.44)
\end{aligned}
$$
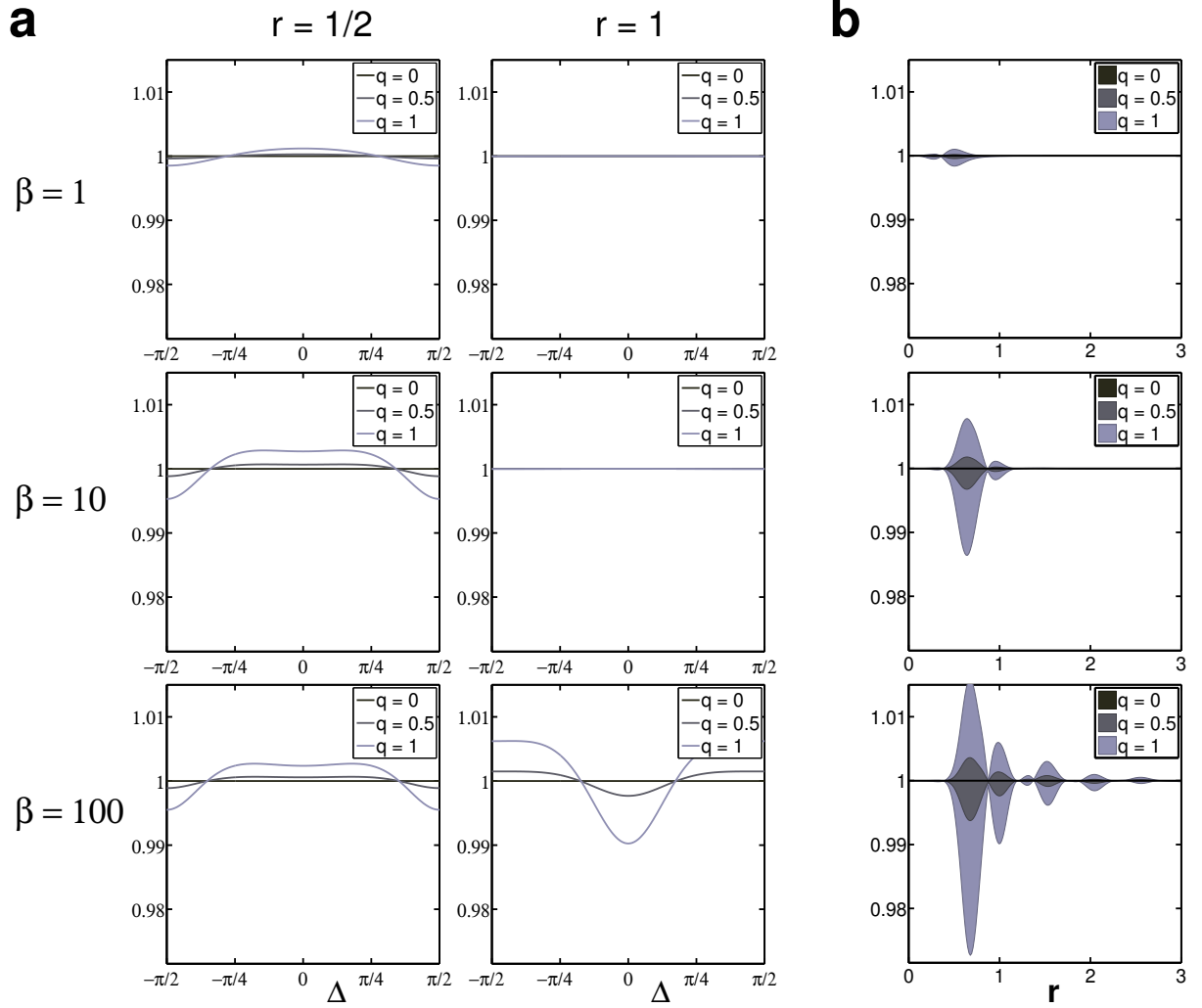
Figure 3.9: Deviations of the approximate marginal density distribution $P_r^{c_2=0}(\Delta)$, Eq.(3.44) from the exact result $P_r(\Delta)$, Eq.(3.43). Shown is the ratio between the two expressions as functions of Δ (**a**) and r (**b**), for $\beta = 1, 10, 100$. (**b**) displays the ranges of $P_r^{c_2=0}(\Delta)/P_r(\Delta)$ for all values of Δ as a function of r. The observed deviations amount to maximally a few percent. Further details are given in the text.
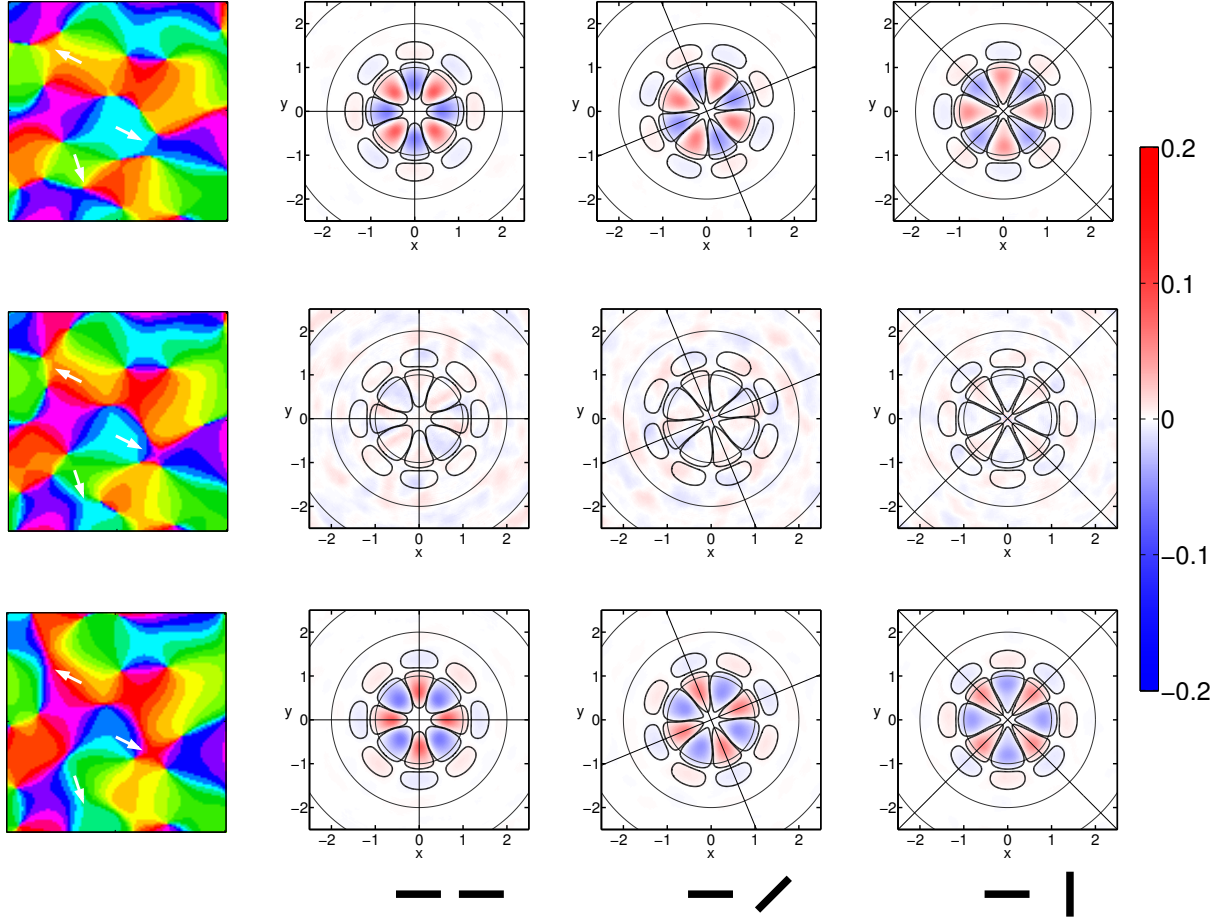
Figure 3.10: Edge co-occurrence statistics in the Gaussian ensemble predicted for different degrees of shift-symmetry breaking. *Upper row: $q = -0.5$, middle row: $q = 0.0$, lower row: $q = 0.5$.* Shown in each row are small regions from synthesized orientation maps *(left)* and the probability modulation $P_{(x,y)}(\theta_d|\theta_c = 0)$ (obtained from $P_{r,\phi}(\Sigma|\Delta)$ in analogy to Eq.(3.39)) for three different values of $\Delta = \theta_d - \theta_c$ *(right)*, $\Delta = 0°$, $45°$, $90°$. Note, that the modulation of the probabilities exhibit a discrete 4-fold rotational symmetry. As explained at the end of this section, Gaussian random fields, by construction, lack any kind of 2-fold component, which, in principle, would also be consistent with Euclidean symmetry. *White arrows* in the leftmost column serve as reference points in the map. Although at a first sight the overall layout of the pattern appears to be preserved, shift symmetry breaking locally induces subtle rearrangements of orientation domains *(arrows)*.

This approximation is compared to the exact result of Eq.(3.43), obtained by numerical integration, in Fig.3.9. We used the model correlation functions (3.8) for $\beta = 1, 10, 100$ and tested different degrees of shift symmetry breaking, $q = 0, 1/2, 1$. Shown in Fig. 3.9(a) is the ratio $P'^{c_2=0}_r(\Delta)/P'_r(\Delta)$ for the indicated values of β evaluated at two separations, $r = 1/2\Lambda$ and $r = 1\Lambda$. Fig. 3.9(b) depicts the same ratio, however as a function of r. The gray regions shows the range of values obtained for all $\Delta \in [-\pi/2, \pi/2]$. The observed deviations amount to maximally a few percent. This shows that Eq.(3.44) already provides a very good approximation to the exact result of (3.43).

Finally we show that the collinear component $P'^{(2)}_r(\Sigma|\Delta)$ in (3.41) vanishes for Gaussian random fields. This follows from the definition of the collinear component

$$P'^{(2)}_r(\Sigma, \Delta) = \sum_{m,n\in\mathbb{N}}^{\text{odd}} p_{mn}(r) \cos(2m\Sigma) \cos(n\Delta) \tag{3.45}$$

where both, m and n, are odd numbers. It has the property

$$P'^{(2)}_r(\Sigma, \Delta) = -P'^{(2)}_r(\Sigma + \pi/2, \Delta). \tag{3.46}$$

However, according to expression (3.42), $P'_r(\Sigma, \Delta)$ in the Gaussian case is periodic in Σ with periodicity $\pi/2$ such that

$$P'_r(\Sigma, \Delta) = P'_r(\Sigma + \pi/2, \Delta).$$

in contrast to (3.46). From this follows that for broken shift symmetry Gaussian random fields cannot have any type of collinear components and merely exhibit cloverleaf modulations in their edge cooccurence statistics, as is apparent in Fig. 3.10.

3.16 Appendix A

In this appendix we calculate the inverse Fourier transform of $P_1(\mathbf{k})$ and $P_2(\mathbf{k})$.

$$P_1(\mathbf{k}) = A\,|\mathbf{k}|^\beta e^{-|\mathbf{k}|^2 B} \quad P_2(\mathbf{k}) = q\,P_1(\mathbf{k})\,e^{4i\arg\mathbf{k}}$$

$P_1(\mathbf{k}) \to C_1(\mathbf{r})$

$$
\begin{aligned}
C_1(\mathbf{r}) &= \frac{1}{2\pi}\int d^2\mathbf{k}\, e^{i\mathbf{k}\,\mathbf{r}}A|\mathbf{k}|^\beta e^{-|\mathbf{k}|^2 B} = \frac{A}{2\pi}\int_0^\infty dk\, k^{1+\beta}e^{-k^2 B}\int_0^{2\pi}d\phi\, e^{ikr\cos\phi} \\
&= A\int_0^\infty dk\, k^{1+\beta}e^{-k^2 B}J_0(kr) = \frac{1}{2}\,A\,B^{-\frac{2+\beta}{2}}\Gamma\big[\frac{2+\beta}{2}\big]\,_1F_1\big(\frac{2+\beta}{2};1;-\frac{\mathbf{r}^2}{4B}\big),
\end{aligned}
$$

where we used formula (6.631) in [54],

$$\int_0^\infty dk\, k^\mu\, e^{-k^2 B}J_\nu(kr) = \frac{r^\nu\,\Gamma[\frac{\nu+\mu+1}{2}]}{2^{\nu+1}B^{\frac{1}{2}(\mu+\nu+1)}\Gamma[\nu+1]}\,_1F_1\big(\frac{\nu+\mu+1}{2};\nu+1;-\frac{r^2}{4B}\big), \tag{3.47}$$

with $\mu = 1 + \beta$, $\nu = 0$. From the definition of A and B follows

$$\frac{1}{2} A B^{-\frac{2+\beta}{2}} \Gamma[\frac{2+\beta}{2}] = 1,$$

such that we get

$$C_1(\mathbf{r}) = {}_1F_1(\frac{2+\beta}{2}; 1, -\frac{|\mathbf{r}|^2}{4B})$$

$P_2(\mathbf{k}) \rightarrow C_2(\mathbf{r})$

$$
\begin{aligned}
C_2(\mathbf{r}) &= \frac{q}{2\pi} \int d^2\mathbf{k}\, e^{i\mathbf{k}\,\mathbf{r}} e^{4i \arg \mathbf{k}} A|\mathbf{k}|^\beta e^{-|\mathbf{k}|^2 B} = \frac{q\,A}{2\pi} \int_0^\infty dk\, k^{1+\beta} e^{-k^2 B} \int_0^{2\pi} d\phi\, e^{ikr \cos(\phi - \arg \mathbf{r})} e^{4i\phi} \\
&= \frac{q\,A}{2\pi} \int_0^\infty dk\, k^{1+\beta} e^{-k^2 B} \int_0^{2\pi} d\phi\, e^{ikr \cos \phi} e^{4i(\phi + \arg \mathbf{r})}.
\end{aligned}
$$

Using the following expansion (see [55], paragraph 9.1.44 and 45, p.361)

$$e^{ikr \cos \phi} = J_0(kr) + 2 \sum_{n=1}^\infty i^n \cos(n\phi)\, J_n(kr),$$

we obtain

$$
\begin{aligned}
C_2(\mathbf{r}) &= q\,A\, e^{4i \arg \mathbf{r}} \int_0^\infty dk\, k^{1+\beta} e^{-k^2 B} J_4(kr) = q|\mathbf{r}|^4 e^{4i \arg \mathbf{r}} \frac{A\, B^{-(\frac{6+\beta}{2})} \Gamma[\frac{6+\beta}{2}]}{768} {}_1F_1(\frac{6+\beta}{2}; 5; -\frac{\mathbf{r}^2}{4B}) \\
&= q(r_1 + ir_2)^4 \frac{A\, B^{-(\frac{6+\beta}{2})} \Gamma[\frac{6+\beta}{2}]}{768} {}_1F_1(\frac{6+\beta}{2}; 5; -\frac{\mathbf{r}^2}{4B})
\end{aligned}
$$

where, again we made use of Eq.(3.47), this time with $\mu = 1 + \beta$, $\nu = 4$.

3.17 Appendix B: Pinwheel densities

We evaluate the integral

$$\rho = \int d\zeta\, p(\zeta)\, \delta(R)\, \delta(I)\, |\mathcal{J}|$$

where

$$p(\zeta) = \frac{1}{(2\pi)^3 c_z c_g^2} \exp\left(-\frac{z\bar{z}}{2c_z}\right) \exp\left(-\frac{\nabla z \nabla \bar{z}}{2c_g}\right)$$

and $\zeta = (R, I, \partial_x R, \partial_y R, \partial_x I, \partial_y I)^T$. The integral over R and I collapses due to the delta functions, such that we just have to perform the integral over ∇z. Using the abbreviation

$$R_x = \partial_x R \qquad R_y = \partial_y R \qquad I_x = \partial_x I \qquad I_y = \partial_y I$$

the integral states

$$\rho = \frac{1}{(2\pi)^3 c_z c_g^2} \int dR_x dR_y dI_x dI_y \, |R_x I_y - R_y I_x| \exp(-\frac{R_x^2 + R_y^2 + I_x^2 + I_y^2}{2c_g})$$

and can be easily evaluated after a coordinate transform to 4-dimensional spherical coordinates,

$$R_x = g \cos\phi \cos\theta_1 \qquad R_y = g \cos\phi \sin\theta_1 \qquad I_x = g \sin\phi \cos\theta_2 \qquad I_y = g \sin\phi \cos\theta_2$$

with

$$0 \leq g \leq \infty, \ 0 \leq \pi \leq \pi/2, \ 0 \leq \theta_1, \theta_2 \leq 2\pi$$

and volume element

$$dR_x dR_y dI_x dI_y = 1/2g^3 \sin(2\phi) dg \, d\phi \, d\theta_1 \, d\theta_2.$$

The integral in this coordinates is

$$
\begin{aligned}
\rho &= \int\limits_0^\infty dg \, \frac{g^5}{32\,\pi^3 c_z c_g^2} \, \exp(-\frac{g^2}{2c_g}) \int\limits_0^{2\pi} d\theta_1 \int\limits_0^{2\pi} d\theta_2 |\sin(\theta_1 - \theta_2)| \int\limits_0^{\pi/2} d\phi \sin(2\phi) \\
&= \int\limits_0^\infty dg \, \frac{g^5}{16\,\pi c_z c_g^2} \, \exp(-\frac{g^2}{2c_g}) \\
&= \frac{1}{2\pi} \frac{c_g}{c_z}.
\end{aligned}
$$

4 Shift-Twist Symmetry and Pattern Selection

4.1 Overview

In the previous chapter we analyzed the signatures that shift-twist symmetry is predicted to leave on the statistics of Gaussian ensembles of orientation maps. Such ensembles are expected to describe the spatial organization of early transient states in cortical development. Such states however are not expected to persist as the developmental dynamics converges towards its attractor states. What can we say about the final outcome of dynamical models of orientation map development? An approach that has proved to be very powerful in pattern forming systems near onset is weakly nonlinear analysis, a multiscale perturbation theory that can identify a comprehensive set of solutions emerging from the unstable homogeneous fixed point and their stability properties. Many results of weakly nonlinear analysis only depend on qualitative and symmetry properties of the dynamics and are thus valid for an entire class of models. This aspect is particularly important in complex biological systems where exact microscopic models are not currently available and potentially will never be.

We use weakly nonlinear analysis to analyze the impact of Euclidean symmetry on pattern selection and, in particular, to examine the question of whether stable pinwheel arrangements exist and what their geometric organization is. We construct a generalized Swift-Hohenberg model [30, 56] symmetric under the Euclidean group $E(2)$ that allows to study the transition from higher $E(2) \times U(1)$ to lower $E(2)$ symmetry by changing a parameter that controls the strength of shift symmetry breaking (SSB). We derive the general form of amplitude equations for stationary planforms and find three classes of stationary solutions: stripe patterns without any pinwheels, pinwheel crystals with pinwheels regularly arranged on a rhombic lattice, and quasi-periodic patterns containing a large number of irregularly positioned pinwheels. We derive general stability criteria for these solutions and establish the existence of a large set of energetically degenerate, biologically realistic solutions. We calculate the phase diagram of all solutions depending on the strength of SSB, the effective strength of nonlocal interactions, and the range of nonlocal interactions. With increasing strength of SSB, pinwheel free patterns are progressively replaced by pinwheel crystals in the phase diagram while both pinwheel free patterns and pinwheel crystals remain stable. Phases of aperiodic pinwheel rich patterns remain basically unaffected. A critical strength of SSB exists above which multistable aperiodic patterns collapse into a single aperiodic state. We also characterize the impact of shift-twist symmetry on the spatial density of pinwheels in aperiodic model solutions.

4.2 Generalized Swift-Hohenberg Models

The spatial structure of an OPM can be represented by a complex field $z(\mathbf{x})$ where $\mathbf{x}$ denotes the 2D position of neurons in the visual cortex, $\theta(\mathbf{x}) = \arg{(z(\mathbf{x}))}/2$ their preferred stimulus orientation, and the modulus $|z(\mathbf{x})|$ is a measure of their selectivity [15]. In this representation, pinwheel centers are zeros of the field $z(\mathbf{x})$. The simplest models for the formation of OPMs are defined by a dynamics

$$\partial_t z(\mathbf{x}, t) = F[z](\mathbf{x}, t). \tag{4.1}$$

where t denotes time and $F[z]$ is a nonlinear operator. We assume that the dynamics is equivariant under translation $T_{\mathbf{y}} z(\mathbf{x}) = z(\mathbf{x} + \mathbf{y})$, shift-twist rotation $R_\alpha z(\mathbf{x}) = e^{2i\alpha} z(\Omega_{-\alpha}\mathbf{x})$ with rotation matrix Ω_ϕ, and shift-twist reflection at the cortical $(1, 0)$ axis $CP z(\mathbf{x}) = \bar{z}(\bar{\mathbf{x}})$, thus expressing the fact that within cortical layers there are no special locations or directions [35]. In addition, if interactions between OPM development and visuotopy are neglected it is also equivariant under global shifts of orientation preference $S_\beta z(\mathbf{x}) = e^{2i\beta} z(\mathbf{x})$ (*shift symmetry*). Shift-twist rotations R, also called *'shift-twists'* in the following, thus consist of a composition of phase shifts S and coordinate rotations D, i.e. $R_\alpha = S_{2\alpha} \circ D_\alpha$ with $D_\alpha z(\mathbf{x}) = z(\Omega_{-\alpha}\mathbf{x})$.

We consider the general class of variational models [15, 57, 22] for which $F[z]$ has the form

$$F[z] = (r + L_0)z + \epsilon r M \bar{z} + N_3[z]. \tag{4.2}$$

Here $L = r + L_0$ is a linear, translation invariant and self-adjoint operator, that accounts for a finite wavelength instability at $r = 0$. N_3 is a general, permutation and shift symmetric cubic nonlinearity which stabilizes the dynamics. The second term involves a complex conjugation $Cz = \bar{z}$ and thus manifestly breaks shift symmetry when $\epsilon \neq 0$. M is assumed to be linear, translation invariant and bounded. Equivariance under rotations, $[MC, R_\alpha] = 0$, requires

$$D_\alpha M D_\alpha^{-1} = S_{-4\alpha} M \tag{4.3}$$

and equivariance under parity $[M, P] = 0$, where $[\cdot]$ denotes the commutator. Most of the results derived subsequently will be generally valid for any model from this symmetry class.

As a concrete example we will also consider the specific model defined by the choices

$$L = r - (k_c^2 + \nabla^2)^2 \tag{4.4}$$

$$N_3[z] = (1 - g)|z(\mathbf{x})|^2 z(\mathbf{x}) - \frac{2 - g}{2\pi\sigma^2} \int d^2y \left(|z(\mathbf{y})|^2 z(\mathbf{x}) + \frac{1}{2} z(\mathbf{y})^2 \bar{z}(\mathbf{x}) \right) e^{-|\mathbf{y} - \mathbf{x}|^2/2\sigma^2} \tag{4.5}$$

$$M = (\partial_x + i\partial_y)^4 (\partial_{xx} + \partial_{yy})^{-2} \tag{4.6}$$

which is the mathematically simplest representative of this model class. Here L is the Swift-Hohenberg operator [56, 30] with critical wavenumber k_c and instability parameter r. N_3 is adopted from [22], where σ sets the range of the nonlocal interactions and g determines whether the local ($g > 1$) or the nonlocal term ($g < 1$) stabilizes the dynamics. M is the simplest differential operator which transforms according to Eq.(4.3). It is unitary with spectrum $e^{4i\arg(\mathbf{k})}$.

4.3 Amplitude Equations

As discussed in the previous chapters, a linear stability analysis reveals that the unselective state $z(\mathbf{x}) = 0$ becomes unstable for $r \geq 0$ and modes on the critical circle $|\mathbf{k}| = k_c$ start to grow. Directly after spontaneous symmetry breaking, when $|z(\mathbf{x})|$ is still small compared to its asymptotic value reached at $t \to \infty$, the nonlinearity $N_3[z]$ can be neglected and the dynamics is controlled by the linear terms. As shown in Chapter 3 the emerging pattern can then be approximated by a random superposition of modes and its statistics is expected to be Gaussian. What can we tell about the dynamics at later times when the nonlinearities become important and the modes start to compete? In particular, what can we say about the attractors? For small values of the control parameter $r \ll 1$, i.e. in the *weakly nonlinear regime*, solutions to the full dynamics can be approximated by planforms,

$$ z(\mathbf{x}) = \sum_{j=0}^{N-1} A_j e^{i\mathbf{k}_j \mathbf{x}}, \ |\mathbf{k}_j| = k_c, $$

consisting of a linear superposition of discrete modes on the critical circle. Thereby the full dynamics Eq.(4.2) of the field $z(\mathbf{x})$ is projected onto the finite dimensional subspace spanned by the amplitudes A_j resulting in *amplitude equations*, a set of coupled nonlinear differential equations describing the dynamics of the amplitudes A_j. Here we derive the amplitude equations for the dynamics Eq.(4.2). In the subsequent sections we then perform a stability analysis of their stationary solutions in order to identify sets of stable patterns. The perturbation theoretical analysis presented follows the treatise of [58] and [34].

The spectrum of L_0 is given by $\lambda(k) = -(k_c^2 - k^2)^2$ and attains its maximum at $k = |k_c|$, where it is zero. Therefore, modes on the critical circle reside in the kernel of the linear operator L_0. Since one is interested in the dynamics in a small neighbourhood above the bifurcation point $r = 0$ one introduces a small parameter $\gamma \geq 0$ and assumes that the solution $z(\mathbf{x}, t)$ and r can both be expanded into a power series in γ,

$$ \begin{aligned} r &= r_1\gamma + r_2\gamma^2 + r_3\gamma^3 + \dots \\ z(\mathbf{x}, t) &= z_1(\mathbf{x}, t)\gamma + z_2(\mathbf{x}, t)\gamma^2 + z_3(\mathbf{x}, t)\gamma^3 + \dots. \end{aligned} \tag{4.7} $$

In general this will be the case when the solution $z(\mathbf{x}, t)$ bifurcates from the homogeneous state in a continuous way. Note that the intrinsic time scale $\tau = r^{-1}$ diverges at the bifurcation point, which means that for $r \to 0$ the dynamics of $z(\mathbf{x}, t)$ is becoming arbitrarily slow, a phenomenon which is known as *critical slowing down* and which can be compensated by considering the dynamics on a slow time scale,

$$ T = r\,t. $$

Expressed in rescaled time units the dynamics Eq.(4.2) becomes

$$ r\frac{\partial}{\partial T} z(\mathbf{x}) = F[z(\mathbf{x})] \tag{4.8} $$

and no longer exhibits any critical slowing down. We combine the ansatz (4.7) with the rescaled

dynamics Eq.(4.8) and obtain

$$
\begin{aligned}
0 &= L_0 z - r\partial_T z + rz + r\epsilon M\bar{z} + N_3[z] \\
&= \gamma(L_0 z_1) + \gamma^2\left(r_1 z_1 + L_0 z_2 - r_1\partial_T z_1 + r_1\epsilon M\bar{z}_1\right) + \\
&\quad + \gamma^3\left(L_0 z_3 + r_1 z_2 + r_2 z_1 - r_1\partial_T z_2 - r_2\partial_T z_1 + r_1\epsilon M\bar{z}_2 + r_2\epsilon M\bar{z}_1 + N_3(z_1, z_1, \bar{z}_1)\right) + \\
&\quad + \gamma^4\left(L_0 z_4 + r_1 z_3 + r_2 z_2 + r_3 z_1 - r_1\partial_T z_3 - r_2\partial_T z_2 - r_3\partial_T z_1 + r_1\epsilon M\bar{z}_3 + r_2\epsilon M\bar{z}_2 + r_3\epsilon M\bar{z}_1 + \right. \\
&\quad\quad \left. + N_3(z_2, z_1, \bar{z}_1) + N_3(z_1, z_2, \bar{z}_1) + N_3(z_1, z_1, \bar{z}_3)\right) + \\
&\quad + \gamma^5(L_0 z_5 + \dots) + \dots
\end{aligned}
\tag{4.9}
$$

Equation (4.9) can only be fulfilled when the terms inside the brackets vanish for every order in γ. This implies conditions of the form

$$
L_0 z_i = r.h.s.
\tag{4.10}
$$

where i denotes the order of the term and the right hand side only depends on z_j with $j < i$. The set of equations (4.10) can be solved in ascending order when the solvability conditions are met, i.e. when the right hand side is orthogonal to the kernel of the adjoint operator $L_0^\dagger$. In our case L_0 is formally self-adjoint and the kernels of $L_0^\dagger$ and L_0 are identical. For the first order in γ we have the condition

$$
L_0 z_1 = 0
$$

which implies that $z_1(\mathbf{x}, T) \in \ker L_0$. The kernel of L_0 is spanned by all Fourier modes $e^{i\mathbf{k}_c\mathbf{x}}$ on the critical circle (and by the secular terms $\mathbf{k}_c\mathbf{x}\, e^{i\mathbf{k}_c\mathbf{x}}$, which are unbounded and thus irrelevant in our present context). The second order term yields to

$$
L_0 z_2 = r_1(-z_1 + \partial_T z_1 - \epsilon M\bar{z}_1)
$$

from which we conclude that $r_1 = 0$, which is the only way to fulfill the compatibility condition, since the term in the brackets resides in the kernel of L_0. The compatibility condition applied to the third order term

$$
L_0 z_3 = -r_2 z_1 + r_2\partial_T z_1 - r_2\epsilon M\bar{z}_1 + N_3(z_1, z_1, \bar{z}_1)
$$

yields a dynamical equation for z_1,

$$
\partial_T z_1 = z_1 + \epsilon M\bar{z}_1 - P_c N_3(z_1, z_1, \bar{z}_1)
\tag{4.11}
$$

where we set $r_2 = 1$ and P_c is the projection operator onto the kernel of L_0. The planform ansatz

$$
z_1(\mathbf{x}) = \sum_{j=0}^{2n-1} A_j(T) e^{i\mathbf{k}_j\mathbf{x}},
$$

which consists of a superposition on $2n$ modes $\mathbf{k}_j = k_c(\cos\alpha_j, \sin\alpha_j)$ on the critical circle, where we require that to each mode also its antiparallel mode is in the set, in combination with Eq.(4.11), yields a set of *amplitude equations*

$$
\dot{A}_j = A_j + \epsilon e^{4i\alpha_j}\bar{A}_{j-} + \sum_{k,l,m} A_k A_l \bar{A}_m e^{-i\mathbf{k}_j\mathbf{x}} P_j N_3(e^{i\mathbf{k}_k\mathbf{x}}, e^{i\mathbf{k}_l\mathbf{x}}, e^{-i\mathbf{k}_m\mathbf{x}})
\tag{4.12}
$$

where P_j denotes the projection onto the Fourier mode $e^{i\mathbf{k}_j}$ and j^- denotes the index of the mode antiparallel to mode j with the corresponding wavevector $\mathbf{k}_{j^-} = -\mathbf{k}_j$.

Next we show that many terms in the triple sum of Eq.(4.12) do not contribute due to symmetry. As a result, the general form of the amplitude equations can be reduced to

$$\dot{A}_j = A_j + \epsilon \bar{A}_{j^-} e^{4i\alpha_j} - \sum_{k=0}^{2n-1} g_{jk} |A_k|^2 A_j - \sum_{k=0}^{2n-1} f_{jk} A_k A_{k^-} \bar{A}_{j^-} \qquad (4.13)$$

with real valued and symmetric matrices g_{jk} and f_{jk} which determine the coupling and competition between modes. They can be expressed in terms of angle-dependent interaction functions $g(\alpha)$ and $f(\alpha)$, which are obtained from the nonlinearity $N_3[z]$ (cf.[58, 30, 22]).

Due to the projection operator P_j only terms $N_3(e^{i\mathbf{k}_k\mathbf{x}}, e^{i\mathbf{k}_l\mathbf{x}}, e^{-i\mathbf{k}_m\mathbf{x}})$ are contributing in which the wave vectors add up to $\mathbf{k}_j$, i.e.

$$\mathbf{k}_k + \mathbf{k}_l - \mathbf{k}_m = \mathbf{k}_j.$$

Since all wave vectors have the same length this condition requires

$$\mathbf{k}_k = \mathbf{k}_j, \quad \mathbf{k}_l = \mathbf{k}_m$$

or

$$\mathbf{k}_k = \mathbf{k}_m, \quad \mathbf{k}_l = \mathbf{k}_j$$

or

$$\mathbf{k}_k = -\mathbf{k}_l := \mathbf{k}_{l^-}, \quad \mathbf{k}_m = -\mathbf{k}_j := \mathbf{k}_{j^-}$$

such that Eq.(4.12) becomes

$$\begin{aligned}
\dot{A}_j = \ & A_j + \epsilon e^{4i\alpha_j} \bar{A}_{j^-} + \sum_{k \neq j} A_j |A_k|^2 e^{-i\mathbf{k}_j\mathbf{x}} P_j N_3(e^{i\mathbf{k}_j\mathbf{x}}, e^{i\mathbf{k}_k\mathbf{x}}, e^{-i\mathbf{k}_k\mathbf{x}}) + \\
& + \sum_{k \neq j} A_j |A_k|^2 e^{-i\mathbf{k}_j\mathbf{x}} P_j N_3(e^{i\mathbf{k}_k\mathbf{x}}, e^{i\mathbf{k}_j\mathbf{x}}, e^{-i\mathbf{k}_k\mathbf{x}}) + \\
& + \sum_{k \neq j,j^-} A_{k^-} A_k \bar{A}_{j^-} e^{-i\mathbf{k}_j\mathbf{x}} P_j N_3(e^{-i\mathbf{k}_k\mathbf{x}}, e^{i\mathbf{k}_k\mathbf{x}}, e^{i\mathbf{k}_j\mathbf{x}}) \\
& + A_j |A_j|^2 e^{-i\mathbf{k}_j\mathbf{x}} P_j N_3(e^{-i\mathbf{k}_j\mathbf{x}}, e^{i\mathbf{k}_j\mathbf{x}}, e^{i\mathbf{k}_j\mathbf{x}})
\end{aligned}$$

which can be brought into the form of Eq.(4.13) by setting

$$\begin{aligned}
g_{jk} &= -\left(e^{-i\mathbf{k}_j\mathbf{x}} P_j N_3(e^{i\mathbf{k}_j\mathbf{x}}, e^{i\mathbf{k}_k\mathbf{x}}, e^{-i\mathbf{k}_k\mathbf{x}}) + e^{-i\mathbf{k}_j\mathbf{x}} P_j N_3(e^{i\mathbf{k}_k\mathbf{x}}, e^{i\mathbf{k}_j\mathbf{x}}, e^{-i\mathbf{k}_k\mathbf{x}}) \right) \\
f_{jk} &= -\frac{1}{2} \left(e^{-i\mathbf{k}_j\mathbf{x}} P_j N_3(e^{-i\mathbf{k}_k\mathbf{x}}, e^{i\mathbf{k}_k\mathbf{x}}, e^{i\mathbf{k}_j\mathbf{x}}) + e^{-i\mathbf{k}_j\mathbf{x}} P_j N_3(e^{i\mathbf{k}_k\mathbf{x}}, e^{-i\mathbf{k}_k\mathbf{x}}, e^{i\mathbf{k}_j\mathbf{x}}) \right)
\end{aligned}$$

for $j \neq k$ and

$$\begin{aligned}
g_{jj} &= -e^{-i\mathbf{k}_j\mathbf{x}} P_j N_3(e^{i\mathbf{k}_j\mathbf{x}}, e^{i\mathbf{k}_j\mathbf{x}}, e^{-i\mathbf{k}_j\mathbf{x}}) \\
f_{jj} &= 0
\end{aligned}$$

for the diagonal elements. For an isotropic system, which we assume here, the matrix elements g_{jk} and f_{jk} only depend on the angle difference $\alpha = |\alpha_k - \alpha_j|$ of the Fourier modes $\mathbf{k}_j = k_c(\cos \alpha_j, \sin \alpha_j)$. Therefore they can be expressed in terms of the continuous functions

$$
\begin{aligned}
g(\alpha) &= -\left(e^{-i\mathbf{k}_0\mathbf{x}} PN_3(e^{i\mathbf{k}_0\mathbf{x}}, e^{i\mathbf{h}(\alpha)\mathbf{x}}, e^{-i\mathbf{h}(\alpha)\mathbf{x}}) + e^{-i\mathbf{k}_0\mathbf{x}} PN_3(e^{i\mathbf{h}(\alpha)\mathbf{x}}, e^{i\mathbf{k}_0\mathbf{x}}, e^{-i\mathbf{h}(\alpha)\mathbf{x}})\right) \quad (4.14) \\
f(\alpha) &= -\frac{1}{2}\left(e^{-i\mathbf{k}_0\mathbf{x}} PN_3(e^{-i\mathbf{h}(\alpha)\mathbf{x}}, e^{i\mathbf{h}(\alpha)\mathbf{x}}, e^{i\mathbf{k}_0\mathbf{x}}) + e^{-i\mathbf{k}_0\mathbf{x}} PN_3(e^{i\mathbf{h}(\alpha)\mathbf{x}}, e^{-i\mathbf{h}(\alpha)\mathbf{x}}, e^{i\mathbf{k}_0\mathbf{x}})\right)
\end{aligned}
$$

where $\mathbf{k}_0 = k_c(1, 0)$ and $\mathbf{h}(\alpha) = k_c(\cos\alpha, \sin\alpha)$. From the definition (4.14) follows that $g(\alpha) = g(\alpha + 2\pi)$ and $f(\alpha) = f(\alpha + \pi)$. However, for the particular nonlinearity considered here, Eq.(4.5),

$$g(\alpha) = g(\alpha + \pi), \tag{4.15}$$

which is due to the fact that $N_3[z]$ belongs to the class of *permutation symmetric* models satisfying $N_3(z_j, z_k, z_l) = N_3(z_l, z_j, z_k)$ (see[22]). The coupling coefficients are given by

$$g_{jk} = (1 - \frac{1}{2}\delta_{jk})g(|\alpha_k - \alpha_j|) \tag{4.16}$$

and

$$f_{jk} = (1 - \delta_{jk} - \delta_{jk-})f(|\alpha_k - \alpha_j|). \tag{4.17}$$

For the nonlinearity Eq.(4.5) one obtains

$$g(\alpha) = g + (2 - g)e(\alpha) \tag{4.18}$$

and

$$f(\alpha) = \frac{1}{2}g(\alpha) \tag{4.19}$$

with $e(\alpha) = 2\exp(-\sigma^2 k_c^2)\cosh(\sigma^2 k_c^2 \cos\alpha)$.

The amplitude equations can be derived from the energy functional

$$
\begin{aligned}
E = &-\sum_{j=0}^{2n-1}\left(A_j\bar{A}_j + \epsilon(A_j A_{j-} e^{-4i\alpha_j} + \bar{A}_j\bar{A}_{j-} e^{4i\alpha_j})\right) \\
&+ \frac{1}{2}\sum_{j=0}^{2n-1}\sum_{k=0}^{2n-1}\left(g_{jk}|A_j|^2|A_k|^2 + f_{jk}A_j A_{j-}\bar{A}_{k-}\bar{A}_k\right)
\end{aligned} \tag{4.20}
$$

and written as a gradient descent

$$\dot{A}_j = -\frac{\delta E}{\delta \bar{A}_j}$$

In the following sections we identify classes of stationary solutions of the amplitude equations (4.13) and determine their stability criteria.

4.4 Stripe Patterns

The simplest solution to Eq.(4.13) is obtained for $n = 1$ and consists of plane waves with wavevector $\mathbf{k} = k_c(\cos\alpha, \sin\alpha)$. The corresponding amplitude equations describe the dynamics of two modes, A_0 and A_{0-} with antiparallel wavevectors, $\mathbf{k}$ and $-\mathbf{k}$,

$$
\begin{aligned}
\dot{A}_0 &= A_0 + \epsilon \bar{A}_{0-} e^{4i\alpha} - \frac{1}{2} g(0) |A_0|^2 A_0 - g(\pi)|A_{0-}|^2 A_0 \\
&= A_0 + \epsilon \bar{A}_{0-} e^{4i\alpha} - \frac{1}{2} g(0) \left(|A_0|^2 - 2|A_{0-}|^2 \right) A_0
\end{aligned}
$$

and

$$
\dot{A}_{0-} = A_{0-} + \epsilon \bar{A}_0 e^{4i\alpha} - \frac{1}{2} g(0) \left(|A_{0-}|^2 - 2|A_0|^2 \right) A_{0-}
$$

The stationary solution is given by

$$
z(\mathbf{x}) = \begin{cases}
i\, e^{2i\alpha} \sqrt{\dfrac{8(1+|\epsilon|)}{3g(0)}} \, \sin(\mathbf{k}\mathbf{x} + \phi) & \text{for } \epsilon \leq -1/2 \\[3ex]
e^{2i\alpha} \left(\sqrt{\dfrac{2(1+2\epsilon)}{g(0)}} \, \cos(\mathbf{k}\mathbf{x} + \phi) + i\, \sqrt{\dfrac{2(1-2\epsilon)}{g(0)}} \, \sin(\mathbf{k}\mathbf{x} + \phi) \right) & \text{for } |\epsilon| \leq 1/2 \\[3ex]
e^{2i\alpha} \sqrt{\dfrac{8(1+|\epsilon|)}{3g(0)}} \, \cos(\mathbf{k}\mathbf{x} + \phi) & \text{for } \epsilon \geq 1/2
\end{cases}
\tag{4.21}
$$

with arbitrary phase ϕ. Hence with SSB orientation angles are not equally represented. For $\epsilon > 0$ cortical area for orientations α and $\alpha + \pi/2$ is recruited at the expense of $\alpha + \pi/4$ and $\alpha + 3\pi/4$ (and vice versa for $\epsilon < 0$). Beyond a critical strength of SSB, here $\epsilon_* = 1/2$, patterns only contain *two* orientations, either α and $\alpha + \pi/2$, for $\epsilon > \epsilon_*$ or $\alpha \pm \pi/4$ for $\epsilon < -\epsilon_*$. As illustrated in Fig. 4.1(a) the preferentially represented orientations are determined by the direction of the wave vector. SSB thus leads to a geometric coupling of position and orientation.
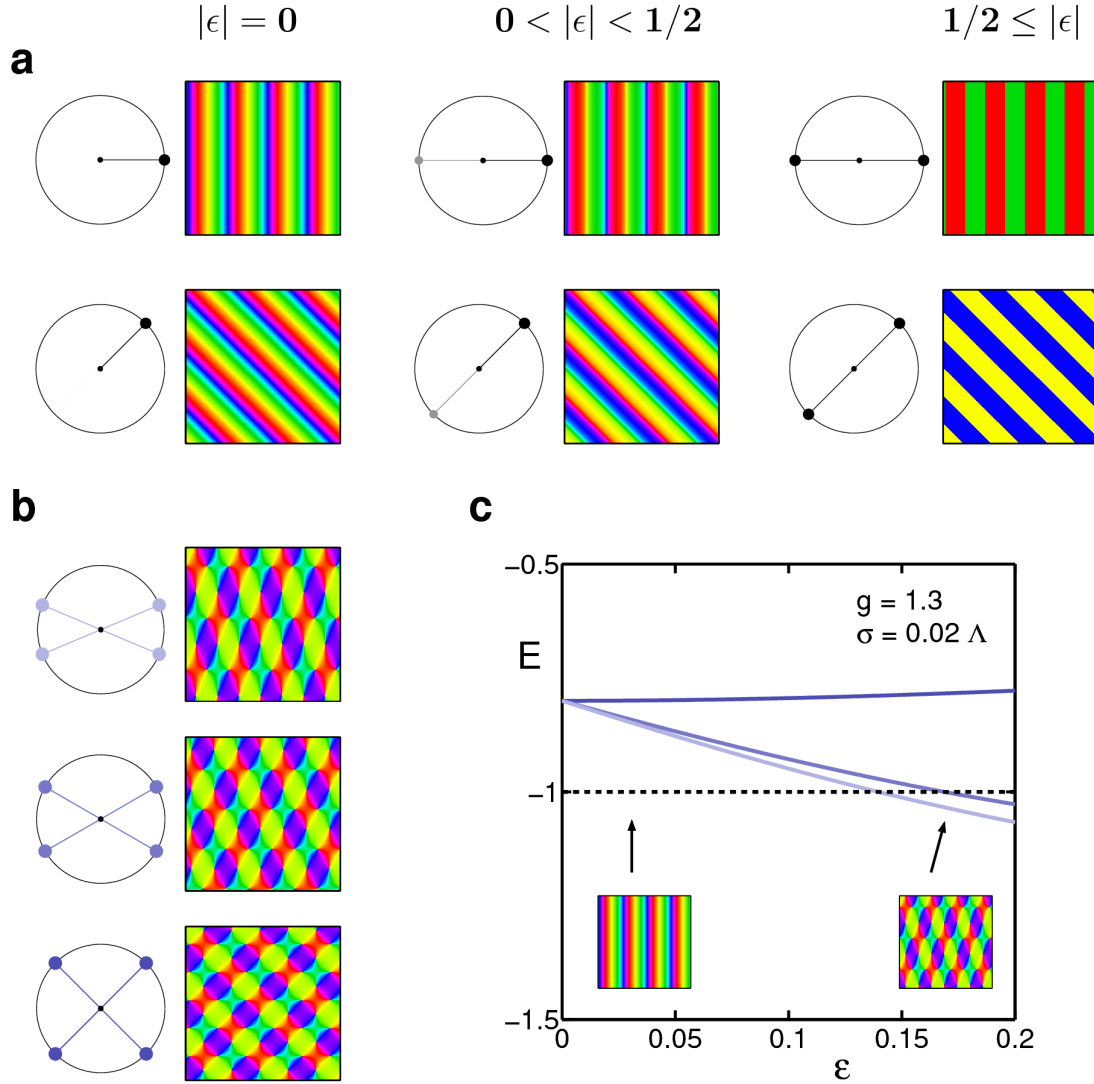
Figure 4.1: ϵ-dependence of plane wave and pinwheel crystal solutions. **(a)** Plane waves with wavevector in horizontal (*top*) and oblique (*bottom*) direction for variable strength of SSB ($\epsilon = 0$, 0.35, 1) **(b)** rPWCs of varying intersection angle α, $\pi/4 \leq \alpha \leq \pi/2$. **(c)** Energy of solutions depends on ϵ and on α. For sufficiently large ϵ rPWCs are energetically favored relative to plane waves. All energies are given in units of the plane waves energy for corresponding ϵ: *dashed*: (normalized) energy of plane waves, *plain*: energies of rPWCs for $\alpha = \pi/4$, $\pi/3$, $\pi/2$.

Since stripe patterns are a special case of solutions discussed in Section 4.6 we postpone their stability analysis to there.

4.5 Pinwheel Crystals

For solutions containing pinwheels, this geometric coupling is of more subtle nature. The simplest class of solutions containing pinwheels are rhombic pinwheel crystals (rPWCs), which exist for

$n = 2$ and consist of two pairs of antiparallel modes which all have the same amplitude, i.e.

$$z(\mathbf{x}) = A_0 e^{i\mathbf{k}_0 \mathbf{x}} + A_1 e^{i\mathbf{k}_1 \mathbf{x}} + A_{0-} e^{-i\mathbf{k}_0 \mathbf{x}} + A_{1-} e^{-i\mathbf{k}_1 \mathbf{x}} \tag{4.22}$$

with

$$A_0 = a e^{i\mu_0}, \; A_1 = a e^{i\mu_1}, \; A_{0-} = a e^{i\nu_0}, \; A_{1-} = a e^{i\nu_1}$$

and wavevectors

$$\mathbf{k}_0 = k_c(\cos\alpha_0, \sin\alpha_0), \quad \mathbf{k}_1 = k_c(\cos\alpha_1, \sin\alpha_1)$$

We consider without loss of generality the case $\alpha_0 = -\alpha/2$ and $\alpha_1 = +\alpha/2$ (Fig.4.1(**b**)). As shown in the Appendix 4.10 the stationary state depends on the angle sums

$$\Sigma_0 := \mu_0 + \nu_0 \text{ and } \Sigma_1 := \mu_1 + \nu_1$$

and fulfills

$$\Sigma_1 = -\Sigma_0$$

and

$$a^2 = \frac{1 + \epsilon\cos(\Sigma_0 + 2\alpha)}{3g(0)/2 + 2g(\alpha) + 2f(\alpha)\cos 2\Sigma_0}$$

The phase Σ_0 is given by the solution branch to

$$0 = \sin 2\Sigma_0 + \epsilon[\sin(\Sigma_0 - 2\alpha) - (2 + 3g_{00}/g_{01})\sin(\Sigma_0 + 2\alpha)],$$

which bifurcates from $\Sigma_0 = \pm\pi/2$ for $\epsilon = 0$. The general solution then reads

$$z(\mathbf{x}) = 2a\left[e^{i\Sigma_0/2}\cos(\mathbf{k}_0\mathbf{x} + \Delta_0/2) + e^{-i\Sigma_0/2}\sin(\mathbf{k}_1\mathbf{x} + \Delta_1/2) \right]$$

with arbitrary Δ_0 and Δ_1. The energy of rhombic pinwheel crystals is

$$E_{rPWC} = -4a^2(1 + |\epsilon|\cos(\Sigma_0 + 2\alpha)) + 2a^4/3g(0)/2 + 2g(\alpha) + 2f(\alpha)\cos 2\Sigma_0.$$

For the model Eqns.(4.4-4.6) the ϵ and α dependence of the energy is shown in Fig.4.1(**c**).

4.6 Quasiperiodic Patterns

Because orientation maps in the brain lack crystalline order an important class of model solutions are aperiodic functions of space. Interestingly, their dependence on SSB is qualitatively different from the periodic solutions discussed above. A large set of quasiperiodic solutions originates from the essentially complex planforms (ECP)

$$z(\mathbf{x}) = \sum_{j=0}^{n-1} A_j e^{il_j \mathbf{k}_j \mathbf{x}} \tag{4.23}$$

that solve Eq.(4.13) for $\epsilon = 0$ [37, 22]. Here, wave vectors $\mathbf{k}_j = k_c(\cos\frac{\pi}{N}j, \sin\frac{\pi}{N}j)$ $(j = 0, \ldots, n-1)$ are distributed equidistantly on the upper half of the critical circle and binary variables $l_j = \pm 1$ determine whether the mode with wave vector $\mathbf{k}_j$ *or* with wave vector $-\mathbf{k}_j$ is active (Fig. 4.2(a) *left column*). We study how these solutions to Eq.(4.13) change when shift
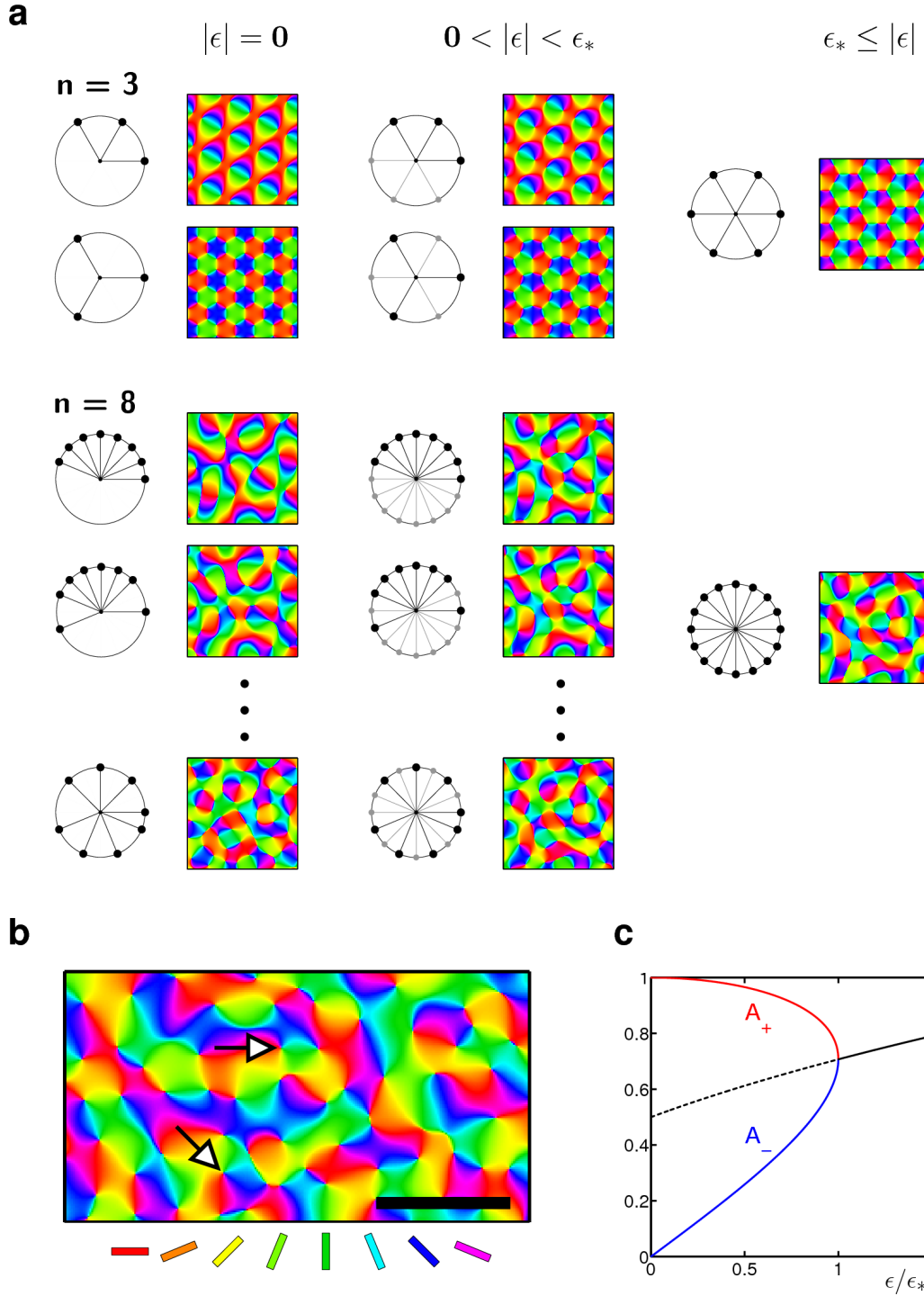
a

Figure 4.2: Solutions of the amplitude equations (Eq.4.13) with full, partially broken and completely broken shift symmetry. **(a)** ECPs. Preferred orientations are color coded [see bars in (b)]. Arrangement of active modes on the critical circle and corresponding OPMs. For n = 3 and 8 there are 2 and 15 different classes of ECPs, respectively. Complete (partial, no) suppression of opposite modes for full (weakly broken, maximally broken) shift symmetry *(left, middle, right column)*. **(b)** OPM in tree shrew V1 (data: L.E.White, Duke Univ., USA). Arrows pinwheel centers. Scale bar 1 mm. **(c)** With increasing degree of symmetry breaking ϵ amplitudes of antiparallel modes A_- grow and eventually (at $\epsilon = \epsilon_*$) reach the same absolute value as active modes A_+.

symmetry is broken. First we give a brief, qualitative summary of the new effects. The details and calculations are given in the subsequent sections.

Shift symmetry breaking manifests itself in a concerted growth of modes antiparallel to the set of active modes. As a consequence, we find that ECPs generalize to

$$z(\mathbf{x}) = \sum_{j=0}^{n-1} \left[A_j^+ e^{il_j \mathbf{k}_j \mathbf{x}} + A_j^- e^{-il_j \mathbf{k}_j \mathbf{x}} \right], \tag{4.24}$$

where A_j^+ refers to the set of active modes in (4.23) and A_j^- to the set of silent modes, which start to grow for $|\epsilon| > 0$. (Fig. 4.2(**a**) *middle column*). The amplitudes $|A_j^-|$ grow with increasing strength of SSB $|\epsilon|$ and eventually reach the same size as the active modes $|A_j^+|$ (Fig. 4.2(**a**) *right column*). For each n there exists a critical value ϵ_*. When $|\epsilon| < |\epsilon_*|$ stationary amplitudes fulfill $a^- = |A_j^-| < |A_j^+| = a^+$, when $|\epsilon| \geq |\epsilon_*|$ the amplitude of antiparallel and active modes are equal, $a^- = a^+$ (Fig.4.2(**c**)). Stationary phases $\phi_j^\pm = \arg A_j^\pm$ obey the condition

$$\phi_j^+ + \phi_j^- = 4 \arg \mathbf{k}_j \qquad \text{if } \epsilon > 0$$

and

$$\phi_j^+ + \phi_j^- = 4 \arg \mathbf{k}_j + \pi \qquad \text{if } \epsilon < 0$$

Interestingly, this particular phase relation is consistent with the result of the previous chapter, cf. Eq.(3.15), since it implies that the correlation function $P_2(\mathbf{k}_j) = \langle a(\mathbf{k}_j) a(-\mathbf{k}_j) \rangle$ of the solutions have the form

$$P_2(\mathbf{k}_j) = q \, P_1(k) e^{4i \arg \mathbf{k}_j}$$

where the index q measures the degree of SSB. It can be defined as

$$q := \frac{\sum_j A_j^+ A_j^- e^{-i\frac{4\pi}{n}j} + c.c.}{\sum_j \left| A_j^+ \right|^2 + \left| A_j^- \right|^2}$$

and ranges in $-1 \leq q \leq 1$. From that definition also follows

$$q = \begin{cases} \epsilon/\epsilon_* & \text{for } |\epsilon| < \epsilon_* \\ \operatorname{sign} \epsilon & \text{for } |\epsilon| \geq \epsilon_* \end{cases}$$

Thus we expect that for $\epsilon \neq 0$ the solutions exhibit a spatial locking of the orientation map to the coordinate system analogous to the coupling observed in Gaussian random fields for a corresponding $q = \epsilon/\epsilon_*$, cf. Section 3.10. Indeed, the general solution can be written as a linear superposition of *even* and *odd* basis functions,

$$z(\mathbf{x}) = \mathcal{N} \sum_{j=0}^{n-1} [\sqrt{1+q} \, z_j^e(\mathbf{x}, \phi_j) + \sqrt{1-q} \, z_j^o(\mathbf{x}, \phi_j)] \tag{4.25}$$

with $z_j^e(\mathbf{x}, \phi_j) = e^{i\frac{2\pi}{n}j} \cos(l_j \mathbf{k}_j \mathbf{x} + \phi_j)$ and $z_j^o(\mathbf{x}, \phi_j) = i e^{i\frac{2\pi}{n}j} \sin(l_j \mathbf{k}_j \mathbf{x} + \phi_j)$, arbitrary phases ϕ_j and an appropriate normalization constant $\mathcal{N}$. Under reflections at an axis parallel to $\mathbf{k}_j$ the even functions z_j^e and odd functions z_j^o transform into z_j^e and $-z_j^o$, respectively. In that sense z_j^e and z_j^o correspond to the even and odd eigenfunctions of the nullspace of $L + \epsilon MC$ (cf.[59]). For $\epsilon > 0$ ($\epsilon < 0$) the even (odd) part dominates the solution which also explains the particular locking of the iso-orientation domains to the coordinate system (the visuotopic map). For $n = 1$ (for which $\epsilon_* = 1/2$) solution (4.25) corresponds to Eq.(4.21).

Stationary states

In this section we calculate the branch of stationary solutions of the amplitude equations

$$\dot{A}_j = A_j + \epsilon \bar{A}_{j-} e^{4i \arg \mathbf{k}_j} - \sum_{k=0}^{2n-1} g_{jk}|A_k|^2 A_j - \sum_{k=0}^{2n-1} f_{jk} A_k A_{k-} \bar{A}_{j-}$$

which originates from the set of essentially complex planforms when shift symmetry is restored. As described above the solution $z(\mathbf{x})$ is assumed to consist of $2n$ modes,

$$z(\mathbf{x}) = \sum_{j=0}^{n-1} \left[A_j^+ e^{il_j \mathbf{k}_j \mathbf{x}} + A_j^- e^{-il_j \mathbf{k}_j \mathbf{x}} \right], \tag{4.26}$$

which are equidistantly distributed on the critical circle. The distinction into $'+'$ and $'-'$ modes (which we also call '*active*' and '*silent*' in the following) is based on the condition that for $\epsilon \to 0$ a given essentially complex planform

$$z(\mathbf{x}) = \sum_{j=0}^{n-1} A_j e^{il_j \mathbf{k}_j \mathbf{x}} \tag{4.27}$$

is retrieved as the limit

$$A_j^+ \to A_j, \qquad A_j^- \to 0.$$

In the following we assume that the interaction function $g(\alpha)$ is π-periodic. The dynamics of active and silent modes is then given by

$$\begin{aligned}
\dot{A}_j^+ &= A_j^+ + \epsilon \bar{A}_j^- e^{4i \arg \mathbf{k}_j} \\
&\quad - A_j^+ \sum_{k=0}^{n-1} g_{jk}|A_k^+|^2 - A_j^+ \sum_{k=0}^{n-1} (1 + \delta_{jk}) g_{jk}|A_k^-|^2 - 2\bar{A}_j^- \sum_{k=0}^{n-1} f_{jk} A_k^+ A_k^- \\
\dot{A}_j^- &= A_j^- + \epsilon \bar{A}_j^+ e^{4i \arg \mathbf{k}_j} \\
&\quad - A_j^- \sum_{k=0}^{n-1} g_{jk}|A_k^-|^2 - A_j^- \sum_{k=0}^{n-1} (1 + \delta_{jk}) g_{jk}|A_k^+|^2 - 2\bar{A}_j^+ \sum_{k=0}^{n-1} f_{jk} A_k^+ A_k^-.
\end{aligned} \tag{4.28}$$

The $n \times n$ matrices g_{jk} and f_{jk} are defined as in Eqn.(4.16) and (4.17)

$$\begin{aligned}
g_{jk} &= (1 - \tfrac{1}{2}\delta_{jk}) g(|\alpha_k - \alpha_j|) \\
f_{jk} &= (1 - \delta_{jk}) f(|\alpha_k - \alpha_j|)
\end{aligned}$$

with regularly spaced $\alpha_j = j\,\pi/n$ and $j = 0, \ldots n-1$. In particular,

$$\begin{aligned}
g_{jj} &= g(0)/2 \\
f_{jj} &= 0
\end{aligned}$$

The matrices g_{jk} and f_{jk} are symmetric and cyclic as their entries only depend on $|k - j|$.

In oder to diagonalize the linear part of the dynamics (4.28), we express A_j^+ and A_j^- by a new set of variables, B_j^+ and B_j^-, obtained from a change of basis

$$
\begin{aligned}
B_j^+ &= \frac{1}{2}(A_j^+ e^{-i\frac{2\pi}{n}j} + \bar{A}_j^- e^{i\frac{2\pi}{n}j}) \\
B_j^- &= \frac{1}{2}(A_j^+ e^{-i\frac{2\pi}{n}j} - \bar{A}_j^- e^{i\frac{2\pi}{n}j}),
\end{aligned}
\tag{4.29}
$$

which has the inverse

$$
\begin{aligned}
A_j^+ &= e^{i\frac{2\pi}{n}j}(B_j^+ + B_j^-) \\
A_j^- &= e^{i\frac{2\pi}{n}j}(\bar{B}_j^+ - \bar{B}_j^-).
\end{aligned}
\tag{4.30}
$$

Expressed in terms of these new variables the system of equations Eq.(4.28) becomes

$$
\begin{aligned}
\dot{B}_j^{\pm} =\ & (1 \pm \epsilon)B_j^{\pm} - B_j^{\pm}\sum_k(2 + \delta_{jk})g_{jk}(|B_k^+|^2 + |B_k^-|^2) + B_j^{\mp}g_{jj}(B_j^+\bar{B}_j^- + \bar{B}_j^+ B_j^-) \\
& \mp 2\,B_j^{\pm}\sum_k f_{jk}\cos\frac{4\pi}{n}(k-j)\,(|B_k^+|^2 - |B_k^-|^2) \mp 2\,B_j^{\mp}\sum_k f_{jk}\cos\frac{4\pi}{n}(k-j)\,(B_k^+\bar{B}_k^- - \bar{B}_k^+ B_k^-) \\
& \pm 2i\,B_j^{\mp}\sum_k f_{jk}\sin\frac{4\pi}{n}(k-j)\,(|B_k^+|^2 - |B_k^-|^2) \pm 2i\,B_j^{\pm}\sum_k f_{jk}\sin\frac{4\pi}{n}(k-j)\,(B_k^+\bar{B}_k^- - \bar{B}_k^+ B_k^-)
\end{aligned}
\tag{4.31}
$$

and has the energy functional

$$
\begin{aligned}
E =\ & -2\sum_{j=0}^{n-1}\left((|B_j^+|^2 + |B_j^-|^2) + \epsilon(|B_j^+|^2 - |B_j^-|^2)\right) + g_{00}\sum_{j=0}^{n-1}\left((|B_j^+|^2 + |B_j^-|^2)^2 - (B_j^+\bar{B}_j^- + \bar{B}_j^+ B_j^-)^2\right) \\
& + 2\sum_{j=0}^{n-1}\sum_{k=0}^{n-1}(|B_j^+|^2 + |B_j^-|^2)\,g_{jk}\,(|B_k^+|^2 + |B_k^-|^2) \\
& + 2\sum_{k,j=0}^{n-1} e^{i\frac{4\pi}{n}(k-j)} f_{jk}(|B_j^+|^2 - |B_j^-|^2 + (B_j^+\bar{B}_j^- - \bar{B}_j^+ B_j^-)) \cdot (|B_k^+|^2 - |B_k^-|^2 - (B_k^+\bar{B}_k^- - \bar{B}_k^+ B_k^-))
\end{aligned}
\tag{4.32}
$$

We write the complex quantities $B_j^{\pm}$ as a product of real amplitude and phase,

$$
B_j^{\pm} = \mathcal{B}_j^{\pm} e^{i\phi_j^{\pm}}
$$

and consider the dynamics of the amplitudes and phases separately. The dynamics of the amplitudes $\mathcal{B}_j^{\pm}$ is given by

$$
\begin{aligned}
\dot{\mathcal{B}}_j^{\pm} =\ & (1 \pm \epsilon)\mathcal{B}_j^{\pm} - \mathcal{B}_j^{\pm}\sum_k(2 + \delta_{jk})g_{jk}[(\mathcal{B}_k^+)^2 + (\mathcal{B}_k^-)^2] + \mathcal{B}_j^{\pm}(\mathcal{B}_j^{\mp})^2 g_{jj}(1 + \cos 2(\phi_j^+ - \phi_j^-)) \\
& \mp 2\mathcal{B}_j^{\pm}\sum_k f_{jk}\cos\frac{4\pi}{n}(k-j)[(\mathcal{B}_k^+)^2 - (\mathcal{B}_k^-)^2] \\
& - 4\mathcal{B}_j^{\mp}\sin(\phi_j^+ - \phi_j^-)\sum_k f_{jk}\mathcal{B}_k^+\mathcal{B}_k^-\cos\frac{4\pi}{n}(k-j)\sin(\phi_k^+ - \phi_k^-) \\
& + 2\mathcal{B}_j^{\mp}\sin(\phi_j^+ - \phi_j^-)\sum_k f_{jk}[(\mathcal{B}_k^+)^2 - (\mathcal{B}_k^-)^2]\sin\frac{4\pi}{n}(k-j) \\
& \mp 4\mathcal{B}_j^{\pm}\sum_k f_{jk}\mathcal{B}_k^+\mathcal{B}_k^-\sin\frac{4\pi}{n}(k-j)\sin(\phi_k^+ - \phi_k^-),
\end{aligned}
\tag{4.33}
$$

while the dynamics of the phases states

$$
\begin{aligned}
\dot{\phi}_j^{\pm} =\ & \mp(\mathcal{B}_j^{\mp})^2\, g_{jj} \sin 2(\phi_j^+ - \phi_j^-) \\
& \mp 4\mathcal{B}_j^{\mp}(\mathcal{B}_j^{\pm})^{-1} \cos(\phi_j^+ - \phi_j^-) \sum_k f_{jk}\mathcal{B}_k^+\mathcal{B}_k^- \cos \frac{4\pi}{N}(k-j) \sin(\phi_k^+ - \phi_k^-) \\
& \pm 2(\mathcal{B}_j^{\pm})^{-1}\mathcal{B}_j^{\mp} \cos(\phi_j^+ - \phi_j^-) \sum_k f_{jk}[(\mathcal{B}_k^+)^2 - (\mathcal{B}_k^-)^2] \sin \frac{4\pi}{n}(k-j).
\end{aligned}
$$

It only depends on $\Omega_j = \phi_j^+ - \phi_j^-$ and thus can be written

$$
\begin{aligned}
\dot{\Omega}_j =\ & -[(\mathcal{B}_j^+)^2 + (\mathcal{B}_j^-)^2]\, g_{jj} \sin 2\Omega_j \\
& -4[(\mathcal{B}_j^+)^{-1}\mathcal{B}_j^- + (\mathcal{B}_j^-)^{-1}\mathcal{B}_j^+] \cos \Omega_j \sum_k f_{jk}\mathcal{B}_k^+\mathcal{B}_k^- \cos \frac{4\pi}{n}(k-j) \sin \Omega_k && (4.34) \\
& +2[(\mathcal{B}_j^+)^{-1}\mathcal{B}_j^- + (\mathcal{B}_j^-)^{-1}\mathcal{B}_j^+] \cos \Omega_j \sum_k f_{jk}[(\mathcal{B}_k^+)^2 - (\mathcal{B}_k^-)^2] \sin \frac{4\pi}{n}(k-j). && (4.35)
\end{aligned}
$$

For the stationary states of the dynamics (4.31) we make the ansatz

$$
\mathcal{B}_j^{\pm} = \mathcal{B}^{\pm} \quad \forall j \in \{1,\dots,n\} \tag{4.36}
$$

motivated by the fact that Eqns.(4.31) are invariant under permutations of the indices j, but not under transpositions $B_j^{\pm} \to B_j^{\mp}$. The dynamics of the phase is then given by

$$
\begin{aligned}
\dot{\Omega}_j =\ & -[(\mathcal{B}^+)^2 + (\mathcal{B}^-)^2]\, g_{jj} \sin 2\Omega_j \\
& -\left(4[(\mathcal{B}^+)^{-1}\mathcal{B}^- + (\mathcal{B}^-)^{-1}\mathcal{B}^+]\mathcal{B}^+\mathcal{B}^- \cos \Omega_j\right)\left(\sum_k f_{jk} \cos \frac{4\pi}{n}(k-j) \sin \Omega_k\right) \\
& +\left(2[(\mathcal{B}^+)^{-1}\mathcal{B}^- + (\mathcal{B}^-)^{-1}\mathcal{B}^+][(\mathcal{B}^+)^2 - (\mathcal{B}^-)^2] \cos \Omega_j\right)\left(\sum_k f_{jk} \sin \frac{4\pi}{n}(k-j)\right)
\end{aligned}
\tag{4.37}
$$

where it is assumed that $\mathcal{B}^{\pm} \neq 0$. The case where $\mathcal{B}^+$ or $\mathcal{B}^-$ vanishes will be considered separately. Due to reflection symmetry $f(\alpha) = f(-\alpha)$, i.e. $f(\alpha)$ is a symmetric function. Hence,

$$
\sum_{k=0}^{n} f_{jk} \sin \frac{4\pi}{n}(k-j) = 0
$$

and the last term in Eq.(4.37) vanishes. Thus, the stationary phases fulfill either $\Omega_j = 0 \bmod 2\pi$ or $\Omega_j = \pi \bmod 2\pi$, respectively. As will become clear below we can restrict to the case $\Omega_j = 0$ $\forall j \in \{1,\dots,n\}$ since this is the only choice for which $A_j^- \to 0$ for $\epsilon \to 0$. The stationary state has to be determined from the two equations

$$
\begin{aligned}
0 =\ & (1 \pm \epsilon)\mathcal{B}^{\pm} - \mathcal{B}^{\pm} \sum_k (2 + \delta_{jk}) g_{jk}[(\mathcal{B}^+)^2 + (\mathcal{B}^-)^2] + 2g_{jj}\mathcal{B}^{\pm}(\mathcal{B}^{\mp})^2 \\
& \mp 2\mathcal{B}^{\pm} \sum_k f_{jk} \cos \frac{4\pi}{n}(k-j)[(\mathcal{B}^+)^2 - (\mathcal{B}^-)^2]
\end{aligned}
\tag{4.38}
$$

By means of the definition

$$
\begin{aligned}
\Sigma &:= (\mathcal{B}^+)^2 + (\mathcal{B}^-)^2 \\
\Delta &:= (\mathcal{B}^+)^2 - (\mathcal{B}^-)^2
\end{aligned}
\tag{4.39}
$$

the solution to Eq.(4.38) can be expressed as follows

$$
\begin{aligned}
\Sigma &= \frac{1}{2\sum_k g_{ij}} \\
\Delta &= \frac{\epsilon}{g_{00} + 2\sum_k f_{jk}\cos\frac{4\pi}{n}(k-j)}
\end{aligned}
$$

or, after introducing a new quantity ϵ_*

$$
\epsilon_*(n) := \frac{g_{00} + 2\sum_{k=0}^{n-1} f_{0k}\cos\frac{4\pi}{n}k}{2\sum_{k=0}^{n-1} g_{0k}}
\tag{4.40}
$$

it can be also written

$$
\begin{aligned}
\Sigma &= \frac{1}{2\sum_k g_{ij}} \\
\Delta &= \frac{\epsilon}{\epsilon_*(n)}\Sigma
\end{aligned}
\tag{4.41}
$$

As will become clear below, $\epsilon_*(n)$ defines the *critical strength* of SSB. The size of ϵ_* depends on the order of the planform, n, as well as on the model's interaction functions $g(\alpha)$ and $f(\alpha)$. For the model 4.5 its value is bounded by $|\epsilon_*(n)| \leq 1/2$, since

$$
\begin{aligned}
|\epsilon_*| &= \left| \frac{g_{00} + 2\sum_{k=0}^{n-1} f_{0k}\cos\frac{4\pi}{n}k}{2\sum_{k=0}^{n-1} g_{0k}} \right| = \frac{\left| \sum_{k=0}^{n-1} g_{0k}\cos\frac{4\pi}{n}k \right|}{\left| 2\sum_{k=0}^{n-1} g_{0k} \right|} \\
&\leq \frac{\left| \sum_{k=0}^{n-1} g_{0k} \right|}{2\left| \sum_{k=0}^{n-1} g_{0k} \right|} = \frac{1}{2}
\end{aligned}
$$

because $f_{0k} = \frac{1}{2}g_{0k} \; \forall k \neq 0$ (cf. Eq.(4.19)). For sufficiently large n the sums in (4.40) can be replaced by integrals, yielding

$$
\epsilon_*(\infty) = \frac{\int_0^{2\pi} d\alpha \, f(\alpha)\,\cos(4\alpha)}{\int_0^{2\pi} d\alpha \, g(\alpha)}
$$

For our model defined by (4.18) we find

$$
\epsilon_*(\infty) = \frac{(2-g)\left(k^2\sigma^2\left(24 + k_c^4\sigma^4\right) I_0(k_c^2\sigma^2) - 8\left(6 + k_c^4\sigma^4\right) I_1(k_c^2\sigma^2)\right)}{k_c^6\sigma^6\left(e^{k_c^2\sigma^2}g + 2(2-g)I_0(k_c^2\sigma^2)\right)}
\tag{4.42}
$$

where I_j denotes the modified Bessel functions of the first kind. Fig.4.3(**a**) graphs $\epsilon_*(\infty)$ as a function of σ/Λ for different values of g. For comparison in Fig.4.3(**b-d**) we also plot the corresponding graphs of $\epsilon_*(n)$ for different values of n. Notice that $\epsilon_*(\infty) \geq 0 \; \forall g \in [0,2]$, $\sigma \in \mathbb{R}_+$,
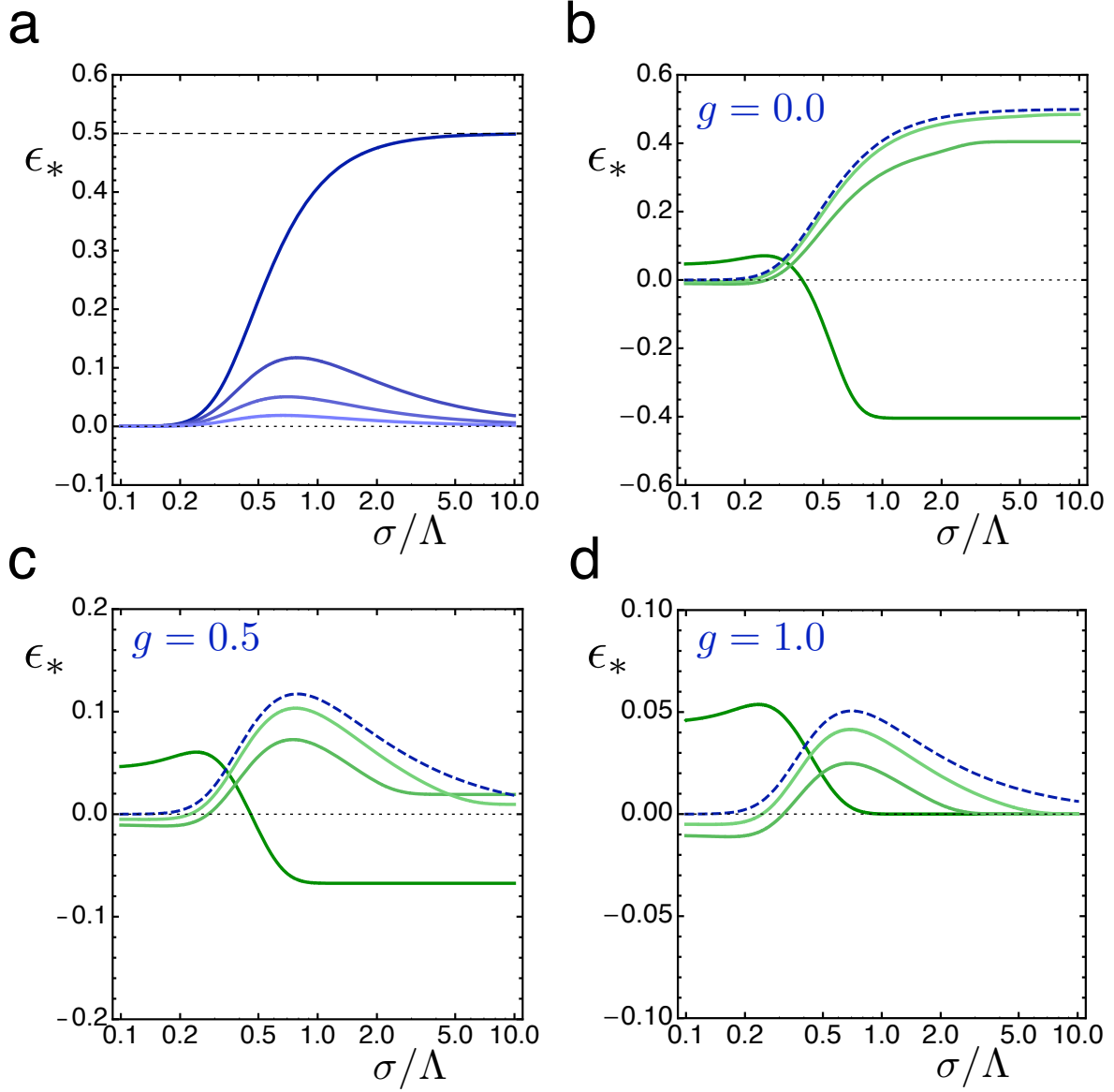
Figure 4.3: Critical strength of shift symmetry breaking $\epsilon_*(n, g, \sigma)$ for different model parameters. **(a)** $\epsilon_*(\infty)$ for different values of g ($g = 0, 0.5\,1.0, 1.5$) **(b-d)** $\epsilon_*(\infty)$ vs $\epsilon_*(n)$ **(b)** $g = 0$, $n = 5, 25, 50$ **(c)** $g = 0.5$, $n = 5, 25, 50$ **(c)** $g = 1.0$, $n = 5, 25, 50$. Further details are given in the text.

whereas $\epsilon_*(n)$ also assumes negative values, especially towards small numbers n or $\sigma \ll \Lambda$. For clarity, in the following we drop the argument of $\epsilon_*(n)$, and simply write ϵ_*.

For the stationary values of $\mathcal{B}^+$ and $\mathcal{B}^-$ then follows

$$
\begin{aligned}
(\mathcal{B}^\pm)^2 &= \frac{1}{2}(\Sigma \pm \Delta) \\
&= \frac{1}{4\sum_k g_{jk}}\left(1 \pm \frac{\epsilon}{\epsilon_*(n)}\right)
\end{aligned}
$$

Since the right hand side has to be real and positive this solution only exists in the interval $\epsilon \leq |\epsilon_*|$ (we assume $g_{ij} > 0, \ \forall i,j$).

An analogous treatment of the cases in which either $\mathcal{B}^+$ or $\mathcal{B}^-$ vanishes yields the following results: For $\mathcal{B}^+ \neq 0$, $\mathcal{B}^- = 0$ the stationary amplitude $\mathcal{B}^+$ reads

$$
(\mathcal{B}^+)^2 = \frac{1}{2\sum_k g_{jk}}\frac{1+\epsilon}{1+\epsilon_*} \tag{4.43}
$$

and for $\mathcal{B}^- \neq 0$, $\mathcal{B}^+ = 0$ we find

$$
(\mathcal{B}^-)^2 = \frac{1}{2\sum_k g_{jk}}\frac{1-\epsilon}{1+\epsilon_*} \tag{4.44}
$$

Eqns. (4.43) and 4.44) provide solutions for $\epsilon \in [-1, \infty)$ and $\epsilon \in (-\infty, 1]$, respectively.

In summary, we have identified three types of stationary solutions

1.
$$
\mathcal{B}^\pm = \sqrt{\frac{1}{4\sum_k g_{jk}}}\sqrt{\left(1 \pm \frac{\epsilon}{\epsilon_*}\right)}, \quad \phi_j^+ - \phi_j^- = 0 \bmod 2\pi, \quad |\epsilon| \leq |\epsilon_*| \tag{4.45}
$$

2.
$$
\mathcal{B}^+ = \sqrt{\frac{1}{4\sum_k g_{jk}}}\sqrt{\frac{2(1+\epsilon)}{1+\epsilon_*}}, \quad \mathcal{B}^- = 0, \quad \phi_j^+ \text{ arbitrary}, \quad \epsilon \geq -1 \tag{4.46}
$$

3.
$$
\mathcal{B}^- = \sqrt{\frac{1}{4\sum_k g_{jk}}}\sqrt{\frac{2(1-\epsilon)}{1+\epsilon_*}}, \quad \mathcal{B}^+ = 0, \quad \phi_j^- \text{ arbitrary}, \quad \epsilon \leq 1 \tag{4.47}
$$

How do the corresponding planforms (4.26) look like? In terms of the amplitudes A^+ and A^- solution (4.45) becomes

$$
\begin{aligned}
|A^\pm|^2 &= \Sigma \pm \sqrt{\Sigma^2 - \Delta^2} \\
&= \frac{1}{2\sum_k g_{jk}}\left(1 \pm \sqrt{1 - (\epsilon/\epsilon_*)^2}\right)
\end{aligned} \tag{4.48}
$$

which, for $\epsilon = 0$, is identical to the solution reported in [22] since then

$$
|A^+| = \frac{1}{2}\sqrt{\frac{1}{\sum g_{jk}}}, \quad |A^-| = 0. \tag{4.49}
$$

A series expansion of $|A^\pm|$ in ϵ around $\epsilon = 0$ gives

$$
|A^+| = \sqrt{\frac{1}{\sum_k g_{jk}}} (1 - O(\epsilon/\epsilon_*)^2)
$$

$$
|A^-| = \sqrt{\frac{1}{\sum_k g_{jk}}} (|\epsilon/\epsilon_*| + O(|\epsilon/\epsilon_*|)^3)
$$

from which we see that antiparallel modes A_j^-, which are completely suppressed for $\epsilon = 0$, start to grow linearly with ϵ (shown in Fig. 4.2(**c**)). At the same time active modes A_j^+ become smaller, such that the sum $|A_j^+|^2 + |A_j^-|^2$ stays constant. With increasing strength of SSB $|\epsilon|$ amplitudes $|A_j^+|$ and $|A_j^-|$ approach each other and eventually collapse to the same value for $|\epsilon| = |\epsilon_*|$.

This collapse persists for values of $|\epsilon|$ beyond $|\epsilon_*|$, which follows from solutions (4.46) and (4.47). For $\epsilon \geq |\epsilon_*|$ solution (4.46) corresponds to

$$
|A^\pm| = |B^\pm| = \sqrt{\frac{1}{2\sum_k g_{jk}} \frac{1+\epsilon}{1+\epsilon_*}}, \tag{4.50}
$$

which at $\epsilon = |\epsilon_*|$ gives the same solution as Eq.(4.48) if $\epsilon_* > 0$. Similarly, For $\epsilon \leq |\epsilon_*|$ solution (4.47) corresponds to

$$
|A^\pm| = |B^\pm| = \sqrt{\frac{1}{2\sum_k g_{jk}} \frac{1-\epsilon}{1+\epsilon_*}}, \tag{4.51}
$$

which at $\epsilon = -|\epsilon_*|$ also yields the same solution as Eq.(4.48) if $\epsilon_* > 0$.

For $\epsilon_* < 0$ the same statements apply, one simply has to replace ϵ by $-\epsilon$. The situation for $\epsilon_* > 0$ is displayed in Fig.4.2(**c**). As indicated by the dotted line in Fig.4.2(**c**) both solutions (4.50) and (4.51) coexist with solution (4.49) in the interval $-|\epsilon_*| \leq \epsilon \leq |\epsilon_*|$. However, we will show below, that for $\epsilon_* > 0$ solutions (4.50) and (4.51) are unstable in this interval, whereas solution (4.49) is stable. For $\epsilon_* < 0$ the situation is reversed (not shown in Fig. 4.2(**c**)). Shift symmetry breaking not only leads to the growth of a given mode A_j^-, but also to a pairwise coupling of its phases to the phase of A_j^+. This coupling occurs in one of two ways, depending on the signs of ϵ and of ϵ_*. First we discuss the case where ϵ_* is *positive*.

For $|\epsilon| \leq \epsilon_*$ where solution (4.45) applies, we find from Eqns. (4.30)

$$
\begin{aligned}
A_j^+ A_j^- &= e^{i\frac{4\pi}{n}j}(|B_j^+|^2 - |B_j^-|^2 + B_j^- \bar{B}_j^+ - B_j^+ \bar{B}_j^-) \\
&= e^{i\frac{4\pi}{n}j}\left(|B_j^+|^2 - |B_j^-|^2 - 2i|B_j^-||B_j^+|\sin(\phi_j^+ - \phi_j^-)\right),
\end{aligned} \tag{4.52}
$$

which due to $\phi_j^+ - \phi_j^- = 0 \bmod 2\pi$ leads to

$$
|A_j^+|e^{i\psi_j^+}|A_j^-|e^{i\psi_j^-} = e^{i4\arg k_j}\left(|B_j^+|^2 - |B_j^-|^2\right),
$$

and thus to the conditions

$$
\psi_j^+ + \psi_j^- = \begin{cases} 4\arg \mathbf{k}_j & \text{for } \epsilon > 0 \text{ and } \epsilon_* > 0 \\ 4\arg \mathbf{k}_j + \pi & \text{for } \epsilon < 0 \text{ and } \epsilon_* > 0 \end{cases} \tag{4.53}
$$

where ψ_j^+ and ψ_j^- denote the phases of the complex amplitudes A_j^+ and A_j^-. Thus the degree of freedom for each pair of mode just consists of *one* arbitrarily chosen phase. Condition (4.53) also applies for $\epsilon > \epsilon_*$ or $\epsilon < -\epsilon_*$, which follows from a substitution of the corresponding solutions, (4.46) or (4.47), into (4.52). As mentioned above, when ϵ_* is *negative* solution (4.45) is unstable. On the other hand solutions (4.46) (phase relation $\psi_j^+ + \psi_j^- = 4 \arg \mathbf{k}_j$) or (4.47) (phase relation $\psi_j^+ + \psi_j^- = \pi + 4 \arg \mathbf{k}_j$) are both stable and coexist in the interval $|\epsilon| < -\epsilon_*$. Beyond that range only one solution is stable, i.e. solution (4.46) for $\epsilon > 0$ and solution (4.46) for $\epsilon < 0$. The result of the stability analysis is summarized in Fig. 4.5 and will be discussed below. Since only the case $\epsilon_* > 0$ is relevant in the context of our study we assume positive valued ϵ_* in the following, unless stated otherwise.

The Degree of Shift Symmetry Breaking

The coupling (4.53) of the phases ψ_j^+ and ψ_j^- has direct impact on the functional form of the correlation function $P_2(\mathbf{k}_j) = \langle a(\mathbf{k}_j) a(-\mathbf{k}_j) \rangle$ which, for a solution, becomes

$$P_2(\mathbf{k}_j) \quad = \quad \langle A_j^+ A_j^- \rangle = e^{i4 \arg \mathbf{k}_j} \left(|B^+|^2 - |B^-|^2 \right).$$

This matches the general form (3.13) derived for random fields of broken shift symmetry. In particular,

$$P_2(\mathbf{k}_j) = \begin{cases} 0 & \text{for } \epsilon = 0 \\ e^{i4 \arg \mathbf{k}_j} |B^+|^2 & \text{for } \epsilon \geq \epsilon_* \\ -e^{i4 \arg \mathbf{k}_j} |B^-|^2 & \text{for } \epsilon \leq -\epsilon_* \end{cases}$$

One way to quantify the *degree* to which shift symmetry breaking affects essentially complex planforms is therefore provided by the measure,

$$\begin{aligned} q \quad &:= \quad \frac{\sum_j \left(P_2(\mathbf{k}_j) e^{-4 \arg \mathbf{k}_j} + \bar{P}_2(\mathbf{k}_j) e^{4 \arg \mathbf{k}_j} \right)}{\sum_j P_1(\mathbf{k}_j)} \\ &= \quad \frac{|B^+|^2 - |B^-|^2}{|B^+|^2 + |B^-|^2}, \end{aligned}$$

which, by means of (4.39) and (4.41) can also be written

$$q = \Delta/\Sigma = \begin{cases} -1 & \text{for } \epsilon \leq -\epsilon_* \\ \epsilon/\epsilon_* & \text{for } -\epsilon_* \leq \epsilon \leq \epsilon_* \\ 1 & \text{for } \epsilon \geq \epsilon_* \end{cases}$$

which shows that there is a linear relationship between the degree of symmetry breaking q and the value of ϵ. This definition is consistent with our previous definition of q in (3.15) and (3.16). Since the effects of SSB on the pattern are maximal for $|\epsilon| \geq \epsilon_*$ where the degree of SSB is either $q = 1$ or $q = -1$, we say that the quantity ϵ_* defines the *critical strength* of shift symmetry breaking.

Explicit Solution

In summary, the solution for different values of ϵ states

$$
z(\mathbf{x}) = \sqrt{\frac{1}{\sum_k g_{jk}}} \cdot
\begin{cases}
\sqrt{\dfrac{2(1+|\epsilon|)}{1+\epsilon_*}} \displaystyle\sum_{j=0}^{n-1} z_j^o(\mathbf{x}, \phi_j) & \text{for } \epsilon \leq -\epsilon_* \\[3ex]
\displaystyle\sum_{j=0}^{n-1} \left(\sqrt{1+q}\, z_j^e(\mathbf{x}, \phi_j) + \sqrt{1-q}\, z_j^o(\mathbf{x}, \phi_j) \right) & \text{for } -\epsilon_* \leq \epsilon \leq \epsilon_* \\[3ex]
\sqrt{\dfrac{2(1+|\epsilon|)}{1+\epsilon_*}} \displaystyle\sum_{j=0}^{n-1} z_j^e(\mathbf{x}, \phi_j) & \text{for } \epsilon \geq \epsilon_*
\end{cases}
\qquad (4.54)
$$

with

$$
\begin{aligned}
z_j^o(\mathbf{x}, \phi_j) &:= i\, e^{2i \arg \mathbf{k}_j}\, \sin(\phi_j + l_j \mathbf{k}_j \mathbf{x}) \\
z_j^e(\mathbf{x}, \phi_j) &:= e^{2i \arg \mathbf{k}_j}\, \cos(\phi_j + l_j \mathbf{k}_j \mathbf{x})
\end{aligned}
$$

and arbitrary phases ϕ_j. The set of functions $z_j^e(\mathbf{x}, \phi_j)$ and $z_j^o(\mathbf{x}, \phi_j)$ span the kernel of $L + \epsilon MC$, respectively, and correspond to the two irreducible representations of reflections: Shift-twist reflections in the axis parallel to $\mathbf{k}_j$, denoted by $(CP)_{\mathbf{k}_j}$, leave $z_j^e(\mathbf{x}, \phi_j)$, invariant,

$$
(CP)_{\mathbf{k}_j} z_j^e(\mathbf{x}, \phi_j) = z_j^e(\mathbf{x}, \phi_j)
$$

whereas

$$
(CP)_{\mathbf{k}_j} z_j^o(\mathbf{x}, \phi_j) = -z_j^o(\mathbf{x}, \phi_j).
$$

We refer to z_j^e as the *even* and to z_j^o as the *odd* basis functions of the kernel of $L + \epsilon MC$, see Fig.4.4. The plane wave solution of Section 4.4 is a special case of Eq.(4.54) for $n = 1$ where $\epsilon_* = 1/2$.

4.7 Stability Analysis of Quasiperiodic Solutions

Next we discuss the stability of all three types of stationary states to intrinsic and extrinsic perturbations.

Intrinsic Stability

First we consider stability to intrinsic perturbations. Small perturbations around any of the stationary states
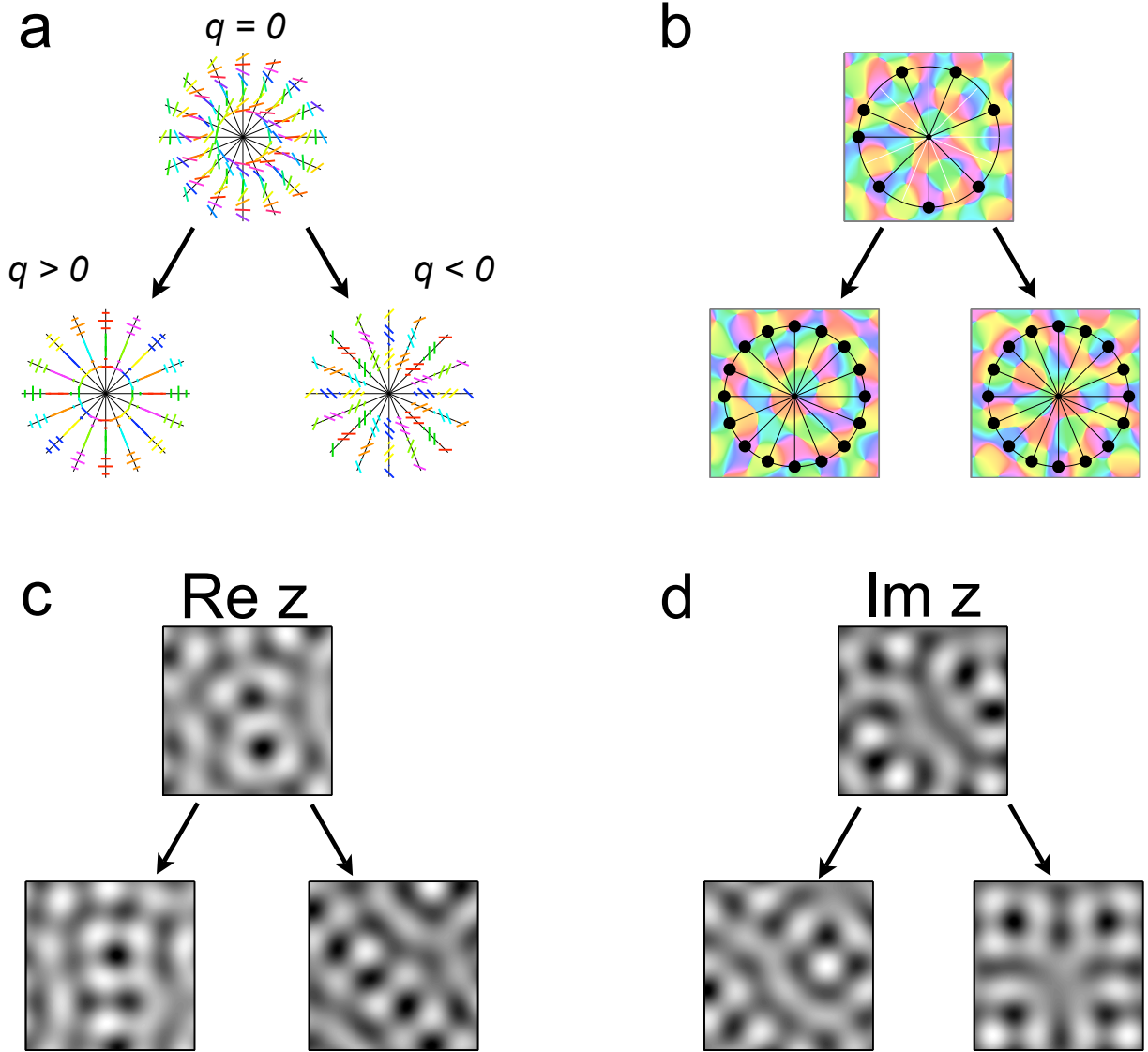
$$
B_j^\pm \to B_j^\pm + \delta B_j^\pm
$$

Figure 4.4: Combinations of even and odd eigenfunctions of the kernel of $L_0 + \epsilon MC$ are the building blocks of the planform solution Eq.(4.54). A general solution is given by a linear superposition of even modes and odd modes, where (**a**) (*lower row*:) for $q = \epsilon/\epsilon_* > 0$ (*right*) the even part dominates and for for $q = \epsilon/\epsilon_* > 0$ (*left*) the odd part dominates. Note how the phases of the even and odd eigenfunctions (indicated by a *colorcode* for the phase or, in our context, orientation) depend on the wavevector's direction (*the different rays*), such that reflection at an axes parallel to the wavevector transforms the eigenfunction to itself when the orientations run perpendicular and parallel to (*left*) or to the negative of itself when the orientations run oblique to the axis defined by the wavevector (*right*). For $q = 0$ both parts are equal and combine to form an essentially complex planform where one mode of each antiparallel pair of modes vanishes (*upper row*). (**b**) Orientation preference maps. Black dots denote the Fourier power of the solution, q as in (a). (**c, d**) Real and complex part of the solution. Note the coupling of iso-orientation domains to the coordinate system similar to the situation in Fig. 3.3 and Fig. 3.4 for $q \neq 0$.

evolve according to the linearized dynamics of Eq.(4.31), i.e.

$$
\begin{aligned}
\delta \dot{B}_j^{\pm} =\ & (1 \pm \epsilon) \delta B_j^{\pm} \\
& - \delta B_j^{\pm} \sum_k (2 + \delta_{jk}) g_{jk}(|B_k^+|^2 + |B_k^-|^2) - B_j^{\pm} \sum_k (2 + \delta_{jk}) g_{jk}(\delta B_k^+ \bar{B}_k^+ + B_k^+ \delta \bar{B}_k^+) \\
& - B_j^{\pm} \sum_k (2 + \delta_{jk}) g_{jk}(\delta B_k^- \bar{B}_k^- + B_k^- \delta \bar{B}_k^-) \\
& + \delta B_j^{\mp} g_{jj}(B_j^+ \bar{B}_j^- + \bar{B}_j^+ B_j^-) + B_j^{\mp} g_{jj}(\delta B_j^+ \bar{B}_j^- + B_j^+ \delta \bar{B}_j^-) + B_j^{\mp} g_{jj}(\delta \bar{B}_j^+ B_j^- + \bar{B}_j^+ \delta B_j^-) \\
& \mp 2\, \delta B_j^{\pm} \sum_k f_{jk} \cos \frac{4\pi}{n}(k - j)\,(|B_k^+|^2 - |B_k^-|^2) \mp 2\, B_j^{\pm} \sum_k f_{jk} \cos \frac{4\pi}{n}(k - j)\,(\delta B_k^+ \bar{B}_k^+ + B_k^+ \delta \bar{B}_k^+) \\
& \pm 2\, B_j^{\pm} \sum_k f_{jk} \cos \frac{4\pi}{n}(k - j)\,(\delta B_k^- \bar{B}_k^- + B_k^- \delta \bar{B}_k^-) \\
& \mp 2\, \delta B_j^{\mp} \sum_k f_{jk} \cos \frac{4\pi}{n}(k - j)\,(B_k^+ \bar{B}_k^- - \bar{B}_k^+ B_k^-) \mp 2\, B_j^{\mp} \sum_k f_{jk} \cos \frac{4\pi}{n}(k - j)\,(\delta B_k^+ \bar{B}_k^- + B_k^+ \delta \bar{B}_k^-) \\
& \pm 2\, B_j^{\mp} \sum_k f_{jk} \cos \frac{4\pi}{n}(k - j)\,(\delta \bar{B}_k^+ B_k^- + \bar{B}_k^+ \delta B_k^-) \\
& \pm 2i\, \delta B_j^{\mp} \sum_k f_{jk} \sin \frac{4\pi}{n}(k - j)\,(|B_k^+|^2 - |B_k^-|^2) \pm 2i\, B_j^{\mp} \sum_k f_{jk} \sin \frac{4\pi}{n}(k - j)\,(\delta B_k^+ \bar{B}_k^+ + B_k^+ \delta \bar{B}_k^+) \\
& \mp 2i\, B_j^{\mp} \sum_k f_{jk} \sin \frac{4\pi}{n}(k - j)\,(\delta B_k^- \bar{B}_k^- + B_k^- \delta \bar{B}_k^-) \\
& \pm 2i\, \delta B_j^{\pm} \sum_k f_{jk} \sin \frac{4\pi}{n}(k - j)\,(B_k^+ \bar{B}_k^- - \bar{B}_k^+ B_k^-) \pm 2i\, B_j^{\pm} \sum_k f_{jk} \sin \frac{4\pi}{n}(k - j)\,(\delta B_k^+ \bar{B}_k^- + B_k^+ \delta \bar{B}_k^-) \\
& \mp 2i\, B_j^{\pm} \sum_k f_{jk} \sin \frac{4\pi}{n}(k - j)\,(\delta \bar{B}_k^+ B_k^- + \bar{B}_k^+ \delta B_k^-)
\end{aligned}
\tag{4.55}
$$

When considering the stability of solution 1 all amplitudes B_k^+ and B_k^- have to be replaced by the stationary solutions Eq.(4.45) such that

$$
B_j^+ = \mathcal{B}^+ e^{i\phi_j}, \qquad B_j^- = \mathcal{B}^- e^{i\phi_j}.
$$

For solutions 2 and 3, where Eqns.(4.46) and (4.47) apply, one type of amplitudes is zero, e.g. $B_k^- = 0$, but the other type has the form

$$
B_j^+ = \mathcal{B}^+ e^{i\phi_j}.
$$

In both cases, the solutions have n continuous degrees of freedom since the phases ϕ_j are arbitrary. Thus, in general, Eq.(4.55) depends on these phases. However, they can be absorbed in the perturbations by setting

$$
\begin{aligned}
\delta B_j^+ \to \delta B_j^+ e^{i\phi_j} &\quad , \quad \delta \bar{B}_j^+ \to \delta \bar{B}_j^+ e^{-i\phi_j} \\
\delta B_j^- \to \delta B_j^- e^{i\phi_j} &\quad , \quad \delta \bar{B}_j^- \to \delta \bar{B}_j^- e^{-i\phi_j}
\end{aligned}
$$

such that all complex amplitudes in Eq.(4.55) are replaced by their absolute values. Eq.(4.55) can be brought into following form

$$
\begin{pmatrix} \delta\mathrm{Re}\dot{\mathbf{B}}^+ \\ \delta\mathrm{Im}\dot{\mathbf{B}}^+ \\ \delta\mathrm{Re}\dot{\mathbf{B}}^- \\ \delta\mathrm{Im}\dot{\mathbf{B}}^- \end{pmatrix} = \left[\begin{pmatrix} \mathbf{1}\lambda^+ & & & \\ & \mathbf{1}\lambda^+ & & \\ & & \mathbf{1}\lambda^- & \\ & & & \mathbf{1}\lambda^- \end{pmatrix} \right.
$$

$$
\left. -2 \underbrace{\begin{pmatrix} a\,\mathcal{B}^+\mathcal{B}^+ & s\,\mathcal{B}^+\mathcal{B}^- & b\,\mathcal{B}^+\mathcal{B}^- & -s\,\mathcal{B}^+\mathcal{B}^+ \\ -s\,\mathcal{B}^+\mathcal{B}^- & d\,\mathcal{B}^-\mathcal{B}^- & s\,\mathcal{B}^-\mathcal{B}^- & -d\,\mathcal{B}^+\mathcal{B}^- \\ b\,\mathcal{B}^+\mathcal{B}^- & -s\,\mathcal{B}^-\mathcal{B}^- & a\,\mathcal{B}^-\mathcal{B}^- & s\,\mathcal{B}^+\mathcal{B}^- \\ s\,\mathcal{B}^+\mathcal{B}^+ & -d\,\mathcal{B}^+\mathcal{B}^- & -s\,\mathcal{B}^+\mathcal{B}^- & d\,\mathcal{B}^+\mathcal{B}^+ \end{pmatrix}}_{\tilde{M}} \right] \begin{pmatrix} \delta\mathrm{Re}\mathbf{B}^+ \\ \delta\mathrm{Im}\mathbf{B}^+ \\ \delta\mathrm{Re}\mathbf{B}^- \\ \delta\mathrm{Im}\mathbf{B}^- \end{pmatrix} \tag{4.56}
$$

where $\mathbf{B}^\pm = (B_0^\pm, B_1^\pm, \dots, B_{n-1}^\pm)$ and

$$
\begin{aligned}
\lambda^\pm &= (1 \pm \epsilon) - \sum_k 2g_{jk}(\mathcal{B}^{+2} + \mathcal{B}^{-2}) - \left(g_{jj} + 2\sum_k f_{jk} \cos\frac{4\pi}{n}(k-j) \right)(\mathcal{B}^{+2} - \mathcal{B}^{-2}) \\
a_{jk} &= (2 + \delta_{jk})g_{jk} + 2f_{ik}\cos\frac{4\pi}{n}(k-j) \\
b_{jk} &= (2 - \delta_{jk})g_{jk} - 2f_{ik}\cos\frac{4\pi}{n}(k-j) \\
d_{jk} &= \delta_{jk}g_{jk} + 2f_{ik}\cos\frac{4\pi}{n}(k-j) \\
s_{jk} &= 2f_{jk}\sin\frac{4\pi}{n}(k-j)
\end{aligned}
$$

Note that $\tilde{M}$ is symmetric since $-s = s^T$, and therefore has real eigenvalues.

Solution 1

We recall that the first type of solution was defined by

$$
\mathcal{B}^\pm = \sqrt{\frac{1}{4\sum_k g_{jk}}}\sqrt{\left(1 \pm \frac{\epsilon}{\epsilon_*}\right)}, \quad \phi_j^+ - \phi_j^- = 0 \bmod 2\pi, \quad |\epsilon| \le |\epsilon_*|
$$

where

$$
\epsilon_* = \frac{g_{00} + 2\sum_{k=0}^{n-1} f_{0k}\cos\frac{4\pi}{n}k}{2\sum_{k=0}^{n-1} g_{0k}}
$$

In particular, for this type of solutions we have

$$
\begin{aligned}
\Sigma &:= \mathcal{B}^{+2} + \mathcal{B}^{-2} &= \frac{1}{2\sum_k g_{ij}} \\
\Delta &:= \mathcal{B}^{+2} - \mathcal{B}^{-2} &= \frac{\epsilon}{g_{00} + 2\sum_k f_{jk}\cos\frac{4\pi}{n}(k-j)}
\end{aligned}
$$

such that

$$\Delta = \epsilon/\epsilon_* \Sigma$$

Therefore,

$$
\begin{aligned}
\lambda^\pm &= (1 \pm \epsilon) - \sum_k 2g_{jk}(\mathcal{B}^{+2} + \mathcal{B}^{-2}) \mp \left(g_{jj} + 2\sum_k f_{jk} \cos\frac{4\pi}{n}(k-j) \right)(\mathcal{B}^{+2} - \mathcal{B}^{-2}) \\
&= (1 \pm \epsilon) - \Sigma \left(\sum_k 2g_{jk} \pm \epsilon/\epsilon_* \left(g_{jj} + 2\sum_k f_{jk}\cos\frac{4\pi}{n}(k-j) \right) \right) \\
&= (1 \pm \epsilon) - (1 \pm \epsilon) \\
&= 0.
\end{aligned}
$$

We assume, without loss of generality, that Im $B_j^+ = 0$ which implies Im $B_j^- = 0$. Phase shifts of the solution are then mediated by perturbations of the form

$$
\begin{aligned}
\mathcal{B}^- \delta\mathrm{Im}B^+ - \mathcal{B}^+ \delta\mathrm{Im}B^- &= 0 \\
\delta\mathrm{Re}B^+ &= 0 \\
\delta\mathrm{Re}B^- &= 0
\end{aligned}
$$

spanning a n-dimensional subspace belonging to the eigenvalue zero. In order to get rid of these zero modes we just consider antisymmetric fluctuations $\delta\mathrm{Im}B^- = -(\mathcal{B}^-/\mathcal{B}^+)\delta\mathrm{Im}B^+$. The linear dynamics (4.56) thus reduces to the $3n \times 3n$ system of equations

$$
\begin{pmatrix} \delta\mathrm{Re}\dot{\mathbf{B}}^+ \\ \delta\mathrm{Im}\dot{\mathbf{B}}^+ \\ \delta\mathrm{Re}\dot{\mathbf{B}}^- \end{pmatrix} = -2 \begin{pmatrix} a\,\mathcal{B}^+\mathcal{B}^+ & 2s\,\mathcal{B}^+\mathcal{B}^- & b\,\mathcal{B}^+\mathcal{B}^- \\ -s\,\mathcal{B}^+\mathcal{B}^- & 2d\,\mathcal{B}^-\mathcal{B}^- & s\,\mathcal{B}^-\mathcal{B}^- \\ b\,\mathcal{B}^+\mathcal{B}^- & -2s\,\mathcal{B}^-\mathcal{B}^- & a\,\mathcal{B}^-\mathcal{B}^- \end{pmatrix} \begin{pmatrix} \delta\mathrm{Re}\mathbf{B}^+ \\ \delta\mathrm{Im}\mathbf{B}^+ \\ \delta\mathrm{Re}\mathbf{B}^- \end{pmatrix}
$$

which can be written as

$$
\begin{pmatrix} \delta\mathrm{Re}\dot{\mathbf{B}}^+ \\ \delta\mathrm{Im}\mathbf{B}^+ \\ \delta\mathrm{Re}\dot{\mathbf{B}}^- \end{pmatrix} = -2 \begin{pmatrix} \mathbf{1}\mathcal{B}^+ & & \\ & \mathbf{1}\mathcal{B}^- & \\ & & \mathbf{1}\mathcal{B}^- \end{pmatrix} \underbrace{\begin{pmatrix} a & s & b \\ s^T & d & s \\ b & s^T & a \end{pmatrix}}_{M} \begin{pmatrix} \mathbf{1}\mathcal{B}^+ & & \\ & \mathbf{1}(2\mathcal{B}^-) & \\ & & \mathbf{1}\mathcal{B}^- \end{pmatrix} \begin{pmatrix} \delta\mathrm{Re}\mathbf{B}^+ \\ \delta\mathrm{Im}\mathbf{B}^+ \\ \delta\mathrm{Re}\mathbf{B}^- \end{pmatrix}
$$

Therefore, since $\mathcal{B}^\pm > 0$, stability of the solution requires that M has positive eigenvalues, or equivalently, since M is symmetric, that M is positive definite. In particular, this implies the submatrix M' defined by

$$
M' = \begin{pmatrix} a & s \\ s^T & d \end{pmatrix} \tag{4.57}
$$

to be positive definite. Next we propose two criteria which provide sufficient, although not necessary, conditions for the *instability* of solution 1:

Proposition. *The $3n \times 3n$ matrix M is **not** positive definite if*

$$\epsilon_* \leq 0$$

or if

$$g_{ij} \geq g_{00}$$

for any pair $i \neq j$.

Proof. Consider the vector $\mathbf{v}$ defined by $v_0 = v_1 = \cdots = v_{n-1} = 1$, $v_n = v_{n+1} = \cdots = v_{2n-1} = 0$, $v_{2n} = v_{2n+1} = \cdots = v_{3n-1} = -1$. Then

$$
\begin{aligned}
\mathbf{v}^T M \mathbf{v} &= 2 \sum_{j,k=1}^{n} (a_{jk} - b_{jk}) \\
&= 4 \sum_{jk} (\delta_{jk} g_{jk} + 2 f_{jk} \cos \frac{4\pi}{n} k) \\
&= 4n \sum_{k} (\delta_{0k} g_{0k} + 2 f_{0k} \cos \frac{4\pi}{n} k) \\
&= 8n \, \epsilon_* \sum_{k} g_{0k}
\end{aligned}
$$

Since for the model considered here $g_{0k} > 0$ it follows that $\mathbf{v}^T M \mathbf{v} \leq 0$ if $\epsilon_* \leq 0$.

In order to prove the second statement take the vector $\mathbf{w}$ defined as $w_i = w_{2n+i} = 1$, $w_j = w_{2n+j} = -1$, $w_k = 0 \; \forall k \notin \{i, j, 2n+i, 2n+j\}$. Then

$$
\begin{aligned}
\mathbf{w}^T M \mathbf{w} &= 4(a_{ii} - a_{ij}) + 4(b_{ii} - b_{ij}) \\
&= 16(g_{00} - g_{ij})
\end{aligned}
$$

and from $g_{ij} \geq g_{00}$ follows that M is not positive definite. $\qquad\square$

Solutions 2 and 3

For the second type of solutions we have two possibilities. Either

$$
(\mathcal{B}^+)^2 = \frac{1}{2 \sum_k g_{jk}} \frac{1 + \epsilon}{1 + \epsilon_*}, \qquad \mathcal{B}^- = 0, \qquad \text{defined for } \epsilon \geq -1
$$

or

$$
(\mathcal{B}^-)^2 = \frac{1}{2 \sum_k g_{jk}} \frac{1 - \epsilon}{1 + \epsilon_*}, \qquad \mathcal{B}^+ = 0, \qquad \text{defined for } \epsilon \leq 1
$$

In the first case the values of $\lambda^\pm$ read

$$
\begin{aligned}
\lambda^\pm &= (1 \pm \epsilon) - \sum_k 2 g_{jk} \mathcal{B}^{+2} \mp \left(g_{jj} + 2 \sum_k f_{jk} \cos \frac{4\pi}{n} (k - j) \right) \mathcal{B}^{+2} \\
&= \frac{(1 \pm \epsilon)(1 + \epsilon_*) - (1 + \epsilon)(1 \pm \epsilon_*)}{1 + \epsilon_*}
\end{aligned}
$$

or

$$
\begin{aligned}
\lambda^+ &= 0 \\
\lambda^- &= -\frac{2(\epsilon - \epsilon_*)}{1 + \epsilon_*}
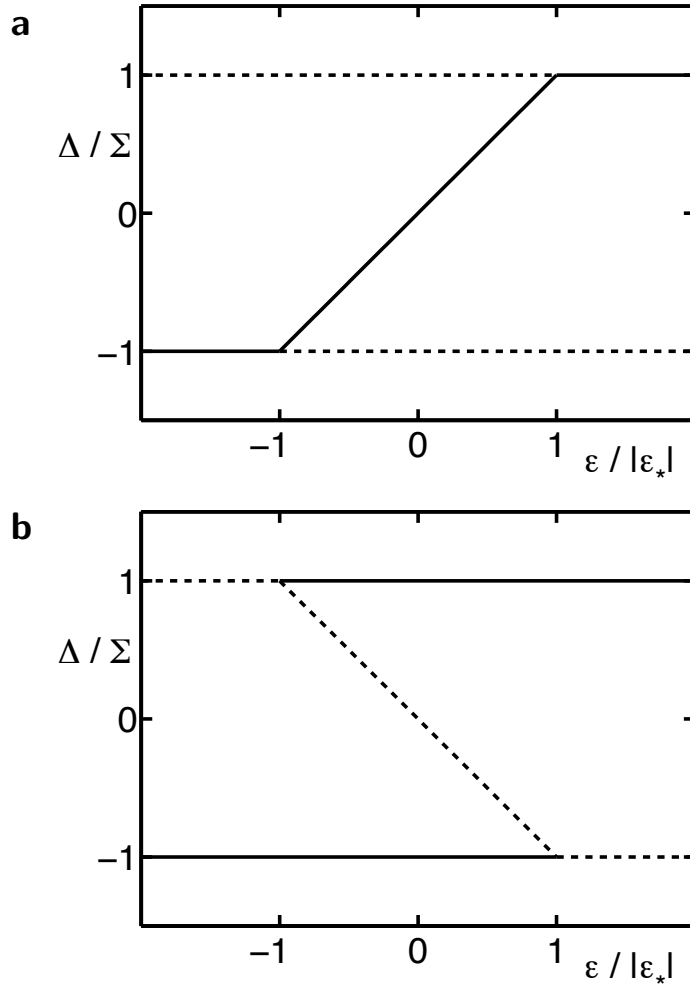\end{aligned}
\tag{4.58}
$$

For the second case we find

Figure 4.5: Bifurcation diagrams for positive (**a**) and negative values of ϵ_* (**b**). Shown is the normalized difference between odd and even components. *Dotted* lines correspond to unstable, *solid* lines to stable solutions.

$$\lambda^{\pm} = (1 \pm \epsilon) - \sum_k 2g_{jk}\mathcal{B}^{-2} \pm \left(g_{jj} + 2\sum_k f_{jk}\cos\frac{4\pi}{n}(k-j)\right)\mathcal{B}^{-2}$$

$$= \frac{(1 \pm \epsilon)(1 + \epsilon_*) - (1 - \epsilon)(1 \mp \epsilon_*)}{1 + \epsilon_*}$$

or

$$\lambda^+ = \frac{2(\epsilon + \epsilon_*)}{1 + \epsilon_*}$$

$$\lambda^- = 0$$

The relevant equation of motions in the first case, obtained by setting $\delta\mathrm{Im}\mathbf{B}^+ = 0$ (in order to eliminate the zeros modes due to the phase degeneracy) and $\mathcal{B}^- = 0$ in Eq.(4.56), state

$$\begin{pmatrix}\delta\mathrm{Re}\dot{\mathbf{B}}^+ \\ \delta\mathrm{Im}\dot{\mathbf{B}}^-\end{pmatrix} = \left(\begin{pmatrix}\cdot & \\ & \mathbf{1}\dot{\lambda}^-\end{pmatrix} - 2\mathcal{B}^{+2}\underbrace{\begin{pmatrix}a & s^T \\ s & d\end{pmatrix}}_{M'^T}\right)\begin{pmatrix}\delta\mathrm{Re}\mathbf{B}^+ \\ \delta\mathrm{Im}\mathbf{B}^-\end{pmatrix}$$

$$\delta\mathrm{Re}\dot{\mathbf{B}}^- = \mathbf{1}\lambda^-\delta\mathrm{Re}\mathbf{B}^-$$

If M' is positive definite, we conclude that the solution is stable if in Eq.(4.58) $\lambda^- < 0$. This is fulfilled when $\epsilon > \epsilon_*$. Similarly, the second case yields a stable solution when $\lambda^+ < 0$, which happens for $\epsilon < -\epsilon_*$. As noted previously M' is positive definite when type-1 solutions are stable in $\epsilon \leq |\epsilon_*|$. Thus, existence of stable type-1 solutions in $\epsilon < |\epsilon_*|$ *guarantees* the stability of solutions 2 and 3 for $\epsilon \geq \epsilon_*$ and $\epsilon \leq -\epsilon_*$, respectively, cf. Fig.(4.5)(**a**).

On the other hand, for $\epsilon_* < 0$, where type-1 solutions are always unstable, solutions 2 and 3 are nevertheless stable, provided that M' is positive definite. This implies *bistability* of solutions 2 and 3 in the interval $\epsilon_* \leq \epsilon \leq -\epsilon_*$, cf. Fig.(4.5)(**b**).

Extrinsic Stability

A planform with n modes is extrinsically stable if it suppresses the growth of additional modes. As shown in [22] modes which are most likely to grow occur at intermediate angles $\alpha = \frac{\pi}{n}(\mathbb{Z} + \frac{1}{2})$, i.e. at half distance from the modes of the planform for which $\alpha_j = \frac{\pi}{n}j$. It is therefore sufficient to consider *intrinsic* stability of the particular planform with $2n$ modes

$$(\tilde{B}_0^{\pm}, \tilde{B}_1^{\pm}, \ldots, \tilde{B}_{2n-1}^{\pm}) := (B_0^{\pm}, 0, B_1^{\pm}, 0, \ldots, B_{n-1}^{\pm}, 0)$$

against fluctuations $\delta\tilde{B}_{2j}^{\pm} := \delta B_j^{\pm}$ and $\delta\tilde{B}_{2j+1}^{\pm} := \delta Z_j^{\pm}$, $j = 0, 1, \ldots, n-1$. Linearizing around this state one sees that the dynamics of the fluctuations $\delta B_j^{\pm}$ decouples from the dynamics of $\delta Z_j^{\pm}$. Whereas the dynamics of $\delta B_j^{\pm}$ is identical to Eq.(4.56), for $\delta\dot{Z}_j^{\pm}$ one finds

$$\delta\dot{Z}_j^{\pm} = \left[(1 \pm \epsilon) - 2\left(\mathcal{B}^{+2} + \mathcal{B}^{-2}\right)\sum_k \tilde{g}_{j,k} \mp 2\left(\mathcal{B}^{+2} - \mathcal{B}^{-2}\right)\sum_k \tilde{f}_{j,k}\cos\frac{4\pi}{n}(k-j-\frac{1}{2})\right]\delta Z_j^{\pm}$$

where

$$\begin{aligned}
\tilde{g}_{j,k} &= g(|\frac{\pi}{n}(k-j-\frac{1}{2})|) \\
\tilde{f}_{j,k} &= f(|\frac{\pi}{n}(k-j-\frac{1}{2})|)
\end{aligned}$$

Assuming intrinsic stability of the solution $(B_0^\pm, B_1^\pm, \ldots, B_{n-1}^\pm)$, the criterion for extrinsic stability becomes

$$(1 \pm \epsilon) - 2\left(\mathcal{B}^{+2} + \mathcal{B}^{-2}\right)\sum_k \tilde{g}_{j,k} \mp 2\left(\mathcal{B}^{+2} - \mathcal{B}^{-2}\right)\sum_k \tilde{f}_{j,k}\cos\frac{4\pi}{n}(k-j-\frac{1}{2}) < 0$$

or, since this expression does not explicitly depend on the index j,

$$(1 \pm \epsilon) - 2\left(\mathcal{B}^{+2} + \mathcal{B}^{-2}\right)\sum_k \tilde{g}_{0,k} \mp 2\left(\mathcal{B}^{+2} - \mathcal{B}^{-2}\right)\sum_k \tilde{f}_{0,k}\cos\frac{4\pi}{n}(k-\frac{1}{2}) < 0. \qquad (4.59)$$

In conclusion, stability of a solution under *extrinsic* perturbations requires that the solution is *intrinsically* stable and that, in addition, condition (4.59) is fulfilled.

Energies

Consistent with the strong interindividual variability of orientation maps in the brain, the dynamics Eq.(4.13) exhibits a potentially exceedingly high number of multistable solutions. The energy of essentially complex planforms can be calculated from Eq.(4.32). For type 1 solutions

$$E_n^{(I)} = -\frac{n}{2\sum_k g_{0k}}(1 + \epsilon^2/\epsilon_*), \qquad (4.60)$$

for solutions 2 and 3 the energy is given by

$$E_n^{(II)} = -\frac{n}{2\sum_k g_{0k}}\frac{(1+\epsilon)^2}{1+\epsilon_*} \qquad (4.61)$$

and

$$E_n^{(III)} = -\frac{n}{2\sum_k g_{0k}}\frac{(1-\epsilon)^2}{1+\epsilon_*}, \qquad (4.62)$$

respectively and does not depend on the variables l_j which identify a particular ECP. Due to the growth of antiparallel modes with increasing $|\epsilon|$ patterns for all different realizations l_j with phases $\phi_j := l_j\Phi_j + \frac{1}{4}(1 - \text{sign}(\epsilon))(1 - l_j)\pi$ (Φ_j arbitrary but fixed) eventually collapse in a single state $z(\mathbf{x}) \propto \sum_{j=0}^{n-1} z_j^{e/o}(\mathbf{x}, \phi_j)$ (Fig.4.2a).

4.8 Phase diagram

To answer how SSB affects pattern selection we calculated the phase diagram for the model specified in Eqns.(4.4-4.6) for various values of ϵ. To this end we calculated the energy of all

solutions found above, that is plane wave solutions, rhombic pinwheel crystals and generalized ECPs up to $n = 25$. For a dense mesh of parameter values in the (σ, g)-plane and fixed ϵ. From this comprehensive list of fixed point energies we obtained the energetic ground state of the model in different regions of the (σ, g)-plane. Fig. 4.6 shows the configurations of ECPs and rPWCs minimizing the energy. Plane waves are progressively replaced by rPWCs with increasing SSB. Depending on the location in parameter space and on ϵ, a particular angle α minimizes the energy (c.f. Fig. 4.1c). Large $n-$ECPs are selected when the dynamics is stabilized by long-range interactions ($g < 1$, $\sigma > \Lambda$). In this parameter regime plane waves and pinwheel crystals are unstable. The degree of SSB q manifested in a given $n-$ECP attractor depends on ϵ and on the location in the phase diagram. Above a critical line defined by $|\epsilon_*(n, g, \sigma)| = |\epsilon|$ antiparallel modes are maximal and $|q| = 1$ (*gray area*), below that line $|q| \leq 1$. Figs. 4.6 and 4.7 show the high sensitivity of the dynamics to even small amounts of SSB, a substantial area in phase is occupied by ECPs with $|q| = 1$ even for $\epsilon = 0.02$.

For the biologically most interesting quasi-periodic ECPs we also determined the regions in the (σ, g)-plane for which a fixed n-ECP is dynamically stable. To this end we used the criteria for extrinsic and intrinsic stability derived in Section 4.7 and calculated the corresponding stability matrices. Our results (shown in Fig. 4.7 for $n = 20$) reveal that the region of stability of an ECP covers a much larger portion of the (σ, g)-plane than the range in which it is the ground state. The overall shape and position of this stability region for large n was found to be insensitive to the strength of shift symmetry breaking.

4.9 Pinwheel Densities

The main impact of shift symmetry breaking on aperiodic pattern solutions is the collapse of multistability between different ECPs at the critical point ϵ_*. The bifurcation analysis given above established that this transition is continuous such that the different n-ECPs become gradually more similar with increasing ϵ until they are identical for $\epsilon = \epsilon_*$. It is thus an interesting question how statistical properties of the spatially irregular pinwheel layouts change with ϵ. To answer this question we calculate the pinwheel densities of essentially complex planforms for arbitrary degree of shift symmetry breaking. We consider the ensemble of solutions $z(\mathbf{x})$,

$$z(\mathbf{x}) \;\; = \;\; \sqrt{\frac{2}{n}} \sum_{j=0}^{n-1} e^{i\frac{2\pi}{n}j}[\sqrt{1+q}\cos(l_j\mathbf{k}_j\mathbf{x}+\phi_j) + i\sqrt{1-q}\sin(l_j\mathbf{k}_j\mathbf{x}+\phi_j)]$$

which is identical to the definition (4.54) up to the normalization factor, which we can freely choose for later convenience, since a rescaling of z does not affect the pinwheel configuration. Here, the phases ϕ_j are random variables, the n-tuple l_j which identifies the active modes of the planforms is held fixed and q denotes the degree of shift symmetry breaking. As shown in Section 3.11 the pinwheel density can be calculated from the joint probability distribution of the field and its gradient $p(z, \nabla z)$. We set, without loss of generality, $\mathbf{x} = 0$ and omit the argument
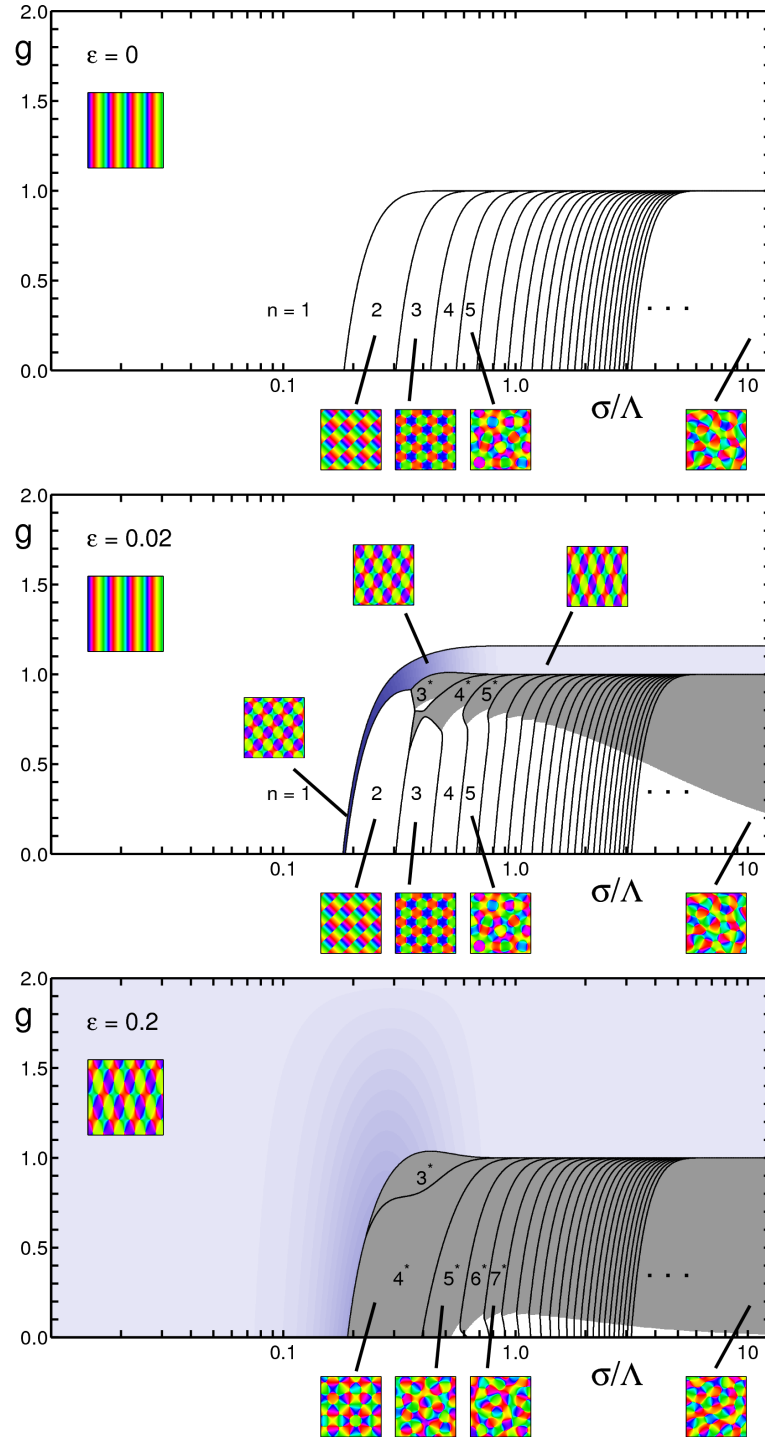
Figure 4.6: Phase diagrams of the model, Eqns.(4.4-4.6), near criticality for variable SSB ϵ. The graph shows the regions of the $g - \sigma/\Lambda$ plane in which n-ECPs and rPWCs have minimal energy ($n = 1 - 25$, $n > 25$ dots). Regions of maximally broken shift symmetry [$\epsilon \geq \epsilon_*(N, g, \sigma)$] shaded in *gray*. Regions where rPWCs prevail is shaded in *blue*, intensity level codes for the included angle α. *(light blue:* $\pi/4 \leq \alpha \leq \pi/2$ *:dark blue)*
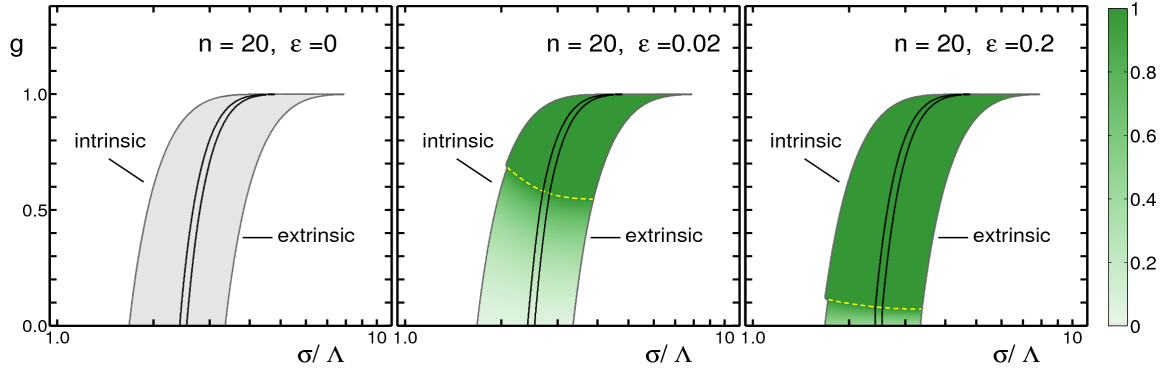
Figure 4.7: Stability regions of ECPs with $n = 20$ active modes. Depicted is the region in the $g - \sigma/\Lambda$ plane for which these planforms are a stable solution of the dynamics for $\epsilon = 0$, 0.02 and 0.2 and coexist with planforms of nearby n, e.g. $n - 1$, $n + 1$. Beyond that region the solution is unstable with respect to *intrinsic* or *extrinsic* perturbations, i.e. growth of additional modes or decaying of active modes, respectively. Inside of the region defined by the black lines the $n = 20$ solution minimizes the energy. For $\epsilon > 0$ the q values range in $[0, 1]$ as displayed by the green colorcode. Dashed yellow line denotes the critical line $\epsilon = \epsilon_*(N, g, \sigma)$, above which $q = 1$.

in the following, such that

$$z = \sqrt{\frac{2}{n}} \sum_{j=0}^{n-1} e^{i\frac{2\pi}{n}j}[\sqrt{1+q}\cos\phi_j + i\sqrt{1-q}\sin\phi_j]$$

$$\nabla z = \sqrt{\frac{2}{n}} \sum_{j=0}^{n-1} e^{i\frac{2\pi}{n}j}l_j\mathbf{k}_j[i\sqrt{1-q}\cos\phi_j - \sqrt{1+q}\sin\phi_j].$$

In the following we decompose z into its real and imaginary part, such that

$$z = R + i\,I.$$

For large n the distribution $p(z, \nabla z)$ can be approximated by a Gaussian

$$P(\mathbf{v}) = \frac{1}{(2\pi)^3\sqrt{\det W}} \exp\left(-\frac{1}{2}\mathbf{v}^T W^{-1}\mathbf{v}\right) \tag{4.63}$$

where

$$\mathbf{v} = (R, I, \partial_x R, \partial_y R, \partial_x I, \partial_y I)^T$$

and W denotes the corresponding covariance matrix

$$W_{ij} = \langle\mathbf{v}_i\mathbf{v}_j\rangle,$$

the average being performed over the angles ϕ_j. First we evaluate the moments involving just the fields, i.e.

$$
\begin{aligned}
\langle R^2 \rangle &= \frac{2}{n} \sum_{j=0}^{n-1} \sum_{k=0}^{n-1} \left\langle \left(\sqrt{1+q} \cos \phi_j \cos \frac{2\pi}{n} j - \sqrt{1-q} \sin \phi_j \sin \frac{2\pi}{n} j \right) \right. \\
&\quad \left. \times \left(\sqrt{1+q} \cos \phi_k \cos \frac{2\pi}{n} k - \sqrt{1-q} \sin \phi_k \sin \frac{2\pi}{n} k \right) \right\rangle \\
&= \frac{1}{n} \sum_{j=0}^{n-1} \sum_{k=0}^{n-1} (1+q) \cos \frac{2\pi}{n} j \, \cos \frac{2\pi}{n} k \, \delta_{jk} + (1-q)\delta_{jk} \sin \frac{2\pi}{n} j \, \sin \frac{2\pi}{n} k \\
&= 1
\end{aligned}
$$

where we used

$$
\langle \cos \phi_j \cos \phi_k \rangle = \frac{1}{2} \delta_{jk} = \langle \sin \phi_j \sin \phi_k \rangle
$$

and

$$
\langle \cos \phi_j \sin \phi_k \rangle = 0.
$$

Similarly, we obtain $\langle I^2 \rangle = 1$ and $\langle R\,I \rangle = 0$. For the moments which involve a single derivative we obtain

$$
\begin{aligned}
\langle R \, \nabla R \rangle &= 0 \\
\langle I \, \nabla I \rangle &= 0
\end{aligned}
$$

and

$$
\begin{aligned}
\langle R \, \nabla I \rangle &= \sqrt{1-q^2} \, \frac{1}{n} \sum_{j=0}^{n-1} \mathbf{k}_j l_j \\
&= \sqrt{1-q^2} \, \vec{\chi} \\
\langle I \, \nabla R \rangle &= -\langle R \, \nabla I \rangle
\end{aligned}
$$

which depend on the *planform anisotropy*,

$$
\vec{\chi} := \frac{1}{n} \sum_{j=0}^{n-1} l_j \mathbf{k}_j,
$$

a measure for how anisotropically the active modes $l_j \mathbf{k}_j$ are distributed on the critical circle. The modulus of $\vec{\chi}$ is small for an isotropic distribution of wavevectors $l_j \mathbf{k}_j$. Without loss of generality we can choose the coordinate system such that $\vec{\chi} = \chi \cdot (1,0)$, which implies that $\langle I \, \partial_y R \rangle$ and $\langle R \, \partial_y I \rangle$ vanish. An estimate for the upper bound on $\chi := |\vec{\chi}|$ for a given n can be given by considering the most anisotropic case, $l_j = 1 \; j = 0 \ldots n-1$, which for $q = 0$ corresponds to planforms where all active modes are distributed on a semicircle

$$
\begin{aligned}
\chi_n^{max} &= \frac{1}{n} \left| \sum_{j=0}^{n-1} \mathbf{k}_j \right| \\
&= \frac{k_c}{n} \left| \sum_{j=0}^{n-1} e^{i \frac{\pi}{n} j} \right| \\
&= \frac{k_c}{n} \left| \frac{2}{1 - e^{i \frac{\pi}{n}}} \right| \stackrel{n \to \infty}{\longrightarrow} 2/\pi \, k_c.
\end{aligned}
$$

For $k_c = |\mathbf{k}| = 1$, which is assumed in the following, $0 \leq \chi_n \leq 1$ since $\chi_n^{max} \leq \chi_1^{max} = k_c$. Note, however, that pinwheels only exist for $n \geq 2$ modes, such that in our case of interest the values of χ_n are actually bounded by

$$0 \leq \chi_n \leq \chi_2^{max} = \sqrt{1/2}.$$

Finally, the nonvanishing moments with two derivatives are

$$\langle (\partial_x R)^2 \rangle = \frac{1}{2} = \langle (\partial_y R)^2 \rangle = \langle (\partial_x I)^2 \rangle = \langle (\partial_y I)^2 \rangle.$$

All together the covariance matrix reads

$$
W \;\; = \;\;
\begin{bmatrix}
1 & . & . & . & \sqrt{1-q^2}\chi & . \\
. & 1 & -\sqrt{1-q^2}\chi & . & . & . \\
. & -\sqrt{1-q^2}\chi & 1/2 & . & . & . \\
. & . & . & 1/2 & . & . \\
\sqrt{1-q^2}\chi & . & . & . & 1/2 & . \\
. & . & . & . & . & 1/2
\end{bmatrix}
$$

The pinwheel density is obtained as described in 3.11 by calculating the expectation value of

$$\rho = \langle \delta(z) | \partial_x R \, \partial_y I - \partial_y R \, \partial_x I | \rangle$$

with respect to the probability density $P(\mathbf{v})$, Eq.(4.63). The average can be performed using polar coordinates,

$$\partial_x R = r \cos\theta, \; \partial_x I = r \sin\theta,$$

$$\partial_y R = s \cos\psi, \; \partial_y I = s \sin\psi$$

and yields the result

$$\hat{\rho}(\chi_n) := \rho(\chi_n)\Lambda^2 = \pi\sqrt{1 - 2(1-q^2)\chi_n^2} \tag{4.64}$$

where $\Lambda = 2\pi/k_c = 2\pi$ denotes the typical wavelength of the pattern.

Distribution of Planform Anisotropies

The energies of essentially complex planforms, however, do not depend on the planform anisotropy. Since they are degenerate with respect to the n-tuple $l = (l_0, \ldots l_{n-1})$, each of the 2^n possible sets occurs with the same likelihood. What can we say about the resulting distribution of $\vec{\chi}$? In the large n limit it can be approximated by a Gaussian distribution with mean zero, since

$$
\begin{aligned}
\langle \vec{\chi}_n \rangle \;\; &= \;\; \frac{1}{n} \sum_{j=0}^{n-1} \langle l_j \, \mathbf{k}_j \rangle \\
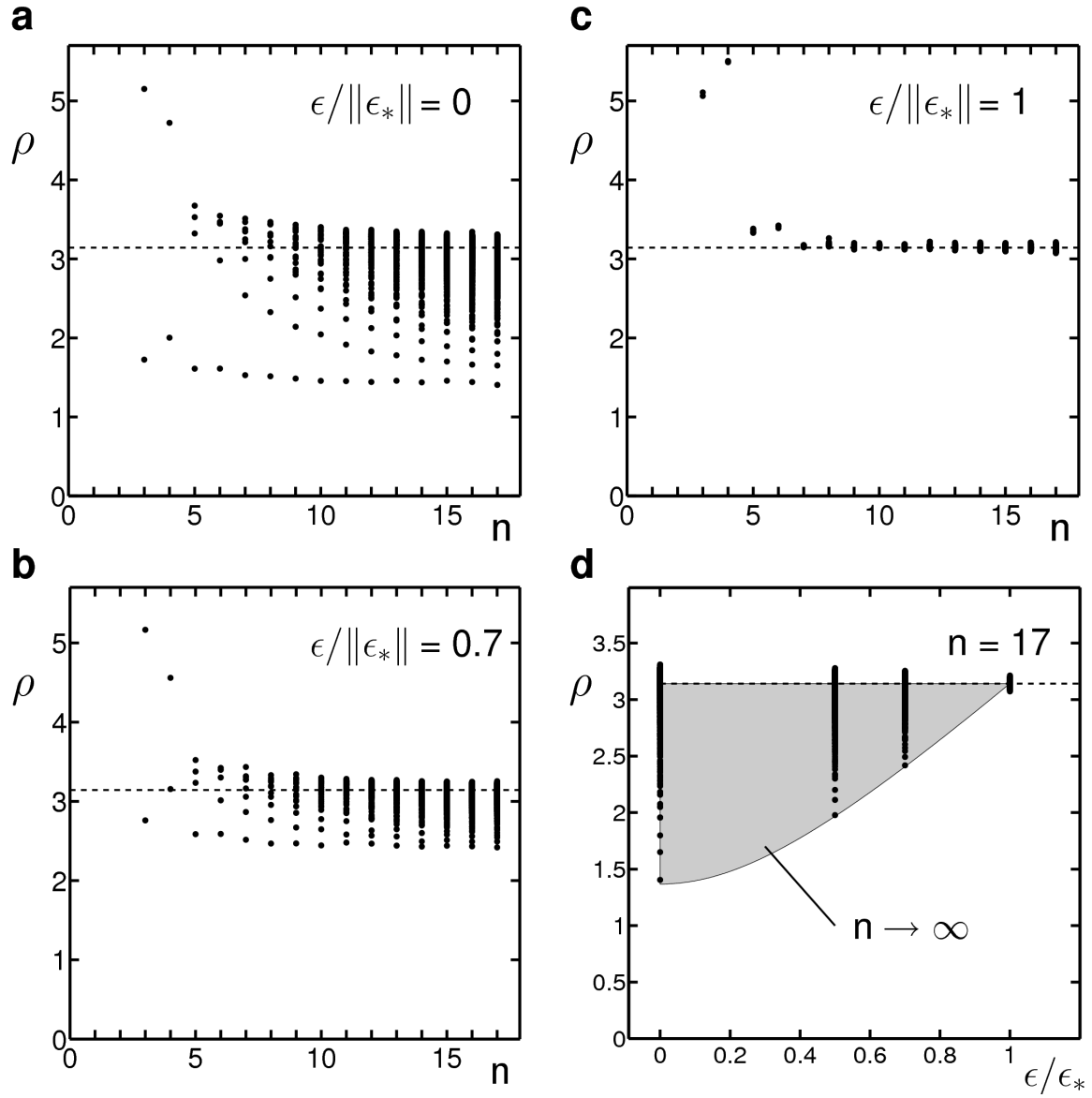&= \;\; 0
\end{aligned}
$$

Figure 4.8: (a)-(c) Pinwheel densities for all realizations of ECPs with $3 \leq n \leq 17$ and different degrees of shift symmetry breaking ϵ. **(d)** Pinwheel densities for $n = 17$ *(dots)* and for $n \rightarrow \infty$ in the Gaussian approximation *(gray region)*.

and variance

$$
\begin{aligned}
\sigma_n^2 &= \langle \|\vec{\chi}_n - \langle \vec{\chi}_n \rangle \| \rangle^2 \\
&= \langle \|\vec{\chi}_n\|^2 \rangle \\
&= \frac{1}{n^2} \sum_{j,j'=0}^{n-1} \langle l_j l_{j'} \rangle \langle \mathbf{k}_j \mathbf{k}_{j'} \rangle \\
&= \frac{1}{n}
\end{aligned}
$$

As a consequence the modulus $\chi_n := \|\vec{\chi}_n\|$ is distributed according to

$$
\begin{aligned}
P_\chi(\chi_n) &= \frac{2\chi_n}{\sigma_n^2} e^{-\frac{\chi_n^2}{\sigma_n^2}} &\qquad (4.65) \\
&= 2n\chi_n \, e^{-n\,\chi_n^2} &\qquad (4.66)
\end{aligned}
$$

Using Eq.(4.64) it is possible to express χ_n in terms of ρ_n

$$
\chi_n = \frac{1}{\pi} \sqrt{\frac{\pi^2 - \rho_n^2}{2(1-q^2)}}
$$

such that

$$
\left| \frac{d\chi_n}{d\rho_n} \right| = \frac{\rho_n}{\pi} (2(\pi^2 - \rho_n^2)(1-q^2))^{-\frac{1}{2}}
$$

Together with Eq.(4.65) one obtains for the probability density of ρ_n

$$
\begin{aligned}
P_\rho(\rho_n) &= P_\chi\left(\chi_n(\rho_n)\right) \left| \frac{d\chi_n}{d\rho_n} \right| \\
&= \frac{\rho_n}{\pi^2(1-q^2)\sigma_n^2} e^{-\frac{\pi^2 - \rho_n^2}{2\pi^2(1-q^2)\sigma_n^2}}
\end{aligned}
$$

which has the mean value

$$
\begin{aligned}
\langle \rho_n \rangle &= \int_0^\pi d\rho_n \rho_n P(\rho_n) \\
&= \pi - \frac{\pi^{\frac{3}{2}}\sqrt{1-q^2} \, e^{-\frac{n}{2(1-q^2)}} \, \Phi_i\left(\sqrt{\frac{n}{2(1-q^2)}}\right)}{\sqrt{2n}}
\end{aligned}
$$

where Φ_i denotes the imaginary part of the error function. For the second moment we obtain

$$
\begin{aligned}
\langle \rho_n^2 \rangle &= \int_0^\pi d\rho_n \rho_n^2 P(\rho_n) \\
&= \pi^2 - \pi^2 \frac{2(1-q^2)(1 - e^{-\frac{n}{2(1-q^2)}})}{n}
\end{aligned}
$$

Furthermore, for large n (and also for $|q| \to 1$) the variance of ρ_n tends to zeros,

$$
\lim_{n\to\infty} \left(\langle \rho_n^2 \rangle - \langle \rho_n \rangle^2 \right) = 0
$$

since

$$\lim_{n \to \infty} \langle \rho_n \rangle = \pi,$$

which means that values ρ_n are sharply peaked around π for sufficiently large n. Also, since

$$0 \leq \chi_n \leq \frac{1}{n} \left| \frac{2}{1 - e^{i\frac{\pi}{n}}} \right| := \chi_n^{max}$$

and

$$\lim_{n \to \infty} \chi_n^{max} = \frac{2}{\pi}$$

one obtains the following estimate for the range of observable pinwheel densities

$$\pi \sqrt{1 - \frac{8}{\pi^2}(1 - q^2)} \leq \lim_{n \to \infty} \rho_n \leq \pi.$$

This predicted range of pinwheel densities agrees well with densities numerically calculated from ECPs. Figure 4.8 depicts that the range of pinwheel densities found for different planforms continuously shrinks with increasing strength of shift symmetry breaking and collapses to a single unique pinwheel density at $\epsilon = \epsilon_*$.

4.10 Appendix: Rhombic Pinwheel Crystals

The equations of motion of the four complex amplitudes read

$$\dot{A}_0 = A_0 + \epsilon \bar{A}_{0-} e^{-2i\alpha} - A_0 \left(g(0) \left[|A_0|^2/2 + |A_{0-}|^2 \right] + g(\alpha) \left[|A_1|^2 + |A_{1-}|^2 \right] \right) - 2\bar{A}_{0-} f(\alpha) A_1 A_{1-}$$

$$\dot{A}_1 = A_1 + \epsilon \bar{A}_{1-} e^{2i\alpha} - A_1 \left(g(0) \left[|A_1|^2/2 + |A_{1-}|^2 \right] + g(\alpha) \left[|A_0|^2 + |A_{0-}|^2 \right] \right) - 2\bar{A}_{1-} f(\alpha) A_0 A_{0-}$$

$$\dot{A}_{0-} = A_{0-} + \epsilon \bar{A}_0 e^{-2i\alpha} - A_{0-} \left(g(0) \left[|A_{0-}|^2/2 + |A_0|^2 \right] + g(\alpha) \left[|A_1|^2 + |A_{1-}|^2 \right] \right) - 2\bar{A}_0 f(\alpha) A_1 A_{1-}$$

$$\dot{A}_{1-} = A_1 + \epsilon \bar{A}_1 e^{2i\alpha} - A_{1-} \left(g(0) \left[|A_{1-}|^2/2 + |A_1|^2 \right] + g(\alpha) \left[|A_0|^2 + |A_{0-}|^2 \right] \right) - 2\bar{A}_1 f(\alpha) A_0 A_{0-}$$

With the ansatz (4.22) they can be written

$$\dot{a} + i\dot{\mu}_0 a = a + \epsilon a e^{-i(\mu_0 + \nu_0 + 2\alpha)} - a^3 \left(3g(0)/2 + 2g(\alpha) \right) - 2a^3 e^{i(\mu_1 + \nu_1 - \mu_0 - \nu_0)} f(\alpha) \quad (4.67)$$

$$\dot{a} + i\dot{\mu}_1 a = a + \epsilon a e^{-i(\mu_1 + \nu_1 - 2\alpha)} - a^3 \left(3g(0)/2 + 2g(\alpha) \right) - 2a^3 e^{i(\mu_0 + \nu_0 - \mu_1 - \nu_1)} f(\alpha)$$

$$\dot{a} + i\dot{\nu}_0 a = a + \epsilon a e^{-i(\mu_0 + \nu_0 + 2\alpha)} - a^3 \left(3g(0)/2 + 2g(\alpha) \right) - 2a^3 e^{i(\mu_1 + \nu_1 - \mu_0 - \nu_0)} f(\alpha)$$

$$\dot{a} + i\dot{\nu}_1 a = a + \epsilon a e^{-i(\mu_1 + \nu_1 - 2\alpha)} - a^3 \left(3g(0)/2 + 2g(\alpha) \right) - 2a^3 e^{i(\mu_0 + \nu_0 - \mu_1 - \nu_1)} f(\alpha)$$

We introduce the abbreviation

$$\Sigma_0 = \mu_0 + \nu_0, \quad \Sigma_1 = \mu_1 + \nu_1$$

$$\Delta_0 = \mu_0 - \nu_0, \quad \Delta_1 = \mu_1 - \nu_1$$

A decomposition of Eqns.4.67 into the real and imaginary part yields two distinct equations for the amplitude

$$\dot{a} = a + \epsilon a \cos(\Sigma_0 + 2\alpha) - a^3 \left(3g(0)/2 + 2g(\alpha) \right) - 2a^3 \cos(\Sigma_1 - \Sigma_0) f(\alpha) \quad (4.68)$$

$$\dot{a} = a + \epsilon a \cos(\Sigma_1 - 2\alpha) - a^3 \left(3g(0)/2 + 2g(\alpha) \right) - 2a^3 \cos(\Sigma_1 - \Sigma_0) f(\alpha)$$

and the phase dynamics

$$
\begin{aligned}
\dot{\Sigma}_0 &= -2\epsilon \sin(\Sigma_0 + 2\alpha) - 4a^2 \sin(\Sigma_1 - \Sigma_0) f(\alpha) \\
\dot{\Sigma}_1 &= -2\epsilon \sin(\Sigma_1 - 2\alpha) + 4a^2 \sin(\Sigma_1 - \Sigma_0) f(\alpha) \\
\dot{\Delta}_0 &= 0 \\
\dot{\Delta}_1 &= 0
\end{aligned}
\tag{4.69}
$$

In order for (4.68) to yield a consistent set of equations the phase variables have to obey particular relations which are discussed next.

Case 1: $\epsilon = 0$

For the case $\epsilon = 0$ we find from Eqns.(4.69)

$$
\begin{aligned}
d/dt \, (\Sigma_1 - \Sigma_0) &= 8a^2 \sin(\Sigma_1 - \Sigma_0) f(\alpha) \\
d/dt \, (\Sigma_1 + \Sigma_0) &= 0
\end{aligned}
\tag{4.70}
$$

which states that the sum $\Sigma_1 + \Sigma_2 = \mu_0 + \nu_0 + \mu_1 + \nu_1$ of all phases is constant and $\Sigma_1 = \Sigma_0 + \pi$ is a stable fixed-point. The stationary amplitude, obtained from Eq.(4.68) is

$$
a^2 = 1/\left(3g(0)/2 + 2g(\alpha) - 2f(\alpha)\right)
\tag{4.71}
$$

and the general solution then reads

$$
z(\mathbf{x}) = 2ae^{i\Sigma_0/2} \left[\cos(\mathbf{k}_0\mathbf{x} + \Delta_0/2) + i \, \cos(\mathbf{k}_1\mathbf{x} + \Delta_1/2)\right]
$$

or with a redefinition of Δ_1 (since it can assume any value)

$$
z(\mathbf{x}) = 2ae^{i\Sigma_0/2} \left[\cos(\mathbf{k}_0\mathbf{x} + \Delta_0/2) + i \, \sin(\mathbf{k}_1\mathbf{x} + \Delta_1/2)\right]
\tag{4.72}
$$

Here the quantities $\Sigma_1, \Delta_1, \Delta_2$ are arbitrary and $z(\mathbf{x})$ is essentially complex, e.g. there is no combination of $\Sigma_1, \Delta_1, \Delta_2$ for which $z(\mathbf{x}) \in \mathbb{R} \;\; \forall \mathbf{x}$.

Case 2: $\epsilon \neq 0$

For $\epsilon \neq 0$ consistency of Eqns.(4.69) requires $\Sigma_1 - 2\alpha = \pm(\Sigma_0 + 2\alpha) + 2\pi \, \mathbb{Z}$. The phase dynamics (4.69) then reads

$$
\begin{aligned}
\dot{\Sigma}_0 &= -2\epsilon \sin(\Sigma_0 + 2\alpha) - 4a^2 f(\alpha) \sin(2\alpha \pm (\Sigma_0 + 2\alpha) - \Sigma_0) \\
\dot{\Sigma}_1 &= \mp 2\epsilon \sin(\Sigma_0 + 2\alpha) + 4a^2 f(\alpha) \sin(2\alpha \pm (\Sigma_0 + 2\alpha) - \Sigma_0)
\end{aligned}
\tag{4.73}
$$

which, for '+' yields

Positive sign:

$$\dot{\Sigma}_0 = -2\epsilon \sin(\Sigma_0 + 2\alpha) - 4a^2 f(\alpha) \sin(4\alpha)$$
$$\dot{\Sigma}_0 = -2\epsilon \sin(\Sigma_0 + 2\alpha) + 4a^2 f(\alpha) \sin(4\alpha)$$

which is consistent only when $\sin(4\alpha) = 0$, i.e. when $\alpha = \pi/4$ or $\alpha = \pi/2$. In both cases the dynamics of Σ_0 states

$$\dot{\Sigma}_0 = -2\epsilon \sin(\Sigma_0 + 2\alpha)$$

a) For $\alpha = \pi/4$ we get

$$\dot{\Sigma}_0 = -2\epsilon \cos \Sigma_0$$

which is stable at $\Sigma_0 = \pi/2 \operatorname{sign} \epsilon$. In that case $\Sigma_1 = 4\alpha + \Sigma_0 + 2\pi \, \mathbb{Z}$ and the stationary amplitude is given by the solution to

$$0 = a(1 - |\epsilon|) - a^3 \left(2g(\alpha) + 3g(0)/2 - 2f(\alpha)\right)$$

that is,

$$a^2 = (1 - |\epsilon|)/ \left(2g(\alpha) + 3g(0)/2 - 2f(\alpha)\right)$$

or

$$a^2 = \frac{1}{2(g(0)/2 + g(\alpha))} \frac{1 - |\epsilon|}{1 + \epsilon_*}$$

with the general definition of ϵ_* for $n = 2$ and arbitrary angle α

$$\epsilon_* = \frac{g(0)/2 + 2f(\alpha) \cos 4\alpha}{g(0) + 2g(\alpha)}$$

b) For $\alpha = \pi/2$ we get

$$\dot{\Sigma}_0 = 2\epsilon \sin \Sigma_0$$

which is stable at $\Sigma_0 = \pi$ for $\epsilon > 0$ and at $\Sigma_0 = 0$ for $\epsilon < 0$. The stationary amplitude is

$$0 = a + \epsilon a \cos(\Sigma_0 + 2\alpha) - a^3 \left(2g(\alpha) + 3g(0)/2 + 2f(\alpha) \cos(\Sigma_0 - \Sigma_1)\right)$$
$$= a(1 + |\epsilon|) - a^3 \left(2g(\alpha) + 3g(0)/2 + 2f(\alpha)\right)$$

or

$$a^2 = (1 + |\epsilon|)/ \left(2g(\alpha) + 3g(0)/2 + 2f(\alpha)\right)$$

or

$$a^2 = \frac{1}{2(g(0)/2 + g(\alpha))} \frac{1 + |\epsilon|}{1 + \epsilon_*}$$

Negative sign:

The more general case, however, which comes with a continuum of angles α, is obtained for the '-' sign in Eq.(4.73), for which $\Sigma_1 = -\Sigma_0 \mod 2\pi$ and

$$\dot{\Sigma}_0 = -2\epsilon \sin(\Sigma_0 + 2\alpha) + 4a^2 f(\alpha) \sin(2\Sigma_0)$$

Stationarity implies

$$a^2 = \frac{\epsilon \sin(\Sigma_0 + 2\alpha)}{2f(\alpha)\sin(2\Sigma_0)}$$

On the other hand, Eq.(4.68) provides an additional equation for the stationary state

$$a^2 = \frac{1 + \epsilon \cos(\Sigma_0 + 2\alpha)}{2g(\alpha) + 3g(0)/2 + 2f(\alpha)\cos(\Sigma_0 - \Sigma_1)} \tag{4.74}$$

Equating both expressions for a^2 we obtain an implicit equation for Σ_0

$$0 = \sin(2\Sigma_0) + \epsilon \left(\sin(\Sigma_0 - 2\alpha) - (2 + \frac{3g(0)}{2g(\alpha)})\sin(\Sigma_0 + 2\alpha) \right) \tag{4.75}$$

For $\epsilon \to 0$ one finds $\Sigma_0 \to 0, \pm\pi/2, \pm\pi$ among which only the solutions $\Sigma_0 = \pm\pi/2$ are stable fixed-points of the phase dynamics. We will restrict our analysis to those two cases. It turns out that energetically $\Sigma_0 = -\pi/2$ is favored for $\epsilon > 0$, whereas $\Sigma_0 = \pi/2$ is favored for $\epsilon < 0$. In order to find solutions to Eq.4.75 for the general case $\epsilon \neq 0$ we used a perturbation series expansion in ϵ or reverted to numerical methods.

The general solution then reads

$$z(\mathbf{x}) = 2a \left(e^{i\Sigma_0/2} \cos(\mathbf{k}_0\mathbf{x} + \Delta_0/2) + e^{i\Sigma_1/2} \cos(\mathbf{k}_1\mathbf{x} + \Delta_1/2) \right)$$

or, after replacing $\Sigma_1 = -\Sigma_0 + 2\pi \mathbb{Z}$ and a redefinition of the arbitrary phases Δ_1 and Δ_2

$$z(\mathbf{x}) = 2a \left(e^{i\Sigma_0/2} \cos(\mathbf{k}_0\mathbf{x} + \Delta_0/2) + e^{-i\Sigma_0/2} \sin(\mathbf{k}_1\mathbf{x} + \Delta_1/2) \right) \tag{4.76}$$

For small $|\epsilon| \ll 1$, where $\Sigma_0 \approx -\text{sign}\ \epsilon\pi/2$, the solution $z(\mathbf{x})$ is essentially complex since

$$z(\mathbf{x}) \approx 2a\ e^{i(-\text{sign}\ \epsilon)\pi/4} \left(\cos(\mathbf{k}_0\mathbf{x} + \Delta_0/2) + i\sin(\mathbf{k}_1\mathbf{x} + \Delta_1/2) \right),$$

This corresponds to Eq.(4.71) for the case $\Sigma_0 = -\text{sign}\ \epsilon\pi/2$, because in the limit $\epsilon \to 0$ from Eq.(4.74) we find

$$a^2 = \frac{1}{2g(\alpha) + 3g(0)/2 + 2f(\alpha)\cos(2\Sigma_0)} \to \frac{1}{2g(\alpha) + 3g(0)/2 - 2f(\alpha)}$$

Stability analysis

In oder to show that the solutions Eq.(4.76) are linearly stable, one has to check the stability under *intrinsic* and *extrinsic* perturbations.

a) Intrinsic perturbations arise within the set of active modes, i.e.

$$(A_0, A_1, A_{0-}, A_{1-}) \rightarrow (A_0 + \delta A_0, A_1 + \delta A_1, A_{0-} + \delta A_{0-}, A_{1-} + \delta A_{1-})$$

around the stationary state which was defined by

$$A_0 = a\, e^{i\mu_0}, \; A_1 = a\, e^{i\mu_1}, \; A_{0-} = a\, e^{i\nu_0}, \; A_{1-} = a\, e^{i\nu_1}$$

where Σ_0 is the solution to Eq.(4.75) and $a = (2g(\alpha) + 3g(0)/2 + 2f(\alpha)\cos(2\Sigma_0))^{-\frac{1}{2}}$. Since $\Sigma_1 = -\Sigma_0$ we have

$$\mu_0 = \frac{1}{2}(\Sigma_0 + \Delta_0) \qquad \nu_0 = \frac{1}{2}(\Sigma_0 - \Delta_0)$$

$$\mu_1 = \frac{1}{2}(\Delta_1 - \Sigma_0) \qquad \nu_1 = -\frac{1}{2}(\Sigma_0 + \Delta_1),$$

Δ_0 and Δ_1 are arbitrary phases.

$$
\begin{aligned}
\delta\dot{\mathbf{A}}_{\mathbf{0}} = & \left(1 - 2a^2\left(g(0) + 2g(\alpha)\right)\right)\delta\mathbf{A}_{\mathbf{0}} - a^2\left(2f(\alpha)e^{i(\nu_1 - \nu_0)} + g(\alpha)e^{i(\mu_0 - \mu_1)}\right)\delta\mathbf{A}_{\mathbf{1}} \\
& -a^2 g(0)e^{i(\mu_0 - \nu_0)}\delta\mathbf{A}_{\mathbf{0-}} - a^2\left(g(\alpha)e^{i(\mu_0 - \nu_1)} + 2f(\alpha)e^{i(\mu_1 - \nu_0)}\right)\delta\mathbf{A}_{\mathbf{1-}} \\
& -a^2 g(0)/2e^{2i\mu_0}\delta\bar{\mathbf{A}}_{\mathbf{0}} - a^2 g(\alpha)e^{i(\mu_1 + \mu_0)}\delta\bar{\mathbf{A}}_{\mathbf{1}} \\
& \left(\epsilon e^{2i\alpha} - a^2 g(0)e^{i(\mu_0 + \nu_0)} - 2f(\alpha)a^2 e^{i(\mu_1 + \nu_1)}\right)\delta\bar{\mathbf{A}}_{\mathbf{0-}} - a^2 g(\alpha)e^{i(\mu_0 + \nu_1)}\delta\bar{\mathbf{A}}_{\mathbf{1-}} \; (4.77)
\end{aligned}
$$

The corresponding equations for $\delta\dot{A}_1, \delta\dot{A}_{0-}, \delta\dot{A}_{1-}$ are obtained from Eq.(4.77) by the replacements

$$
\begin{aligned}
\delta\dot{A}_1 : \quad & (\mu_0, \mu_1, \nu_0, \nu_1 \leftrightarrow \mu_1, \mu_0, \nu_1, \nu_0) \text{ and } (A_0, A_1, A_{0-}, A_{1-} \leftrightarrow A_1, A_0, A_{1-}, A_{0-}) \\
\delta\dot{A}_{0-} : \quad & (\mu_0, \mu_1, \nu_0, \nu_1 \leftrightarrow \nu_0, \nu_1, \mu_0, \mu_1) \text{ and } (A_0, A_1, A_{0-}, A_{1-} \leftrightarrow A_{0-}, A_{1-}, A_0, A_1) \\
\delta\dot{A}_{1-} : \quad & (\mu_0, \mu_1, \nu_0, \nu_1 \leftrightarrow \nu_1, \nu_0, \mu_1, \mu_0) \text{ and } (A_0, A_1, A_{0-}, A_{1-} \leftrightarrow A_{1-}, A_{0-}, A_1, A_0)
\end{aligned}
$$

The equations for $\delta\dot{\bar{A}}_0, \delta\dot{\bar{A}}_1, \delta\dot{\bar{A}}_{0-}, \delta\dot{\bar{A}}_{1-}$ are obtained from the previous ones after complex conjugation. Linear stability with respect to intrinsic perturbations is given when the resulting 8×8 matrix only exhibits eigenvalues with negative real parts.

b) The stationary state is stable against extrinsic perturbations, when the growth of any additional mode is suppressed. Assuming the test mode $Be^{i\mathbf{kx}}$ has a wavevector $k = k_c(\cos\beta, \sin\beta)$. When $\epsilon \neq 0$ we also have to take into account the dynamics of the opposite mode B_- to close the system of equations. The linearized dynamics of B and B_- in the vicinity of a stationary pinwheel crystal solution $(a, \mu_0, \mu_1, \nu_0, \nu_1)$ and $B = 0 = B_-$ hence reads

$$
\begin{aligned}
\dot{B} = & (B + \epsilon\bar{B}_- e^{4i\beta} - 2a^2 B\left(g(\beta + \alpha/2) + g(\beta - \alpha/2)\right) \\
& -2a^2\bar{B}_-\left(f(\beta + \alpha/2)e^{i(\mu_0 + \nu_0)} + f(\beta - \alpha/2)e^{i(\mu_1 + \nu_1)}\right)
\end{aligned}
$$

$$
\begin{aligned}
\dot{B}_- = & (B_- + \epsilon\bar{B}e^{4i\beta} - 2a^2 B_-\left(g(\beta + \alpha/2) + g(\beta - \alpha/2)\right) \\
& -2a^2\bar{B}\left(f(\beta + \alpha/2)e^{i(\mu_0 + \nu_0)} + f(\beta - \alpha/2)e^{i(\mu_1 + \nu_1)}\right)
\end{aligned}
$$

$$
\begin{pmatrix} \dot{B} \\ \dot{B}_- \\ \dot{\bar{B}} \\ \dot{\bar{B}}_- \end{pmatrix} = \begin{pmatrix} x & \cdot & \cdot & y \\ \cdot & x & y & \cdot \\ \cdot & \bar{y} & x & \cdot \\ \bar{y} & \cdot & \cdot & x \end{pmatrix} \begin{pmatrix} B \\ B_- \\ \bar{B} \\ \bar{B}_- \end{pmatrix}
$$

with

$$
\begin{aligned}
x &= 1 - 2a^2 \left(g(\beta + \alpha/2) + g(\beta - \alpha/2) \right) \\
y &= \epsilon e^{4i\beta} - 2a^2 \left(f(\beta + \alpha/2) e^{i(\mu_0 + \nu_0)} + f(\beta - \alpha/2) e^{i(\mu_1 + \nu_1)} \right)
\end{aligned}
$$

The criterion for extrinsic stability thus states that the two degenerate eigenvalues $\lambda_\pm = x \pm |y|$ have to be negative for all angles β.

5 The Taming of the Shrew

> Tree shrews have the highest brain to body mass ratio of any animal, even higher than humans.
>
> *(Wikipedia, Feb.2008)*

5.1 Overview

The previous two chapters gave us an understanding of the impact that shift-twist symmetry is predicted to have in models of visual cortical development. In Chapter 3, we found that shift-twist symmetry is predicted to lead to a four-fold angular modulation of the two point statistics of the pattern of preferred orientations and that these can be assessed by the correlation function C_2 and the orientation cooccurrence histogram. We analyzed the mathematical structure of orientation cooccurence histograms and found that they can also exhibit a two-fold component in general. Such a two-fold component, however, can only occur in a non-Gaussian ensemble. In Chapter 4 we found that dynamical models of visual cortical pattern formation are highly sensitive to broken shift symmetry and that already the presence of very weak terms consistent with shift-twist symmetry are predicted to strongly impact on the statistics of the emerging patterns.

It is thus time to ask whether the predicted signatures of shift-twist symmetry can be empirically verified in the structure of actual visual cortical maps. Answering this question is the topic of the current chapter. We will analyze a large dataset of orientation preference maps recorded in the tree shrew visual cortex. From these data we will calculate the two correlation functions, C_1 and C_2, and the orientation cooccurrence histogram P and quantify their four- and two-fold angular dependence.

We find that there are statistically highly significant signatures of shift-twist symmetry in the layout of the tree shrew maps:

1. Shift symmetry breaking in the brain is found to be of negative type.

2. We find clear deviations of the map statistics from Gaussianity indicated by a substantial two-fold component of the orientation cooccurrence histogram.

3. The absolute strength of shift symmetry breaking appears to be relatively weak, such that shift symmetric models can be considered a valuable approximation.

For all quantities estimated from the experimental data we provide confidence intervals and significance values based on custom designed nonparametric permutation tests.
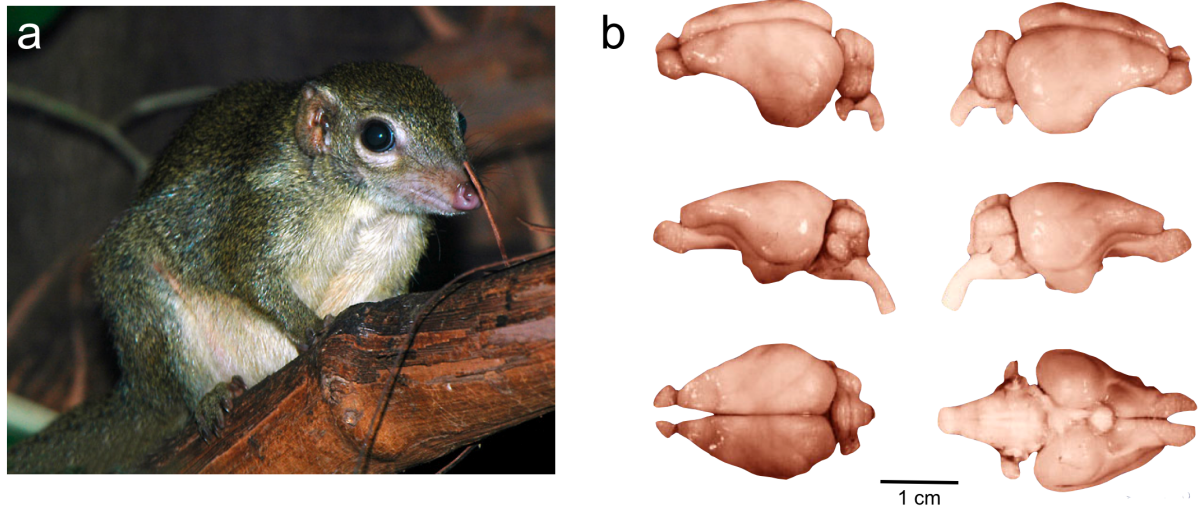
Figure 5.1: (**a**) Tree shrew (*tupaia glis*) and (**b**) its brain (adapted from the brain collection, University of Madison: www.brainmuseum.org).

5.2 Biological Background

The tree shrew is a small, highly visual mammal indigenous to Southeast Asia. Superficially it displays similarities to the squirrel in its external appearance and behaviour (Fig. 5.1). However, while squirrels are rodents, tree shrews are assigned to an order of their own, Scandentia, and are more closely related to primates than rodents [60, 61, 62, 63, 64]. The visual system of the tree shrew has been well studied, anatomically and electro-physiologically [65, 66, 67, 68, 60], and in recent years ongoing research has added important new insights into the functional architecture of its visual cortex by the use of optical imaging techniques and advanced tracing methods [27, 69, 70, 71]. In the following we give a summary of basic facts relevant in the context of our study.

Tree shrews have large, laterally oriented eyes and a binocular visual field of $60°$ [63, 65]. Their primary visual cortex is located at the occipital poles of each brain hemisphere and can be divided into a dorsal and a ventral part: The central, binocular portion of the contralateral visual hemifield ($\approx 0 - 30°$) is represented on the dorsal surface, whereas the remaining part on the ventral surface represents the monocular portion of the contralateral visual hemifield ($\approx 30° - 150°$) and is driven by stimuli to the contralateral eye [65, 60]. Electro-physiological recordings revealed sharp orientation tuning in neurons of layer 2/3 . The selectivities of neurons for orientation and for visual stimulus position are topographically arranged in two cortical maps, the orientation map and visuotopic map, both of which can been obtained using optical imaging [27, 69, 70]. Depicted in Fig.2.1(**a**) are the cortical responses to whole field gratings of four orientation ($0°$, $45°$, $90°$, $135°$), which are combined into an orientation map in Fig.2.1(**b**). The optical imaging signal undergoes a sharp transition along a line in rostro-medial direction, which corresponds to the V1/V2 border as revealed by Nissl staining in [69]. The visuotopic map was first imaged by Bosking et al. [27] (shown in Fig. 2.7(**a**)) which confirmed previous electro-physiological recordings by Kaas et al. [65], indicating that the central visual field is mapped onto the cortical surface in a relatively undistorted and isotropic manner. Note that
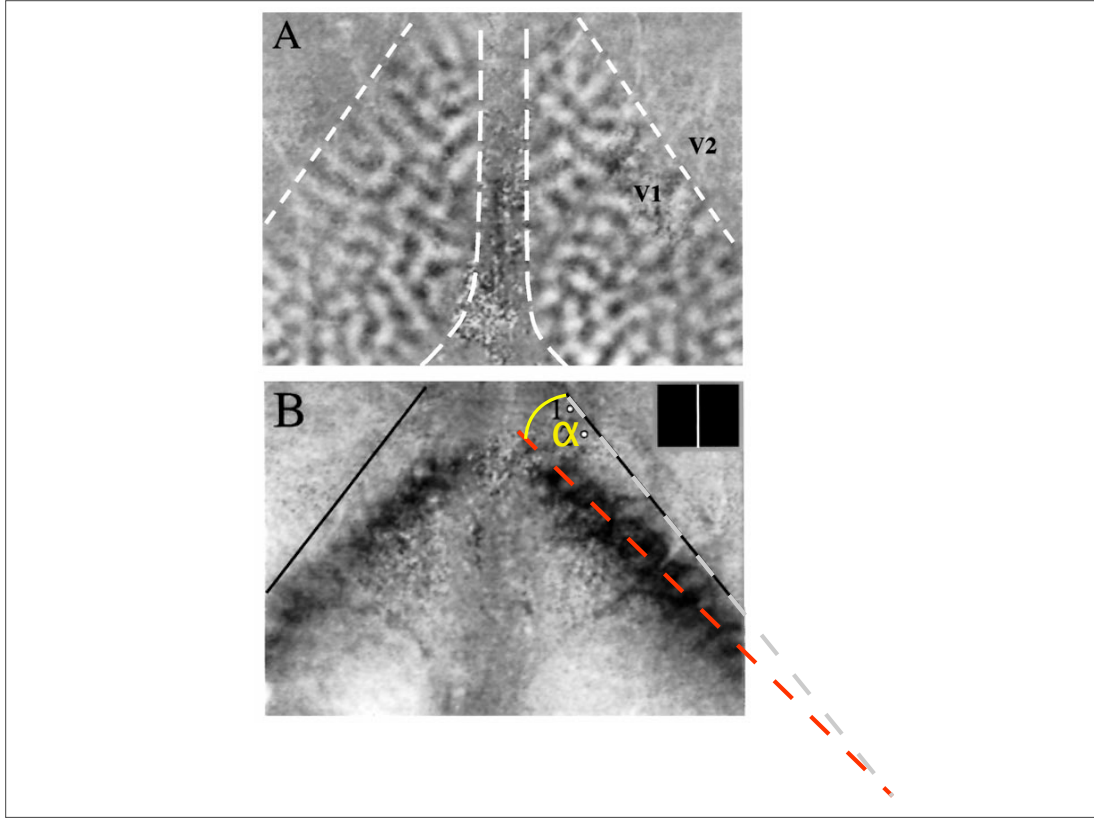
Figure 5.2: (a) Relative orientation of V1/V2 border and the representation of the vertical meridian. (**A**) Orientation column pattern in a pair of left and right hemispheres in tree shrew. Dotted straight lines represent the V1/V2 borders. (**B**) Activity pattern elicited by a long bar aligned with the vertical meridian. The angle is approximately 5°. (*adapted from* [69].)

since only the dorsal part of the visual cortex is accessible to optical imaging the imaged region only comprises the central, binocular part of the visual field. A subsequent study, again by Bosking et al. [69], provided a refined picture: Simultaneous optical imaging of both hemispheres allowed to delineate the representation of the lower part of the vertical meridian, which was found to be tilted with respect to the V1/V2 border. It thus does not coincide with the V1/V2 border itself, as previously believed. Rather, this study revealed a compressed representation of the *ipsilateral* visual field in the cortical area between the V1/V2 border and the representation of the vertical meridian (see Fig. 5.2). A further study by Bosking et al. [70] confirmed that the central visual field representation is essentially isotropic and provided the following estimates of the cortical magnification factor: $206 \mu m/°$ for the vertical and $174 \mu m/°$ for the horizontal direction. The ratios of vertical to horizontal magnification factor in two cases where both were examined were 1.03 and 0.98. As a rule of thumb, roughly 5° of visual space are represented by $1mm$ of visual cortex.

5.3 Methods

In this study we analyze a large dataset of tree shrew orientation maps imaged in the Fitzpatrick laboratory and gratefully provided by Len E. White (Duke University Medical Center, Durham, USA). The dataset contains optical imaging data of 24 adult animals *(tupaia belangeri)*: 21 left hemispheres, 1 right hemisphere (TS111) and 2 double hemispheres (TS9762, TS9805) - in total 26 hemispheres. Details on the experimental setup and on the data acquisition are described in [27] for the single hemisphere experiments and in [69] for the double hemisphere experiments.

Optical Imaging

Optical imaging of intrinsic signals was accomplished using an enhanced video acquisition system (Optical Imaging Inc.) as described in [27, 69]. Images were acquired directly through the thinned bone overlying the V1 area. The cortex was illuminated with orange (605nm) or red light (700nm) and visualized with a tandem lens macroscope attached to a low noise video camera. The stimuli consisted of moving, high-contrast rectangular wave gratings oriented at $0°$, $45°$, $90°$, or $135°$. The averaged response to each grating was subtracted from the averaged response to the orthogonal grating to obtain difference images. Difference images were 655×480 pixel in resolution, with either 62 pixels (double hemispheres) or 75 pixels (single hemispheres) per millimeter. Difference images were clipped to ± 3 standard deviations from the median of intensity distribution, then rescaled to fit into the range $[0, 255]$, converted to 8 bit grayscale images and exported in TIFF format [72].

Preprocessing

Region of Interest (ROI)

We defined a region of interest (ROI) for each hemisphere containing the imaged part of area V1, excluding large bloodvessels.

Filtering

Overall drift components and long-wavelength fluctuations of signal intensity were removed by high-pass filtering as follows: Both difference images $D_{0°-90°}(\mathbf{x})$ and $D_{45°-135°}(\mathbf{x})$ were combined to a complex field

$$Z(\mathbf{x}) = D_{0°-90°}(\mathbf{x}) + i\, D_{45°-135°}(\mathbf{x}),$$

the unfiltered polar map. Inside the ROI we then calculated a high-pass filtered image $Z_{hp}(\mathbf{x}) = Z(\mathbf{x}) - Z'(\mathbf{x})$ by subtracting the local mean

$$Z'(\mathbf{x}) = \frac{1}{W'(\mathbf{x})} \mathcal{F}^{-1}\left\{ \tilde{K}'(\mathbf{k})\tilde{Z}(\mathbf{k}) \right\},$$

where $\mathcal{F}$ denotes Fourier transform and

$$\tilde{K}'(\mathbf{k}) = \frac{1}{1 + e^{-\left(k_{hp} - |\mathbf{k}|\right)/\sigma_{hp}}}$$

is the Fermi-function which depends on the high-pass cutoff frequency k_{hp} and a parameter controlling the steepness σ_{hp}. Normalization by the weight $W'(\mathbf{x}) = \int_{ROI} d^2\mathbf{y}\, K'(x-y)$ accounts for the boundary of the ROI. We used $\sigma_{hp} = 0.05\, k_{hp}$ and $k_{hp} = 2\pi/\lambda_{hp}$ with $\lambda_{hp} = 1.2mm$, approximately twice the typical spacing of orientation columns (see below).

Similarly, high-frequency noise was removed by means of the low pass filter

$$\tilde{K}(\mathbf{k}) = \frac{1}{1 + e^{-(k_{lp} - |\mathbf{k}|)/\sigma_{lp}}}$$

where $\sigma_{lp} = 0.05\, k_{lp}$ and $k_{lp} = 2\pi/\lambda_{lp}$ with $\lambda_{lp} = 0.2mm$. The normalization is set to $W(\mathbf{x}) = \int_{ROI} d^2\mathbf{y}\, K(x-y)$ and we end up with the band-pass filtered polar map,

$$z(\mathbf{x}) = \frac{1}{W(\mathbf{x})} \mathcal{F}^{-1}\left\{ \tilde{K}(\mathbf{k}) \tilde{Z}_{hp}(\mathbf{k}) \right\}.$$

For more details of this filtering technique and a thorough discussion on the advantages of using a Fermi-function instead of the widely used Gaussian the reader is referred to [73].

Scaling

Before averaging over all maps it is useful to rescale individual maps in units of their intrinsic lengthscale. This was achieved by appropriate spatial rescaling of each frame. Depicted in Fig. 5.3(**a**) are the radial projections of the correlation function $C_1(\mathbf{r})$ for all individual cases (see Chapter 3 for their definition and Section 5.4 for how they are obtained). They all exhibit a stereotype shape sketched in Fig. 5.3(**b**) with a quadratic maximum at the origin. We define the *intrinsic lengthscale* Λ_{int} as the location of the second peak. It provides a robust estimate for the average separation of adjacent orientation columns and is straightforward to measure. The values of Λ_{int} of all maps are depicted in Fig. 5.3(**c**) and fluctuate around a mean

$$\bar{\Lambda}_{int} = 650 \pm 30\mu m$$

which is consistent with previous results on the mean wavelength [73]. Expressed in pixels, $\bar{\Lambda}_{int}$ corresponds to either 48.8 or 40.3 pixels, depending on the pixel/mm resolution used for the particular experiment (see above). Each map was rescaled to achieve $\Lambda_{int} = 50$ pixel. Rescaling was linear and isotropic and implemented by a resampling of all data points on a new grid using spline interpolation. Correlation functions of the scaled ensemble are depicted in Fig. 5.3(**d**). Such rescaling leads to an almost complete collapse of the individual correlation functions. The shape of the correlation functions of individual maps are thus basically the same. This observation supports the 'ensemble picture' developed in Chapter 3.

Rotation and Flipping

For the purpose of our study it is essential to relate the orientation maps to the organization of the visuotopic map in area V1. Since we want to analyze the relationship between preferred orientation and space in the same coordinate system we first rotate each map in order to align the V1/V2 parallel to the y-axis, paying attention that the caudal part, where the upper part of the visual field is represented, points to the top (see Fig. 5.4(**a**)). Then we apply an additional
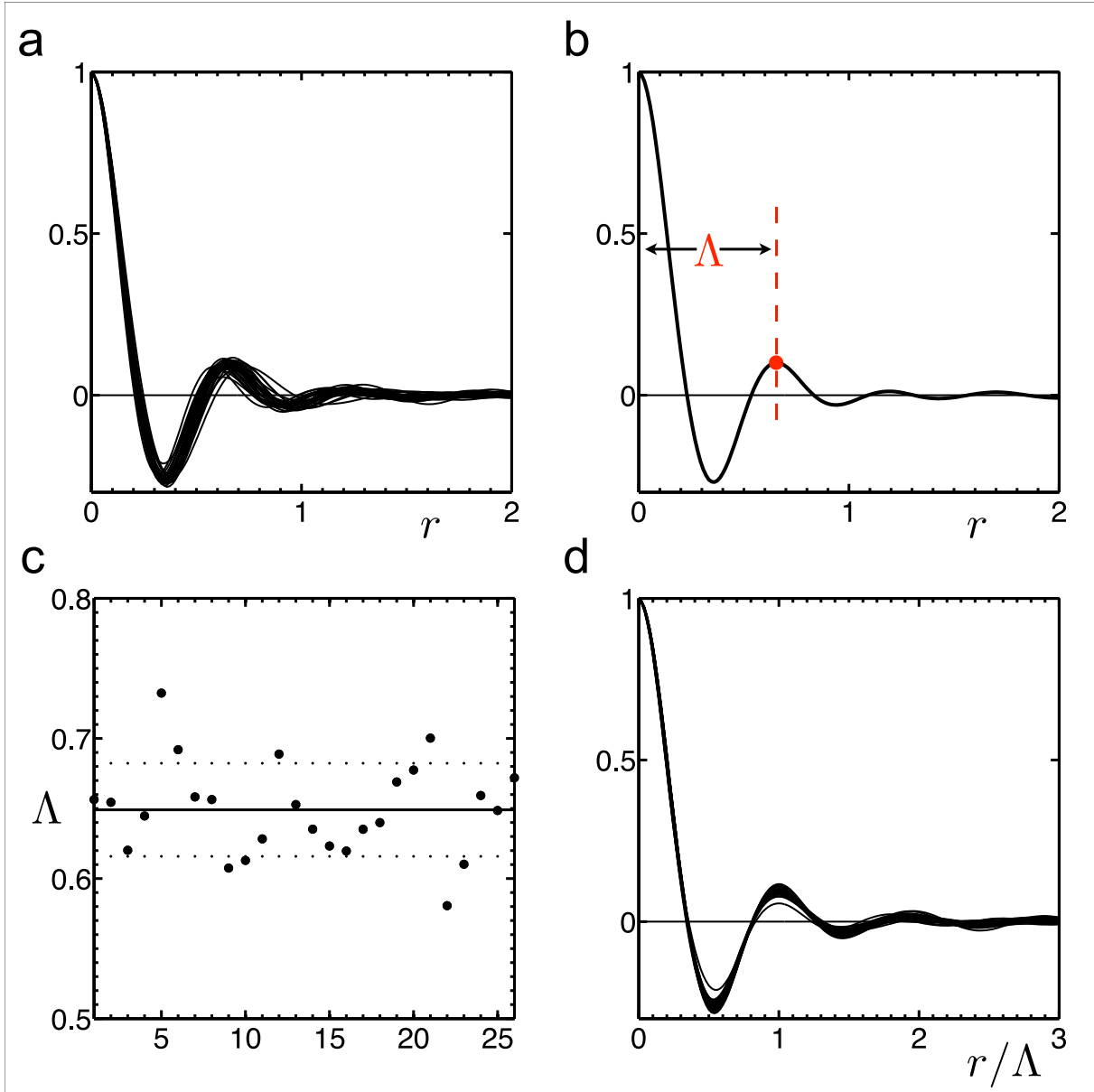
Figure 5.3: Correlation functions $C_1(r)$ and wavelengths of tree shrew orientation maps. (**a**) angular average correlation functions $C_1(r)$ of the 26 brain hemispheres analyzed (r in mm units). (**b**) Illustration of wavelength estimation from an individual correlation function (r in mm units). (**c**) Hemisphere to hemisphere variability of the wavelength Λ (in mm units). (**d**) Correlation functions collapse after a spatial rescaling of individual hemisphere which normalizes their wavelengths to $\Lambda = 1$. Here length is given in units of the typical wavelength (of the individual maps).

small rotation to account for the tilt angle α_t between V1/V2 border and vertical meridian (Fig. 5.4(**b**)). The same fixed value $\alpha_t = 5°$ was used for all maps. This procedure is based on our best estimate from the cases published in [69] and on the fact that shape and layout of area V1 look stereotypical among different animals [72]. Finally, the aligned maps are mirror imaged at the y-axis, such that left hemispheres are mapped onto the right visual hemifield and vice versa (Fig. 5.4(**c**)).
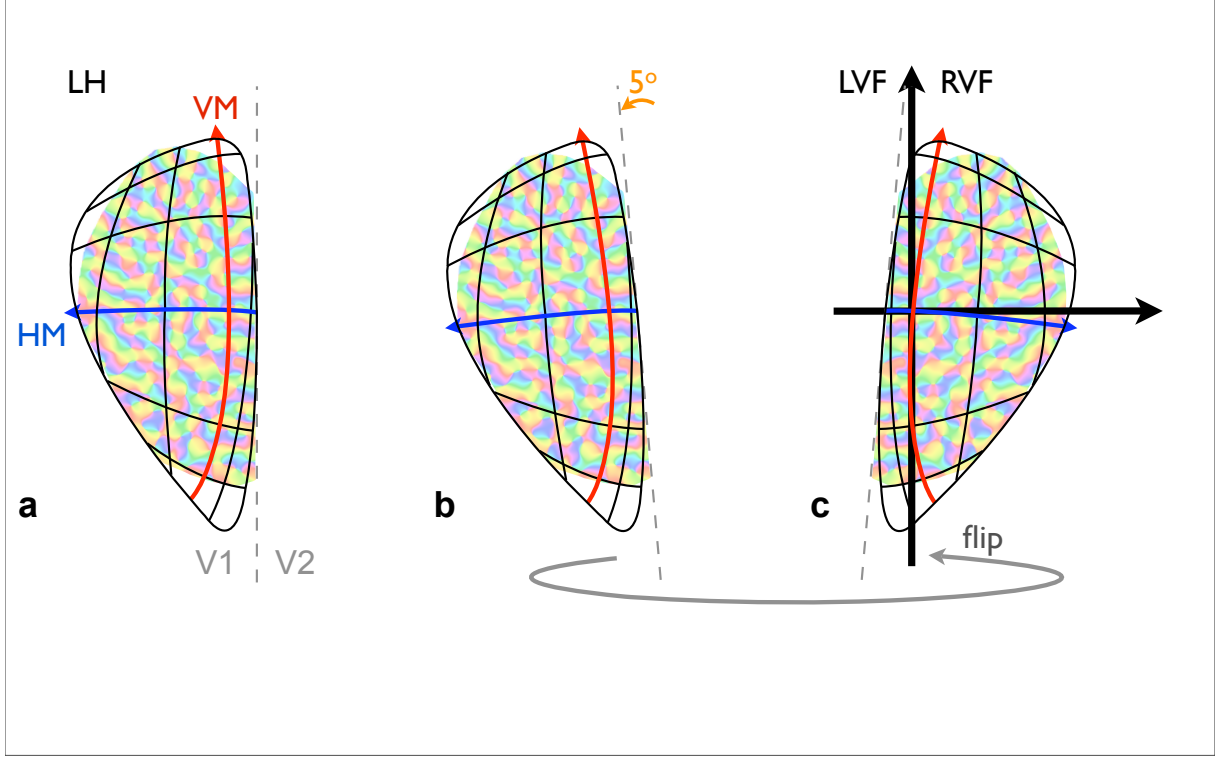
Figure 5.4: Rotation and Flipping of Orientation Maps. To superimpose the maps of visual space and align the projected horizontal and vertical axes, maps (**a**) where rotated (**b**) and flipped at the vertical axis (**c**). Details are given in the text.

Variance Normalization

In order to remove any overall bias with respect to cardinal or oblique orientations we normalize the variances of the real and imaginary part of each map such that

$$\langle \operatorname{Re} z \operatorname{Re} z \rangle = \frac{1}{2} = \langle \operatorname{Im} z \operatorname{Im} z \rangle.$$

The results of the following analysis, however, remain essentially unaffected when recalculated without such variance normalization.

5.4 Results

Correlation functions

The correlation functions $C_1(\mathbf{r})$ and $C_2(\mathbf{r})$ were obtained as follows: First we calculated individual correlation functions for each map z_j,

$$C_{1,j}(\mathbf{r}) \;\; = \;\; \frac{1}{A} \int\limits_{ROI} d^2\mathbf{x} \, z_j(\mathbf{x}) \bar{z}_j(\mathbf{x} + \mathbf{r})$$

$$C_{2,j}(\mathbf{r}) \;\; = \;\; \frac{1}{A} \int\limits_{ROI} d^2\mathbf{x} \, z_j(\mathbf{x}) z_j(\mathbf{x} + \mathbf{r})$$

where A denotes the area of the particular ROI. Then we average over all N maps in the ensemble

$$C_1(\mathbf{r}) \;\; = \;\; \frac{1}{N} \sum_j C_{1,j}(\mathbf{r})$$

$$C_2(\mathbf{r}) \;\; = \;\; \frac{1}{N} \sum_j C_{2,j}(\mathbf{r}).$$

Note that variance normalization implies $C_1(0) = 1$. The resulting correlation functions and their Fourier transforms $P_1(\mathbf{k})$ and $P_2(\mathbf{k})$ are shown in Fig. 5.5.

Let us first discuss $C_1(\mathbf{r})$ and the powerspectrum $P_1(\mathbf{k})$ (Fig. 5.5**(a,e)**). Both functions are essentially isotropic and exhibit no spatial anisotropies in correlation lengths and wavelengths. Their averaged radial parts, defined as

$$C_1(r) \;\; = \;\; \frac{1}{2\pi} \int\limits_0^{2\pi} d\phi \, C_1(r\cos\phi, r\sin\phi)$$

$$P_1(k) \;\; = \;\; \frac{1}{2\pi} \int\limits_0^{2\pi} d\phi \, P_1(k\cos\phi, k\sin\phi)$$

are plotted in Fig. 5.6**(a,b)**, together with the 95% confidence interval (shaded region), which was estimated using 10^5 bootstrap samples. Each bootstrap sample is obtained by recalculating $C_1(r)$ and $P_1(r)$ for a pseudo ensemble based on

$$C_{1,j}^{bs} = C_{1,X_j},$$

where $X_j \in \{1, 2, \ldots N\}$ denotes a random number, which is randomly drawn from the set of integers $\{1, 2, \ldots N\}$ with replacement.

In order to assess the statistical significance of $C_1(r)$ and $P_1(k)$, i.e. whether $C_1(r)$ and $P_1(k)$ are significantly different from zero, we perform a permutation test consisting of recalculating C_1, however this time based on

$$C_{1,j}^{perm}(\mathbf{r}) = \frac{1}{V} \int\limits_{ROI} d^2\mathbf{x} \, z_j(\mathbf{x}) \bar{z}_{\sigma(j)}(\mathbf{x} + \mathbf{r}),$$
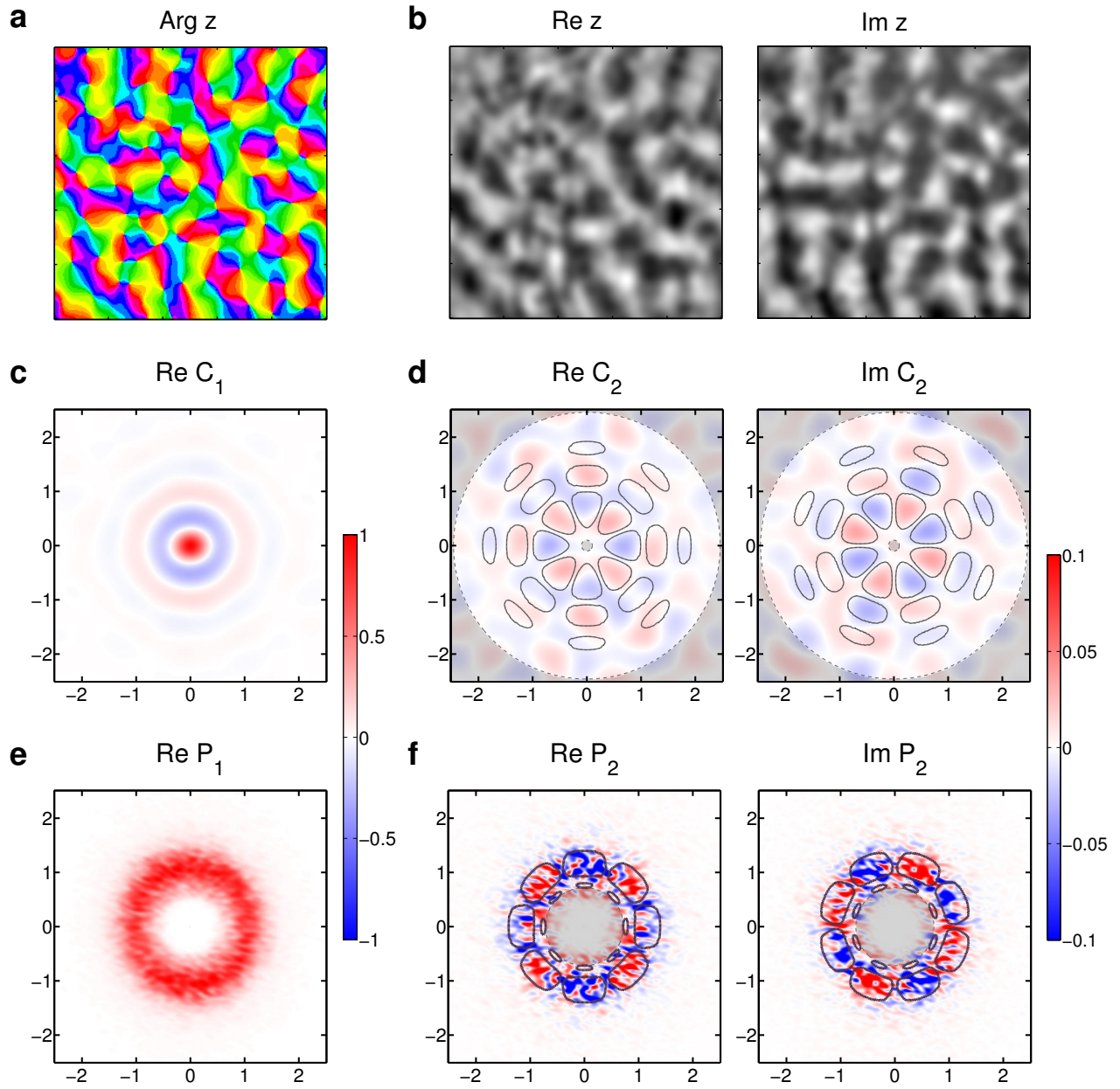
Figure 5.5: Spatial structure and two point correlations of orientation preference maps in the tree shrew visual cortex. (**a**) Example of an orientation map (case TS9815). (**b**) Real and imaginary parts of the orientation map shown in (a). (**c-f**) 2-d correlation functions $C_1(\mathbf{r})$, $C_2(\mathbf{r})$ and their Fourier transforms $P_1(\mathbf{k})$ (the power spectral density) and $P_2(\mathbf{k})$. For (c) and (e) one unit corresponds to 1Λ, for (d) and (f) to $2\pi/\Lambda$.
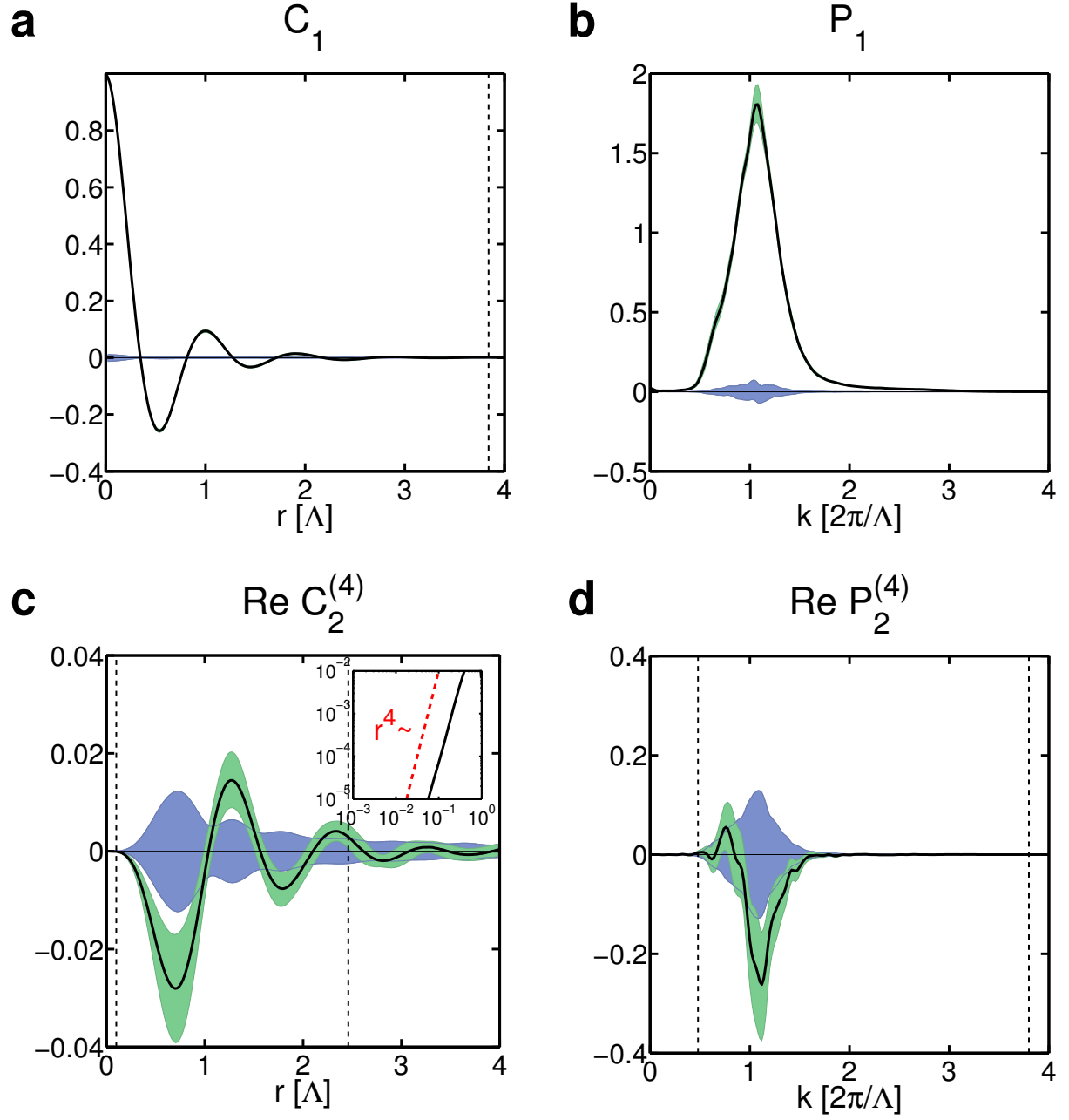
Figure 5.6: Monopole and quadrupole ('cloverleaf') component of the correlation functions. (**a** and **b**): Radial projections of the correlation function $C_1(\mathbf{r})$ and of the powerspectrum $P_1(\mathbf{k})$. (**c** and **d**): Real parts of the quadrupole component of $C_2(\mathbf{r})$ and of $P_2(\mathbf{k})$. Axes r and k displayed in units of typical wavelength Λ_{int} and typical wavenumber $2\pi/\Lambda_{int}$, respectively. *Green shaded regions*: bootstrap confidence interval. *Blue shaded regions*: 5% significance level.

a Im $C_2^{(4)}$

b Im $P_2^{(4)}$
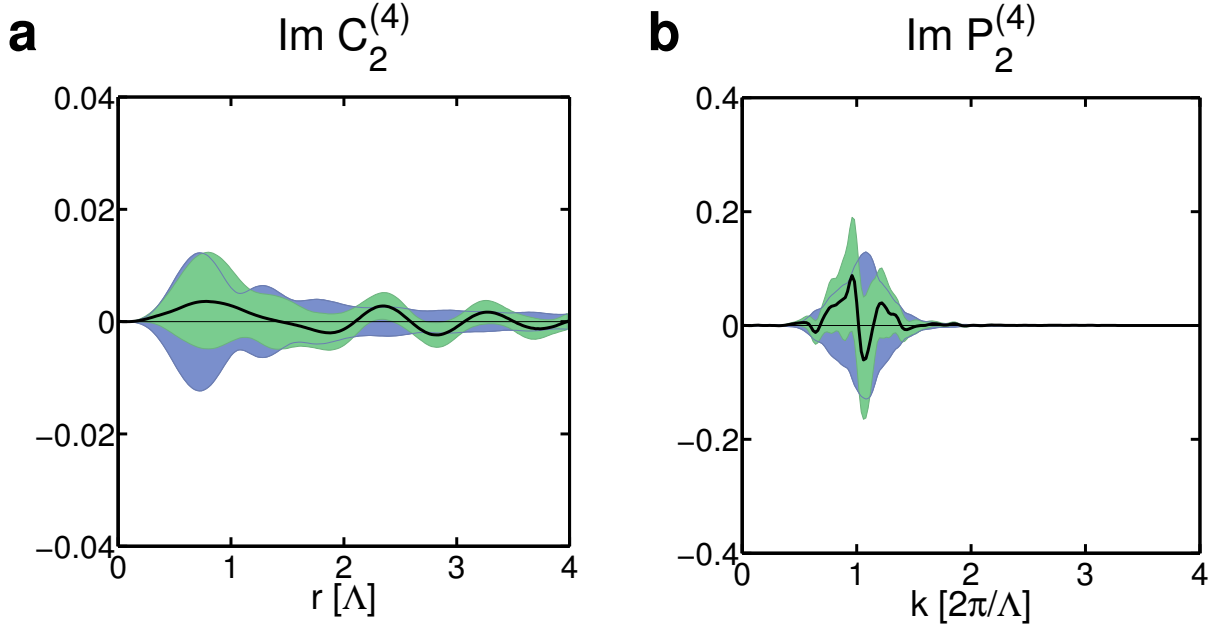
Figure 5.7: Imaginary parts of the quadrupole component of $C_2(\mathbf{r})$ and of $P_2(\mathbf{k})$. Same conventions as in Fig.5.6(**c**) and (**d**).

where $\sigma : \{1, 2, \ldots N\} \to \{1, 2, \ldots N\}$ denotes a random permutation of the indices with the additional requirement $\sigma(j) \neq j$, $\forall j \in \{1, 2, \ldots N\}$, since two maps z_i and z_j from different hemispheres should are expected to be statistically independent and therefore uncorrelated. The corresponding averaged radial parts, after ensemble averaging, are denoted by $C_1^{perm}(r)$ and $P_1^{perm}(r)$. Their distributions for 10^5 permutations are indicated by the gray shaded regions marking the 95% confidence interval. We conclude that within the analyzed range (4 intrinsic typical lengthscales) $C_1(r)$ and the powerspectrum $P_1(k)$ are highly significant (see below for details of how we define significant regions in this context). In particular, $P_1(k)$ exhibits a uni-modal peak at about one intrinsic wavenumber $k_{int} = 2\pi/\Lambda_{int}$, where Λ_{int} denotes the intrinsic wavelength, defined above.

The real and imaginary parts of $C_2(\mathbf{r})$ and $P_2(\mathbf{k})$ are shown in Fig. 5.5(**d**, **f**). Interestingly, they both exhibit a cloverleaf modulation consistent with the case $q < 0$ discussed in Chapter 3. How significant is this effect? Is there a way to estimate q? In order to quantify the effect we represent $C_2(\mathbf{r})$ in polar coordinates (r, ϕ), project out the 4th Fourier component with respect to $\phi = \arg \mathbf{r}$,

$$C_2^4(r) \;:=\; \frac{1}{2\pi} \int d\phi \, C_2(r, \phi) e^{-4i\phi}$$

and obtain the amplitude of the cloverleaf modulation, denoted by $C_2^4(r)$. We proceed the same way with $P_2(\mathbf{k})$ whose cloverleaf modulation is called $P_2^4(k)$. In general, these amplitudes are complex valued. However, we remind the reader that the general form of $C_2(\mathbf{r})$ consistent with the basic symmetry assumptions requires

$$C_2(\mathbf{r}) = f(r)\, e^{4i \arg \mathbf{r}} \text{ with } f(r): \ \mathbb{R} \to \mathbb{R}.$$

The resulting cloverleaf modulation, say, of Re $C_2(\mathbf{r})$, is therefore tightly locked to the x- and y-axis, along which it assumes its maximal (or minimal) values (see Fig. 3.2 in Chapter 3). A *complex* valued $f(r)$ would, in general, induce a rotation of the entire cloverleaf with the consequence that its principal axes no longer match the x- and y-axis. Such a scenario, however, is only conceivable for broken mirror symmetry. The same considerations apply to $P_2(\mathbf{k})$. Depicted in Fig. 5.6(**c**,**d**) and Fig. 5.7(**a**,**b**) are the real and imaginary parts of $C_2^4(r)$ and $P_2^4(k)$ for the tree shrew dataset. The 95% confidence intervals (shaded in green) are estimated using 10^5 random bootstrap samples (as described above). In order to assess the significance of the effect we compute the distribution of C_2^4 and P_2^4 of a corresponding *shift symmetric* ensemble, which is obtained by replacing each map $z_j(\mathbf{x})$ in the ensemble by a phase shifted map

$$z_j(\mathbf{x}) \to e^{i\phi_j} z_j(\mathbf{x}),$$

where $\phi_j \in [0, 2\pi]$ denotes a random phase. From the original dataset this procedure creates an artificial ensemble of maps, in which shift symmetry is restored. The distribution of cloverleaf components for the shift symmetrized ensemble is shown in blue, demarkating the 95% confidence interval for 10^5 randomized ensembles. Due to finite sample size ($N = 26$) it fluctuates about its average value which, by symmetry, has to be zero. We are now in a position to identify the significant part of the signal. As an example we consider Re $C_2^4(r)$ and define the *significant part* of Re $C_2^4(r)$ as the maximal interval $[r_{min}, r_{max}]$ within the analyzed region of r for which Re $C_2^4(r_{min})$ and Re $C_2^4(r_{max})$ lie outside of the 95% confidence interval of the shift symmetric distribution. The locations of r_{min} and r_{max} are indicated by the dotted lines in Fig. 5.6(**c**). We conclude that the oscillations observed in Re $C_2^4(r)$ are statistically significant in the domain $r \in [0.1,\ 2.46] \cdot \Lambda$ and reveal a clear signature of shift symmetry breaking. Furthermore, since Im $C_2^4(r)$ is not significantly different from zero, the observed cloverleaf structure is consistent with the theoretical predictions of Chapter 3, derived under the assumption that rotation and mirror symmetry both apply. In addition, the component $C_2^4(r)$ behaves as $\sim r^4$ for small r (inset of Fig. 5.6(**c**)) as predicted from our analysis of shift-twist symmetric ensembles, Eq.(3.4). The statistical analysis of $P_2^{(4)}(k)$ is performed in an analogous manner. Fig. 5.6(**d**) shows the real and imaginary part of the average cloverleaf component of $P_2(\mathbf{k})$ together with their respective confidence intervals (in green). The corresponding distribution from the shift symmetrized ensemble is shown in blue, the dotted lines demarkate the statistical significant part. Whereas Re $P_2^{(4)}(k)$ is significantly different from zero, Im $P_2^{(4)}(k)$ is not, in agreement with the theoretical prediction. Again, a clear signature of broken shift symmetry.

Estimation of *q* values

A simple and convenient way to quantify the degree of shift symmetry breaking is given by the order parameter q defined as

$$q = \langle Q(k) \rangle_k$$

where

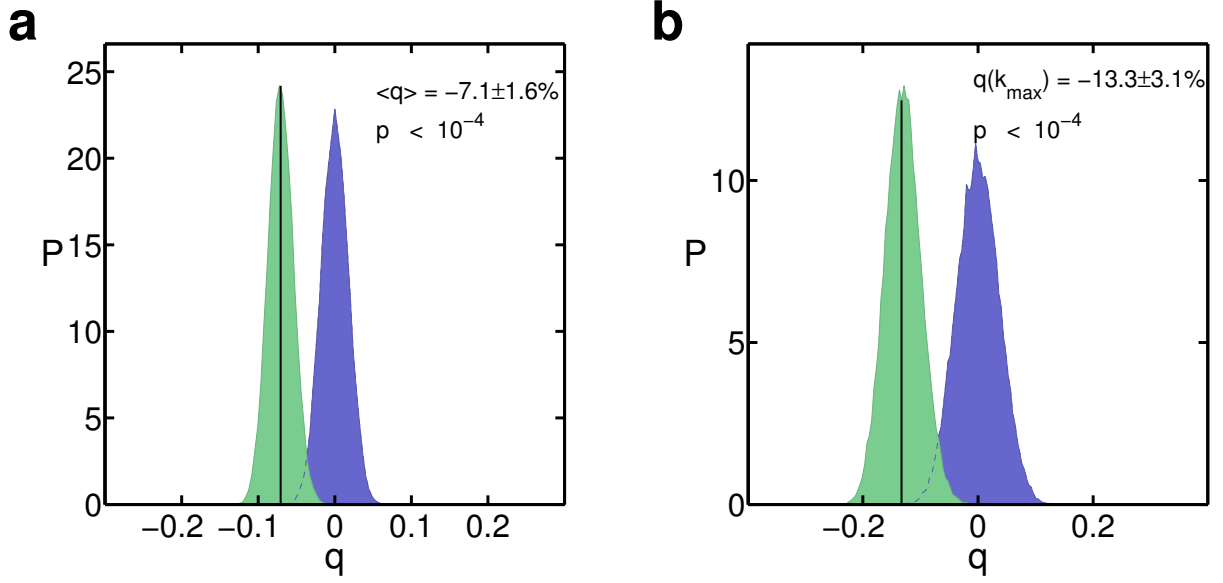$$Q(k) = \text{Re } P_2^{(4)}(k)/P_1(k)$$

Figure 5.8: Significance and strength of the two measures for shift symmetry breaking, q (**a**) and q_* (**b**). *Black lines:* sample estimate. *Green histogram:* distribution of bootstrap samples. *Blue histogram:* distribution of shift randomized samples.

and the brackets $\langle \cdot \rangle$ denote the average with respect to the normalized weight $P_1(k)/\int_0^\infty dk\, P_1(k)$. We find

$$q = -7.1 \pm 2\%$$

where the confidence interval for q is estimated from 10^5 bootstrap ensembles, which generates the distribution shown in Fig. 5.8(**a**). The null hypothesis of full shift symmetry whose distribution is computed from the shift-symmetrized ensemble (blue histogram), cannot explain the q value of the tree shrew dataset and is rejected on the basis of a significance level $p < 10^{-5}$. Unlike in our model of Chapter 3, where for simplicity we proposed a constant value $Q(k) = const = q$ one can see in Fig. (5.6)(**d**) that Re $P_2^{(4)}(k)$, and therefore $Q(k)$, exhibits a sign flip at $k_0 \approx 0.9\, k_{int}$ inside the significant region. Although mostly negative it also gets positive for small wavenumbers $k < k_0$. The maximal effect, however, is expected to happen around the location $k \approx k_{max}$ at which the powerspectrum $P_1(k)$ reaches its peak. Thus, as an alternative measure of shift symmetry breaking we might as well consider

$$q_* := Q(k_{max})$$

As expected, the effect is stronger

$$q_* = -13.3 \pm 3\%$$

and is again highly significant ($p < 10^{-5}$), see Fig. 5.8(**b**).

Optimizing the tilt angle

Although great care was taken while determining the V1/V2 border (methods sections) we cannot rule out that there might be a source of variability at that part of the preprocessing. Similarly,

our best guess for the tilt angle, globally set to $\alpha_t = 5°$, may turn out to be neither constant across all animals, nor accurate enough. V1/V2 borders were assigned individually by visual inspection of the optical imaging signal, before any statistical analysis. The question remains, how an error of a few degrees, at that preprocessing stage would affect the q estimation later. Consider a hypothetical ensemble of N orientation maps with a tight coupling to the visuotopic map as discussed in Chapter 3, for which the V1/V2 angle and the tilt angle are *exactly* known. After a proper alignment of the vertical meridian to the y-axis and measurement of the individual correlation functions, $C_{2,j}(\mathbf{r})$ exhibits a cloverleaf modulation, whose principal axes are locked to the x- and y-axis of the coordinate system. If, instead, some error occurred such that the vertical meridian and y-axis are tilted relatively to each other, say by an angle μ_j, the axes of the cloverleaf would also rotate by μ_j, as shown next: If, say, for the correctly aligned map

$$C_{2,j}(\mathbf{r}) = \int_{ROI} d^2\mathbf{y}\, z(x)z(x+y)$$

then for the misaligned map

$$
\begin{aligned}
C_{2,j}^{\mu}(\mathbf{r}) &= \int_{\mathcal{R}_\mu(ROI)} d^2\mathbf{x}\, z\left(\Omega_{-\mu}\mathbf{x}\right) z\left(\Omega_{-\mu}(\mathbf{x}+\mathbf{r})\right) \\
&= \int_{ROI} d^2\mathbf{x}\, z(\mathbf{x})z\left(\mathbf{x}+\Omega_{-\mu}\mathbf{r})\right) \\
&= C_{2,j}(\Omega_{-\mu}\mathbf{r})
\end{aligned}
$$

where j denotes the particular case in the ensemble. The same applies to the Fourier transform

$$P_{2,j}^{\mu}(\mathbf{k}) = P_{2,j}(\Omega_{-\mu}\mathbf{k}).$$

Now, assuming

$$P_{2,j}(\mathbf{k}) = Q_j(k)\, e^{4i\arg\mathbf{k}}\, P_{1,j}(k)$$

with $Q_j(k) \in \mathbb{R}$ and $Q_j(k) \leq 0$ for the correctly aligned maps, then

$$P_{2,j}^{\mu_j}(\mathbf{k}) = e^{4i\mu_j}Q_j(k)\, e^{4i\arg\mathbf{k}}\, P_{1,j}(k)$$

for the misaligned ones. Since

$$\left|\text{Re }e^{4i\mu_j}Q_j(k)\right| \leq \left|\text{Re }Q_j(k)\right| \quad \text{for } Q_j(k) \in \mathbb{R}$$

it is clear that any misalignment will yield to an underestimate of $|q|$ or $|q_*|$ and therefore dilute the strength of the effect. How would our estimates of q and q_* change if we could correct for this hypothetical misalignment? We can find an upper bound for q and q_* since we know $P_{2,j}^{(4)}(k)$ of each map j: As shown in Fig. 5.7(**b**) $P_{2,j}^{(4)}(k)$ is complex, even though in general $|\text{Im }P_{2,j}^{(4)}(k)| \ll |\text{Re }P_{2,j}^{(4)}(k)|$. Since q and q_* are based on $P_2^{(4)}(k) = \frac{1}{N}\sum_{j=1}^{N} P_{2,j}^{(4)}(k)$ all $P_{2,j}^{(4)}(k)$ should sum up coherently in order to yield a maximal effect. For q or q_* that will be the case when $\langle P_{2,j}^{(4)}(k)\rangle_k \in \mathbb{R}$ or $P_{2,j}^{(4)}(k_{max}) \in \mathbb{R}$, respectively. Hence the corresponding optimal correction angles can be obtained from

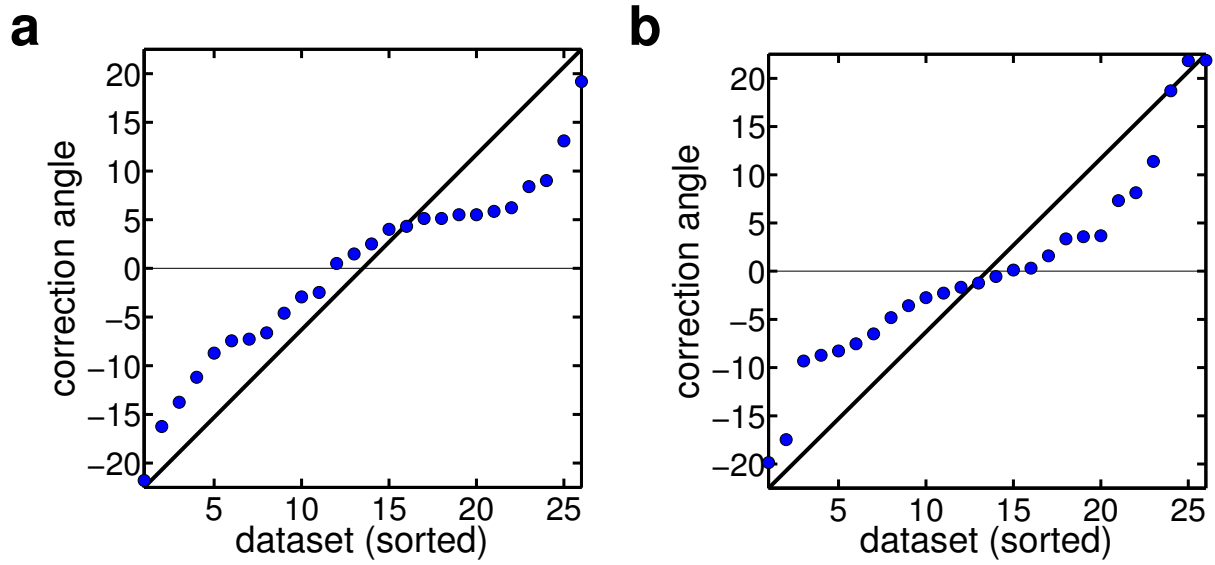$$\alpha_j = \arg\langle P_{2,j}^{(4)}(k)\rangle_k \quad \text{or} \quad \alpha_j = \arg P_{2,j}^{(4)}(k_{max})$$

Figure 5.9: Correction angles that maximize (**a**) the q and (**b**) the q_* estimate obtained from each hemisphere.
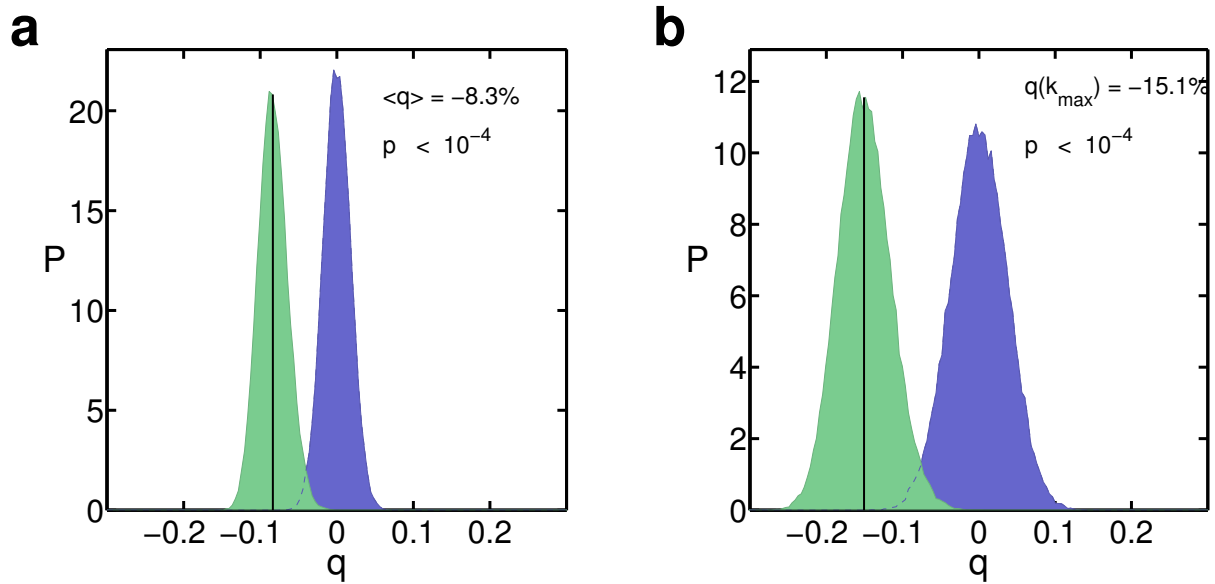

Figure 5.10: Shift symmetry breaking, reassessed after optimizing the tilt angles. q (**a**) and q_* (**b**). *Black lines:* sample estimate. *Green histogram:* distribution of bootstrap samples. *Blue histogram:* distribution of shift randomized samples.

as follows: A tilt μ_j applied to the *j-th* frame induces a phase shift $\alpha_j \rightarrow \alpha'_j = \alpha_j + 4\mu_j$. Real values correspond to either $\alpha'_j = 0$ or $\alpha'_j = \pi$. In order to keep the correction angle as small as possible μ_j is chosen

$$\mu_j = \begin{cases} -1/4\,\alpha_j & : \pi/2 \leq \alpha_j \leq \pi/2 \\ -1/4\,(\alpha_j - \pi) & : \text{else} \end{cases}$$

which restricts its range to $\mu_j \in [-\pi/8, \pi/8]$. The distributions of correction angles optimizing q and q_* are shown in Fig. 5.9(**a**) and (**b**), respectively. Note that the majority of angles accumulates within the range of $\pm 7°$ .The optimized values for q and q_* are

$$q = -8.3 \pm 2\% \quad \text{and } q_* = -15.1 \pm 4\%,$$

their distribution, inferred from a bootstrap of 10^5 samples, is shown in Fig.(5.10). We conclude that perfect control over the tilt and V1/V2 angle may yield to a noticeable but not dramatic increase of the observed effect by about $10 - 15\%$.

Testing the q estimator

How reliable is our estimate of q? We use ensembles of Gaussian random fields (GRFs) in order to address this question. The number and the size of random maps (the number of hypercolumns) and the powerspectrum are chosen such as to approximate the tree shrew dataset. Each ensemble consisted of 20 random maps (spatial extension of $L = 13\Lambda$ and $\Lambda = 50$ pixel) drawn according to the model of Chapter 3 for fixed control parameter $\beta = 10$ and variable degree of shift symmetry breaking $q_{GRF} \in \{-1.0, -0.9, -0.8, \dots, 1.0\}$. For each ensemble we then estimate q and q_* as described above. Those estimates are compared to the actual values of q_{GRF} in Fig. 5.11. Errorbars demarkate the central 95% of the distribution for 10^5 bootstraps. We conclude that both estimators work very well despite some systematic bias at large $|q_{GRF}|$ values of up to $\sim 8\%$. For small values $|q_{GRF}| \leq 0.2$, however, the exact value lies within the confidence region of the estimator.

Pair Cooccurence Histograms

In the previous subsection we presented strong evidence that the orientation map layout in tree shrews is coupled to the visuotopic map as predicted by broken shift symmetry. The observed coupling is consistent with the predicted effect derived in Chapter 3 from the basic Euclidean symmetry assumption. The strength of the effect is relatively small but highly significant: quantified by q and q_* it ranges in the order of -10%. Moreover, it occurs with negative sign, which predicts that domains coding for oblique orientations should have a tendency to arrange parallel to the x- and y-axis, whereas cardinal domains should preferentially arrange along the diagonals. Is this really the case? Given the magnitude of the effect it is clear that we need a sensitive method to check this prediction.

It turns out that the pair co-occurrence statistics provides exactly the tool we need. The histograms for $\Delta = \{0, \pi/8, \pi/4, 3\pi/8, \pi/2\}$ of our tree shrew dataset are shown in Fig. 3.10(**b-f**). A comparison to the theoretical histograms calculated for Gaussian random fields reveals
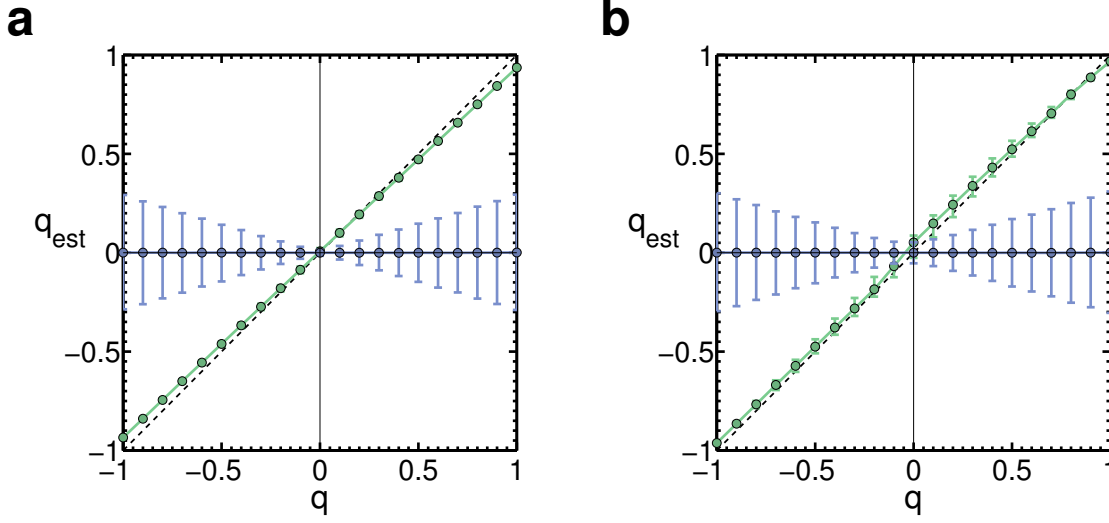
a

b

Figure 5.11: Validation of q estimator using surrogate data. Graphs of q-estimates (q in (**a**) and q_* in (**b**)) as a function of the model parameter q of the Gaussian random map ensemble. *Blue:* significance boundary calculated from shift randomized maps.

interesting correspondence and discrepancy.

Let us first discuss the matching part. All histograms exhibit a cloverleaf modulation, which is most visible in the last histogram ($\Delta = \pi/2$). A comparison with the Gaussian case Fig.3.10 reveals that the 4-fold modulation is consistent with negative q, confirming our expectation. Indeed, from the first histogram one can read of that 0° iso-orientation domains are more likely to extend along the diagonals rather than along the cardinal directions. This also means that domains for oblique orientations run preferentially along the horizontal and vertical directions, rather than along the diagonal.

However, contrary to the Gaussian case, the modulation cannot be explained by the cloverleaf alone. In fact it appears that superposed on top of it there is an additional 2-fold modulation which distinguishes collinear from parallel arrangements. This can be seen best for $\Delta = 0$ and separations $r \leq 1\Lambda_{int}$, where collinear arrangements encounter more suppression than parallel ones. This is an interesting departure from the Gaussian case, where, for negative q, both arrangements are suppressed to the same degree. This asymmetry is also apparent in the remaining histograms, however it becomes attenuated for larger Δ and vanishes for $\Delta = \pi/2$. The principal axis of this 2-fold modulation rotates with angle $\Delta/2$, which is also the case for the symmetry axes of the cloverleaf modulation (black lines).

Can we disentangle the 4-fold ('cloverleaf') from the 2-fold ('collinear') part and quantify their respective contribution to the overall modulation? The general form of $P_{r,\phi}(\Sigma|\Delta)$ derived in Chapter 3 states

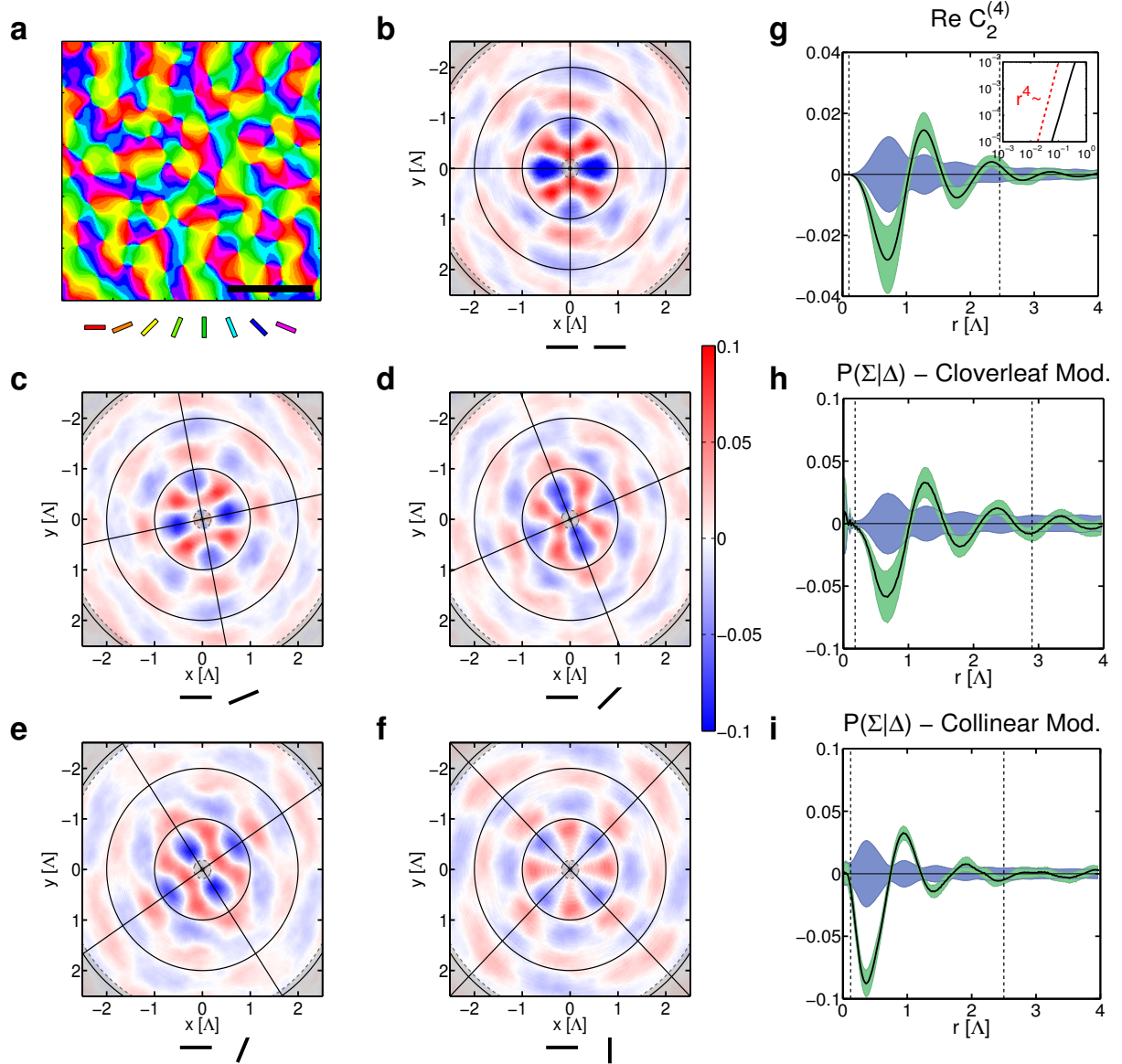$$P_{r,\phi}(\Sigma|\Delta) = \sum_{m,n\in\mathbb{N}} c_{mn}(r) \cos(2m(\Sigma - \phi)) \cos(n\Delta)$$

Figure 5.12: Spatial structure of orientation cooccurrence histograms of tree shrew orientation maps. (**a**) Example of a tree shrew orientation map, *scale bar* corresponds to one typical wavelength Λ. (**b-f**) Orientation cooccurrence histograms for five difference angles (*see bars below each plot*). (**g**) Cloverleaf projection of C_2 with significance borders *(blue)* and confidence intervals *(green)*. Inset: log-log plot of initial rise as compared to $\sim r^4$ *(dotted line)*. (**h-i**) Cloverleaf and collinear modulation of the orientation cooccurrence histogram. Confidence intervals and significance borders as in (g).

with $c_{00} = 1/\pi$ and $c_{mn} = 0$ for odd $m + n$. Here we argue that the cloverleaf part is given by

$$P_{r,\phi}^{(4)}(\Sigma|\Delta) = \sum_{m,n\in2\mathbb{N}} c_{mn}(r)\,\cos(2m(\Sigma - \phi))\cos(n\Delta)$$

whereas the 2-fold modulation is provided by

$$P_{r,\phi}^{(2)}(\Sigma|\Delta) = \sum_{m,n\in2\mathbb{N}+1} c_{mn}(r)\,\cos(2m(\Sigma - \phi))\cos(n\Delta).$$

This can be seen in Fig. 3.8(**b**), where collinear and parallel arrangements are displayed in the row $\Delta = 0$ at positions $\Sigma - \phi = 0 \bmod \pi$ and $\Sigma - \phi = \pi/2 \bmod \pi$, respectively. For $m \in 2\mathbb{N}$

$$\cos 2m(\Sigma - \phi)\cos(n\Delta) = \cos 2m(\Sigma - \phi + \mathbb{Z}\cdot\pi/2)\cos(n\Delta)$$

such that the corresponding modulation affects collinear and parallel arrangements equally. Hence $P_{r,\phi}^{(4)}$ is invariant under discrete shifts

$$\phi \to \phi + \mathbb{Z}\cdot\pi/2,$$

which explains the 4-fold or cloverleaf structure. In contrast, for $m \in 2\mathbb{N}+1$ collinear and parallel arrangements are modulated in opposite ways since

$$\cos 2m(\Sigma - \phi)\cos(n\Delta) = -\cos 2m(\Sigma - \phi + \mathbb{Z}\cdot\pi/2)\cos(n\Delta).$$

Correspondingly, $P_{r,\phi}^{(2)}$ lacks $\pi/2$ symmetry but is symmetric under

$$\phi \to \phi + \mathbb{Z}\cdot\pi$$

with explains its basic 2-fold structure.

Quantification

As a simple way to quantify the 2-fold and 4-fold modulation in the tree shrew pair cooccurence histogram we consider the approximation

$$P_{r,\phi}(\Sigma|\Delta) \approx \frac{1}{\pi} + c_{11}(r)\cos(\Sigma - \phi)\cos\Delta + c_{20}(r)\cos(2\Sigma - 2\phi)$$

and compute the coefficients $c_{11}(r)$ and $c_{02}(r)$, which are depicted in Fig. 5.12(**h, i**). On a scale of Λ_{int} both components exhibit oscillations in r which are progressively damped towards larger separations. The collinear suppression peaks at approximately -6% for $r \approx 0.7\Lambda$ for the cloverleaf and at approximately -8% for $r \approx 0.3\Lambda$ for the collinear part. Both modulations thus are of *negative* type. The 95% confidence interval *(shown in green)* is calculated from 10^5 bootstrap ensembles. The statistical significance of these oscillations is assessed by comparison with the shift randomized ensemble, as described above *(shown in blue)*. Dotted lines indicate the interval where oscillations are considered to be significantly different from zero. Furthermore, the course of $c_{02}(r)$ closely follows the oscillation of $C_2^{(4)}(r)$, the cloverleaf component of the correlation function $C_2(r)$.

Shift-Twist Randomization

The 2-fold modulation in the pair occurrence histograms is remarkable for several reasons. First, it reveals the non-Gaussian aspect of the map statistics. Therefore, in order to arrive at a comprehensive description of the map statistics higher order correlations of $z(\mathbf{x})$ cannot be ignored.

Suppose we could remove all nontrivial higher order correlations in the tree shrew dataset, while keeping the second order statistics unchanged: How would the pair occurrence histograms look like? Following the argument above any 2-fold modulation should then have disappeared since the new map ensemble would have Gaussian statistics. Can we confirm this? A simple method to randomize the tree shrew dataset in that particular way is given next:

1. For each preprocessed polar map $z_j(\mathbf{x})$ we compute the Fourier transform $a_j(\mathbf{k})$.

2. For each pair of antiparallel modes $(a_j(\mathbf{k}), a_j(-\mathbf{k}))$ the complex amplitudes are multiplied by a random complex phase,

$$
\begin{aligned}
a_j(\mathbf{k}) &\rightarrow a_j(\mathbf{k})e^{i\phi(\mathbf{k})} \\
a_j(-\mathbf{k}) &\rightarrow a_j(-\mathbf{k})e^{-i\phi(\mathbf{k})}.
\end{aligned}
$$

This randomizes the amplitudes but leaves $P_{1,j}(\mathbf{k}) = |a_j(\mathbf{k})|^2$ and $P_{2,j}(\mathbf{k}) = a_j(\mathbf{k})a_j(-\mathbf{k})$ invariant.

3. The randomized map is then obtained by the inverse Fourier transform $a_j(\mathbf{k}) \rightarrow z_j(\mathbf{x})$.

The pair occurrence statistics for such a shift-twist randomized ensemble is shown in Fig. 5.13. It reveals a clear 4-fold modulation but no indication of a 2-fold modulation. This is confirmed by computing the components $c_{1,1}(r)$ and $c_{2,0}(r)$. Whereas $c_{2,0}(r)$ appears unaltered, $c_{1,0}(r)$ is not significantly different from zero (dotted lines refer to the significant region of the original tree shrew dataset).
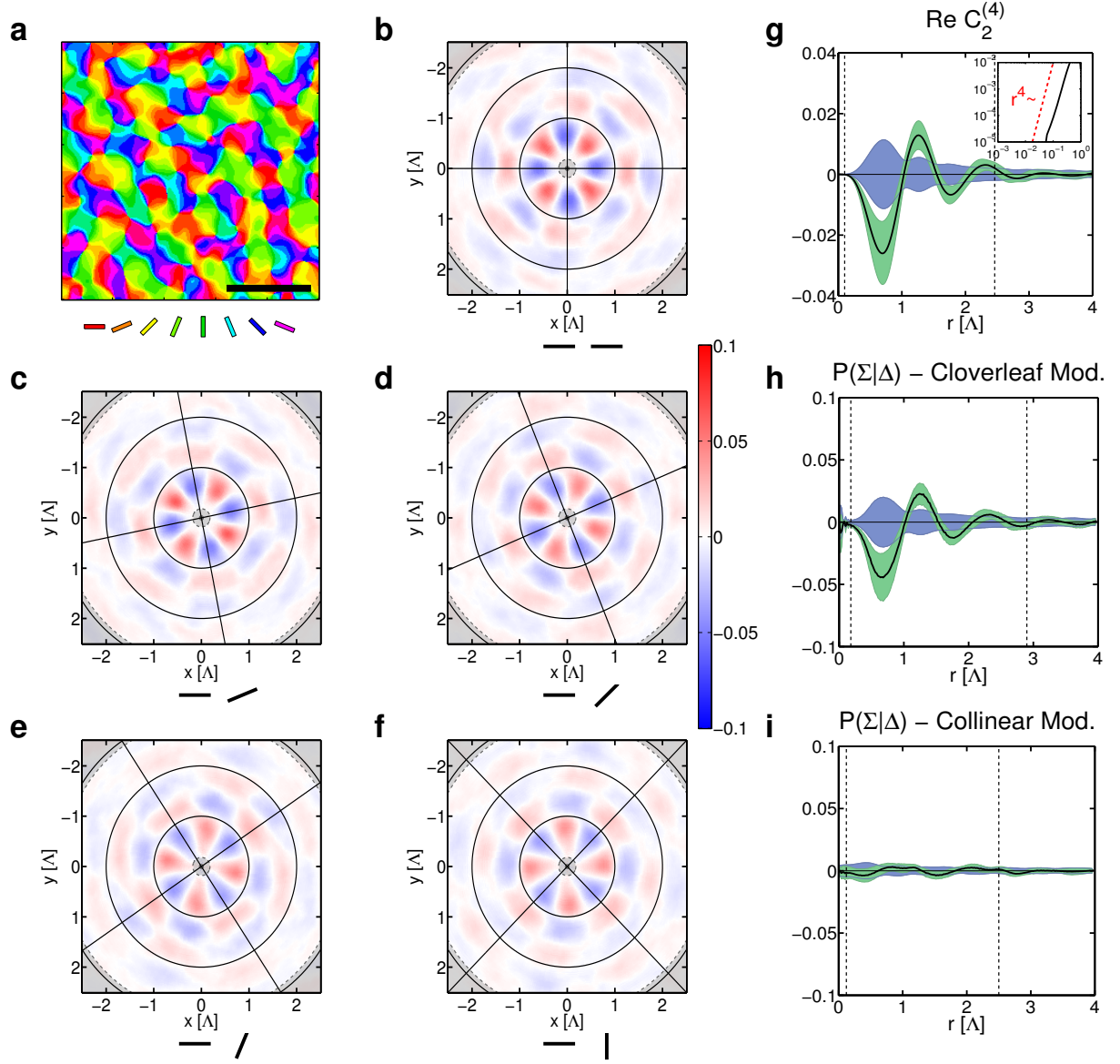
Figure 5.13: Shift-twist randomization extinguishes the collinear modulation of the orientation cooccurrence histogram but leaves the four-fold components of C_2 and P_2 largely unaffected. All panels depict results from shift-twist randomized data, conventions as in Fig. 5.12.

6 Learning Contour Correlations

> Si non e vero, e ben trovato.
>
> *(Italian Saying)*

6.1 Overview

This chapter answers the main questions revealed by comparing the theoretical predictions of Chapters 3 and 4 and the empirical observations of Chapter 5. In Chapters 3 and 4 we studied the consequences of shift-twist symmetry on the orientation map layout when shift symmetry is broken. It turned out that shift symmetry breaking occurs in one of two possible ways, depending on the sign of q and ϵ, which are introduced as phenomenological parameters and yet remain unspecified at that stage of analysis. In Chapter 5 we have shown that the signatures of shift-twist symmetry in the tree shrew dataset are consistent with a negative sign of q which suggests $\epsilon < 0$. In addition, the cooccurrence statistics of preferred orientations was found to exhibit a 2-fold component that cannot be reproduced in a Gaussian map ensemble and is also absent from the ground states of the abstract model studied in Chapter 4. Finally, the overall degree of shift-symmetry breaking was found to be low, although dynamical models (Chapter 4) are predicted to be highly sensitive to relatively weak symmetry breaking terms. Why is the strength of shift symmetry breaking so low? What is the origin of the two-fold component? Why is shift symmetry breaking of negative type?

To answer these questions we here examine a model in which pattern formation in the visual cortex is driven by the statistics of natural scene stimuli. We study map formation within the framework of the elastic network model [17, 19], a simple model for the activity dependent development of orientation preference. In its original form the elastic net describes how a sequence of afferent activity patterns elicited by a sequence of randomly oriented, isolated point stimuli leads to the formation of visuotopic and orientation preference maps via a competitive Hebbian learning rule. We propose a generalization of the elastic net for a much broader class of stimuli, e.g. spatially extended contours. This allows to examine how the higher order statistics of visual scenes affects map formation. In natural images pairs of edges exhibit a strong tendency to occur in collinear arrangements [52]. To model this we define a simple stimulus ensemble which consists of pairs of oriented edges and exhibits a variable degree of collinearity κ. The dynamics of the order parameter field $z(\mathbf{x})$, averaged over this stimulus ensemble, yields an effective dynamics of the form of Eq.(2.4), which still depends on the stimulus statistics, although implicitly through the correlation functions of the stimulus ensemble. A linear stability analysis reveals the characteristic time and length scales of the emerging pattern and, moreover, yields an analytic expression for ϵ. It turns out that the sign of ϵ depends on the statistics of the stimulus ensemble. In particular, we find that in a collinear world $\epsilon < 0$. We check this prediction by numerical integration of the model dynamics for appropriately chosen parameter sets. Signatures

of shift-twist symmetry are found in the correlation functions and the pair occurrence histogram. Intriguingly we also observe a 2-fold non-Gaussian contribution like in the tree shrew dataset. We conclude that the shift symmetry breaking of the type and strength observed in tree shrew orientation maps can be induced and explained by the fact that shift symmetry is broken in the statistics of natural images.

6.2 The Elastic Net

The elastic net [17, 19] models how sequences of afferent activity patterns representing visual stimuli lead to the formation of visuotopic and orientation preference maps via a competitive Hebbian learning rule. A stimulus S is described by two parameters: $\mathbf{r} \in \mathbb{R}^2$, its position in visuotopic coordinates and $s = |s|e^{2i\theta}$, the orientation θ and orientation selectivity $|s|$, to which it drives the activated neurons. The pattern of orientation preferences is represented by a complex field $z(\mathbf{x}) : \mathbb{R}^2 \to \mathbb{C}$. An additional field $\mathbf{R}(\mathbf{x}) : \mathbb{R}^2 \to \mathbb{R}^2$ describes the receptive field center positions of the neurons at cortical location $\mathbf{x} \in \mathbb{R}^2$. The elicited cortical activity $E(\mathbf{x}|S; z, R)$ depends on the state of the fields and of the actual stimulus. The fields are updated according to following modification rule [34]

$$
\begin{aligned}
\delta z(\mathbf{x}) &= \epsilon\left[(s - z(\mathbf{x}))\,E(\mathbf{x}|S; z, R) + \eta\,\Delta z(\mathbf{x})\right] \\
\delta \mathbf{R}(\mathbf{x}) &= \epsilon\left[(\mathbf{r} - \mathbf{R}(\mathbf{x}))\,E(\mathbf{x}|S; z, R) + \eta\,\Delta \mathbf{R}(\mathbf{x})\right]
\end{aligned}
\tag{6.1}
$$

where the learning rate $\epsilon > 0$ determines the size of a single update and $\eta > 0$ controls the strength of the lateral coupling mediated by the Laplace operator, which drives neighbouring neurons to develop similar feature selectivities. The modification by a single stimulus $S = (\mathbf{r}, s)$ is proportional to the cortical activation

$$
E(\mathbf{x}|S; z, R) = \frac{e^{-\left(|\mathbf{r}-R(\mathbf{x})|^2 + |s-z(\mathbf{x})|^2\right)/2\sigma^2}}{\int d^2\mathbf{x}'\, e^{-(|\mathbf{r}-R(\mathbf{x}')|^2 - |s-z(\mathbf{x}')|^2)/2\sigma^2}}
$$

which is normalized

$$
\int d^2\mathbf{x}\, E(\mathbf{x}|S; z, R) = 1
$$

This normalization induces competition (also called "soft competition" [19]) between remote cortical sites since the total amount of activation distributed among the activated sites is kept fixed. According to that rule neurons are activated when the distance between their selectivities and the stimulus is smaller than σ. Therefore, σ can be interpreted as the size of the receptive field. On the other hand σ controls the size of the coactivated domains and thus the scale of the emerging pattern. Averaged over a statistically stationary sequence of random stimuli, the dynamics of Eq.(6.1) can be written [34]

$$
\begin{aligned}
\partial_t z(\mathbf{x}) &= \langle (s - z(\mathbf{x}))\,E(\mathbf{x}|S; z, R) + \eta\,\Delta z(\mathbf{x})\rangle_{\mathcal{S}} \\
\partial_t \mathbf{R}(\mathbf{x}) &= \langle (\mathbf{r} - \mathbf{R}(\mathbf{x}))\,E(\mathbf{x}|S; z, R) + \eta\,\Delta \mathbf{R}(\mathbf{x})\rangle_{\mathcal{S}}
\end{aligned}
\tag{6.2}
$$

where the average is taken with respect to a stimulus ensemble $\mathcal{S}$. For simplicity it is assumed that stimulus positions $\mathbf{r}$ are homogeneously distributed over the visual field and that $s \in \mathbb{C}$ occurs at random locations on a circle $|s| = s_0$ such that each stimulus orientation has the same

probability [17]. In the following analysis we also consider more general distributions $p(s) = p(|s|)$. Once the stimulus ensemble is fixed the dynamics (6.2) only depends on the two parameters σ and η.

The homogeneous state $z_0(\mathbf{x}) = 0$, $\mathbf{R}_0(\mathbf{x}) = \mathbf{x}$ is a stationary state of the dynamics (6.2). A linear stability analysis reveals whether small fluctuations around this state are damped or, in contrary, are amplified and eventually lead to the formation of orientation columns. The linearized dynamics of $z(\mathbf{x})$ in the vicinity of the homogeneous state is given by

$$\partial_t z(\mathbf{x}) = \left(\frac{\langle |s|^2 \rangle}{2\sigma^2} - 1 \right) z(\mathbf{x}) - \frac{\langle |s|^2 \rangle}{8\pi\sigma^4} \int d^2\mathbf{y}\, e^{-|\mathbf{x}-\mathbf{y}|^2/4\sigma^2} z(\mathbf{y}) + \eta\, \Delta z(\mathbf{x}) \tag{6.3}$$

It uncouples from the dynamics of the visuotopic map $\mathbf{R}(\mathbf{x})$ and depends on the stimulus variance $\langle |s|^2 \rangle = \int d^2s\, |s|^2 p(|s|)$ [13]. Furthermore, it is equivariant under rotations and phase shifts of $z(\mathbf{x})$. The Fourier modes $a(\mathbf{k}) = \frac{1}{2\pi} \int d^2\mathbf{x}\, z(\mathbf{x}) e^{-i\mathbf{k}\mathbf{x}}$ evolve according to

$$\partial_t a(\mathbf{k}) = \lambda(k)\, a(\mathbf{k}) \tag{6.4}$$

where

$$\lambda(k) = \left[-1 + \frac{\langle |s|^2 \rangle}{2\sigma^2}(1 - e^{-\sigma^2 k^2}) \right] - \eta\, k^2 \tag{6.5}$$

denotes the growth rate of modes with $|\mathbf{k}| = k$. For the following we assume $\langle |s|^2 \rangle = 2$, which can always be achieved by a proper rescaling of the cortical space. Then $\lambda(k)$ has a single maximum at

$$k_* = \frac{1}{\sigma}\sqrt{-\ln\eta} \tag{6.6}$$

provided that $\eta \leq 1$, cf. Fig.6.1(**a**). This mode will grow if

$$0 < \lambda(k_*) = -1 + 1/\sigma^2(1 - \eta) + \eta/\sigma^2 \ln\eta$$

which is fulfilled for $\sigma < \sigma_*$ with

$$\sigma_* = \sqrt{1 - \eta + \eta \ln\eta} \tag{6.7}$$

The typical wavelength Λ of the emerging pattern expected at the bifurcation onset is given by

$$\Lambda = 2\pi/k_* = 2\pi\sigma/\sqrt{-\ln\eta}$$

and scales linearly with σ.

In conclusion, the linear stability analysis of the elastic net reveals that a stream of random oriented point stimuli is sufficient to induce a finite wavelength instability of the unselective state $z(\mathbf{x}) = 0$ in the parameter regime $\eta < 1$ and $\sigma < \sigma_*(\eta)$, cf. Fig. 6.1(**b**).

6.3 Generalization of the Elastic Net

The approach of Durbin and Mitchison, due to its simplicity and intuitive appeal, has become very popular as a framework for modelling the development and interaction of cortical maps in the visual cortex [16, 74, 75].
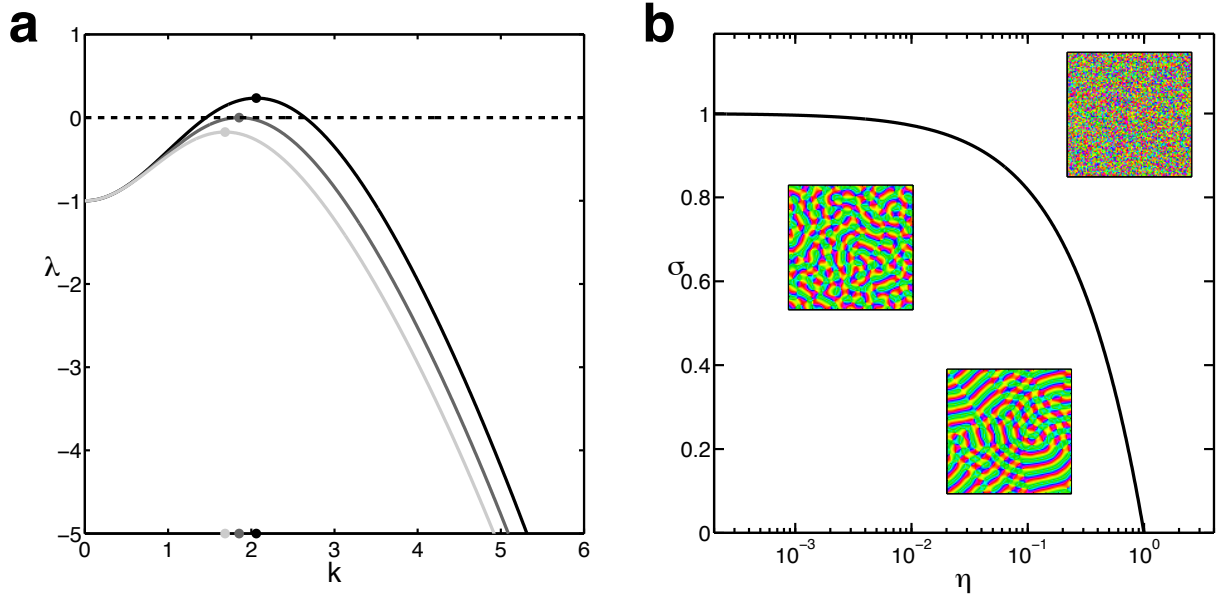
Figure 6.1: a) The homogeneous solution $z = 0$ is linearly stable when fluctuations at all spatial frequencies k are damped. This is the case when the growth rate $\lambda(k) < 0$ (*light gray*, $\sigma = 1.1\sigma_*$). At the point $\sigma = \sigma_*$ (*gray line*) the system becomes marginally unstable against fluctuations with $k = k_{crit}$, the critical wavenumber, (*gray dot*) where $\lambda(k_{crit}) = 0$. For $\sigma < \sigma_*$ a band of spatial frequencies grouped around the critical wavenumber starts to grow (*black line*, $\sigma = .9\sigma_*$). For all cases $\eta = 1/4$. **b)** The critical size of the coactivated domain σ_* depends on the lateral coupling strength η (*black line*). Inside the region $\sigma < \sigma_*(\eta)$ a pattern develops, outside of this region only the homogeneous state is stable (*as illustrated by the insets*).

However, one might wonder whether the stimulus ensemble used in those studies - sequences of isolated, oriented point stimuli, one stimulus at each time step - is not an oversimplified picture of the visual input to cortical neurons since it ignores the fact (discussed in the next section) that oriented edges in natural images often are part of a common contour and thus do not occur in isolation. Certainly the symmetry of Eq.(6.3) under orientation shifts is questionable in principle and the most obvious factor that will break this symmetry is the occurrence of oriented contours in typical visual scenes.

Here we generalize the elastic net in a way which allows to use contours, as extracted from a set of natural images, to train the network. Depending on the spatial resolution applied for the analysis of a visual scene, oriented entities appear to be primarily 1-dimensional, e.g. lines and curves, but also 2-dimensional, e.g. oriented textures, or 0-dimensional, e.g. isolated oriented points. We propose to describe such a scene by a complex contour field

$$S(\mathbf{r}) = \sum_{j=1}^{N_0} \chi_j^{(0)}(\mathbf{r})\, s_j^{(0)}(\mathbf{r}) + \sum_{k=1}^{N_1} \chi_k^{(1)}(\mathbf{r})\, s_k^{(1)}(\mathbf{r}) + \sum_{l=1}^{N_2} \chi_l^{(2)}(\mathbf{r})\, s_l^{(2)}(\mathbf{r})$$

where $\chi^{(0)}(\mathbf{r})$ denotes a point density, $\chi^{(1)}(\mathbf{r})$ a line density and $\chi^{(2)}(\mathbf{r})$ is a regular 2-d density. The indices j, k and l count the individual 0-, 1- and 2-dimensional objects in the scene. The fields $s(\mathbf{r})$ denote the orientation preference to which cortical neurons are driven by this part of

the stimulus. For example, a collection of N oriented point stimuli can be described by

$$S^{(0)}(\mathbf{r}) = \sum_{j=1}^{N} \delta(\mathbf{r} - \mathbf{r}_j) \, e^{2i\theta_j}$$

where $\mathbf{r}_j$ denotes the location and θ_j the orientation of the j-th edge. For a curve $\mathcal{C} : [t_0, t_1] \to \mathbb{R}^2$ we would have a contribution

$$S^{(1)}(\mathbf{r}) = \left(\int_{t_0}^{t_1} dt \, \|\mathcal{C}'(t)\| \, \delta \left(\mathbf{r} - \mathcal{C}(t) \right) \right) e^{2i\theta(\mathbf{r})}$$

where $\theta(\mathbf{r})$ corresponds to the angle formed by the tangent vector of the curve at $\mathbf{r} \in \mathcal{C}$. Finally, for oriented textures defined over a domain $\mathcal{T} \subset \mathbb{R}^2$

$$S^{(2)}(\mathbf{r}) = \chi(\mathbf{r}) s(\mathbf{r})$$

where $\chi(\mathbf{r})$ is given by the characteristic function of the texture,

$$\chi(\mathbf{r}) = \begin{cases} 1 & \mathbf{r} \in \mathcal{T} \\ 0 & \text{elsewhere} \end{cases}$$

and $s(\mathbf{r})$ is a function $s : \mathcal{T} \subset \mathbb{R}^2 \to \mathbb{C}$.

We generalize the dynamics as follows

$$
\begin{aligned}
\partial_t z(\mathbf{x}) &= \left\langle \int d^2\mathbf{r} \, (S(\mathbf{r}) - z(\mathbf{x})) \, E(\mathbf{x}, \mathbf{r}) \right\rangle_{S(r) \in \mathcal{S}} - \eta \, \Delta z(\mathbf{x}) \\
\partial_t \mathbf{R}(\mathbf{r}) &= \left\langle \int d^2\mathbf{r} \, (\mathbf{r} \, \chi(\mathbf{r}) - \mathbf{R}(\mathbf{r})) \, E(\mathbf{x}, \mathbf{r}) \right\rangle_{S(r) \in \mathcal{S}} - \eta \, \Delta \mathbf{R}(\mathbf{x})
\end{aligned}
\tag{6.8}
$$

with

$$E(\mathbf{x}, \mathbf{r}) = \frac{e^{-\left(|\mathbf{R}(\mathbf{r}) - \mathbf{x}|^2 + |s(\mathbf{r}) - z(\mathbf{x})|^2 \right)/2\sigma^2}}{\int d^2\mathbf{r}' \chi(\mathbf{r}') \int d^2\mathbf{x}' \, e^{-(|\mathbf{R}(\mathbf{r}') - \mathbf{x}'|^2 - |s(\mathbf{r}') - z(\mathbf{x}')|^2)/2\sigma^2}}.$$

The dynamics (6.8) is a gradient descent and has the Lyapunov functional

$$F = -2\sigma^2 \langle \ln \int d^2\mathbf{r}' \chi(\mathbf{r}') \int d^2\mathbf{x}' e^{-(|\mathbf{R}(\mathbf{r}') - \mathbf{x}'|^2 + |s(\mathbf{r}') - z(\mathbf{x}')|^2)/2\sigma^2} \rangle + \eta \int d^2\mathbf{x}' \left(|\nabla z(\mathbf{x}')|^2 + |\nabla \mathbf{R}(\mathbf{x}')|^2 \right).$$

6.4 The Statistics of Natural Images
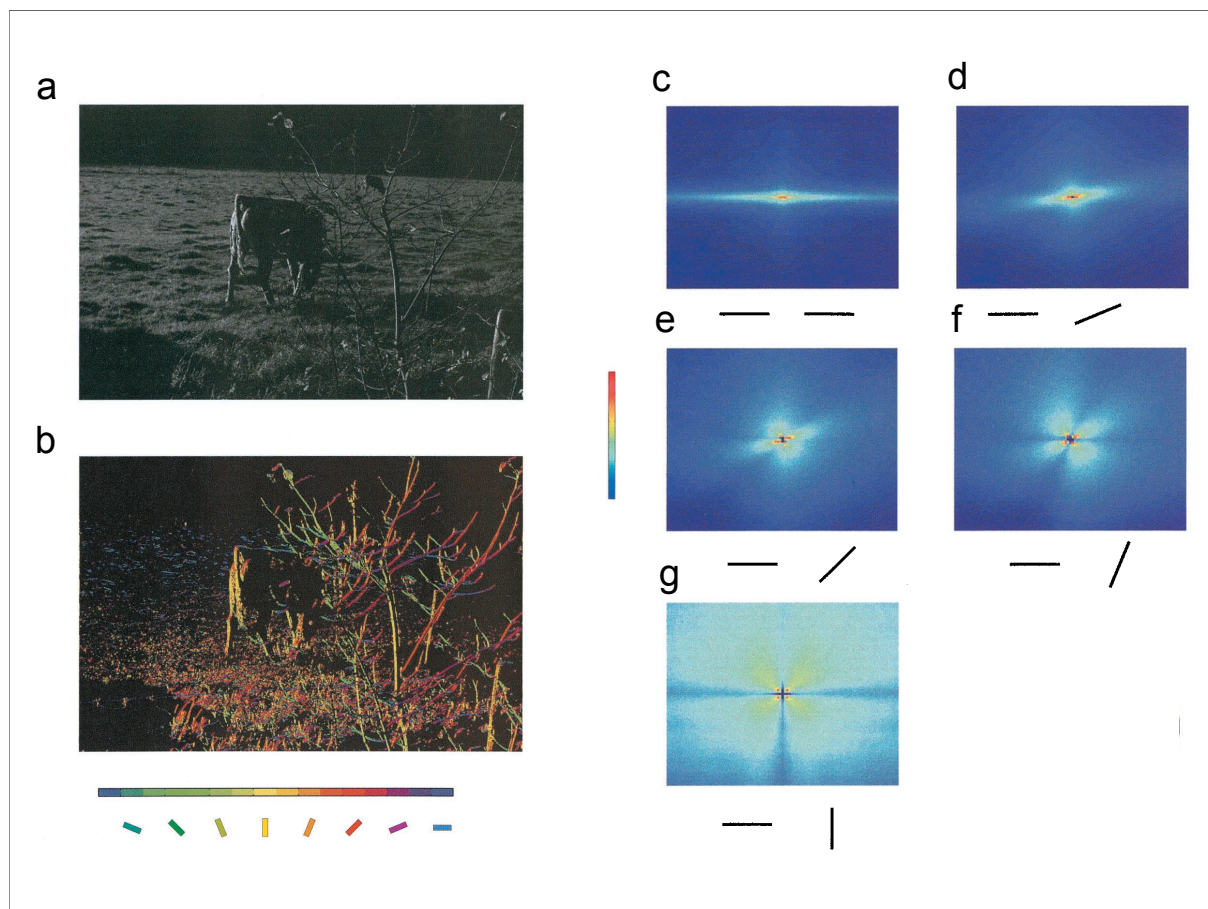
Figure 6.2: Statistics of natural scenes. (**a**) Natural scene. (**b**) contour-filtered scene (colors code orientation as indicated by the *bars below*). (**c-g**) Cooccurrence histograms for orientations shown below the graphs (*left:* central orientation θ_c, *right:* distal orientation θ_d). As suggested by the colorcode high probabilities are shown in red, low probabilities in blue. The range of values was not provided in absolute numbers and in fact differs considerably across subplots [76]. (*adapted from* [52]).

Orientations in natural images are spatially correlated due to the fact that they are often part of a common contour. In recent years efforts have been made to characterize and to quantify their statistics [77, 52, 78, 79, 80, 81]. Here we briefly summarize the main result of Sigman et al. [52] who computed the pair occurrence statistics of oriented edges for a large dataset of natural images. Each picture (e.g. Fig. 6.2(**a**)) was first processed with a set of spatially localized oriented filters in order to determine the local orientation and orientation energy (defined as the maximum overlap of the local image patch with filters of any orientation) at each pixel **r**. In our notation these quantities would correspond to $\theta(\mathbf{r})$ and $|s(r)|$, respectively. Depending on their orientation energy and on an appropriately chosen threshold, $s_{th} \in \mathbb{R}$, pixels were then divided into two groups, 'oriented pixels' ($|s(\mathbf{r})| \geq s_{th}$) and 'non-oriented pixels' ($|s(\mathbf{r})| < s_{th}$). In our notation this binary classification would correspond to the characteristic function $\chi(\mathbf{r})$ of that particular image. The set of 'oriented pixels' obtained by this procedure is displayed

in Fig. 6.2(**b**), a colorcode is used to depict the orientations $\theta(\mathbf{x})$. The space dependence of the probability of finding pairs of line segments with a relative orientation of 0°, 22.5°, 45°, 67.5° and 90° is shown in Fig. 6.2(**c-g**). It is not uniform and exhibits a strong bias for collinear arrangements (Fig. 6.2(**c**)). As the relative difference in orientation between the two segments increases, two effects were observed: the main lobe of the histogram (which in the iso-oriented case extends in the collinear direction) rotates and shortens, and a second lobe appears at 90° from the first (Fig.6.2(**c-g**)). This effect progressed smoothly until the relative orientation of the two segments was 90°, where the two lobes were arranged in a symmetrical configuration.

It is interesting to compare these findings with the cooccurence histograms for orientation maps (cf. Chapters 3 and 5). The two principal axes discussed there exactly match the symmetry axes of the lobes in [52], with respect to their locations and also to the way they rotate when $\Delta = \theta_d - \theta_c$ increases. This should not come as a surprise: Although the overall shapes of the joint probability densities have little in common, e.g. oscillatory behaviour in r (the relative separation of the two locations) and cloverleaf modulations for OPMs vs. algebraic decay and strong collinear component for natural images [52], their symmetry properties have to be the same. This is a consequence of the general form of the pair occurrence histogram $P_{(r,\phi)}(\theta_c, \theta_d)$, Eq.(3.40), which also applies to the distribution of edges in natural images when the basic symmetry assumptions of Section 3.14 are fulfilled.

Accordingly, we expect that a decomposition of the pair occurrence histogram $P_{(r,\phi)}(\theta_c, \theta_d)$ of natural images into its direct summands

$$P_{(r,\phi)} = \frac{1}{\pi} \oplus P_{(r,\phi)}^{(2)} \oplus P_{(r,\phi)}^{(4)}$$

(cf. Eq.(3.41)) exhibits a strong 2-fold contribution, due to the predominant collinear bias, and a 4-fold component, which Sigman et al. attributed to shapes with closed contours, e.g. circles or ellipses. Indeed, the authors of [52] observe that the contribution from cocircular segments of a given Δ (i.e. edges lying on a common circular contour) to the histogram will have a 4-fold symmetry and rotate with $\Delta/2$. However, our analysis in Chapter 3 showed that this property is a general consequence of Euclidean symmetry and will occur whether contour ensembles contain circular closed shapes or not. An example for such an ensemble without closed contours is shown in Fig. 6.3(**c**).
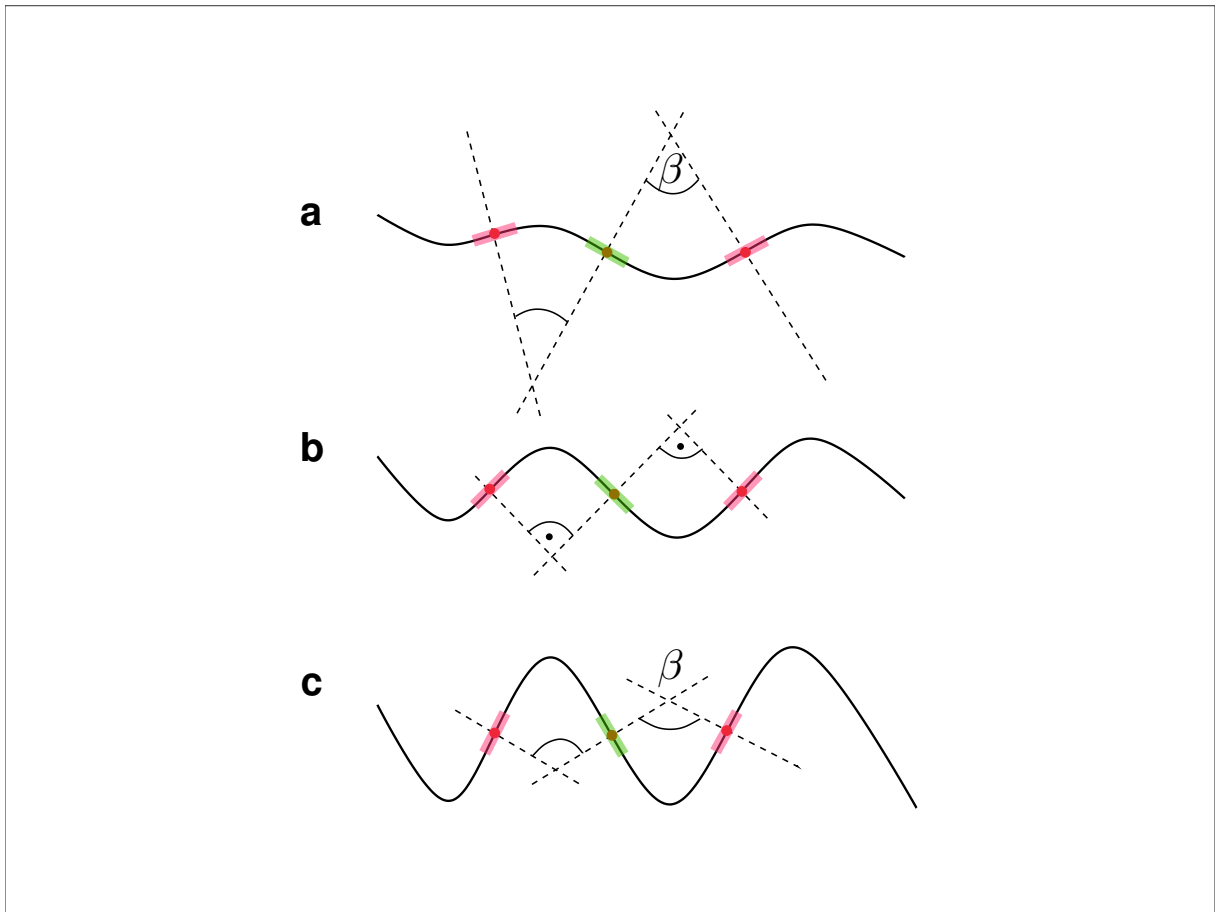
Figure 6.3: Curves with (**a**) curvilinear and also (**c**) cocircular contributions. (**b**) represents a limiting case. It suffices to investigate the intersection angles β of the normals at neighbouring turning points. If $0 \leq \beta \leq \pi/2$ then subsequent pairs of edges on the curve do not contribute to cocircular statistics, whereas for $\pi/2 < \beta \leq \pi$ they do.

6.5 Driving Hebbian Learning with Pairs of Contour Elements

Could the statistics of natural images, in particular its predominant feature, collinearity of line segments, possibly have an effect on the orientation map layout? Since is not possible to address this question using the elastic net in its original formulation by Durbin and Mitchison we will use the generalized model, Eq.(6.8), in combination with an adequate stimulus ensemble, as our starting point. As a simple stimulus ensemble one could for example consider random curves, or a discretized version of such, consisting of $N \geq 2$ oriented line segments. It is already very interesting to study the simplest case, $N = 2$, as shown in the following.

We consider an ensemble of pair stimuli, consisting of two line segments of orientation s_1 and s_2 at variable locations $\mathbf{r}_1$ and $\mathbf{r}_2$. A single realization thus can be written as

$$S(\mathbf{r}) = s_1\delta(\mathbf{r} - \mathbf{r}_1) + s_2\delta(\mathbf{r} - \mathbf{r}_2).$$

Assuming that stimuli occurring at different times are statistically independent, the sequence of stimuli can be modeled by a stationary spatiotemporal point process, defined by a stimulus rate

$p(\mathbf{r}_1, \mathbf{r}_2, s_1, s_2)$ which, due to translation invariance and spatial homogeneity, can be written as a product

$$p(\mathbf{r}_1, \mathbf{r}_2, s_1, s_2) = p_d(\mathbf{r}_2 - \mathbf{r}_1) \, p_s(s_1, s_2 | \mathbf{r}_2 - \mathbf{r}_1)$$

with the normalizations

$$\int d^2\mathbf{r} \, p_d(\mathbf{r}) = 1$$

and

$$\int d^2 s_1 \int d^2 s_2 \, p_s(s_1, s_2 | \mathbf{r}) = 1.$$

Now that we have defined the ensemble for a general stimulus rate we can perform ensemble averages and calculate some of its basic statistics.

For the average stimulus density (in a unit time interval) we obtain

$$\rho(\mathbf{x}) = \langle \sum_{j=1}^{2} \delta(\mathbf{x} - \mathbf{r}_j) \rangle = \int d^2\mathbf{r}_1 \int d^2\mathbf{r}_2 \, p_d(\mathbf{r}_2 - \mathbf{r}_1) \sum_{j=1}^{2} \delta(\mathbf{x} - \mathbf{r}_j) = 2,$$

i.e. per unit of time and unit of square length we will expect, on average, two line segments (that is, one stimulus pair).

For the correlation functions we obtain

$$
\begin{aligned}
C_1(\mathbf{y} - \mathbf{x}) = \frac{1}{2}\langle S(\mathbf{x})\bar{S}(\mathbf{y}) \rangle &= \frac{1}{2}\langle \sum_{j,k} s_j \bar{s}_k \delta(\mathbf{x} - \mathbf{r}_j)\delta(\mathbf{y} - \mathbf{r}_k) \rangle \\
&= \frac{1}{2}\langle \sum_j s_j \bar{s}_j \delta(\mathbf{x} - \mathbf{r}_j)\delta(\mathbf{y} - \mathbf{x}) \rangle + \frac{1}{2}\langle \sum_{j,k \neq j} s_j \bar{s}_k \delta(\mathbf{x} - \mathbf{r}_j)\delta(\mathbf{y} - \mathbf{r}_k) \rangle \\
&= \langle |s|^2 \rangle \delta(\mathbf{y} - \mathbf{x}) + c_1(\mathbf{y} - \mathbf{x}) \qquad\qquad (6.9)
\end{aligned}
$$

and

$$
\begin{aligned}
C_2(\mathbf{y} - \mathbf{x}) = \frac{1}{2}\langle S(\mathbf{x})S(\mathbf{y}) \rangle &= \frac{1}{2}\langle \sum_{j,k} s_j s_k \delta(\mathbf{x} - \mathbf{r}_j)\delta(\mathbf{y} - \mathbf{r}_k) \rangle \\
&= \frac{1}{2}\langle \sum_j s_j s_j \delta(\mathbf{x} - \mathbf{r}_j)\delta(\mathbf{y} - \mathbf{r}_j) \rangle + \frac{1}{2}\langle \sum_{j,k \neq j} s_j s_k \delta(\mathbf{x} - \mathbf{r}_j)\delta(\mathbf{y} - \mathbf{r}_k) \rangle \\
&= \langle s^2 \rangle \delta(\mathbf{y} - \mathbf{x}) + c_2(\mathbf{y} - \mathbf{x}) \qquad\qquad (6.10)
\end{aligned}
$$

where we split off the singular part and denote the regular part by

$$
\begin{aligned}
c_1(\mathbf{r}) &= \langle s_1 \bar{s}_2 \delta(\mathbf{x} - \mathbf{r}_j)\delta(\mathbf{x} + \mathbf{r} - \mathbf{r}_k) \rangle \\
&= p_d(\mathbf{r}) \int d^2 s_1 \int d^2 s_2 \, (s_1 \bar{s}_2) \, p_s(s_1, s_2 | \mathbf{r}_2 - \mathbf{r}_1 = \mathbf{r}) \\
c_2(\mathbf{r}) &= \langle s_1 s_2 \delta(\mathbf{x} - \mathbf{r}_j)\delta(\mathbf{x} + \mathbf{r} - \mathbf{r}_k) \rangle \\
&= p_d(\mathbf{r}) \int d^2 s_1 \int d^2 s_2 \, (s_1 s_2) \, p_s(s_1, s_2 | \mathbf{r}_2 - \mathbf{r}_1 = \mathbf{r})
\end{aligned}
$$

To start to understand the effects of the visual world's two point statistics on orientation map development, studying the case $N = 2$ is sufficient, since one could, in principle, measure $p(\mathbf{r}_1, \mathbf{r}_2, s_1, s_2)$ for natural images and then use it in our model. Let us now discuss the dynamics.

For the stimulus ensemble $\mathcal{S}$ defined above the averaged dynamics has the form

$$\partial_t z(\mathbf{x}) = \langle (s_1 - z(\mathbf{x}))E_1(\mathbf{x}) + (s_2 - z(\mathbf{x}))E_2(\mathbf{x}) \rangle_{\mathcal{S}} + \eta \, \Delta z(\mathbf{x})$$
$$\partial_t \mathbf{R}(\mathbf{x}) = \langle (\mathbf{r}_1 - \mathbf{R}(\mathbf{x}))E_1(\mathbf{x}) + (\mathbf{r}_2 - \mathbf{R}(\mathbf{x}))E_2(\mathbf{x}) \rangle_{\mathcal{S}} + \eta \, \Delta \mathbf{R}(\mathbf{x}) \qquad (6.11)$$

where we define

$$E_j(\mathbf{x}) = \frac{e^{-\left(|\mathbf{r}_j - \mathbf{R}(\mathbf{x})|^2 + |s(\mathbf{r}_j) - z(\mathbf{x})|^2\right)/2\sigma^2}}{\sum_{k=1}^{2} \int d^2\mathbf{x}' \, e^{-(|\mathbf{r}_k - \mathbf{R}(\mathbf{x}')|^2 - |s(\mathbf{r}_k) - z(\mathbf{x}')|^2)/2\sigma^2}}.$$

Again, the homogeneous unselective pattern $z_0(\mathbf{x}) = 0$, $\mathbf{R}_0(\mathbf{x}) = \mathbf{x}$ is a stationary state. The linearized dynamics of z decouples from the dynamics of $\mathbf{R}$ in the vicinity of the homogeneous state and has the form

$$\partial_t z(\mathbf{x}) = \int d^2\mathbf{y} \left[\left(\frac{\delta F[z(\mathbf{x})]}{\delta z(\mathbf{y})} \right)_{(z_0,\mathbf{R}_0)} z(\mathbf{y}) + \left(\frac{\delta F[z(\mathbf{x})]}{\delta \bar{z}(\mathbf{y})} \right)_{(z_0,\mathbf{R}_0)} \bar{z}(\mathbf{y}) \right] \qquad (6.12)$$

where

$$F[z] \;\; = \;\; \langle (s(\mathbf{r}_1) - z(\mathbf{x})) \, E_1(\mathbf{x}) \rangle + \langle (s(\mathbf{r}_2) - z(\mathbf{x})) \, E_2(\mathbf{x}) \rangle + \eta \, \Delta z(\mathbf{x}).$$

First, we calculate the first part

$$\left(\frac{\delta F[z(\mathbf{x})]}{\delta z(\mathbf{y})} \right)_{(z_0,\mathbf{R}_0)} = -\delta(\mathbf{x} - \mathbf{y}) \left\langle \sum_{j=1}^{2} E_j(\mathbf{x}) \right\rangle_{(z_0,\mathbf{R}_0)} + \left\langle \sum_{j=1}^{2} s_j \frac{\delta E_j(\mathbf{x})}{\delta z(\mathbf{y})} \right\rangle_{(z_0,\mathbf{R}_0)} + \eta \, \Delta \delta(\mathbf{x} - \mathbf{y})$$

and then the second part

$$\left(\frac{\delta F[z(\mathbf{x})]}{\delta \bar{z}(\mathbf{y})} \right)_{(z_0,\mathbf{R}_0)} = \left\langle \sum_{j=1}^{2} s_j \frac{\delta E_j(\mathbf{x})}{\delta \bar{z}(\mathbf{y})} \right\rangle_{(z_0,\mathbf{R}_0)}.$$

The terms appearing in the first expression are

$$\left\langle \sum_{j=1}^{2} E_j(\mathbf{x}) \right\rangle_{(z_0,\mathbf{R}_0)} = \left\langle \frac{\sum_{j=1}^{2} e^{-\left(|\mathbf{x} - \mathbf{r}_j|^2 + |s_j|^2\right)/2\sigma^2}}{2\pi\sigma^2 \sum_{k=1}^{2} e^{-|s_k|^2/2\sigma^2}} \right\rangle$$
$$= 1$$

and

$$\left\langle \sum_{j=1}^{2} s_j \frac{\delta E_j(\mathbf{x})}{\delta z(\mathbf{y})} \right\rangle_{(z_0,\mathbf{R}_0)} = \left\langle \frac{\sum_{j=1}^{2} |s_j|^2 e^{-|\mathbf{x} - \mathbf{r}_j|^2/2\sigma^2} e^{-|s_j|^2/2\sigma^2}}{4\pi\sigma^4 \sum_{k=1}^{2} e^{-|s_k|^2/2\sigma^2}} \right\rangle \delta(\mathbf{x} - \mathbf{y})$$
$$- \left\langle \frac{\sum_{j,k=1}^{2} s_j \bar{s}_k \, e^{-(|\mathbf{x} - \mathbf{r}_j|^2 + |\mathbf{y} - \mathbf{r}_k|^2)/2\sigma^2} e^{-(|s_j|^2 + |s_k|^2)/2\sigma^2}}{8\pi^2\sigma^6 (\sum_{k=1}^{2} e^{-|s_k|^2/2\sigma^2})^2} \right\rangle \qquad (6.13)$$

In order to keep the calculation clear we make the simplifying assumption that stimuli s_k all have the same absolute value ("orientation energy"), $|s_k| = |s|$, and just differ in their phases. Since we assume that there is no bias for any orientation (which is a consequence of the shift-twist symmetry of the stimulus ensemble) the marginal distribution reads

$$p_s(s_k) = \int d^2 s_j\, p(s_k, s_j) = \frac{1}{2\pi s} \delta(|s_k| - |s|).$$

Furthermore,

$$\langle |s_k|^2 \rangle = |s|^2.$$

The expression then simplifies to

$$\left\langle \sum_{j=1}^{2} s_j \frac{\delta E_j(\mathbf{x})}{\delta z(\mathbf{y})} \right\rangle_{(z_0, \mathbf{R}_0)} = \frac{\langle |s|^2 \rangle}{2\sigma^2} \delta(\mathbf{x} - \mathbf{y}) - \frac{\langle |s|^2 \rangle}{16\pi\sigma^4} e^{-|\mathbf{x}-\mathbf{y}|^2/4\sigma^2} - \frac{\langle s_1 \bar{s}_2\, e^{-(|\mathbf{x}-\mathbf{r}_1|^2 + |\mathbf{y}-\mathbf{r}_2|^2)/2\sigma^2} \rangle}{16\pi^2\sigma^6}$$

and we finally obtain

$$\left(\frac{\delta F[z(\mathbf{x})]}{\delta z(\mathbf{y})} \right)_{(z_0, \mathbf{R}_0)} = \delta(\mathbf{x} - \mathbf{y}) \left(\frac{\langle |s|^2 \rangle}{2\sigma^2} - 1 \right) - \frac{\langle |s|^2 \rangle}{16\pi\sigma^4} e^{-|\mathbf{x}-\mathbf{y}|^2/4\sigma^2} \tag{6.14}$$
$$- \frac{1}{16\pi^2\sigma^6} \int d^2\mathbf{r}_1 d^2\mathbf{r}_2\, c_1(\mathbf{r}_2 - \mathbf{r}_1)\, e^{-(|\mathbf{x}-\mathbf{r}_1|^2 + |\mathbf{y}-\mathbf{r}_2|^2)/2\sigma^2} + \eta\, \Delta\delta(\mathbf{x} - \mathbf{y})$$

or, expressed in terms of C_1 (cf. Eq.(6.9)),

$$\left(\frac{\delta F[z(\mathbf{x})]}{\delta z(\mathbf{y})} \right)_{(z_0, \mathbf{R}_0)} = \delta(\mathbf{x} - \mathbf{y}) \left(\frac{\langle |s|^2 \rangle}{2\sigma^2} - 1 \right)$$
$$- \frac{1}{16\pi^2\sigma^6} \int d^2\mathbf{r}_1 d^2\mathbf{r}_2\, C_1(\mathbf{r}_2 - \mathbf{r}_1)\, e^{-(|\mathbf{x}-\mathbf{r}_1|^2 + |\mathbf{y}-\mathbf{r}_2|^2)/2\sigma^2} + \eta\, \Delta\delta(\mathbf{x} - \mathbf{y}).$$

A comparison with Eq.(6.3) shows that the linearized dynamics for $N = 2$, Eq.(6.12), reduces to the case $N = 1$ in the limit $c_1(\mathbf{r}_2 - \mathbf{r}_1) \to \langle |s|^2 \rangle \delta(\mathbf{r}_2 - \mathbf{r}_1)$, when $P_d(\mathbf{r}) \to \delta(\mathbf{r})$. If $C_1(\mathbf{r})$ is rotation invariant, which we assume here, then the first part of the linearization is equivariant under rotations and phase shifts.

Let us now calculate the second term, which is obtained by linearization with respect to $\bar{z}$:

$$\left(\frac{\delta F[z(\mathbf{x})]}{\delta \bar{z}(\mathbf{y})} \right)_{(z_0, \mathbf{R}_0)} = \left\langle \sum_{j=1}^{2} s_j \frac{\delta E_j(\mathbf{x})}{\delta \bar{z}(\mathbf{y})} \right\rangle_{(z_0, \mathbf{R}_0)}.$$

Going through the same steps as before, most of the terms vanish due to $\langle s^2 \rangle = 0$ and we are left with a single remaining term

$$\left(\frac{\delta F[z(\mathbf{x})]}{\delta \bar{z}(\mathbf{y})} \right)_{(z_0, \mathbf{R}_0)} = -\left\langle \frac{\sum_{j,k}^{2} s_j s_k\, e^{-(|\mathbf{y}-\mathbf{r}_k|^2 + |\mathbf{x}-\mathbf{r}_j|^2)/2\sigma^2} e^{-|s|^2/\sigma^2}}{32\pi^2\sigma^6 e^{-|s|^2/\sigma^2}} \right\rangle \tag{6.15}$$
$$= -\frac{1}{16\pi^2\sigma^6} \int d^2\mathbf{r}_1 d^2\mathbf{r}_2 c_2(\mathbf{r}_2 - \mathbf{r}_1)\, e^{-(|\mathbf{y}-\mathbf{r}_2|^2 + |\mathbf{x}-\mathbf{r}_1|^2)/2\sigma^2}$$

All together, up to linear order we find

$$
\partial_t z(\mathbf{x}) = \left(\frac{\langle |s|^2 \rangle}{2\sigma^2} - 1 \right) z(\mathbf{x}) - \frac{\langle |s|^2 \rangle}{16\pi\sigma^4} \int d^2\mathbf{y} \, e^{-|\mathbf{x}-\mathbf{y}|^2/4\sigma^2} z(\mathbf{y}) - \eta \Delta z(\mathbf{x})
$$

$$
- \frac{1}{16\pi^2\sigma^6} \int d^2\mathbf{y} \int d^2\mathbf{r}_1 d^2\mathbf{r}_2 \, c_1(\mathbf{r}_1 - \mathbf{r}_2) \, e^{-(|\mathbf{x}-\mathbf{r}_1|^2 + |\mathbf{y}-\mathbf{r}_2|^2)/2\sigma^2} z(\mathbf{y})
$$

$$
- \frac{1}{16\pi^2\sigma^6} \int d^2\mathbf{y} \int d^2\mathbf{r}_1 d^2\mathbf{r}_2 \, c_2(\mathbf{r}_1 - \mathbf{r}_2) \, e^{-(|\mathbf{x}-\mathbf{r}_1|^2 + |\mathbf{y}-\mathbf{r}_2|^2)/2\sigma^2} \bar{z}(\mathbf{y}) \qquad (6.16)
$$

or in k-space, after a Fourier transform,

$$
\partial_t a(\mathbf{k}) = \left[-1 + \frac{\langle |s|^2 \rangle}{2\sigma^2} (1 - \frac{e^{-\sigma^2 |\mathbf{k}|^2}}{2}) - 2\pi \, p_1(\mathbf{k}) \frac{e^{-\sigma^2 |\mathbf{k}|^2}}{4\sigma^2} - \eta |\mathbf{k}|^2 \right] a(\mathbf{k})
$$

$$
- 2\pi \, p_2(\mathbf{k}) \frac{e^{-\sigma^2 |\mathbf{k}|^2}}{4\sigma^2} \, \bar{a}(-\mathbf{k}), \qquad (6.17)
$$

where $p_1(\mathbf{k})$ and $p_2(\mathbf{k})$ denote the Fourier transforms $c_1(\mathbf{r})$ and $c_2(\mathbf{r})$. Again, for $p_1(\mathbf{k}) \to \langle |s|^2 \rangle / (2\pi)$ and $p_2(\mathbf{k}) \to 0$ (which corresponds to the limit $c_1(\mathbf{r}) \to \langle |s|^2 \rangle \delta(\mathbf{r})$, $c_2(\mathbf{r}) \to \langle s^2 \rangle \delta(\mathbf{r}) = 0$ discussed above) we obtain the same result for $\lambda(k)$ as in the case $N = 1$, Eq.(6.5). Note that the terms in Eqns.(6.16) and (6.17) which occur with a *negative sign* originate from taking the derivative of the *normalization term* in the denominator of the activities E_j (cf. Eqns.(6.13) and (6.15)) as required by the chain rule, except of the term involving the Laplacian. We will come back to this point later.

6.6 A Collinear Stimulus Ensemble

As a specific example we propose a simple stimulus ensemble consisting of random pairs of oriented stimuli with an adjustable degree of collinearity κ, $0 \leq \kappa \leq 1$. For simplicity the spatial distance between both stimuli is drawn from a Gaussian distribution with zero mean and standard deviation $d \geq 0$. The stimulus distribution states

$$
p(\mathbf{r}_1, \mathbf{r}_2, s_1, s_2) = \frac{1}{2\pi d^2} e^{-|\mathbf{r}_1 - \mathbf{r}_2|/2d^2} \left(\frac{1}{(2\pi s)^2} (1 - \kappa) \, \delta(|s_1| - |s|) \delta(|s_2| - |s|) + \right.
$$

$$
\left. + \kappa \, \delta(s_1 - |s| \, e^{2i \arg(\mathbf{r}_2 - \mathbf{r}_1)}) \delta(s_1 - s_2) \right) \qquad (6.18)
$$

and is chosen such that for $\kappa = 0$ the orientations of both stimuli in the pair are uncorrelated, whereas for $\kappa = 1$ they are strictly collinear.

For the spatial density of stimuli we obtain

$$
\rho(\mathbf{x}) = \langle \sum_{j=1}^{2} \delta(\mathbf{x} - \mathbf{r}_j) \rangle
$$

$$
= \int d^2\mathbf{r}_1 d^2\mathbf{r}_2 d^2 s_1 d^2 s_2 \, p(\mathbf{r}_1, \mathbf{r}_2, s_1, s_2) \sum_{j=1}^{2} \delta(\mathbf{x} - \mathbf{r}_j)
$$

$$
= 2 \cdot ((1 - \kappa) + \kappa)
$$

$$
= 2
$$

For the nonsingular part of the correlation functions we find

$$
\begin{aligned}
c_1(\mathbf{r}) &= \langle s_1 \bar{s}_2 \, \delta(\mathbf{x} - \mathbf{r}_1) \delta(\mathbf{x} + \mathbf{r} - \mathbf{r}_2) \rangle && (6.19) \\
&= \int d^2 s_1 d^2 s_2 \, p(\mathbf{x}, \mathbf{x} + \mathbf{r}, s_1, s_2) \, s_1 \bar{s}_2 \\
&= \frac{\kappa \langle |s|^2 \rangle}{2\pi d^2} \, e^{-|\mathbf{r}|^2 / 2d^2}
\end{aligned}
$$

which is rotation symmetric and

$$
\begin{aligned}
c_2(\mathbf{r}) &= \langle s_1 s_2 \, \delta(\mathbf{x} - \mathbf{r}_1) \delta(\mathbf{x} + \mathbf{r} - \mathbf{r}_2) \rangle && (6.20) \\
&= \int d^2 s_1 d^2 s_2 \, p(\mathbf{x}, \mathbf{x} + \mathbf{r}, s_1, s_2) \, s_1 s_2 \\
&= \frac{\kappa \langle |s|^2 \rangle}{2\pi d^2} \, e^{-|\mathbf{r}|^2 / 2d^2} \, e^{4i \arg \mathbf{r}}
\end{aligned}
$$

such that

$$
c_2(\mathbf{r}) = e^{4i \arg \mathbf{r}} c_1(\mathbf{r}). \tag{6.21}
$$

Their Fourier transforms are given by

$$
\begin{aligned}
p_1(\mathbf{k}) &= \frac{1}{2\pi} \int d^2 \mathbf{r} \frac{\kappa \langle |s|^2 \rangle}{2\pi d^2} e^{-|\mathbf{r}|^2 / 2d^2} e^{i \mathbf{k} \mathbf{r}} && (6.22) \\
&= \frac{\kappa \langle |s|^2 \rangle}{2\pi} e^{-\frac{1}{2} |\mathbf{k}|^2 d^2}
\end{aligned}
$$

and

$$
\begin{aligned}
p_2(\mathbf{k}) &= \frac{1}{2\pi} \int d^2 \mathbf{r} \frac{\kappa \langle |s|^2 \rangle}{2\pi d^2} e^{-\mathbf{r}^2 / 2d^2} e^{4i \arg \mathbf{r}} e^{i \mathbf{k} \mathbf{r}} && (6.23) \\
&= \frac{\kappa \langle |s|^2 \rangle \left(4|\mathbf{k}|^2 d^2 - 24 + e^{-\frac{1}{2}|\mathbf{k}|^2 d^2} (24 + 8|\mathbf{k}|^2 d^2 + |\mathbf{k}|^4 d^4) \right)}{2\pi |\mathbf{k}|^4 d^4} e^{4i \arg \mathbf{k}}
\end{aligned}
$$
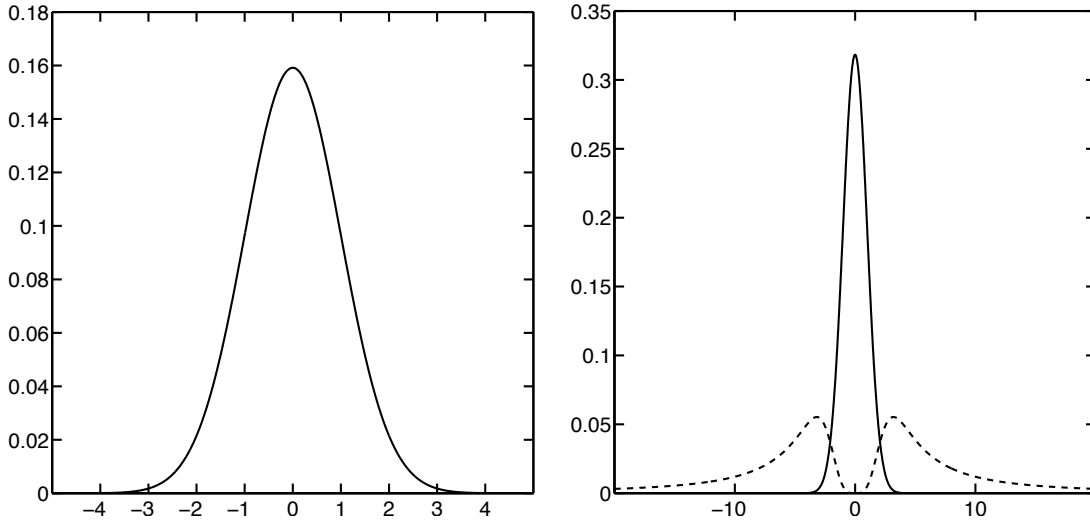
Figure 6.5: Monopole and quadrupole ('cloverleaf') parts of the correlation functions. (**a**): Radial projection of the correlation function $c_1(\mathbf{r})$, which is identical to the projection of cloverleaf part of $c_2(\mathbf{r})$ due to Eq.(6.21). (**b**): Radial projection of $p_1(\mathbf{k})$ *(full line)* and cloverleaf part of $p_2(\mathbf{k})$ *(dotted line)*.
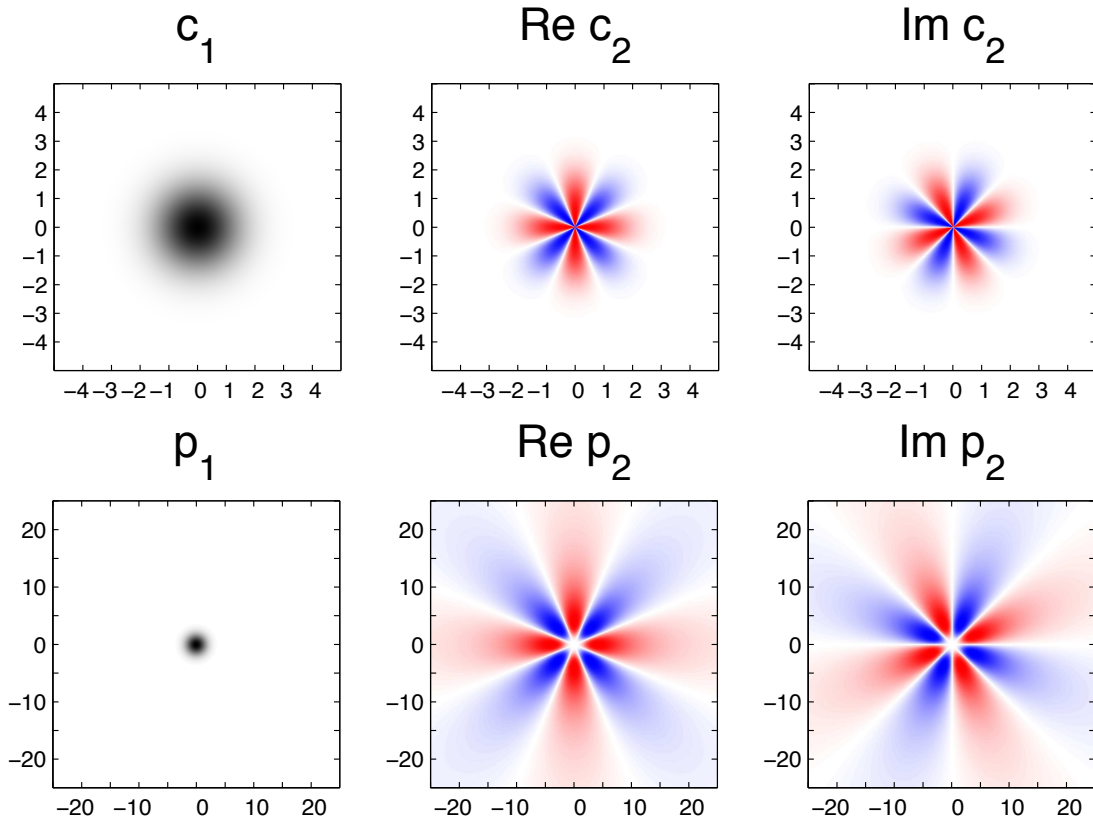
Figure 6.4: Regular part of the 2D-correlation functions $c_1(\mathbf{r})$ and $c_2(\mathbf{r})$ and their Fourier transforms $p_1(\mathbf{k})$ and $p_2(\mathbf{k})$ for the example stimulus ensemble defined in Eq.(6.18) for the parameter set ($d = 1$, $\kappa = 1$).

An example of the regular correlation functions $c_1(\mathbf{r})$, $c_2(\mathbf{r})$ and their Fourier transforms $p_1(\mathbf{k})$, $p_2(\mathbf{k})$ is depicted in Fig. 6.4 for the parameter set $d = 1, \kappa = 1$. The real and complex parts of c_2 and p_2 reveal a cloverleaf modulation which only vanishes when the degree of collinearity $\kappa = 0$. Their 0-th and 4-th angular Fourier components, $c_1^{(0)}(r), c_2^{(4)}(r)$ and $p_1^{(0)}(k), p_2^{(4)}(k)$ (see Chapter 3 for their definition) are shown in Fig. 6.5. Note that the apparent fact that $|p_2^{(4)}(k)| \le p_1^{(0)}(k)$ is not fulfilled is not a contradiction to our previous statement, $|P_2(\mathbf{k})| \le |P_1(\mathbf{k})|$ (cf. Eq. (3.14)), since $P_1(k) = p_1(k) + \langle |s|^2 \rangle / (2\pi)$ and hence is shifted by a positive constant. The collinear stimulus ensemble thus exhibits a clear signature of shift-twist symmetry, quantified by the order parameter

$$
\begin{aligned}
q(|\mathbf{k}|) &= P_2(\mathbf{k})\, e^{-4i \arg \mathbf{k}} / P_1(|\mathbf{k}|) \\
&\frac{\kappa}{1+\kappa} \frac{\left(4|\mathbf{k}|^2 d^2 - 24 + e^{-\frac{1}{2}|\mathbf{k}|^2 d^2}(24 + 8|\mathbf{k}|^2 d^2 + |\mathbf{k}|^4 d^4)\right)}{|\mathbf{k}|^4 d^4\, e^{-\frac{1}{2}|\mathbf{k}|^2 d^2}}
\end{aligned}
$$

which scales as $\kappa/(1+\kappa)$ with the degree of collinearity κ. Note that $q(k)$ assumes *positive* values for all wave numbers k in the possible range of values $0 \le \kappa \le 1$, $d \ge 0$. We expect this also to be the case for natural images. However, shift symmetry breaking as we observed it in the tree shrew dataset occurs with a *negative* q. Can we understand this sign flip in the statistics within our simple model?

Using Eqns.(6.22) and (6.23) in Eq.(6.17) one obtains for the linearized dynamics

$$
\begin{aligned}
\partial_t a(\mathbf{k}) &= \left[-1 + \frac{\langle |s|^2 \rangle}{2\sigma^2} \left(1 - \frac{e^{-\sigma^2|\mathbf{k}|^2}(1 + \kappa e^{-\frac{1}{2}|\mathbf{k}|^2 d^2})}{2} \right) - \eta|\mathbf{k}|^2 \right] a(\mathbf{k}) \\
&\quad - \frac{\kappa \langle |s|^2 \rangle e^{-\sigma^2|\mathbf{k}|^2}\left(4|\mathbf{k}|^2 d^2 - 24 + e^{-\frac{1}{2}|\mathbf{k}|^2 d^2}(24 + 8|\mathbf{k}|^2 d^2 + |\mathbf{k}|^4 d^4)\right)}{4\sigma^2 |\mathbf{k}|^4 d^4} e^{4i \arg \mathbf{k}} \bar{a}(-\mathbf{k})
\end{aligned}
\tag{6.24}
$$

As already noted the dynamics of the original elastic net is retrieved in the limit $d \to 0$, $\kappa = 1$ (cf. Eq.(6.5)). We use the normalization $\langle |s|^2 \rangle = 2$. In analogy to Eq.(6.5) we define $\lambda_{d,\kappa}(k)$ as the prefactor of $a(\mathbf{k})$,

$$
\lambda_{d,\kappa}(k) = -1 + \frac{1}{\sigma^2} - \frac{e^{-\sigma^2 k^2}(1 + \kappa e^{-\frac{1}{2}k^2 d^2})}{2\sigma^2} - \eta k^2
\tag{6.25}
$$

For general (d, κ) the maximum of $\lambda_{d,\kappa}(k)$ is reached at $k = k_{max}$ which is defined by the solution of

$$
-\ln 2\eta = \sigma^2 k^2 - \ln(1 + \kappa(1 + \frac{d^2}{2\sigma^2})e^{-\frac{1}{2}k^2 d^2})
$$

and can be obtained numerically. For fixed σ

$$
\lambda_{d,\kappa}(k) \ge \lambda_{0,1}(k)
$$

where $\lambda_{0,1}(k)$ equals the linear growth rate of the original elastic net, Eq.(6.5). Also, $k_{max}(d, \kappa)$ quickly approaches the asymptotic value
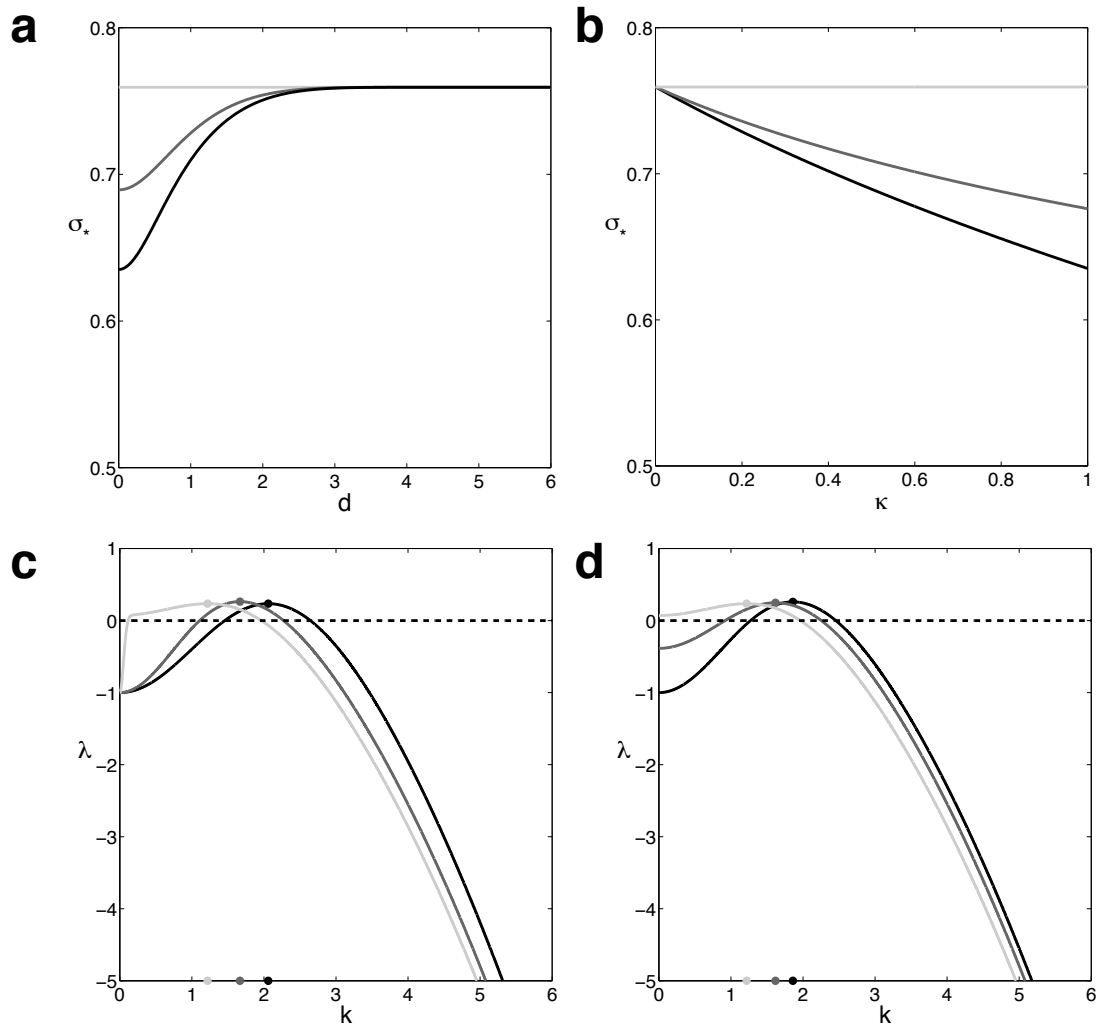
$$
k_\infty^{max} = \frac{1}{\sigma}\sqrt{-\ln 2\eta}
$$

Figure 6.6: (**a,b**) The critical value σ_* depends on the parameters of the stimulus ensemble, d and κ. (**c,d**) The critical wavelength of the pattern at $\sigma = \sigma_*$ depends on the parameters of the stimulus ensemble, d and κ. In all plots $\eta = 1/4$.
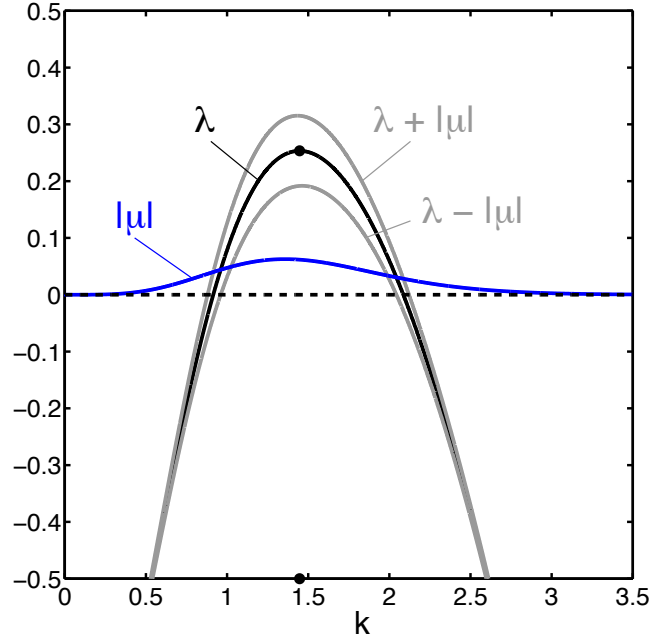
Figure 6.7: Illustration of the spectrum of the shift symmetric and the shift symmetry breaking linear terms, $\lambda(k)$ and $\mu(k)$ in Eq.(6.26) and (6.27). Note that $\mu(k) \to 0$ for $k \to 0$ and $k \to \infty$.

in the limit $d \to \infty$ or $\kappa \to 0$. Similarly, the critical value σ_* (the value of σ at which a pattern starts to grow) now depends also on d and κ (cf. Fig. 6.6).

Let us consider the question raised above, whether our model is able to explain the sign flip in the correlation functions. Eq.(6.24) can be rewritten as

$$\partial_t a(\mathbf{k}) = \lambda(\mathbf{k})a(\mathbf{k}) - e^{4i \arg \mathbf{k}}\mu(\mathbf{k})\bar{a}(-\mathbf{k})$$

with

$$\lambda(\mathbf{k}) = -1 + \frac{\langle|s|^2\rangle}{2\sigma^2}\left(1 - \frac{e^{-\sigma^2|\mathbf{k}|^2}(1 + \kappa e^{-\frac{1}{2}|\mathbf{k}|^2 d^2})}{2}\right) - \eta|\mathbf{k}|^2 \tag{6.26}$$

$$\mu(\mathbf{k}) = \frac{\kappa\langle|s|^2\rangle e^{-\sigma^2|\mathbf{k}|^2}\left(4|\mathbf{k}|^2 d^2 - 24 + e^{-\frac{1}{2}|\mathbf{k}|^2 d^2}(24 + 8|\mathbf{k}|^2 d^2 + |\mathbf{k}|^4 d^4)\right)}{4\sigma^2|\mathbf{k}|^4 d^4} \tag{6.27}$$

The linearized dynamics of the fastest growing modes with $|\mathbf{k}| = k_{max}(d,\kappa)$ then, after a proper rescaling of the fields, can be written

$$\partial_t a(\mathbf{k})|_{|\mathbf{k}|=k_{max}} = \left(a(\mathbf{k}) - \frac{\mu(\mathbf{k})}{\lambda(\mathbf{k})}e^{4i \arg \mathbf{k}}\bar{a}(-\mathbf{k})\right)_{\mathbf{k}=k_{max}} \tag{6.28}$$

After setting

$$\epsilon = \mu(k_{max})/\lambda(k_{max})$$

we see that Eq.(6.28) is formally equivalent to the linear part of the amplitude equations for planforms in presence of shift-twist symmetry, Eq.(4.13), and identical up to the negative sign before the ϵ term, which originates in the normalization term in the activity rule. We now

understand that this minus sign induces a sign flip in the statistics: the analysis of the pattern selection in Chapter 4 suggests that the emerging orientation maps will form *odd* solutions, if the stimulus statistics is *even*, as is the case of a collinear stimulus ensemble. These results also indicate which factors can influence the absolute strength of shift-symmetry breaking in the spatial map structure. As expected, ϵ grows linearly with κ, thus a visual world with stronger collinearity is in general expected to lead to a higher degree of shift symmetry breaking. However, it also depends on d, the spatial scaled of contour correlations and on η, the strength of lateral coupling. As shown in Fig.6.8, ϵ in general decays to zero for $d/\Lambda_{max} \gg 1$ and also in the shift symmetric limit $d \to 0$. In between it assumes a maximum near $d = \Lambda_{max}/2$. This maximal value (and the size of ϵ for arbitrary d) is strongly dependent on the lateral coupling strength η and the degree of collinearity κ.
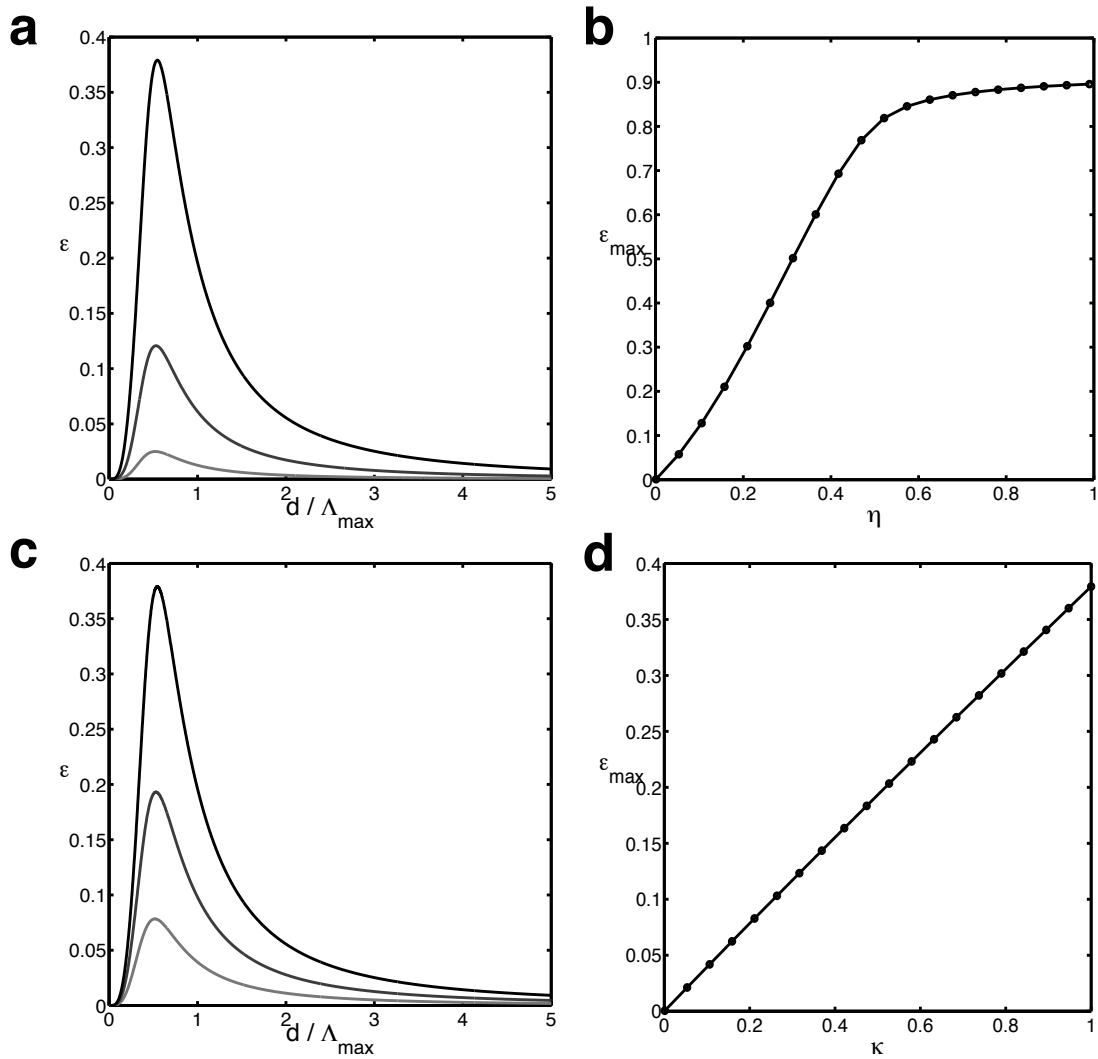
Figure 6.8: Strength of the shift symmetry breaking linear term in the generalized elastic network model. (**a**) ϵ depends on the spatial scale of contour correlations and goes to 0 for large d. (different curves: $\eta = 1/40, 1/10, 1/4$, fixed $\kappa = 1$). (**b**) The maximum value of ϵ strongly depends on η ($\kappa = 1$, fixed). In particular, ϵ can be made arbitrarily small, even for maximal collinearity $\kappa = 1$, in the limit of weak lateral coupling $\eta \to 0$. (**c, d**) same as (**a,** b) but for $\kappa = 0.2, 0.5, 1$ and fixed $\eta = 1/4$.

There are, thus, several scenarios in which weak degrees of shift symmetry breaking are expected. Firstly, if the degree of collinearity in visual scenes was relatively low. However even if the degree of collinearity was high, ϵ can also assume low values, if either lateral coupling strength is low or the range of contour correlations is large, or if a combination of these conditions applies. The simulations reported in the following demonstrate that in fact orientation maps with low degree of shift symmetry breaking can be formed even if κ is relatively large.

6.7 Numerical Simulations

In this section we present a numerical method to integrate the dynamics Eq.(6.11). For the initial part of the dynamics, $t \sim \tau := 1/\lambda$, we expect to see the results that are in line with the linearized dynamics examined in the previous section. For larger times, $t \gg \tau$, where the full nonlinearity has to be taken into account, it will be interesting to compare the patterns with the planform attractors of the generalized Swift-Hohenberg equation (Chapter 4).

The dynamics Eq.(6.11) has the form

$$\partial_t z(\mathbf{x}) = N[z(\cdot)] + \eta \Delta z(\mathbf{x}) \tag{6.29}$$

and can be split into a nonlinear integral operator $N[z(\cdot)]$ and a linear differential operator $\eta \Delta z(\mathbf{x})$. The latter part of the dynamics therefore consists of the diffusion equation,

$$\partial_t z(\mathbf{x}) = \eta \Delta z(\mathbf{x})$$

which can be exactly integrated in the Fourier representation,

$$a(\mathbf{k}, t + \delta t) = a(\mathbf{k}, t) e^{-\eta |\mathbf{k}|^2 \delta t}$$

where δt denotes the size of the time step. Numerically this integration scheme is exact and stable for arbitrary δt. We can use this fact by splitting the integration of Eq.(6.29) in two steps, consisting of an explicit integration of the nonlinear part, by the application of an Adams-Bashford step,

$$\delta N(\mathbf{x}, t + \delta t) = \frac{\delta t}{2}(3N[z(\cdot, t) - N[z(\cdot, t - \delta t)])$$

and a subsequent exact integration of the diffusion part in Fourier representation,

$$a(\mathbf{k}, t + \delta t) = \left(\delta \hat{N}(\mathbf{k}, t + \delta t) + a(\mathbf{k}, t) \right) e^{-\eta |\mathbf{k}|^2 \delta t}$$

The resulting integration scheme

$$z(\mathbf{x}, t) \rightarrow \delta N(\mathbf{x}, t + \delta t) \rightarrow \delta \hat{N}(\mathbf{k}, t + \delta t) \rightarrow a(\mathbf{k}, t + \delta t) \rightarrow z(\mathbf{x}, t + \delta t)$$

consists of two Fourier transforms, one explicit and one spectral step.

The field $z(\mathbf{x})$ was discretized on a quadratic lattice with 100×100 grid points representing an area of size $[0, L] \times [0, L]$. The integration time step δt was either set to a fraction of the intrinsic time scale, $\delta t_i = \tau/10$, or to a fraction of the characteristic time scale for the decay of the pattern under the influence of the diffusion term, $\delta t_d = \frac{1}{20}(\eta k_{max}^2)^{-1}$. If $\delta t_i > \delta t_d$ then δt_d was used, otherwise δt_i.
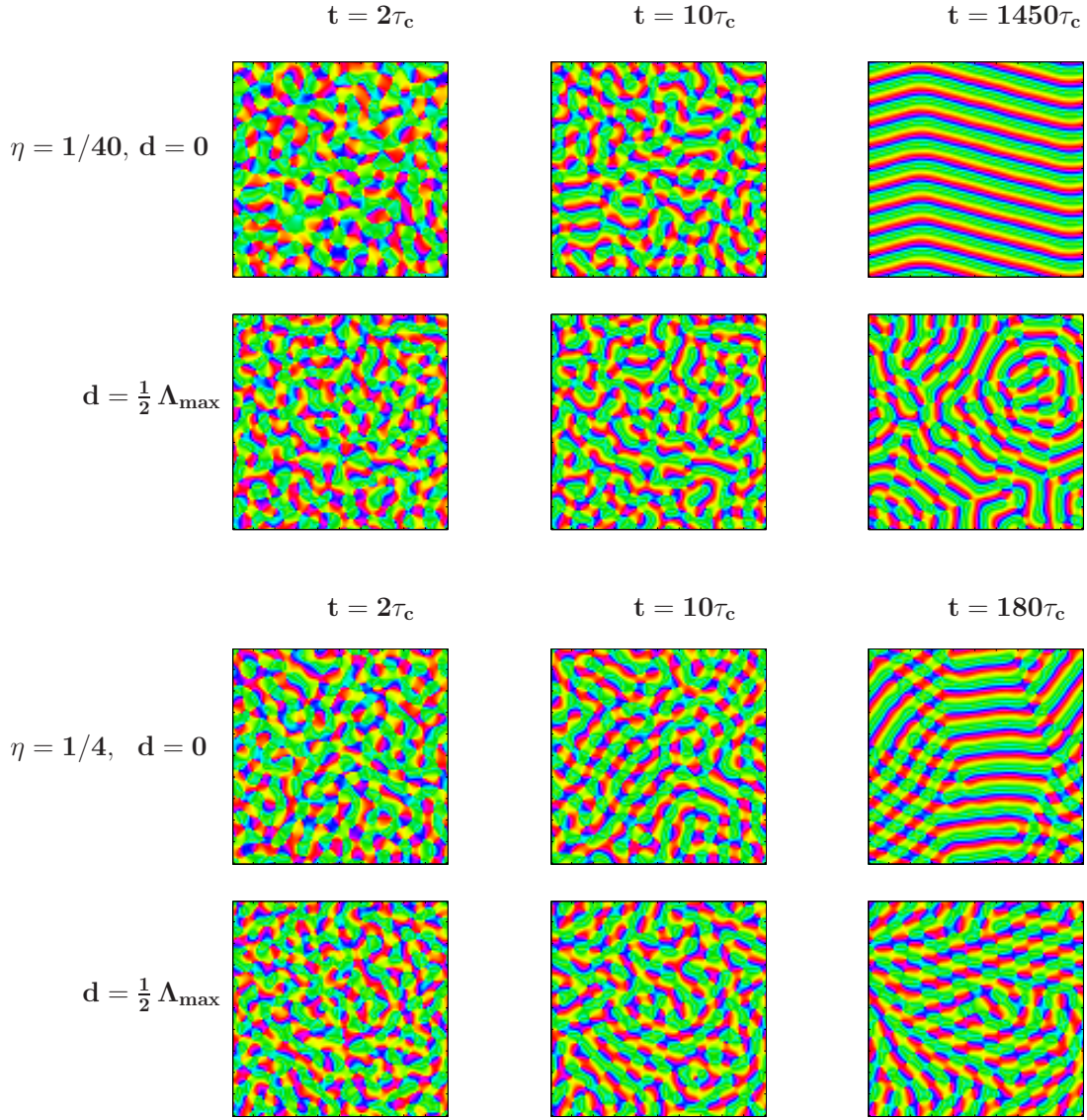
Figure 6.9: Simulations of the generalized elastic network model with full shift-symmetry ($d = 0$) and with broken shift symmetry $d \neq 0$. Simulations were performed with low ($\eta = 1/40$, *upper two rows*) and high strength of the lateral coupling ($\eta = 1/4$, *lower two rows*). Times are specified in units of the intrinsic timescale τ_c. For all cases the degree of collinearity is set to $\kappa = 1$.
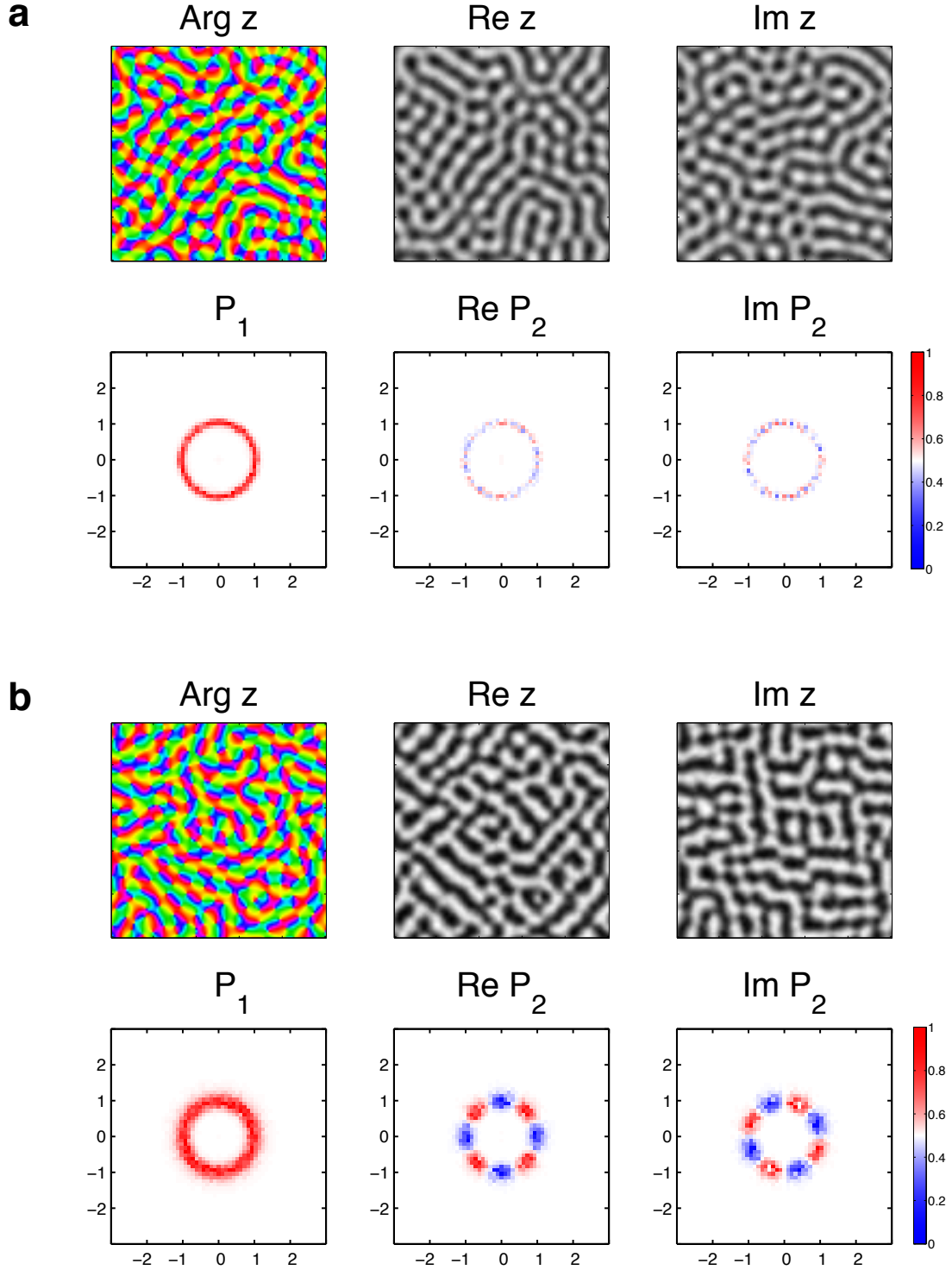
Figure 6.10: Spatial correlation structure of orientation maps (at $t = 10\tau_c$) for strong lateral coupling ($\eta = 1/4$). (**a**) $d = 0$, shift symmetric case. *First row:* map of preferred orientations *(left)*, difference maps for horizontal/vertical *(middle)* and left/right oblique *(right)* orientations. *Second row:* 2D-Fourier transforms $P_1(\mathbf{k})$ and $P_2(\mathbf{k})$ of correlation functions $C_1(\mathbf{r})$ and $C_2(\mathbf{r})$ of the pattern. (**b**), $d = 1/2\Lambda_{max}$, shift symmetry is broken. conventions as in (a).

Calculation of the nonlinear term

$$N[z(\cdot)] = \langle (s_1 - z(\mathbf{x})) \, E_1(\mathbf{x}) + (s_2 - z(\mathbf{x})) \, E_2(\mathbf{x}) \rangle_{\mathcal{S}}$$

requires an average over the stimulus ensemble $\mathcal{S}$ with respect to the stimulus density defined in Eq.(6.18), which was approximated by an average over a large number of random pair stimuli. The number of stimuli presented in each time step δt was chosen to match the criterion

$$\mathrm{std}(N[z(\cdot)]) \leq \frac{1}{4} \lim_{t \to \infty} \frac{1}{L^2} \int d^2\mathbf{x} \, |z(\mathbf{x}, t)|$$

in order to control the noise level of the nonlinear term. For the specified system size $4 \cdot 10^4$ samples in each time step turned out to be a sufficiently large number. Periodic boundary conditions were used in every respect, including the evaluation of the distance $|\mathbf{r}_2 - \mathbf{r}_1|$ of two random stimuli and of the distance $|\mathbf{r} - \mathbf{x}|$ between the receptive field center $\mathbf{x}$ of a cortical unit and a stimulus at $\mathbf{r}$. Initial conditions were set to be random white noise of a small amplitude, $|z(\mathbf{x}, t = 0)| \ll |z(\mathbf{x}, t \to \infty)|$. Different seeds of the random number generator where chosen for different realizations. The system size L was set to $L = 11 \cdot \Lambda$, where $\Lambda = 2\pi/k_{max}$ is the typical wavelength of the fastest growing mode and $\sigma = 0.9 \cdot \sigma_*$. The quantities, k_{max} and σ_* which both depend on κ and d, were calculated for each parameter set (d, κ) before the simulation in order to adjust the values L and σ. Time was measured in units of the intrinsic time scale $\tau := 1/\lambda_{d,\kappa}$, which also depends on (d, κ).

6.8 Results

Figure 6.10(**b**) shows that a cloverleaf signature becomes visible in early patterns ($t = 10\tau_c$) obtained from a numerical simulations, shown in Fig.6.9, when the predicted ϵ value assumes large values, compared to Fig. 6.10(**a**), where $\epsilon = 0$ since $d = 0$, which corresponds to the shift-symmetric case. Interestingly, the signature which results from the collinear stimulus ensemble is of the *negative* type. This is also confirmed in the orientation co-occurrence statistics, Fig. 6.11 and Fig. 6.12, which were obtained for to different values of η. For a weak lateral coupling, $\eta = 1/40$, Fig. 6.11(**h,i**), we observe both, a 4-fold and a 2-fold component very similar to the ones in the tree shrew dataset, Fig. 5.12(**h,i**). Both signatures are of the negative type and fairly weak. For strong coupling, $\eta = 1/4$, 6.12(**h,i**), again, both components are of the negative type. However, whereas the 2-fold component is comparable in size to the case for weak coupling, the 4-fold component has become much stronger and dominates the orientation co-occurrence histogram Fig.6.12(**a-f**). For longer times of the simulations $t \gg 10\tau_c$, Fig. 6.9, we observe that pinwheels annihilate and patterns develop into stripes (when the stimulus ensemble has no collinear component and is shift symmetric, $d = 0$) or into rhombic pinwheel crystals, when symmetry breaking is expected to be relatively strong, see Fig. 6.9 (*bottom row*). In any case, for asymptotically long times we find that patterns become too regular to explain realistic, aperiodic and pinwheel reach patterns. Presumably this is due to the lack of any type of long range interactions which are required by the model discussed in Chapter 4. It would be interesting to examine whether more complex, space filling stimuli could potentially induce such type of interactions.
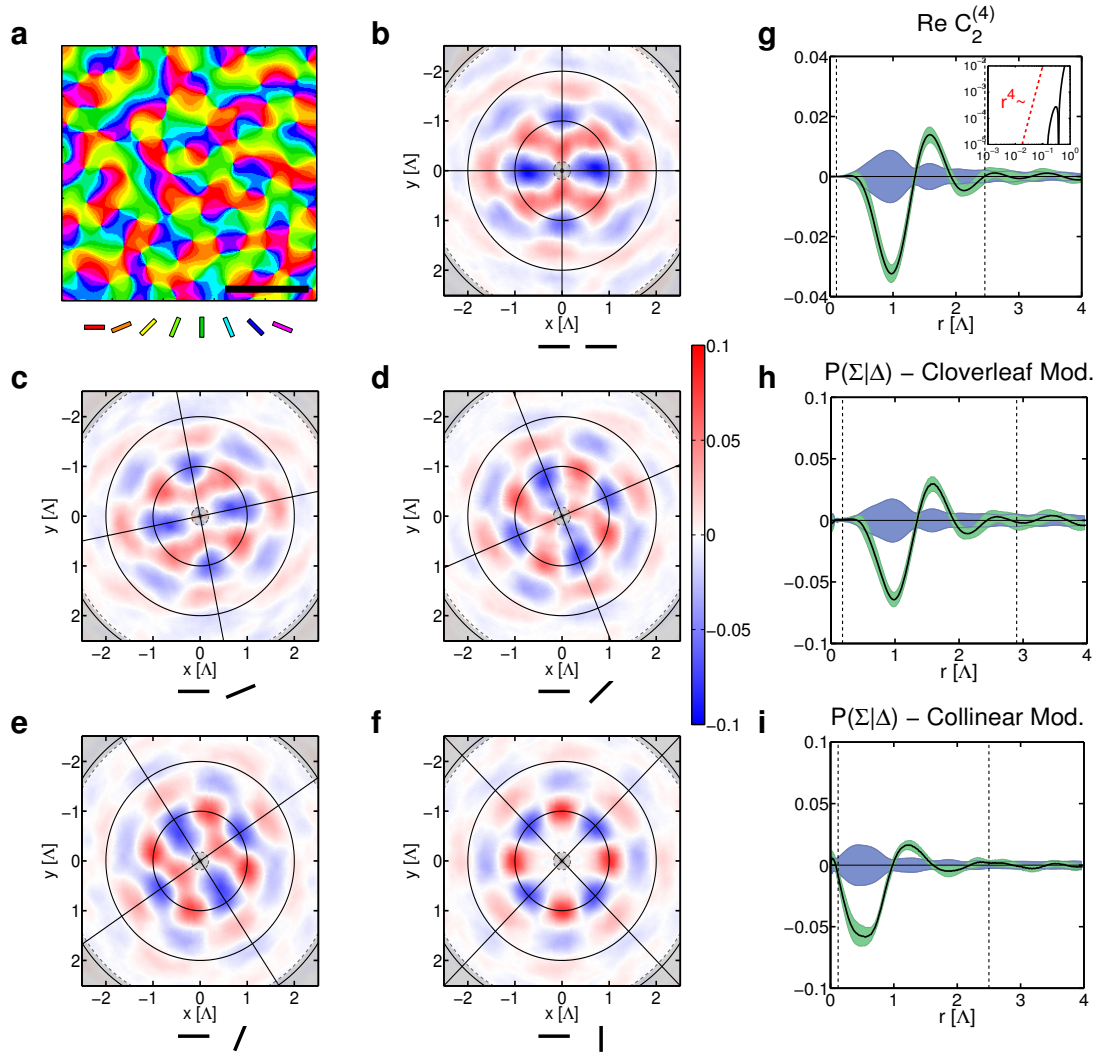
Figure 6.11: Cooccurrence statistics of preferred orientations in the generalized elastic net model for *weak* lateral coupling $\eta = 1/40$ and ($d = 1/2\,\Lambda_{max},\ t = 10\tau_c$). All panels as in Fig. 5.12. Note the quantitative and qualitative similarity with the experimental results.
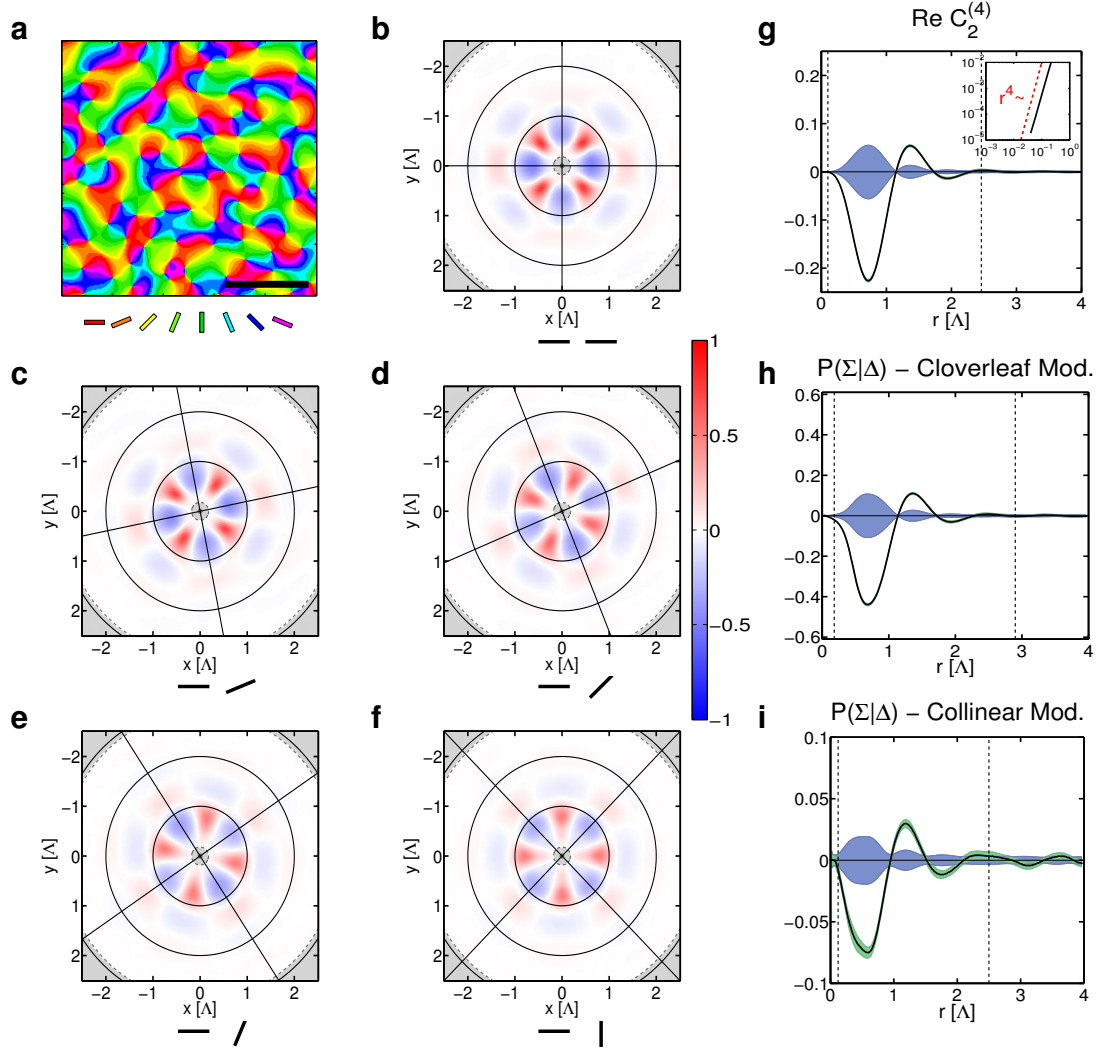
Figure 6.12: Cooccurrence statistics of preferred orientations in the generalized elastic net model for *strong* lateral coupling $\eta = 1/4$ and ($d = 1/2\,\Lambda_{max}$, $t = 10\tau_c$). All panels as in Fig. 5.12. In comparison to the case shown in Fig. 6.11 the size of the cloverleaf component of the cooccurence histogram (**h**) has increased by almost one order of magnitude, whereas the size of the collinear component (**i**) remains similar.

7 Summary and Discussion

Let me end on a more cheerful note. The miracle of the appropriateness of the language of mathematics for the formulation of the laws of physics is a wonderful gift which we neither understand nor deserve. We should be grateful for it and hope that it will remain valid in future research and that it will extend, for better or for worse, to our pleasure, even though perhaps also to our bafflement, to wide branches of learning.

(Eugene Wigner (1960))

In this thesis, we have studied the impact of shift-twist symmetry and shift symmetry breaking on the dynamics and outcome of pattern formation during visual cortical development. We have examined theoretically and through the analysis of experimental data obtained from the tree shrew visual cortex how shift-twist symmetry impacts on the layout of orientation preference columns, a system of visual processing modules that emerges in the visual cortex at about the time of eye opening and that is believed to form through dynamical self-organization driven by neuronal activity and visual experience.

In Chapter 3 we identified the predicted signatures of shift-twist symmetry in statistical ensembles of orientation preference maps, which are accessible to experimental testing. This analysis revealed that shift-twist symmetry manifests itself in the appearance of a second nontrivial correlation function C_2 with a four-fold angular symmetry and a characteristic cloverleaf shape. We defined an order parameter q which quantifies the degree of broken shift symmetry, and can assume positive and negative values in the range from -1 to 1. We find that shift symmetry breaking induces a coupling of the orientation map to the visuotopic map. For $q > 0$ domains in the orientation map which are selective for cardinal orientations ($0°$ and $90°$) tend to organize along the horizontal and vertical axes of the visuotopic map, whereas oblique domains tend to organize along the two oblique axes. For $q < 0$ the opposite is found, i.e. cardinal domains organize along the two oblique axes, oblique domains along the horizontal and vertical axes. This effect becomes more pronounced with increasing $|q|$. We introduced an analytically tractable family of Gaussian ensembles and showed that their pinwheel densities are insensitive to the degree of broken shift-symmetry. We conclude that the strict lower bound on the pinwheel density at the initial stage of map formation, derived by Wolf and Geisel [13] under the assumption of shift symmetry does not change when the shift symmetry assumption is relaxed. We also examined the general mathematical structure of orientation cooccurrence histograms and showed that

they are, in general, predicted to exhibit both a 2-fold and 4-fold angular symmetry, although Gaussian ensembles cannot express a 2-fold component.

In Chapter 4 we examined the impact of shift-twist symmetry on dynamical models of orientation map development. To this end we derived the general form of amplitude equations for a cellular instability with shift-twist symmetric linear part and calculated their stationary solutions and stability. Shift symmetry breaking was mediated by introducing a novel term, linear in z, weighted by factor ϵ, that controls the strength of symmetry breaking. We found that such models are highly sensitive to the presence of terms imposed by shift-twist symmetry. We characterized the impact of shift symmetry breaking on the different pattern phases and found that it differs qualitatively for periodic and aperiodic patterns. With increasing shift symmetry breaking, phases of pinwheel free stripe patterns are gradually replaced by rhombic pinwheel crystals. Phases of irregular aperiodic, pinwheel rich patterns are basically robust with respect to shift symmetry breaking. For such patterns shift symmetry breaking above a critical level ϵ_* leads to a collapse of the massive multistability of different solutions that is found for low degrees of symmetry breaking. Up to this critical level, models exhibiting $E(2)$ and $E(2) \times U(1)$ symmetry seem to be topologically conjugate to one another. Statistical measures of shift symmetry breaking, as those developed in Chapter 3, are predicted to be highly sensitive reporters of the presence of even weak symmetry breaking terms in this regime. For $\epsilon \neq 0$ solution planforms exhibit shift symmetry breaking, much in the way encountered in the Gaussian ensembles, which can be quantified by q. For quasiperiodic attractors of dynamical models we find $q = \epsilon/\epsilon_*$. The Swift-Hohenberg model of Euclidean symmetry considered here predicts that aperiodic pinwheel rich patterns resembling the architecture of the primary visual cortex are only stable when long-range interactions dominate pattern selection, confirming previous predictions of a model of higher $E(2) \times U(1)$ symmetry [37].

In Chapter 5 we analyzed a large dataset of orientation preference maps from the tree shrew visual cortex for the predicted signatures of shift-twist symmetry. For all quantities estimated from the experimental data we provide confidence intervals and significance values based on custom designed nonparametric permutation tests. We found that there are statistically highly significant signatures of shift-twist symmetry in the layout of the tree shrew maps. We calculated the correlation function of the map ensemble and extracted the degree of shift symmetry breaking from the cloverleaf component of C_2, which amounts to approximately $q \approx -10\,\%$. Hence shift symmetry breaking in the tree shrew visual cortex is of negative type and appears to be relatively weak. Furthermore, we find clear deviations of the map statistics from Gaussianity indicated by a substantial two-fold component of the orientation cooccurrence histogram, which is always absent in Gaussian ensembles. This two-fold component which also occurs with a negative sign indicates that within a radius of one typical wavelength Λ around a given site with a given orientation preference *less* cortical area is recruited to detect collinear contour arrangements but *more* cortical area is recruited to detect parallel arrangements. This finding stands in apparent contrast to (1) the statistics of oriented edges in natural scenes, which exhibit a strong bias for collinear arrangements [52] as well as to (2) the axial specificity of long range connections in the tree shrew visual cortex, which, over distances typically larger that Λ, are much more likely to link collinear sites rather than parallel ones [27].

To explain these findings, in Chapter 6, we studied a biologically motivated model in which pattern formation is driven by pairs of contour stimuli mimicking the statistics of natural scene stimuli. We study map formation within the framework of the elastic network model [17, 19], a

simple model for the activity dependent development of orientation preference. In its original form the elastic net describes how a sequence of afferent activity patterns elicited by a sequence of randomly oriented, isolated point stimuli leads to the formation of visuotopic and orientation preference maps via a competitive Hebbian learning rule. We propose a generalization of the elastic net for a much broader class of stimuli, e.g. spatially extended contours. This allows to examine how the higher order statistics of visual scenes affect map formation. In natural images pairs of edges exhibit a strong tendency to occur in collinear arrangements [52]. To model this we define a simple stimulus ensemble which consists of pairs of oriented edges and exhibits a variable degree of collinearity κ. The dynamics of the order parameter field $z(\mathbf{x})$, averaged over this stimulus ensemble, yields an effective dynamics of the form studied in 4, which still depends on the stimulus statistics, although implicitly through the correlation functions of the stimulus ensemble. A linear stability analysis reveals the characteristic time and length scales of the emerging pattern and, moreover, yields an analytic expression for ϵ. It turns out that the sign of ϵ depends on the statistics of the stimulus ensemble. In particular, we find that in a collinear world $\epsilon < 0$. We check this prediction by numerical integration of the model dynamics for appropriately chosen parameter sets. Signatures of shift-twist symmetry are found in the correlation functions and the pair occurrence histogram. Intriguingly we also observe a 2-fold non-Gaussian contribution like in the tree shrew dataset. We conclude that the shift symmetry breaking of the type and strength observed in tree shrew orientation maps can be induced by the fact that shift symmetry is broken in the statistics of natural images.

Our study is not the first one to point to the fundamental role of Euclidean symmetry in the architecture of the visual cortex and to question how it might affect the structure of orientation maps. Several papers have been published on this subject within the last few years, by Bressloff et al. [23, 82, 47, 83], Thomas and Cowan [59], Lee and Kardar [57] and Mayer et al. [84, 85]. In the following we shortly discuss how these contributions relate to the results of this thesis.

Bressloff et al. of [23] were the ones who introduced the term "shift-twist" symmetry to the neuroscience community and showed how group theoretical concepts of quite abstract nature could be applied to explain certain types of visual hallucination patterns experienced when taking drugs. Guided by the insight that the rules of lateral connectivity in the brain are only respected when rotations of the orientations map are applied together with rotations of the visutopy they developed a dynamical model for the neural activity patterns in the visual cortex by assuming that the orientation map, which defines the arrangement of the neurons, already exists and has a crystalline order. By a linear stability analysis they predicted and classified the activity patterns, that would spontaneously form, once the drug amount exceeds a critical threshold. The class of solutions was restricted to periodic patterns. It turned out that shift-twist symmetry is necessary in order to explain a certain type of hallucination pattern, which would otherwise not occur. Whereas in [23] (periodic) orientation maps are *a priori* assumed, in later papers Bressloff et al. also consider the development of orientation maps, again in a shift-twist symmetric framework. However, the type of pattern is again restricted to periodic solutions (stripes, rhombic pinwheel crystals, hexagons), and the apparent irregularities of realistic patterns are rather attributed to disorder [47]. At the end of his latest paper [83] Bressloff mentions that shift twist symmetry predicts a coupling of the orientation map to the visuotopic map, however, he draws this conclusion within the context of a linear stability analysis, and no attempt is made to actually calculate or to further specify the attractors with the nonlinearity.

The study of Thomas et al. [59], in a similar spirit as Bressloff's, aims at developing a theory

for small systematic variations of the visuotopic map, whose progression on a large scale is assumed regular and undistorted, and predicts that these variations in the visuotopic map are related to systematic variations of the orientation preference map. In particular it predicts a correlation between the gradient of the orientation map and the Jacobian of retinotopic map. This study is motivated by a report of Das and Gilbert [86] who claim to see such systematic variations co-occurring in both maps on a length scale of $50\mu m$. Thomas *et al.* examine the coupled dynamics of variations z and δR over preexisting maps and determine the modes which first become unstable. Depending on the parameters the resulting orientation map is predicted to consist exclusively of even or of odd eigenfunctions. They do, however not consider linear combination of both. In terms of our results this compares to the regime where symmetry is maximally broken, either $\epsilon/\epsilon_* > 1$ or $\epsilon/\epsilon_* < -1$, for which we also find that the solution is described either by a superposition of exclusively even or odd modes. However, the interesting regime, $|\epsilon|/\epsilon_* \ll 1$ is not addressed in Thomas *et al.*'s theory, neither in Bressloff's. Also, similar to the work of Bressloff *et al.* this analysis is restricted to patterns which are regular, having the periodicity of a rhombic or hexagonal lattice, and thus is unable to address the issue of higher order planforms, which result in much more realistic patterns, which are irregular and aperiodic.

In their paper from 2003 Lee and Kardar use a model similar to a Swift-Hohenberg equation (2.10) for modelling orientation map development. A local, stabilizing nonlinearity is assumed. The authors are aware of the fact that such a local nonlinearity, will eventually result in stripe patterns without pinwheels as a consequence of pinwheel annihilation. Their intention in this paper is to demonstrate that shift-twist symmetry contributes a stabilizing factor for pinwheels and thus explains why pinwheel configurations are stable. Retinotopy is assumed to be fixed, like in our case and shift symmetry breaking is achieved by introducing a linear convolution term. However, the way their kernel transforms under spatial rotations, implies a 2-fold symmetry, not a 4-fold symmetry like in our case, and thus describes the situation of a vector field v which transforms into $-v$ when rotated by 180° and not into itself as the field of orientations z does. Due to this reason their results differ from ours in many respects. Lee and Kardar attempted to determine a lower bound on the defect density, but failed to obtain a closed form solution for general degree of shift symmetry breaking. Nevertheless, they derive expressions for the limiting cases of zero and maximal degree of shift symmetry breaking, and find that the results differ. In conclusion, for vector fields the defect density depends on the degree of shift symmetry breaking, unlike in the case of orientation maps, where we found that the pinwheel density remains the same. This is not surprising, since for vector fields $v(\mathbf{x})$ the general form of $C_2(\mathbf{r}) = \langle v(\mathbf{0})v(\mathbf{r})\rangle$ reads $C_2(x, y) = (x + iy)^2 f(|x^2 + y^2|)$. Second order derivatives of $C_2(\mathbf{r})$ when evaluated at $\mathbf{r} = 0$ now generally do not vanish, therefore the covariance matrix in Eq.(3.28) will explicitly depend on $f(0)$. Lee and Kardar performed numerical simulations of the dynamical equation (for one single fixed value of shift symmetry breaking, though) to determine the attractor of the dynamics and found that the shift symmetric dynamics exhibits plane wave solutions (as expected), whereas shift symmetry breaking typically results in 'pinwheel crystals'. From this observation they conclude that pinwheels are stabilized by shift-twist symmetry. Apparently these 'pinwheel crystals' consist of two pairs of modes whose wavevectors are orthogonal to each other. As we have shown in Chapter (4) pinwheel crystals are indeed expected to occur in a large region of parameter space for sufficiently strong symmetry breaking, where they progressively invade regions where stripes are found. However, our theory predicts that in general they should form intersection angles of 45° (and not 90°). This apparent discrepancy can be traced back to the same cause mentioned before. We found that pinwheel crystals are energetically favored

to stripe patterns once a certain strength of symmetry breaking is reached (Fig.4.1), although they might still be coexisting with stripes. In this sense, the statement of Lee and Kardar agrees with our result. However, our conclusions are striking different. Compared to real orientation maps the pinwheel density of pinwheel crystals is too small and the patterns are too regular. We claim that shift symmetry breaking on its own cannot account for the patterns observed in the brain and that an alternative mechanism is needed in order to explain realistic patterns, such as provided by the specific type of long-range interactions discussed in Chapter 4 and 2.

Another system in which pinwheel crystals are observed, however, this time with the predicted crossing angle of 45°, was studied by Mayer *et al.* and reported in [84, 85]. But again, also this type of model is unable to predict realistic, irregular and aperiodic patterns of orientation maps.

To summarize, we find that all studies on the possible effects of shift-twist symmetry on orientation map development in the brain, which have been performed so far, yield an incomplete description of the situation in the brain, since these findings are restricted to the analysis of periodic solutions, i.e. stripes, pinwheel crystals or pinwheel hexagons.

This thesis is the first to analyze the consequences of shift-twist symmetry and of shift symmetry breaking on the pattern selection and pinwheel stability for a realistic type of aperiodic solutions. In particular, we find that in the region of phase space where aperiodic solutions occur pinwheel production is *insensitive* to shift symmetry breaking, opposed to the result of Lee and Kardar. Whereas all previous studies addressed the limiting case of maximally broken shift symmetry, we analyze the entire range from the full shift symmetric to the full shift-twist symmetric case. We don't find an all or nothing phenomenon in our models, but instead, observe a continuous transition and reorganization of the phases as a function of the parameter ϵ/ϵ_* controlling the degree of shift symmetry breaking.

Our study is the first one to clearly demonstrate shift symmetry breaking in experimental observations. In fact, our findings stresses the gradual nature of the effect, since shift symmetry breaking in the tree shrew visual cortex turns out to be relatively weak. Our results reveals a non-Gaussian statistics of orientation preference maps and a coupling to the visuotopic map of the negative type. These are main features that theoretical studies have to explain and that are not predicted by the generic approaches used in our theoretical studies in Chapters 3 and 4 or by any of the previously published theoretical works.

The results of the final chapter show that the effects above can be explained by models that take natural scene statistics and cortical activity patterns into account. All of the non-anticipated phenomena observed in the tree shrew dataset, i.e. negative type coupling and non-Gaussian statistics of orientation maps, revealed by a non-vanishing 2-fold component in the pair co-occurrence statistics, naturally emerge when map development is considered to occur as the result of competitive Hebbian learning in the primary visual cortex which is induced by afferent cortical activity patterns elicited by naturally occurring visual scenes. Our analysis shows that the characteristic features of such scenes, collinearity of their constituting contour elements, as well as their symmetry under Euclidean transformations exerts a net effect on the dynamics of the orientation maps which leads to a shift symmetry breaking in the linear terms exactly of the type *a priori* postulated in Chapters 2-4. We can also provide an explanation for the observation that the signatures of shift-twist symmetry in the brain are of the negative type, which at first appears contra-intuitive, since the statistics of contour elements of the visual world is of positive type. We find that this sign flip occurs as a consequence of the competition between neurons in

the visual cortex, which is introduced by the competitive Hebbian scenario. Interestingly, this sign flip has the consequence that less cortical space is devoted to the coding of combinations of features which occur with a higher than average probability. This can be best seen by comparing Fig.5.12(**b**) to Fig.**6.2**(**c**). The high degree of collinearity in natural images contrast with the reduced probability of collinear arrangements in the orientation preference maps. Why spend cortical resources to code for the obvious? It would be an interesting question to find out whether an interpretation of our findings in terms of redundancy reduction[87] could be useful.

The particular type of shift-twist symmetry induced coupling of the orientation map to the visuotopic map presented here and the predictions that this coupling is controlled by the statistics of natural scenes is novel in the field. Contrary to the situation found for other pairs of neural selectivities, such as orientation preference and ocular dominance, or orientation preference and direction selectivity, where clear evidence for correlations between both systems of maps exists, the situation is, until now, unclear for orientation preference and visuotopy, and the results in literature do conflict. Whereas Das and Gilbert claim to see systematic variations in and correlations between the local rates of change of both, orientation selectivity and spatial selectivity in the cat on a scale of $50 - 100\,\mu m$[86] (this result inspired Thomas *et al.* to their analysis [59]) a subsequent study of Buzas *et al.* [88], also performed in the cat visual cortex, found no evidence of such type of correlations in the receptive field scatter and OPM scatter. But also see [89, 90, 70]. Anyway, this type of correlation, which was motivated from early days simulations of the elastic net [17] predicts correlations in the *rate* of change (which is a scalar and local quantity) of the orientation preference and visuotopic map. Our results suggest that it might be useful to reassess this and similar data with respect to *nonlocal* correlations, which also takes relative positions of cortical sites and relative orientation preferences into account. In any case our findings clearly report that correlations of the orientation to the visuotopic map on a scale of $500 - 1000\mu m$ do exist. These particular correlations are consistent with the predictions from shift symmetry and yield clear evidence that shift symmetry is weakly broken in the visual cortex. Orientation map and visuotopic map are thus not independent.

Given the complexity of the neural substrate and the number of compromising factors which one faces when analyzing data from the living brain it is amazing that at the end of the day a structure in the dataset appears which can be understood in terms of a simple symmetry principle. Symmetries have a long story of success in physics and point to some order which is deeply rooted in the fundamental equations of our world. That they turn out to be a useful concept for understanding an organisational aspect of the neural system, points at the essential role attributed to self-organisation in the developing brain.

Bibliography

[1] N. V. Swindale, J. A. Matsubara, and M. S. Cynader. Surface organization of orientation and direction selectivity in cat area 18. *J Neurosci*, 7(5):1414–1427, May 1987.

[2] G. G. Blasdel. Orientation selectivity, preference, and continuity in monkey striate cortex. *J Neurosci*, 12(8):3139–3161, Aug 1992.

[3] Kenichi Ohki, Sooyoung Chung, Prakash Kara, Mark Hubener, Tobias Bonhoeffer, and R Clay Reid. Highly ordered arrangement of single neurons in orientation pinwheels. *Nature*, 442(7105):925–928, Aug 2006.

[4] David Hubel. *Eye, Brain, and Vision*. Scientific American Library. Henry Holt & Company, 1988.

[5] D. H. Hubel and T. N. Wiesel. Receptive fields, binocular interaction and functional architecture in the cat's visual cortex. *J Physiol*, 160:106–154, Jan 1962.

[6] A. Grinvald, R. D. Frostig, E. Lieke, and R. Hildesheim. Optical imaging of neuronal activity. *Physiol Rev*, 68(4):1285–1366, Oct 1988.

[7] T. Bonhoeffer and A. Grinvald. Iso-orientation domains in cat visual cortex are arranged in pinwheel-like patterns. *Nature*, 353(6343):429–431, Oct 1991.

[8] T. Bonhoeffer and A. Grinvald. The layout of iso-orientation domains in area 18 of cat visual cortex: optical imaging reveals a pinwheel-like organization. *J Neurosci*, 13(10):4157–4180, Oct 1993.

[9] B. Chapman, M. P. Stryker, and T. Bonhoeffer. Development of orientation preference maps in ferret primary visual cortex. *J Neurosci*, 16(20):6443–6453, Oct 1996.

[10] M. C. Crair, D. C. Gillespie, and M. P. Stryker. The role of visual experience in the development of columns in cat visual cortex. *Science*, 279(5350):566–570, Jan 1998.

[11] L. E. White, D. M. Coppola, and D. Fitzpatrick. The contribution of sensory experience to the maturation of orientation selectivity in ferret visual cortex. *Nature*, 411(6841):1049–1052, Jun 2001.

[12] J. Sharma, A. Angelucci, and M. Sur. Induction of visual orientation modules in auditory cortex. *Nature*, 404(6780):841–847, Apr 2000.

[13] Fred Wolf and Theo Geisel. Spontaneous pinwheel annihilation during visual development. *Nature*, 395:73–78, 1998.

[14] N. V. Swindale. A model for the formation of ocular dominance stripes. *Proc R Soc Lond B Biol Sci*, 208(1171):243–264, Jun 1980.

[15] N. V. Swindale. A model for the formation of orientation columns. *Proc R Soc Lond B Biol Sci*, 215(1199):211–230, May 1982.

[16] N. V. Swindale. The development of topography in the visual cortex: a review of models. *Network*, 7(2):161–247, May 1996.

[17] R. Durbin and G. Mitchison. A dimension reduction framework for understanding cortical maps. *Nature*, 343(6259):644–647, Feb 1990.

[18] Obermayer, Blasdel, and Schulten. Statistical-mechanical analysis of self-organization and pattern formation during the development of visual maps. *Physical Review A*, 45(10):7568–7589, May 1992.

[19] E. Erwin, K. Obermayer, and K. Schulten. Models of orientation and ocular dominance columns in the visual cortex: a critical comparison. *Neural Comput*, 7(3):425–468, May 1995.

[20] A. A. Koulakov and D. B. Chklovskii. Orientation preference patterns in mammalian visual cortex: a wire length minimization approach. *Neuron*, 29(2):519–527, Feb 2001.

[21] Myoung Won Cho and Seunghwan Kim. Understanding visual map formation through vortex dynamics of spin hamiltonian models. *Phys. Rev. Lett.*, 92(1):018101, Jan 2004.

[22] Fred Wolf. Symmetry, multistability, and long-range interactions in brain development. *Phys. Rev. Lett.*, 95(20):208701, 2005.

[23] P C Bressloff, J D Cowan, M Golubitsky, P J Thomas, and M C Wiener. Geometric visual hallucinations, euclidean symmetry and the functional architecture of striate cortex. *Philos Trans R Soc Lond B*, 356(1407):299–330, Mar 2001.

[24] O.D. Creutzfeldt. *Cortex Cerebri: performance, structural and functional organization of the cortex.* Oxford University Press, 1995.

[25] S. LeVay and S.B. Nelson. *Columnar Organization of the visual cortex.*, chapter 11, pages 266–315. Macmillan, Houndsmill, 1991.

[26] G. G. Blasdel and G. Salama. Voltage-sensitive dyes reveal a modular organization in monkey striate cortex. *Nature*, 321(6070):579–585, 1986.

[27] W H Bosking, Y Zhang, B Schofield, and D Fitzpatrick. Orientation selectivity and the arrangement of horizontal connections in tree shrew striate cortex. *J. Neurosci.*, 17(6):2112–2127, Mar 1997.

[28] B Chapman, I Godecke, and T Bonhoeffer. Development of orientation preference in the mammalian visual cortex. *J Neurobiol*, 41(1):18–24, Oct 1999.

[29] E. Bodenschatz, W. Pesch, and G. Ahlers. Recent developments in rayleigh-benard convection. *Annual Review of Fluid Mechanics*, 32:709–778, 2000.

[30] M. C. Cross and P. C. Hohenberg. Pattern formation outside of equilibrium. *Rev. Mod. Phys.*, 65(3):851, Jul 1993.

[31] A. Kudrolli and J. P. Gollub. Localized spatiotemporal chaos in surface waves. *Phys. Rev. E*, 54(2):R1052–R1055, Aug 1996.

[32] A. Kudrolli, B. Pier, and J. P. Gollub. Superlattice patterns in surface waves. *Phys. D*, 123(1-4):99–111, 1998.

[33] K. D. Miller. A model for the development of simple cell receptive fields and the ordered arrangement of orientation columns through activity-dependent competition between on- and off-center inputs. *J Neurosci*, 14(1):409–441, Jan 1994.

[34] Fred Wolf. *Strukturbildung in der Entwicklung des visuellen Kortex*. PhD thesis, Goethe University, Frankfurt, Germany, 1999.

[35] V. Braitenberg and A. Schüz. *Cortex: statistics and geometry of neuronal connectivity*. Springer, Berlin, 1998.

[36] N. D. Mermin. The topological theory of defects in ordered media. *Reviews of Modern Physics*, 51(3):591+, July 1979.

[37] Fred Wolf. Les houches 2003 lecture notes. In *Methods and Models in Neurophysics*. Elsevier, Amsterdam, 2005.

[38] E. M. Callaway and L. C. Katz. Emergence and refinement of clustered horizontal connections in cat striate cortex. *J Neurosci*, 10(4):1134–1153, Apr 1990.

[39] S. Löwel and W. Singer. Selection of intrinsic horizontal connections in the visual cortex by correlated neuronal activity. *Science*, 255(5041):209–212, Jan 1992.

[40] A. Das and C. D. Gilbert. Long-range horizontal connections and their role in cortical reorganization revealed by optical recording of cat primary visual cortex. *Nature*, 375(6534):780–784, Jun 1995.

[41] M. Weliky and L. C. Katz. Functional mapping of horizontal connections in developing ferret visual cortex: experiments and modeling. *J Neurosci*, 14(12):7291–7305, Dec 1994.

[42] E. S. Ruthazer and M. P. Stryker. The role of activity in the development of long-range horizontal connections in area 17 of the ferret. *J Neurosci*, 16(22):7253–7269, Nov 1996.

[43] R. Malach, Y. Amir, M. Harel, and A. Grinvald. Relationship between intrinsic connections and functional architecture revealed by optical imaging and in vivo targeted biocytin injections in primate striate cortex. *Proc Natl Acad Sci U S A*, 90(22):10469–10473, Nov 1993.

[44] Alessandra Angelucci, Jonathan B Levitt, Emma J S Walton, Jean-Michel Hupe, Jean Bullier, and Jennifer S Lund. Circuits for local and global signal integration in primary visual cortex. *J Neurosci*, 22(19):8633–8646, Oct 2002.

[45] K. E. Schmidt, R. Goebel, S. Löwel, and W. Singer. The perceptual grouping criterion of colinearity is reflected by anisotropies of connections in the primary visual cortex. *Eur J Neurosci*, 9(5):1083–1089, May 1997.

[46] S Löwel and W Singer. *Experience-Dependent Plasticity of Intracortical Connections*, volume Perceptual Learning, pages 3–18. MIT Press, 2002.

[47] Paul C Bressloff and Jack D Cowan. The functional geometry of local and horizontal connections in a model of v1. *J Physiol Paris*, 97(2-3):221–236, Mar 2003.

[48] B. Chapman and M. P. Stryker. Origin of orientation tuning in the visual cortex. *Curr Opin Neurobiol*, 2(4):498–501, Aug 1992.

[49] J. Zinn-Justin. *Quantum Field Theory and Critical Phenomena*. Clarendon Press / Oxford Science Publications, Oxford, 2nd edition, 1993.

[50] R.J. Adler. *The Geometry of Random Fields.* Wiley, New York, 1981.

[51] Matthias Kaschube, Fred Wolf, Theo Geisel, and Siegrid Löwel. Genetic influence on quantitative features of neocortical architecture. *J Neurosci*, 22(16):7206–7217, Aug 2002.

[52] M Sigman, G A Cecchi, C D Gilbert, and M O Magnasco. On a common circle: natural scenes and gestalt rules. *Proc. Natl. Acad. Sci. U. S. A.*, 98(4):1935–1940, Feb 2001.

[53] P.G. de Gennes and J. Prost. *The Physics of Liquid Crystals.* Oxford Science Publications, 1993.

[54] Izrail S. Gradshtein and Iosif Ryzhik. *Table of Integrals, Series, and Products.* Academic Press, New York, 6th edition, 2000.

[55] Milton Abramowitz and Irene A. Stegun. *Handbook of Mathematical Functions with Formulas, Graphs, and Mathematical Tables.* Dover, New York, ninth dover printing, tenth gpo printing edition, 1964.

[56] J. Swift and P. C. Hohenberg. Hydrodynamic fluctuations at the convective instability. *Phys. Rev. A*, 15(1):319–328, Jan 1977.

[57] Ha Youn Lee, Mehdi Yahyanejad, and Mehran Kardar. Symmetry considerations and development of pinwheels in visual maps. *Proc. Natl. Acad. Sci. U. S. A.*, 100(26):16036–16040, Dec 2003.

[58] P. Manneville. *Dissipative Structures and Weak Turbulence.* Academic Pres, San Diego, CA, 1990.

[59] Peter J Thomas and Jack D Cowan. Symmetry induced coupling of cortical feature maps. *Phys. Rev. Lett.*, 92(18):188101, May 2004.

[60] J.S. Lund, D. Fitzpatrick, and A.L. Humphrey. *Cerebral cortex.*, volume 3, chapter The striate visual cortex in the tree shrew., pages 157 – 205. Plenum Press, 1985.

[61] R. D. Martin. *Primate Origins and Evolution. A phylogenetic reconstruction.* Princeton University Press, Princeton NJ, 1990.

[62] D. Fitzpatrick. The functional organization of local circuits in visual cortex: insights from the study of tree shrew striate cortex. *Cereb Cortex*, 6(3):329–341, 1996.

[63] Jon Kaas. Convergences in the modular and areal organization of the forebrain of mammals: implications for the reconstruction of forebrain evolution. *Brain Behav Evol*, 59(5-6):262–272, 2002.

[64] Jan E Janecka, Webb Miller, Thomas H Pringle, Frank Wiens, Annette Zitzmann, Kristofer M Helgen, Mark S Springer, and William J Murphy. Molecular and genomic data identify the closest living relative of primates. *Science*, 318(5851):792–794, Nov 2007.

[65] J. H. Kaas, W. C. Hall, H. Killackey, and I. T. Diamond. Visual cortex of the tree shrew (tupaia glis): architectonic subdivisions and representations of the visual field. *Brain Res*, 42(2):491–496, Jul 1972.

[66] A. L. Humphrey, L. C. Skeen, and T. T. Norton. Topographic organization of the orientation column system in the striate cortex of the tree shrew (tupaia glis). ii. deoxyglucose mapping. *J Comp Neurol*, 192(3):549–566, Aug 1980.

[67] K. S. Rockland and J. S. Lund. Widespread periodic intrinsic connections in the tree shrew visual cortex. *Science*, 215(4539):1532–1534, Mar 1982.

[68] K. S. Rockland and J. S. Lund. Intrinsic laminar lattice connections in primate visual cortex. *J Comp Neurol*, 216(3):303–318, May 1983.

[69] W. H. Bosking, R. Kretz, M. L. Pucak, and D. Fitzpatrick. Functional specificity of callosal connections in tree shrew striate cortex. *J Neurosci*, 20(6):2346–2359, Mar 2000.

[70] William H Bosking, Justin C Crowley, and David Fitzpatrick. Spatial coding of position and orientation in primary visual cortex. *Nat Neurosci*, 5(9):874–882, Sep 2002.

[71] Francois Mooser, William H Bosking, and David Fitzpatrick. A morphological basis for orientation tuning in primary visual cortex. *Nat Neurosci*, 7(8):872–879, Aug 2004.

[72] L. E. White. Personal communication.

[73] Matthias Kaschube. *Pattern Selection in the Visual Cortex*. PhD thesis, Göttingen University, 2005.

[74] N. V. Swindale, D. Shoham, A. Grinvald, T. Bonhoeffer, and M. Hübener. Visual cortex maps are optimized for uniform coverage. *Nat Neurosci*, 3(8):822–826, Aug 2000.

[75] Geoffrey J Goodhill. Contributions of theoretical modeling to the understanding of neural map development. *Neuron*, 56(2):301–311, Oct 2007.

[76] G A Cecchi. personal communication, 2008.

[77] Daniel L. Ruderman and William Bialek. Statistics of natural images: Scaling in the woods. *Physical Review Letters*, 73(6):814+, 1994.

[78] W S Geisler, J S Perry, B J Super, and D P Gallogly. Edge co-occurrence in natural images predicts contour grouping performance. *Vision Res*, 41(6):711–724, Mar 2001.

[79] Matthias Kaschube, Fred Wolf, Theo Geisel, and S. Löwel. The prevalence of colinear contours in the real world. *Neurocomputing*, 38-40:1335, 2001.

[80] Norbert Krüger and Florentin Wörgötter. Multi-modal estimation of collinearity and parallelism in natural image sequences. *Network*, 13(4):553–576, Nov 2002.

[81] James H Elder and Richard M Goldberg. Ecological statistics of gestalt laws for the perceptual organization of contours. *J Vis*, 2(4):324–353, 2002.

[82] Paul C Bressloff and Jack D Cowan. An amplitude equation approach to contextual effects in visual cortex. *Neural Comput*, 14(3):493–525, Mar 2002.

[83] Paul C Bressloff. Spontaneous symmetry breaking in self-organizing neural fields. *Biol Cybern*, 93(4):256–274, Oct 2005.

[84] Norbert Mayer, J. Michael Herrmann, and Theo Geisel. Curved feature metrics in models of visual cortex. *Neurocomputing*, 44-46:533–539, 2002.

[85] N. Michael Mayer, Matthew Browne, J. Michael Herrmann, and Minoru Asada. Symmetries, non-euclidean metrics, and patterns in a swift-hohenberg model of the visual cortex. *Biol Cybern*, 99(1):63–78, Jul 2008.

[86] A. Das and C. D. Gilbert. Distortions of visuotopic map match orientation singularities in primary visual cortex. *Nature*, 387(6633):594–598, Jun 1997.

[87] H. Barlow. Redundancy reduction revisited. *Network*, 12(3):241–253, Aug 2001.

[88] Peter Buzas, Maxim Volgushev, Ulf T Eysel, and Zoltan F Kisvarday. Independence of visuotopic representation and orientation map in the visual cortex of the cat. *Eur J Neurosci*, 18(4):957–968, Aug 2003.

[89] P. A. Hetherington and N. V. Swindale. Receptive field and orientation scatter studied by tetrode recordings in cat area 17. *Vis Neurosci*, 16(4):637–652, 1999.

[90] N. V. Swindale and H.-U. Bauer. Application of kohonen's self-organizing feature map algorithm to cortical maps of orientation and direction preference. *Proc.R.Soc.Lond. B*, 265:827–838, 1998.

Acknowledgments

Lebenslauf

Name   Michael Schnabel

Ausbildung

1993   Abitur am Bischof Neumann Gymnasium in Königstein/Ts.

1993 - 1994   Zivildienst

1994 - 1996   Johann-Wolfgang-Goethe Universitat, Frankfurt am Main
                 Physikstudium, Vordiplom

1996 - 1999   Universität Regensburg, Physikstudium, Diplom

seit 2000   Doktorand in der Abteilung Nichtlineare Dynamik
                 bei Prof. Dr. Theo Geisel am Max-Planck Institut für Dynamik
                 und Selbstorganisation, Göttingen

2001   Sommerschule "Dynamics of Neural Networks"
                 (D. Kleinfeld, S. Seung, M. Tsodyks),
                 Kavli Institute for Theoretical Physics, Santa Barbara, USA

2002   Sommerschule: "Non-equilibrium in Physics and Biology"
                 (A. Buka, P. Coullet, L. Kramer) in Peyresq, Frankreich

2003   Sommerschule "Methods and Models in Neurophysics"
                 (C. Chow, B. Gutkin, D. Hansel, C. Meunier, I. Segev)
                 in Les Houches, Frankreich

2004   Teilnahme am "Workshop on Nodal Domains"
                 (U. Smilansky, G. Foltin)
                 Weizmann Institute of Science, Rehovot, Israel

2008   Teilnahme am Workshop "Anatomy, Development, and
                 Evolution of the Brain"
                 (K. Kosik, A. Koulakov, G. Lemke, S. Solla, S. Wang),
                 Kavli Institute for Theoretical Physics, Santa Barbara, USA